

AD-A138 382

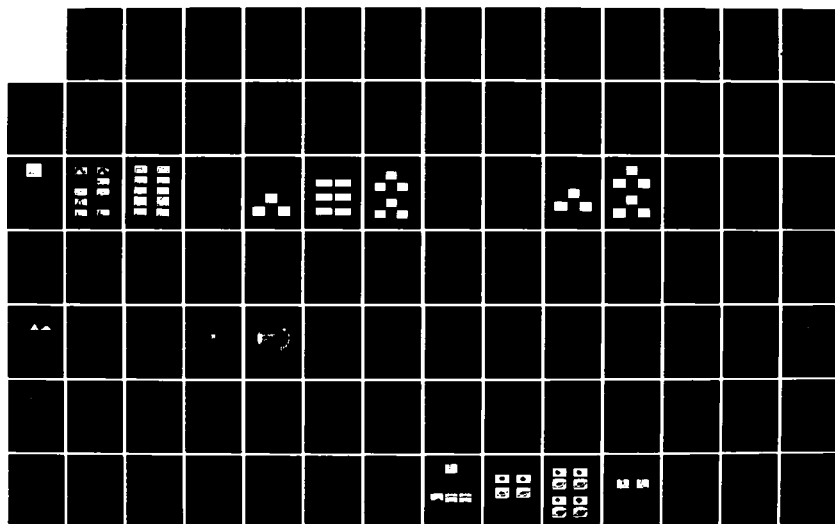
SCALING STUDIES OF EFFICIENT RAMAN CONVERTERS(U)
 NORTHROP RESEARCH AND TECHNOLOGY CENTER PALOS VERDES
 PENINSULA CA H KOMINE ET AL. 01 JUL 83 NRTC-83-09R
 N00014-81-C-0637

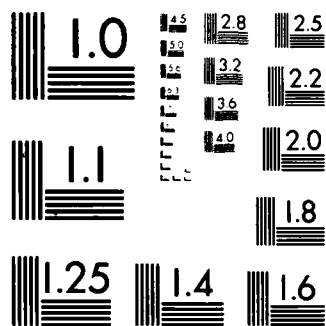
1/3

UNCLASSIFIED

F/G 20/6

NL





MICROCOPY RESOLUTION TEST CHART
NATIONAL BUREAU OF STANDARDS-1963-A

ADA130382

DTIC FILE COPY

10

NRTC-83-09R

SCALING STUDIES OF EFFICIENT RAMAN
CONVERTERS

FINAL REPORT

JULY 1, 1983

DTIC
ELECTE
JUL 18 1983
A

NORTHROP

Research and Technology Center

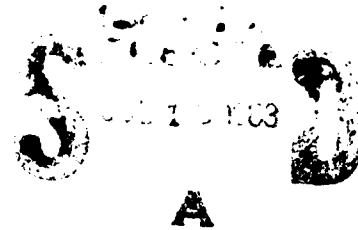
33 07 15 006

NRTC-83-09R

SCALING STUDIES OF EFFICIENT RAMAN
CONVERTERS

FINAL REPORT

JULY 1, 1983



The views and conclusions contained in this document are those of the authors and should not be interpreted as necessarily representing the official policies, either expressed or implied, of the Defense Advanced Research Projects Agency, the Office of Naval Research, or the United States Government.

REPORT DOCUMENTATION PAGE		READ INSTRUCTIONS BEFORE COMPLETING FORM
1. REPORT NUMBER NRTC-83-09R	2. GOVT ACCESSION NO. AD-A130382	3. RECIPIENT'S CATALOG NUMBER
4. TITLE (and Subtitle) Scaling Studies of Efficient Raman Converters		5. TYPE OF REPORT & PERIOD COVERED FINAL REPORT May, 1981 - April, 1983
		6. PERFORMING ORG. REPORT NUMBER
7. AUTHOR(s) Dr. H. Komine, Principal Investigator Associate Investigators: Dr. S. J. Brosnan, Mr. W.H. Long, Jr, Drs. J. Holliday & E. Stappaerts		8. CONTRACT OR GRANT NUMBER(s) N00014-81-C-0637
9. PERFORMING ORGANIZATION NAME AND ADDRESS Northrop Research and Technology Center One Research Park Palos Verdes Peninsula, CA 90274		10. PROGRAM ELEMENT, PROJECT, TASK AREA & WORK UNIT NUMBERS Organization 350
11. CONTROLLING OFFICE NAME AND ADDRESS LtCol Rettig Benedict, Jr. Defense Advanced Research Projects Agency Arlington, Virginia 22209		12. REPORT DATE 1 July 1983
		13. NUMBER OF PAGES 198
14. MONITORING AGENCY NAME & ADDRESS (if different from Controlling Office) Office of Naval Research 1030 East Green Street Pasadena, CA 91106		15. SECURITY CLASS. (of this report) UNCLASSIFIED
		15a. DECLASSIFICATION/DOWNGRADING SCHEDULE
16. DISTRIBUTION STATEMENT (of this Report) Unlimited <div style="border: 1px solid black; padding: 5px; display: inline-block; margin-top: 10px;">This document has been approved for public release and sale; its distribution is unlimited.</div>		
17. DISTRIBUTION STATEMENT (of the abstract entered in Block 20, if different from Report) Unlimited		
18. SUPPLEMENTARY NOTES		
19. KEY WORDS (Continue on reverse side if necessary and identify by block number) XeF laser (heated); injection locking; Raman conversion; blue-green lasers; Raman beam cleanup; repetitively-pulsed excimer laser; flowing hydrogen cell		
20. ABSTRACT (Continue on reverse side if necessary and identify by block number) This report contains the results of analytical and experimental work which address various technical issues relevant to the scalability of a Raman converter system to higher pulse energy and repetition rate for submarine laser communications (SLC) applications. Specific areas investigated included (1) heated XeF laser injection locking, (2) repetitively-pulsed XeF laser Raman converter design, and (3) scaling studies of Raman amplifiers in regard to conversion efficiency and beam quality. The heated XeF laser injection		

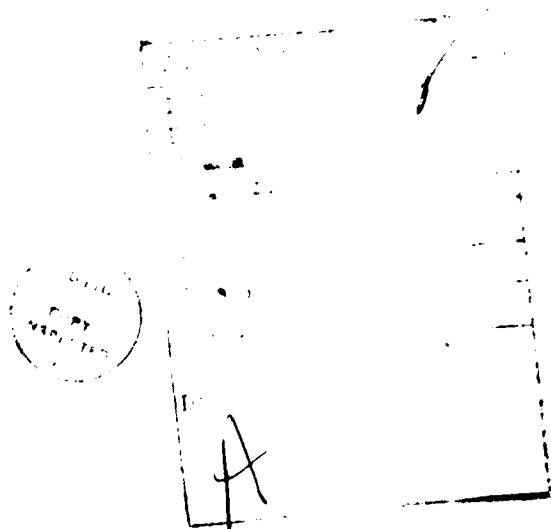
UNCLASSIFIED

SECURITY CLASSIFICATION OF THIS PAGE (When Data Entered)

locking was observed and characterized by the output energy in the injected spectrum relative to the free-running broadband case using injected power levels of 10^{-5} times the laser output. Injecting at the 353 nm band peak using a tunable frequency-doubled dye laser, greater than 90% of the laser energy was locked to the injected spectrum at room temperature. As the temperature was increased, the locking efficiency decreased to 72% at 140°C and 43% at 170°C. Injecting at 351.2 nm peak showed 57% locking at 140°C with only a modest suppression of lasing at 353 nm as well as at 351.1 nm peak. The observed spectra and time evolution of the lasing transitions suggest that the XeF upper states are being populated by one or more mechanisms besides the $V=1 \rightarrow V=0$ vibrational relaxation path. For example, multiquantum vibrational relaxation paths in a kinetics code with appropriated coupling rates yield qualitative agreement with the data. In separate experiments at room temperature, injection locking of up to 500 ns XeF laser pulses was demonstrated with injection pulse lengths as short as 35 ns. This suggests that appropriate electric-discharge pumped XeF lasers with spectral tuning may be useful as injection radiation source to control larger, e-beam excited XeF lasers.

For high average power applications with good conversion efficiency and beam quality, Raman cells will require flowing hydrogen medium to remove heat deposited in the gas. Thus, the flow and acoustics management was investigated to derive conceptual and preliminary designs for a subscale experiment. Analyses showed that density nonuniformities on the order of 10^{-5} are required to achieve good beam quality (e.g., 1.2 x diffraction-limit). Such flow medium control constraints require a further technological development to achieve the beam quality goals for SLC applications.

Raman converter scaling analysis addressed the dependence of Stokes conversion efficiency and beam quality on pump beam quality and competing effects. A Raman amplifier model with temporal (bandwidth) and spatial (diffraction) effects, as well as dispersive effects (group velocity and Raman induced), has been used to generate code simulations for cases of interest. One important case is the "beam clean-up" feature of a Raman amplifier, in which a good quality Stokes beam can be amplified efficiently by an aberrated pump beam under certain conditions. This prediction was tested experimentally, and nearly diffraction-limited Stokes output was demonstrated with greater than 50% pump depletion using a several times diffraction-limited pump beam.



SECURITY CLASSIFICATION OF THIS PAGE (When Data Entered)

TABLE OF CONTENTS

	Page
LIST OF FIGURES	i
LIST OF TABLES	iv
1.0 SUMMARY	1
2.0 INTRODUCTION	4
2.1 Technical Approach	4
2.2 Background and Scope	9
2.2.1 Injection Locking of Heated XeF Laser	9
2.2.2 Repetitively Pulsed XeF Laser Raman Conversion	11
2.2.3 Raman Converter Scaling and Beam Quality Analysis	12
3.0 XeF LASER INJECTION LOCKING	15
3.1 Short Pulse Injection Seeding	15
3.2 Heated XeF Injection Locking	20
3.3 XeF Gain Measurements	30
4.0 REPETITIVELY-PULSED XeF LASER RAMAN CONVERTER	33
4.1 Overall System Description and Test Plan	34
4.2 Rep-pulsed XeF Injection Laser	37
4.3 Repetitively-Pulsed Raman Converter Design	42
4.3.1 Energy Deposition and Acoustics	42
4.3.2 Flow Design.	47
5.0 RAMAN CONVERTER SCALING STUDIES.	50
5.1 Stokes Injection Analysis	50
5.1.1 Superfluorescence.	50
5.1.2 Parasitics	52
5.1.3 Four-Wave Mixing	56
5.1.4 Spectral Correlation	62

TABLE OF CONTENTS (Continued)

	Page
5.2 Raman Amplifier Modeling	63
5.2.1 Temporal Effects (Bandwidth)	63
5.2.2 Spatial Effects (Beam Quality).	69
5.2.3 Raman (nonlinear) Dispersion.	74
5.3 Broadband Raman Amplifier Experiment with Aberrated Pump Beam	78
5.3.1 Experimental Apparatus.	78
5.3.2 Stokes Beam Quality Measurements.	79
6.0 CONCLUSIONS	84
7.0 REFERENCES.	86
APPENDIX A . . . Conceptual Design for the Upgrade of the DARPA/Maxwell Rep-Rated XeF Laser	
APPENDIX B . . . Flowing Raman Cell Experiment Design -- A Tradeoff Study	
APPENDIX C . . . A Proposal for the Design and Fabrication of a Flow System for the DARPA/NRTC Hydrogen Raman Cell	

LIST OF FIGURES

	Page
Figure 2.1-1 Schematic of Excimer Laser and Frequency Converter. . . .	5
Figure 2.1-2 Second-Order Raman Amplifier/Photon Efficiency vs. Amplifier Length.	6
Figure 2.2-1 XeF Laser Efficiency Versus Fill Temperature.	9
Figure 2.2-2 XeF Laser Spectrum.	10
Figure 3.1-1 SWAT Injection Locking Experimental Setup	16
Figure 3.1-2 Spectrum of Injected Pulse.	17
Figure 3.1-3 Injection Locking Data.	18
Figure 3.1-4 Injection Locking Data.	19
Figure 3.2-1 Heated XeF Laser Injection Locking Experimental Schematic	21
Figure 3.2-2 XeF Laser Spectrum at 170°C with $M = 1.67$ Resonator . . .	21
Figure 3.2-3 Injection Locking Scan of the XeF 351 nm Band	22
Figure 3.2-4 XeF Laser Spectrum.	23
Figure 3.2-5 XeF Laser Spectrum.	23
Figure 3.2-6 Hot Injection Experimental Schematic for $M = 1.33$ Un- stable Resonator.	25
Figure 3.2-7 XeF Laser Spectrum at 140°C with $M = 1.33$ Resonator . . .	26
Figure 3.2-8 XeF Laser Spectrum at 140°C with 351 nm Injection	27
Figure 3.2-9 XeF Laser Spectrum at 140°C with 353 nm Injection	27
Figure 3.2-10 Relative Time History	29
Figure 3.3-1 Temporally Resolved Gain Experiment	30
Figure 3.3-2 Cold XeF Gain Data.	31
Figure 3.3-3 Cold XeF Steady State Gain vs. Wavelength	32
Figure 4.1-1 Rep-Pulsed XeF Laser Injection-Locking/Raman Conversion Overall System Schematic.	34

LIST OF FIGURES (Continued)

	Page
Figure 4.2-1	Short Pulse Injection Gain Temporal Profile Model. . . . 38
Figure 4.2-2a	Injection Laser Cavity Configuration 39
Figure 4.2-2b	Injection Laser Cavity Configuration 40
Figure 4.3-1	Illustration of Beam Energy Deposition in Raman Cell . . 43
Figure 4.3-2	Raman Amplifier Power Conversion and Power Deposition Into Gas as a Function of Position in an 8 m Cell. . . . 45
Figure 4.3-3	Cross Section of Raman Cell Cavity 48
Figure 4.3-4	Flow Design Schematic Cross Section. 49
Figure 5.1-1	Stokes Input Level vs. Gain for Saturated Amplification and Spontaneous Raman Scattering 53
Figure 5.1-2	Scattering by Optical Substrates vs. RMS Surface Rough- ness at Various Wavelengths. 55
Figure 5.1-3	Parasitics Stokes Input Level vs. Fresnel Number for Isotropic Scattering Efficiency of 1%. 56
Figure 5.1-4	S_2 Buildup With No Injection 58
Figure 5.1-5	S_2 Buildup With 10^{-5} Injection 59
Figure 5.1-6	S_2 Buildup with 10^{-3} Injection 59
Figure 5.1-7	Wavevector Diagram for Four-Wave Mixing. 60
Figure 5.2-1	Real and Imaginary Spectra of χ_3^{1111} in the Vicinity of the $Q_{01}(1)$ Mode of H_2 at the Motionally Narrowed Line- width Minimum. 65
Figure 5.2-2	Forward Raman Gain, Normalized to Its Monochromatic Value, Versus Laser Bandwidth/Molecular Linewidth 66
Figure 5.2-3	Conversion Efficiency for Broadband and Monochromatic Pumping. 67

LIST OF FIGURES (Continued)

	Page
Figure 5.2-4 Power Conversion Efficiency for Second Stokes Broadband Converter.	68
Figure 5.2-5 Conversion Efficiency of Broadband, Dispersive Converter	69
Figure 5.2-6 K-Vector Diagram for Amplification of Plane Wave Stokes by Pump Beam with Divergence θ_p	70
Figure 5.2-7 Geometry Showing Temporal Correlation Requirements for Divergent Beams.	71
Figure 5.2-8 Apodized Beam.	73
Figure 5.2-9 Far-Field of Apodized Beam	73
Figure 5.2-10 Phase Front Aberration Due to Turbulent Medium	73
Figure 5.2-11 Far-Field of Aberrated Beam.	73
Figure 5.2-12 Far-Field Profile of Stokes Output	73
Figure 5.2-13 RMS Intensity-Averaged Phase Increment in Small-Signal Regime	75
Figure 5.2-14 RMS Stokes Phase Shift in Depletion Regime	76
Figure 5.2-15 Spectrum of Accumulated Stokes Phase	76
Figure 5.2-16 RMS Stokes Phase Shift in Depletion Regime for Dispersive Converter	77
Figure 5.2-17 Spectrum of Accumulated Stokes Phase for Dispersive Converter.	77
Figure 5.3-1 Raman Conversion with Clean/Aberrated Pump Beam Experimental Schematic	78
Figure 5.3-2 Pump and Depleted Pump Pulses.	80
Figure 5.3-3 Raman Amplifier Conversion with Good Quality Pump and Stokes Beams	80
Figure 5.3-4 Aberrator: Etched Microscope Glass Slides 0.3 cm Thick	81
Figure 5.3-5 Aberrator: Plexiglass Plate 1.25 cm Thick	81

LIST OF FIGURES (Continued)

		Page
Figure 5.3-6	Amplified Stokes Beam Interferogram and Phase Front Analysis.	82
Figure 5.3-7	Amplified Stokes Beam Inteferogram and Phase Front Analysis.	82
Figure 5.3-8	Pump and Depleted Pump Pulses with Aberrator: Etched Microscope Slides	83
Figure 5.3-9	Pump and Depleted Pump Pulses with Aberrator: Plexi-glass Plate	83

LIST OF TABLES

Table 2.1-1	List of Raman Shifted Wavelengths (nm0 in the Blue-Green Region Starting from XeF Laser at 351 nm.	4
Table 3.2-1	Heated XeF Laser Spectral Distribution.	24
Table 3.2-2	Heated XeF Laser Spectral Distribution with M = 1.33 Resonator	29
Table 4.1-1	XeF Laser Specifications.	35
Table 4.1-2	H ₂ Raman Converter Specifications	36

1.0

SUMMARY

This report contains the results of analytical and experimental work which address various technical issues relevant to the scalability of a Raman converter system to high pulse energy and repetition rate operation envisioned for a ground-based submarine laser communication (SLC) system.

During a previous research program, Northrop Research and Technology Center (NRTC) had carried out scaling studies of efficient Raman converters for applications such as blue-green laser communication. In the course of this study, we have demonstrated injection locking of an e-beam pumped XeF laser to a narrow spectral bandwidth with high efficiency. Experiments on an optimized Raman oscillator have shown high conversion into the Stokes outputs in agreement with theoretical calculations. Raman amplifier experiments have also achieved 43% power conversion into the second Stokes (blue-green) output in excess of a joule from a long pulse (1 μ s) XeF laser radiation for the first time.

A new program was undertaken to address (1) heated XeF laser injection locking performance, (2) repetitively-pulsed Raman converter design, and (3) scaling studies of Raman amplifiers in regard to conversion efficiency and beam quality.

The main objective of the XeF laser injection locking experiment was to measure the single line extraction efficiency at elevated temperatures where increased laser efficiency has been observed over the room temperature operation. Previous injection locking experiments at room temperature showed narrow bandwidth ($\Delta\lambda \approx 0.006$ nm) extraction on the 353 nm band peak with greater than 90% of the free-running e-beam excited XeF laser output. The 351 nm band laser emission under free-running conditions was very weak and easily suppressed from lasing when injection locked at 353 nm. However, the results obtained from the present experiments indicate that free-running 351 nm output increases with temperature and becomes increasingly more difficult to suppress by injection locking on the 353 nm band. For example, at 140°C, narrow bandwidth extraction at 353 nm peak was observed at up to 72% of the total free-running XeF laser output. This extraction value decreased to 43% at 170°C where the heated XeF laser peak efficiency has been reported. Injection locking on the 351 nm band was also performed at elevated temperatures. The best extraction was observed

when the injection laser wavelength was tuned to the 351.2 nm peak where 57% of the total XeF output at 140°C was locked to the injected spectrum. However, unlike the spectral narrowing of the 353 nm band, the 351.2 nm injection locking did not completely suppress a neighboring 351.1 nm laser emission originating from the $V=1$ level of XeF^* . Furthermore, the output of the 353 nm emission was not affected significantly under 351.2 nm injection locking even though the two transitions are believed to originate from a common upper level.

The XeF emission spectra under various injection laser wavelengths indicated that the upper laser level cannot be described simply by $V=0$ and $V=1$ vibrationally excited states of the XeF^* molecule. One modification to an XeF^* kinetics code included multi-quantum vibrational relaxation paths (e.g., $V=2 \rightarrow V=0$, etc.). It is found that a suitable choice of these relaxation rates can yield simulated laser outputs which qualitatively match the observed temporal evolution of the 351 nm and 353 nm emission. However, the measurement of the multi-quantum relaxation and coupling rates were not pursued.

The possibility of injection locking the long-pulse XeF laser with short injection pulses was also investigated at room temperature. For these experiments, the injection wavelength was tuned to the 353 nm band peak, and the pulse duration was varied from 35 ns to 240 ns. Injection locking was observed with XeF pulse lengths of up to 500 ns in all pulse widths tested, indicating that a suitable electric-discharge-pumped XeF laser may provide adequate injection radiation to control larger, e-beam excited XeF lasers.

The analysis of repetitively pulsed Raman converter consisted of preliminary designs for an XeF laser injection locking source, 3-beam XeF laser beam quality management, and a hydrogen Raman cell with a closed-cycle flow loop and acoustic suppression. The injection laser is needed to define the laser bandwidth and polarization, and the laser beam quality control is required to achieve the requisite pump beam quality for the Raman converter to operate efficiently. The flow and acoustics management is necessary to operate good beam quality Raman converters at moderate to high average power levels. The design analysis for the flow and acoustics management was performed by Poseidon Research under a subcontract work. Preliminary designs incorporate flow geometries and muffler configurations that are quite distinct from those of the

laser cavities. Since heat deposition and chemical compatibility problems are generally more relaxed in a Raman converter as compared with typical high power lasers, material selection and engineering appear to be less demanding in a Raman converter. However, requirements of good beam quality output (e.g., $1.2 \times$ diffraction-limited) from a long Raman cell call for density non-uniformities on the order of 10^{-5} which are much less than those demonstrated in conventional flow loops. Further technological development in this area is needed to achieve the beam quality goals for SLC applications.

The extension of the Raman converter scaling studies addressed Stokes conversion efficiency and beam quality dependence on pump and Stokes radiation as well as Raman medium. For example, the Stokes injection requirements have been analyzed in further detail to take into account the effects of superfluorescence, parasitic oscillation, four-wave mixing, and spectral correlation. It is found that a certain minimum injection intensity is needed to control a Raman amplifier, thereby establishing a scaling factor for maximum amplification. Raman amplifier modeling has been refined considerably to include temporal and spatial effects of the pump and Stokes radiation fields. Dispersive effects have also been incorporated in this new formulation in a systematic way to investigate the magnitude of group velocity (linear) dispersion and Raman induced (nonlinear) dispersion. Computer codes based on these models which include three-dimensional wave propagation have been generated to yield simulation of various cases of interest. One important and practical case investigated involves amplification of a low-intensity, good-beam-quality Stokes radiation by an aberrated pump beam. Under certain conditions, the output Stokes beam could be generated with much better beam quality than that of the pump beam, demonstrating a "beam clean-up" feature of a Raman amplifier. Implementing such features in actual devices is of considerable value, since pump laser beam quality requirement is decoupled from the Raman shifted output. An experimental verification of the beam clean-up property of a Raman amplifier has been carried out, and the preliminary measurements have demonstrated amplification of a nearly diffraction-limited Stokes beam by a few times diffraction-limited pump beam with pump depletion exceeding 50%.

2.0 INTRODUCTION

2.1 Technical Approach

An efficient blue-green laser source is being sought for a strategic submarine communication system as well as other applications. The rare-gas halide excimer lasers developed over the past few years appear to meet the requirement on efficiency and scalability, but the wavelength of their near-UV emission must be shifted into the blue-green spectral region. A novel conversion scheme for efficient wavelength shifting was conceived at Northrop Research and Technology Center in 1977. This concept, based on higher-Stokes-order Raman scattering in molecular gases, uses a Raman oscillator-amplifier combination to achieve optimized conversion into a particular Stokes order.

The Raman oscillator-amplifier concept is generally applicable in various media [GZ78]. In atomic vapors, large electronic Raman shifts are adequate to convert UV wavelengths into the visible region in a single Stokes shift [BD78]. In contrast, Raman shifting in gases such as H_2 , D_2 , CH_4 , etc. require multiple Stokes shifts to generate the visible output [LSB79]. A list of wavelengths which can be generated starting from an XeF laser, using these Raman media, is shown in Table 1, together with the quantum-efficiency for each case.

TABLE 2.1-1 LIST OF RAMAN SHIFTED WAVELENGTHS (nm)
IN THE BLUE-GREEN REGION STARTING FROM
XeF LASER AT 351 nm

Combination	Output (nm)	Quantum Efficiency
$2H_2$	495.5	71
$H_2 + HD$	482.7	73
$2HD$	470.6	75
$H_2 + D_2$	468.5	75
$HD + D_2$	457.2	77
$2D_2$	444.3	79

A schematic of the complete system is shown in Figure 2.1-1 for the case of double-shifting in a single Raman gas. It consists of an excimer laser (XeF), two Raman cells, and optical components. A small fraction of the laser output is sent through a beam reducing telescope, T_1 , and focused into a single-pass Raman oscillator cell through lens L_1 . This oscillator is operated several times above threshold, such that its output consists primarily of first and second Stokes orders, each with an energy on the order of 25 percent of the laser energy. Near-diffraction-limited beams can be obtained from this oscillator through the use of a tight focusing geometry. The Stokes beams are re-collimated with lens L_2 , sent through a filter, F , which transmits all orders up to the selected one but stops all the higher ones, and injected in the amplifier cell, RA , through a beam combining mirror, BC .

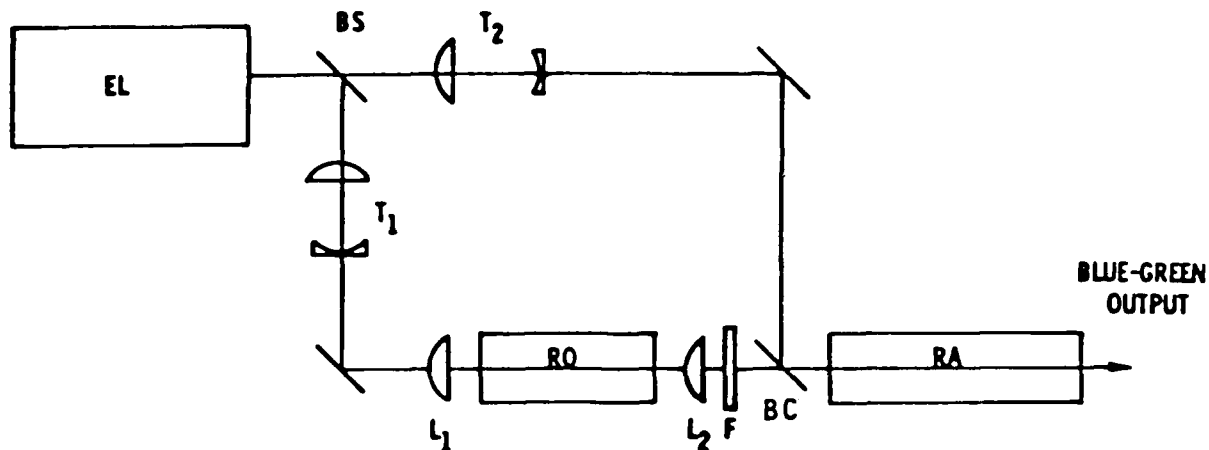


FIGURE 2.1-1 SCHEMATIC OF EXCIMER LASER AND FREQUENCY CONVERTER.
 EL = EXCIMER LASER, F = FILTER, BC = BEAM COMBINER,
 T_1/T_2 = TELESCOPES, L_1/L_2 = LENSES, RO = RAMAN
 OSCILLATOR, RA = RAMAN AMPLIFIER

As the pump beam and the injected Stokes beams travel through the amplifier, a sequential energy transfer takes place from one order to the next one, until most of the pump laser energy has been transferred to the selected order. A typical example of photon conversion is shown in Figure 2.1-2, which applies

to the case of a second order shifter. It should be noted that, even though no energy is injected at orders higher than the second one, radiation at such wavelengths can still be generated through four-wave mixing processes. As is illustrated in Figure 2.1-2, if the amplifier gain is sufficiently high, this

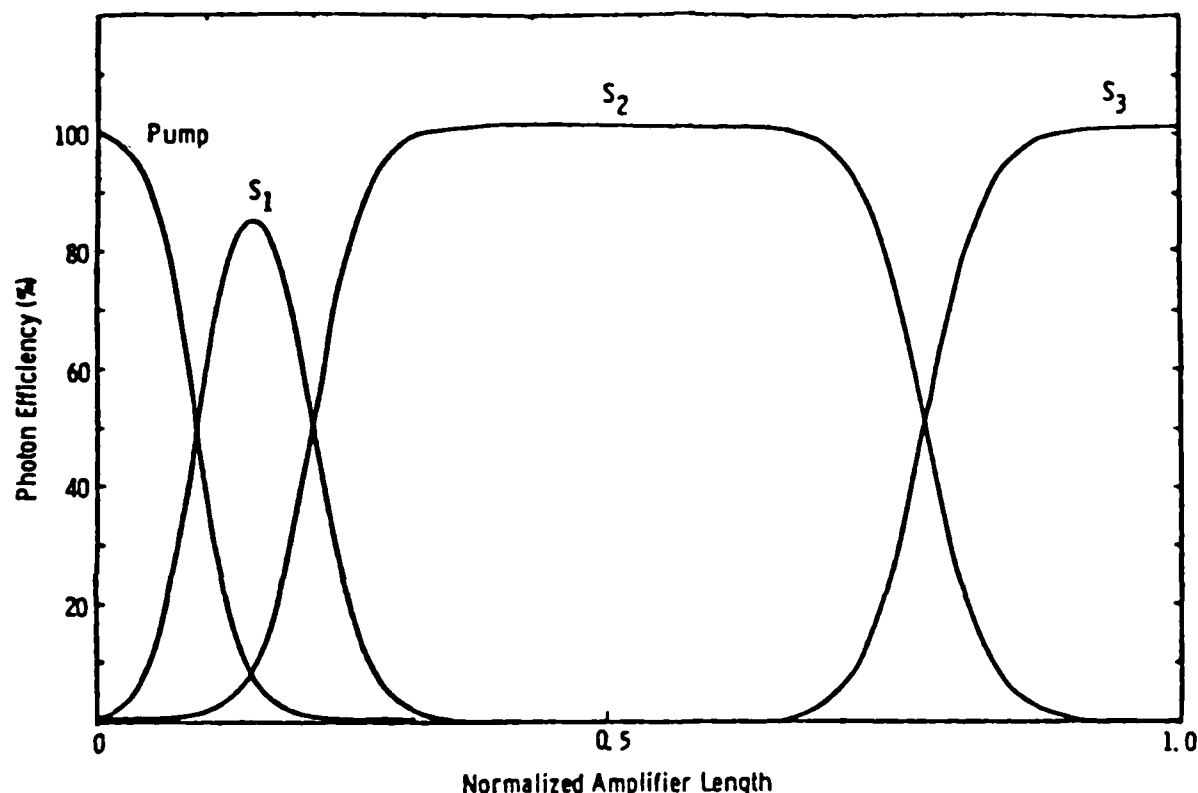


FIGURE 2.1-2 SECOND-ORDER RAMAN AMPLIFIER/PHOTON EFFICIENCY VS. AMPLIFIER LENGTH

unwanted radiation can be further amplified by stimulated Raman scattering, thus resulting in a lower efficiency for the selected second order. For this reason, the gain must be kept within a certain range, typically within $\pm 40\%$ of the mean value. In practice, this requires the use of nearly rectangular beam and pulse profiles, and shot-to-shot power fluctuations within the above range. The efficiency of the undesired mixing processes can further be minimized through the use of nearly collimated beams in the amplifier since this eliminates angular phase-matching.

The initial experiments on the Raman oscillator-amplifier scheme used hydrogen gas as the Raman medium and a frequency-tripled Nd:YAG laser (355 nm) as an

UV pump laser [KS79]. Amplifier photon conversion efficiencies as high as 51 percent have been obtained for the second Stokes order (503 nm) output, in very good agreement with computer calculations. The laser pulse length in these experiments was relatively short (6 ns), which limits the amplifier energy conversion efficiency because of reduced Raman gain at the leading and trailing edges of the pulse. For longer, nearly rectangular pulses, and flat-topped beam profiles as obtained with large Fresnel number unstable resonators, conversion efficiencies approaching the quantum limit should be possible for second and third Stokes order converters.

In order to assess the scaling feasibility of this wavelength shifting technique for larger energies and longer pulse lengths, an analytical and experimental investigation was carried out, initially under DARPA Contract N00014-80-C-0442 [KSB81]. The objectives of the investigation were two-fold: First, to demonstrate narrow spectral bandwidth output with a 1 μ s XeF laser pulse via injection locking; second, to generate a Raman converter scaling model along with supporting experimental data. The motivation for achieving a narrow-bandwidth XeF laser output was to meet the bandwidth requirement on the Raman-shifted blue-green output for communication applications. The Raman shifting experiment was aimed at demonstrating efficient XeF-to-blue-green conversion with up to 1 μ s pulse length and over a joule output.

The injection locking experiment achieved spectral narrowing of the room temperature XeF laser emission band near 353 nm to a bandwidth of 0.006 nm under ~ 1 μ s e-beam excitation. A narrowband output of up to 10 J from an unstable resonator was obtained with an injected power of ~ 200 W which corresponds to an injection power ratio of about $2\sim 3 \times 10^{-5}$ relative to the laser output power [WKS81].

The Raman converter scaling studies consisted of system design analyses and a verification of an oscillator-amplifier scheme using the injection locked XeF laser. Key results of the analyses included energy limitation of an optimized superfluorescent oscillator which generates Stokes injection beams of sufficient intensity and beam quality. As a consequence of this limitation, amplifier energy scaling is found to be dependent on system configurations; one

such scheme utilizes a preamplifier stage to satisfy constraints on amplifier power gain per stage. A key parameter that defines the dimensional scale of these systems is optical beam fluence on cell windows and beam combining mirror; optical damage limitation has been identified to be one of the most critical technology constraints.

The Raman oscillator-amplifier experiments demonstrated the basic scaling feasibility of long pulse ($\sim 1 \mu\text{s}$) conversion at a blue-green energy level in excess of 1 J for the first time. This was achieved with XeF to blue-green energy conversion efficiency of 34% in the Raman amplifier, supporting the prospects for scaling to higher energies [KSB82].

These investigations have been extended to address other important technical issues under a follow-on contract, and the results are presented in this report. The follow-on investigations dealt with three areas of XeF laser/Raman converter technologies:

- (1) Narrow linewidth extraction efficiency in heated XeF laser media;
- (2) Repetitively pulsed XeF laser/ H_2 Raman conversion technology;
- (3) Raman converter scaling analyses for high-energy device applications and beam quality constraints on laser/Raman converter systems.

A brief discussion on the background material relevant to these areas is included in the next section, along with a description of the scope of this investigation. The results of the present investigation are presented in Sections 3.0, 4.0, and 5.0, corresponding to the three areas listed above.

2.2 Background and Scope

2.2.1 Injection Locking of Heated XeF Laser

Experiments performed during the initial phase of this program clearly demonstrate that efficient narrow-line operation of a room temperature XeF laser can be accomplished by injection-locking to a much lower power narrow-line laser. Thus far, the line narrowing has been limited by the spectral width of the injection source. This indicated further narrowing, below the 0.5 cm^{-1} achieved in the present experiments, may be possible, although the present line widths are compatible with the SLC mission. It is more important to understand the injection-locking performance of the XeF laser at elevated temperature since this is a more efficient operating regime. By raising the gas temperature, an appreciable enhancement in output energy and laser efficiency is achieved [Ch79,HMJ79]. This is illustrated in Figure 2.2-1, which is adapted from [HMJ79]. A factor of three efficiency increase is obtained when the temperature is raised from 300K to 450K.

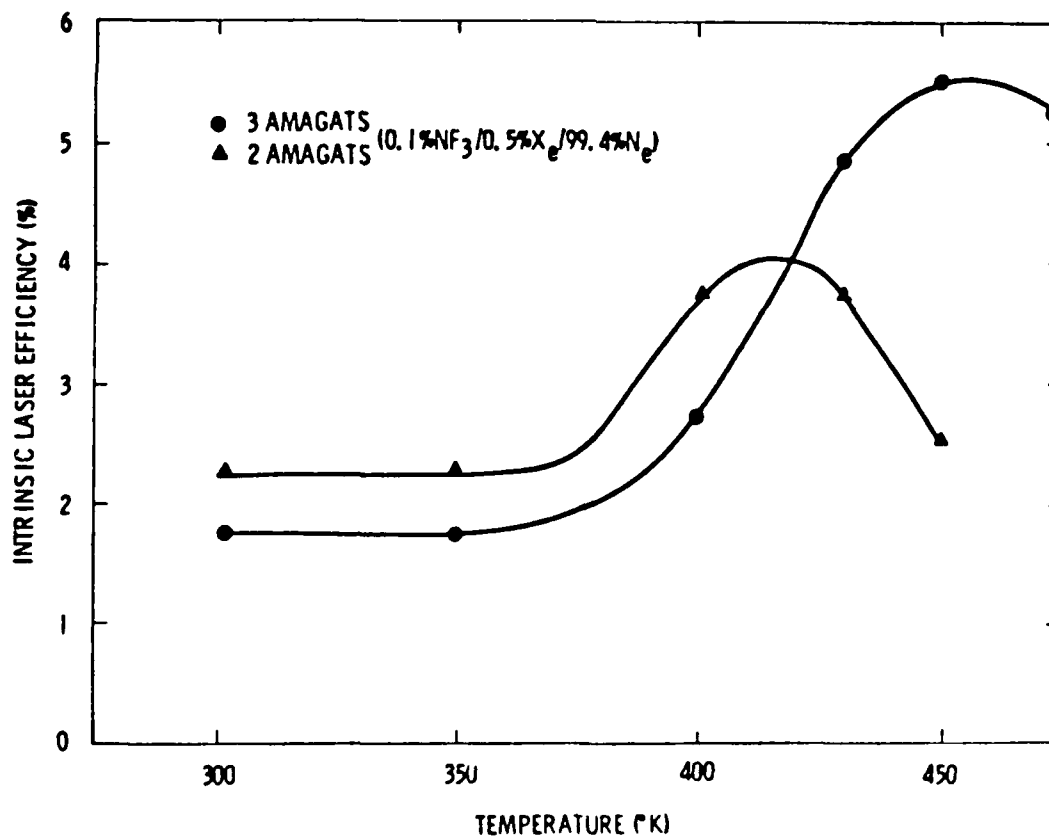


FIGURE 2.2-1 XeF LASER EFFICIENCY VERSUS FILL TEMPERATURE

In addition to enhanced energy extraction, however, the heated XeF laser also exhibits significant changes in its output spectrum [HMJ79]. In particular, the 351 nm laser line, which is either weak or absent at room temperature, dominates the output at elevated temperatures. This is seen in Figure 2.2-2 which shows XeF laser spectra obtained at various gas temperatures. The 351 nm line has contributions from both the (0,2) and 1,4) bands of the XeF B \rightarrow X transition. Thus, with the addition of the remaining output at 353 nm (due to the 0,3 band), the heated XeF laser operates on three vibrational transitions. This clearly is not compatible with the SLC mission and presents additional complications for injection-locking the laser to obtain single line operation.

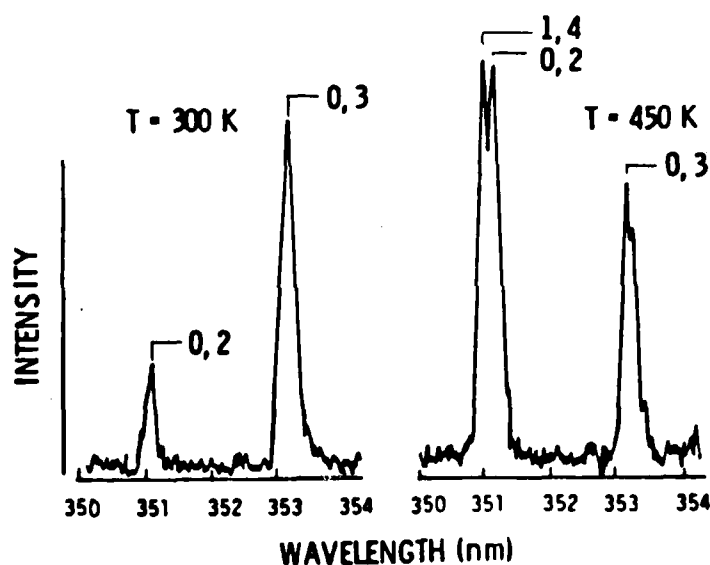


FIGURE 2.2-2 XeF LASER SPECTRUM

Task (1) of the present investigation consisted of a series of experiments on injection locking characteristics of a heated XeF laser. The experiments were designed to measure locking efficiency of the XeF transitions in the 351 and 353 nm bands and to determine the time-resolved spectral output and polarization as a function of injection source pulse length and peak power. In parallel with these measurements, locking efficiency calculations were carried out with a computer code which includes XeF* vibrational relaxation to simulate injection locking. Comparison of the results with the measurements was aimed at gaining a better understanding of the injection locking properties of the XeF

laser, especially the dependence of locking efficiency on parameters such as the vibrational relaxation rate and paths.

2.2.2 Repetitively Pulsed XeF Laser Raman Conversion

Raman conversion for high average power applications with stringent beam quality requirements are anticipated to operate with a flowing gas medium due to heat removal and baseline medium homogeneity constraints. Unlike laser gas flow loops, Raman gas flow geometry is unique in terms of aperture to length aspect ratio. The basic issue is the technology of a Raman cell with a suitable closed-cycle flow loop which enables efficient Raman conversion of long-pulse XeF laser output into blue-green at a high pulse repetition rate with near diffraction-limited beam quality. Therefore, parameteric measurements are needed to generate a data base on efficiency and beam quality of a Raman converter equipped with a gas flow system. An experimental test plan includes design and fabrication of a Raman converter with flow system and realization of a well-controlled XeF laser as prerequisites for this task. In particular, the spectral bandwidth, polarization, and beam quality of the XeF laser must be compatible with the Raman converter requirements. Injection locking of the XeF laser should satisfy the bandwidth and polarization requirements.

The Raman converter for this experiment is designed on the basis of currently projected performance of the DARPA/Maxwell repetitively pulsed XeF laser. It is expected that the laser will have nominal output energies of about 10 J per pulse at a repetition rate of 10 pps. A preliminary analysis of heat deposition into hydrogen gas under these operating conditions indicates that a static gas would develop a radial temperature (density) gradient which will result in severe thermal lens effect and beam distortion. Since such medium degradation can substantially reduce Raman conversion efficiency, an adequate gas flow appears to be essential for pulse energies and repetition rates being considered. Therefore, a Raman converter with a flow system has been analyzed as a critical experimental apparatus for this program.

For the design and fabrication of a Raman converter with a closed-cycle flow system, a subcontract was awarded to Poseidon Research. Under this arrangement, Poseidon Research carried out a design trade-off analysis based on con- parameters provided by NRTC.

A preliminary design of a Raman converter for the DARPA/Maxwell repetitively pulsed XeF laser indicated that nearly diffraction-limited beam quality is needed to demonstrate high conversion efficiencies of blue-green output as well as to investigate the effects of flow on the converter performance. Currently, this requirement is unlikely to be satisfied unless necessary modifications to the flow system are made to eliminate disturbances in the laser chamber. Therefore, analysis and design of the laser flow loop and acoustics suppression become an integral part of this task. This work was performed by Poseidon Research under a separate subcontract.

2.2.3 Raman Converter Scaling and Beam Quality Analysis

Analysis of Raman converter systems based on oscillator-amplifier concept has been previously carried out in terms of optimum design within the framework of material and Raman medium constraints. Key results of this analysis included energy limitation of an optimized oscillator, amplifier system configuration versus energy scaling, and identification of critical technology issues relevant to converter systems design with stringent beam quality requirements.

Briefly, the function of an oscillator is to generate nearly diffraction-limited multiple-order Stokes beams with high efficiency. The Stokes pulse length should be as close to the pump pulse length as possible in order to provide injection signal to an amplifier over most of the amplifier pump pulse. A single-pass superfluorescent oscillator can meet these requirements under proper conditions of pump energy and focusing geometry.

The basic constraint imposed on the oscillator design is saturation of the Raman medium. The volume of hydrogen gas accessible to Raman scattering is defined by a diffraction-limited focal area and an effective interaction length given by the confocal parameter of the focused pump beam. Experiments [KS79] have shown that such a focused pumping geometry can generate nearly diffraction-limited Stokes beams in agreement with theoretical model calculations. Since a hydrogen molecule is excited into the first vibrational level for each pump laser photon scattered into Stokes radiation, the ground state population is continually depleted during the Raman conversion process until gain

is saturated (thereby terminating the process). This saturation process becomes increasingly important for longer pulse lengths because Stokes generation requires a certain intensity level to sustain efficient operation. Consequently, longer pulses require larger confocal parameters to prevent premature Stokes pulse termination.

The cell length required to permit longer confocal parameters is constrained by optical damage limitations of the cell windows. It is found that in the tight-focusing geometry (i.e., length \gg confocal parameter), the length scales as the three-fourth power of the laser pulse length for a given value of damage fluence threshold. The pump energy required to drive an oscillator at several times the Stokes threshold is proportional to pulse length. Thus, in a superfluorescent oscillator, the output Stokes energy is governed by the pulse length.

The Raman oscillator energy scaling imposes a certain Stokes injection level in a Raman amplifier. The amplifier gain must be sufficiently high to deplete the pump for a given injection level. Since the Stokes injection level is fixed by the laser pulse length, a question arises as to the maximum amplifier gain allowed without deleterious effects due to competing processes. These processes include amplified spontaneous emission (Raman superfluorescence), parasitic oscillations, and four-wave mixing. Each of these processes can generate uncontrolled input radiation at the Stokes frequency, thereby effectively introducing noise injection that could potentially degrade conversion efficiency and/or beam quality. The conditions under which these competing processes become important have been analyzed and discussed in this report; they, in turn, prescribe scaling relations for an oscillator-amplifier configuration in terms of power gain constraints.

For the ground-based SLC system, the beam quality of the blue-green laser is required to be nearly diffraction-limited. Since the blue-green beam is generated in a Raman converter, a detailed understanding of the relationship between the quality of the amplified second Stokes beam and the quality of the pump and injected Stokes beams is necessary. This relationship itself depends on Raman converter parameters such as pressure and small signal gain. Thus,

one of the goals of this program included a theoretical and experimental study of this problem. An exact computer model, recently developed at NRTC, was used for the theoretical analysis. This model accepts arbitrary amplitude and phase profiles for all the beams involved in the Raman process, and calculates the output beam profiles and conversion efficiencies. Experiments have been performed to verify some of the predictions of the model.

3.0 XeF LASER INJECTION LOCKING

This section describes our experimental, as well as theoretical, results for injection locking e-beam pumped XeF lasers. Section 3.1 deals with the short pulse injection locking of a cold XeF laser, while the heated XeF injection locking experiments are described in section 3.2. Time resolved gain measurements are presented in section 3.3. Finally, the injection locking, modeling studies are detailed in section 3.4.

3.1 Short Pulse Injection Seeding

Considerable advantage is gained if high power, long pulse XeF lasers can be injection locked with low power, short pulse injection sources. This type of injection source would be cheaper to build, more compact, and more reliable. For instance, the source could be a discharge pumped XeF laser. This technology is presently capable of producing such an injection source.

Experiments were conducted to demonstrate short injection pulse injection locking of an e-beam pumped, room temperature, XeF laser, which produced optical pulses of 500 ns on the 353 nm band. In addition to demonstrating injection locking with as short an injection pulse as possible, efficient injection locking and large injection ratios were also desired.

Shown in Figure 3.1-1 is the experimental schematic of the short pulse injection locking experiment performed on the SWAT (Short Wavelength Advanced Test-bed) device which is an e-beam excited XeF laser. A flash lamp pumped, grating tuned Candela dye laser and a KDP doubling crystal provided a tunable UV injection source. This UV injection beam was sent through a Pockels cell pulse slicer which produced a pulse width variable from 35 ns to 240 ns. The injection beam was then injected into the SWAT unstable resonator cavity via a 90% reflecting 7 m concave back mirror. The output coupling mirror was an HR with a 3 m convex curvature. The mirrors were spaced 2 m apart and, thus, configured a confocal unstable resonator with a magnification of 2.33. The output

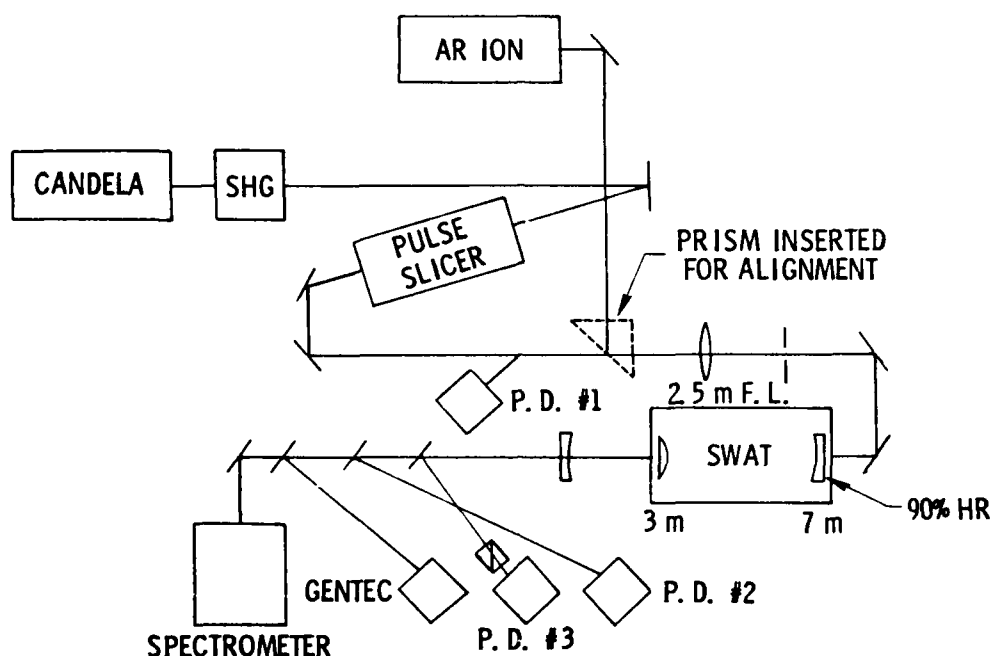


FIGURE 3.1-1 SWAT INJECTION LOCKING EXPERIMENTAL SETUP

energy of the laser was monitored with a Gentec pyroelectric detector and the spectrum was recorded with a Spex 3/4 m spectrometer and Reticon diode array. Photodiode #1 monitored the injection signal, photodiode #2 monitored the laser output directly, and photodiode #3 monitored the laser output after passing through a polarizer. An argon ion laser was used as an alignment beam.

The spectrum of the injected signal is shown in Figure 3.1-2. The spacings between diodes was .01 nm and the resolution was limited by the spectrometer to ~ .02 nm. When the spectrum was measured with an etalon, it was found to have a bandwidth of 0.0064 nm. A noteworthy feature of the injection spectrum was its symmetry. One indication that injection locking had occurred was that the SWAT spectrum was transformed from a broad asymmetric one to one that was as narrow and as symmetric as the injection source's spectrum.

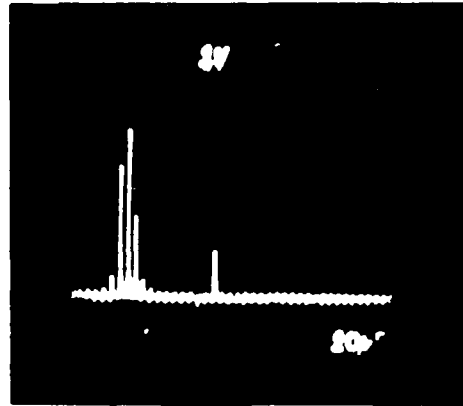


FIGURE 3.1-2 SPECTRUM OF INJECTED PULSE
(A SINGLE SPIKE NEAR THE CENTER OF TRACE IS A DEFECTIVE ELEMENT.)

The results of the experiment are presented in Figures 3.1-3 and 3.1-4. The data presented are the e-beam gun voltage, the injection pulse width, the SWAT lasing signal monitored directly with a photodiode, the SWAT lasing signal monitored after passing through a polarizer, and the SWAT lasing spectrum. All the scope traces were set at a horizontal sweep speed of 200 ns/division, and all show a timing reference mark near the end of the traces.

For the case of the free running laser, four points are of interest. First, the laser pulse had a fast rise of about 75 ns. Second, the laser pulse turned on approximately 1050 ns ahead of the reference signal. Third, the laser pulse had the same temporal shape when monitored by a photodiode directly or by a photodiode with a polarizer. Fourth, the laser spectrum had an asymmetric shape caused by a broad red tail. In these spectra longer wavelength is toward the lefthand side.

For the case of a 240 ns injection pulse, several changes were observed which were indicative that injection locking occurred. First, the rise time of the laser pulse had lengthened to approximately 150 ns. Second, the laser pulse turned on nearly 150 ns sooner than the free running case. Third, the lasing spectrum had narrowed and become symmetric. Better examples of the narrowed and symmetric spectrum are exhibited in Figure 3.1-4 for injection pulses of 70 ns and 35 ns. As with the 240 ns injection pulse case, the slower rise time and advanced turn on time for the lasing pulse were evident. In addition,

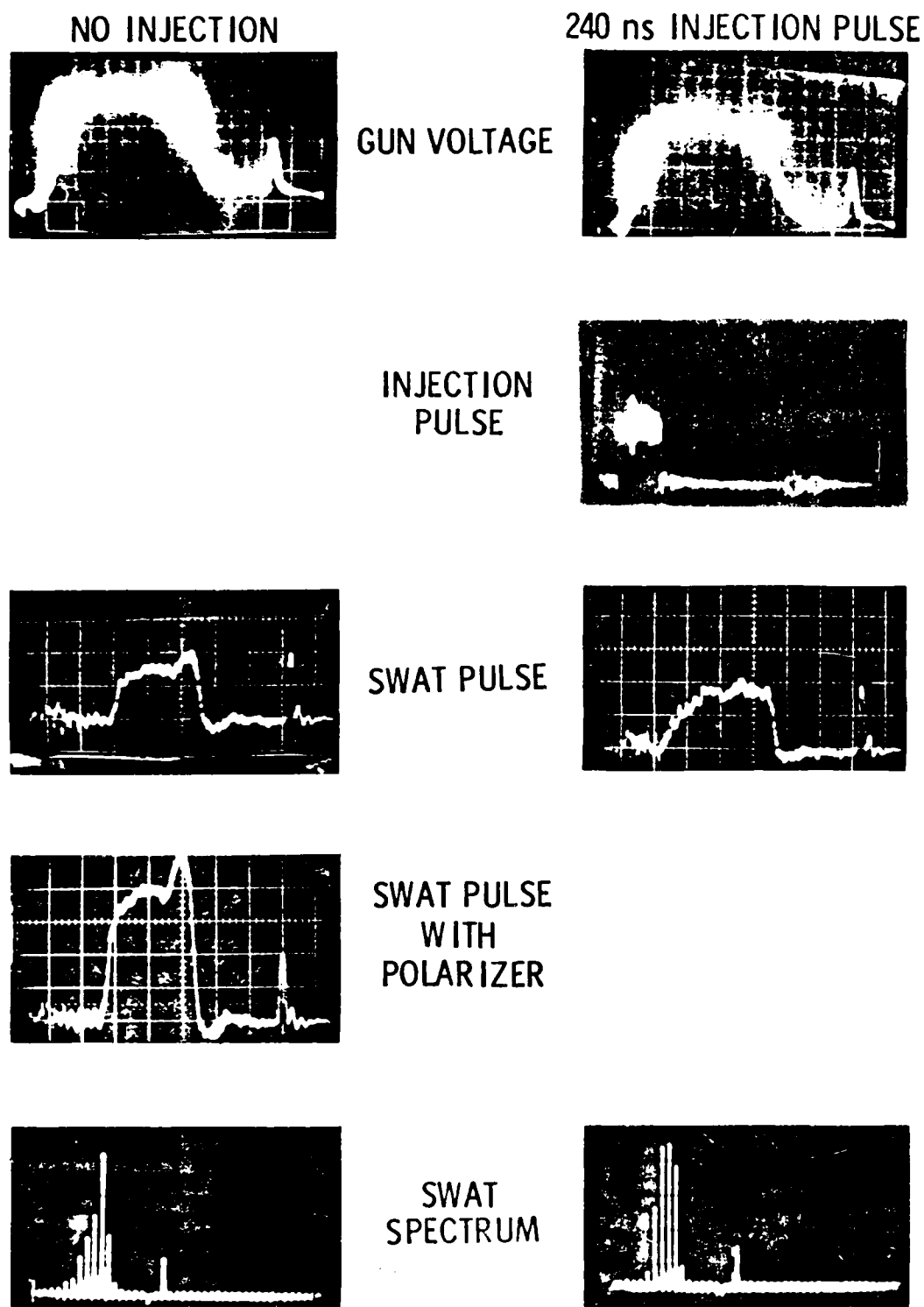


FIGURE 3.1-3 INJECTION LOCKING DATA

70 ns INJECTION PULSE



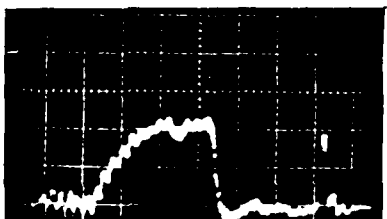
35 ns INJECTION PULSE



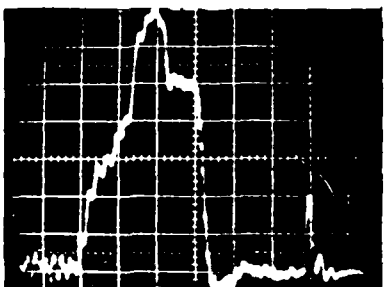
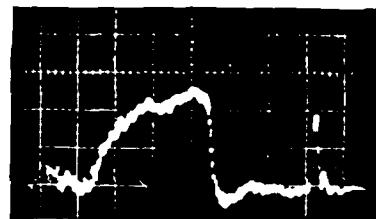
GUN VOLTAGE



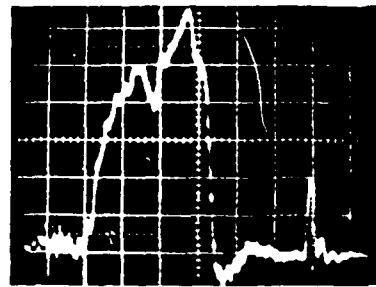
INJECTION
PULSE



SWAT PULSE



SWAT PULSE
WITH
POLARIZER



SWAT
SPECTRUM

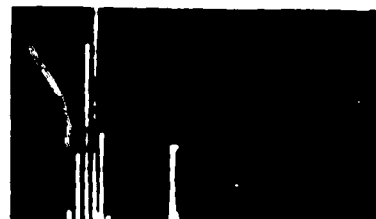


FIGURE 3.1-4 INJECTION LOCKING DATA

there was a marked difference in the lasing output monitored by the photodiodes with and without a polarizer. This can be taken as further evidence injection locking had occurred. When the laser was free running, it was unpolarized. Therefore, the polarizer made no difference in the temporal response the photodiode detected. However, the injection source was polarized so the SWAT laser would have also been polarized if it had been injection locked. What was observed was an initial polarization locking of SWAT by the injection locking, followed by rapid depolarization. This depolarization was probably caused by induced birefringence of the quartz windows which were internal to the cavity optics.

Greater than 90 percent of the free running laser energy was extracted in injection locked pulses of approximately 500 ns, using an injection pulse as narrow as 35 ns and with an injection ratio of 10^5 . This clearly demonstrates the feasibility of efficient injection locking of long pulse e-beam pumped XeF lasers with short injection pulses.

3.2 Heated XeF Injection Locking

Heated XeF injection locking experiments were performed using an unstable resonator magnification of $M = 1.67$ and $M = 1.33$. The $M = 1.67$ experimental schematic is shown in Figure 3.2-1. The tunable UV injection source was the same as described in section 3.1. The injection signal was introduced into the confocal unstable resonator through a 2 mm hole in the 10 m concave HR back mirror. Monochrometers were used as band pass filters in order to monitor the temporal evolution of both the 351 nm and 353 nm bands on photodiodes. The laser output energy was recorded with a pyroelectric energy meter and the laser spectrum was recorded on the spectrometer -- OMA system.

The experimental parameters were as follows:

T	=	170°C
Ne	=	3 amagats
Xe	=	0.23%
NF ₃	=	0.075%
J _{EB}	=	9A/cm ²
V _{EB}	=	390 kV

Injection ratio $\sim 10^5$

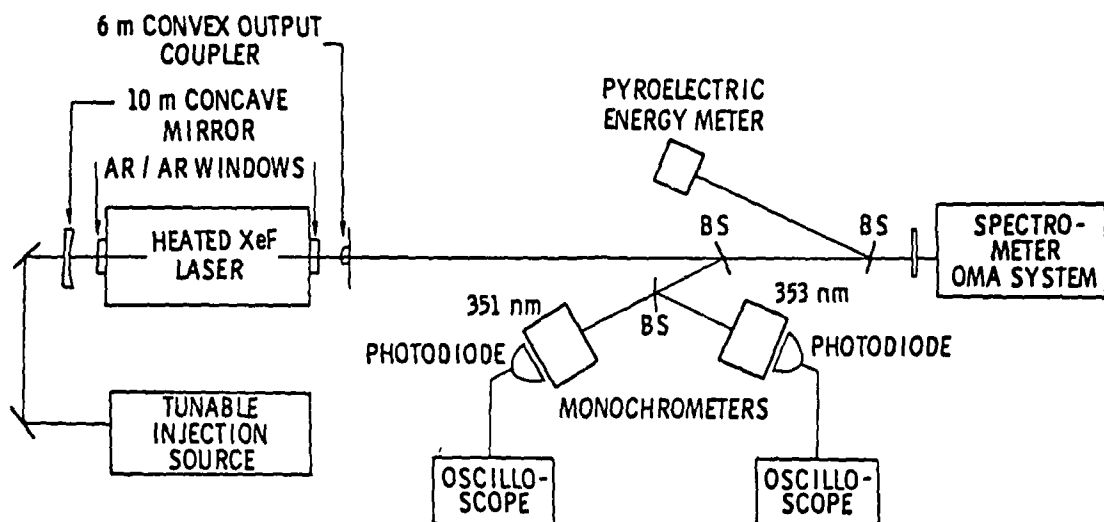


FIGURE 3.2-1 HEATED XeF LASER INJECTION LOCKING
EXPERIMENTAL SCHEMATIC

Figure 3.2-2 shows the OMA traces for the free-running laser. Note in all the OMA traces, longer wavelength is to the right which is opposite to the spectra of section 3.1. For the free-running case, the 353 nm band exhibited its characteristic asymmetric spectrum with a long red tail. The 351 nm band had two major components. The dominant peak was the 351.2 nm line, and the lesser

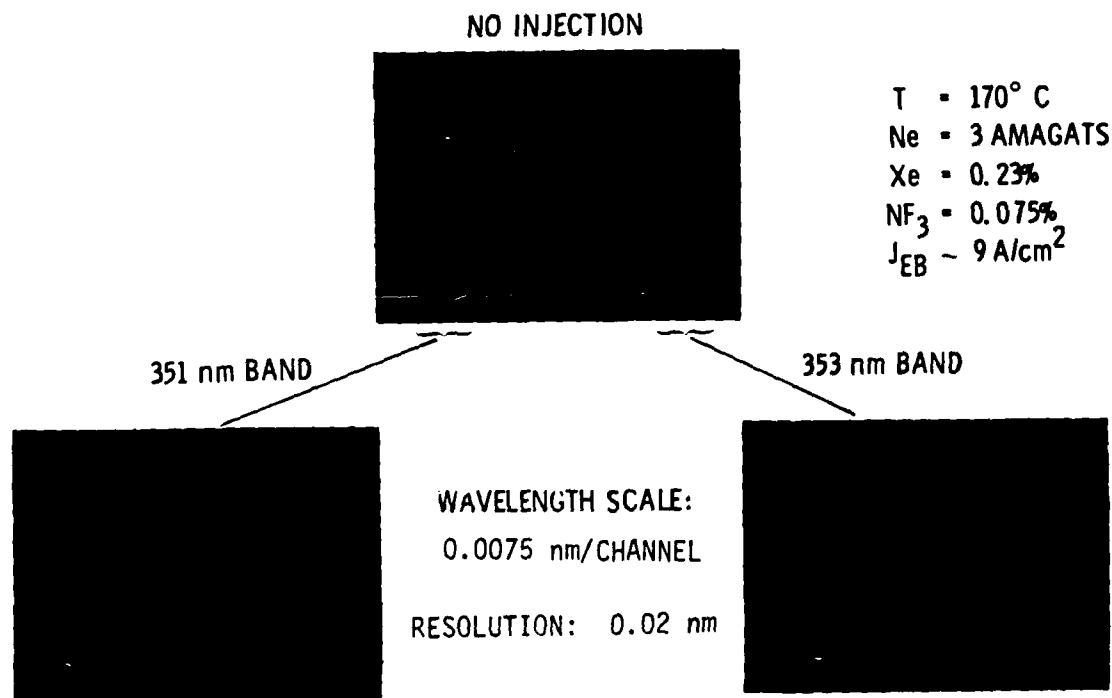


FIGURE 3.2-2 XeF LASER SPECTRUM AT 170°C WITH M = 1.67 RESONATOR

peak was the 351.1 nm line. Figure 3.2-3 shows a series of spectra in which the injection signal was tuned from a wavelength which was 0.03 nm to the red of the 351.1 nm line toward line center of the 351.2 nm line. As is evident, the injection signal forced a significant amount of the laser's energy into the injected line, but it did not exert complete control even when injected on line center of the 351.2 nm line which was the dominant line in the free-running laser.



$$\lambda_{inj.} = \lambda_{351.1} + 0.03 \text{ nm}$$



$$\lambda_{inj.} = \lambda_{351.1} + 0.09 \text{ nm}$$



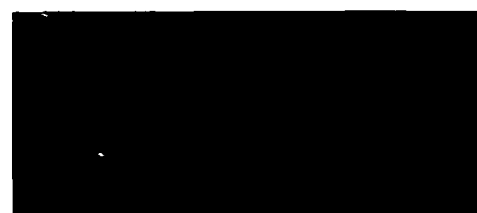
$$\lambda_{inj.} = \lambda_{351.1} + 0.06 \text{ nm}$$



$$\lambda_{inj.} = \lambda_{351.1} + 0.12 \text{ nm}$$



$$\lambda_{inj.} = \lambda_{351.1} + 0.08 \text{ nm}$$



$$\lambda_{inj.} = \lambda_{351.1} + 0.13 \text{ nm} = \lambda_{351.2}$$

FIGURE 3.2-3 INJECTION LOCKING SCAN OF THE XeF 351 nm BAND

Figure 3.2-4 shows the spectra for both the 351 nm and 353 nm bands when the injection signal has tuned to line center of the 351.2 nm line, compared with the free-running spectra, the 351.2 nm line was enhanced, and the 351.1 nm line and 353 nm band were suppressed. The reverse effect was seen in Figure 3.2-5

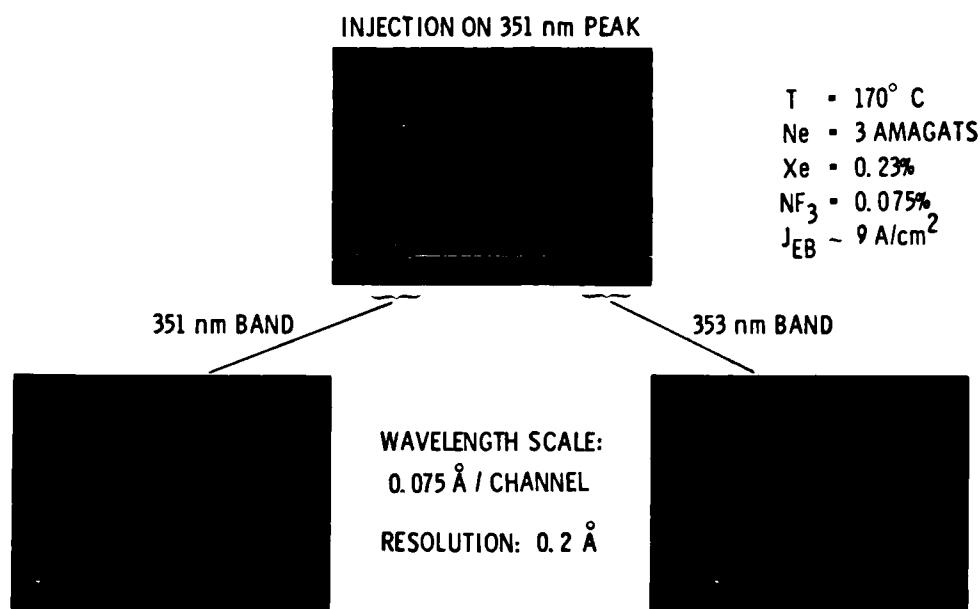


FIGURE 3.2-4 XeF LASER SPECTRUM

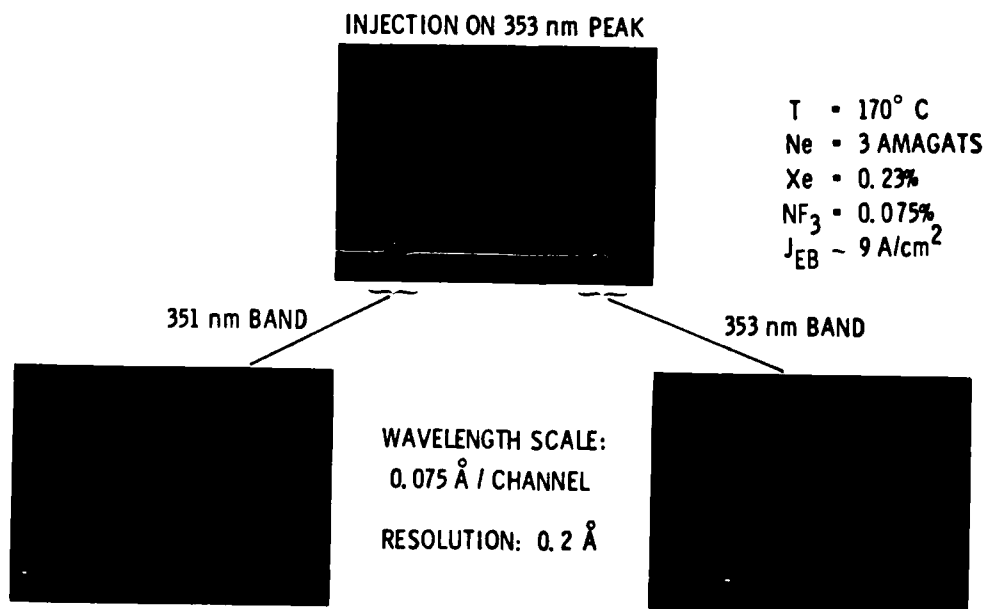


FIGURE 3.2-5 XeF LASER SPECTRUM

when the injection source was tuned to the peak of the 353 nm band. Not only was the 353 nm line enhanced, the spectrum was narrowed and made symmetric as expected. Both of the 351 nm lines were suppressed relative to the free-running case.

These results are summarized in Table 3.2-1. The energy distribution for each line for the case of no injection, injection on 351.2 nm, and injection on 353 nm is shown. As can be seen, only moderate control is gained by injection. A net transfer of only ~10% into the desired line occurred.

TABLE 3.2-1 HEATED XeF LASER SPECTRAL DISTRIBUTION

INJECTION SOURCE	EMISSION PEAK		
	351.1 nm	351.2 nm	353.2 nm
NO INJECTION	24%	42%	34%
INJECTION ON 351.2 nm PEAK	15% ($\Delta = -9\%$)	53% ($\Delta = +11\%$)	32% ($\Delta = -2\%$)
INJECTION ON 353.2 nm PEAK	19% ($\Delta = -5\%$)	38% ($\Delta = -4\%$)	43% ($\Delta = +9\%$)

The experimental configuration for the $M = 1.33$ unstable resonator hot injection experiment is given in Figure 3.2-6. Instead of the injection signal

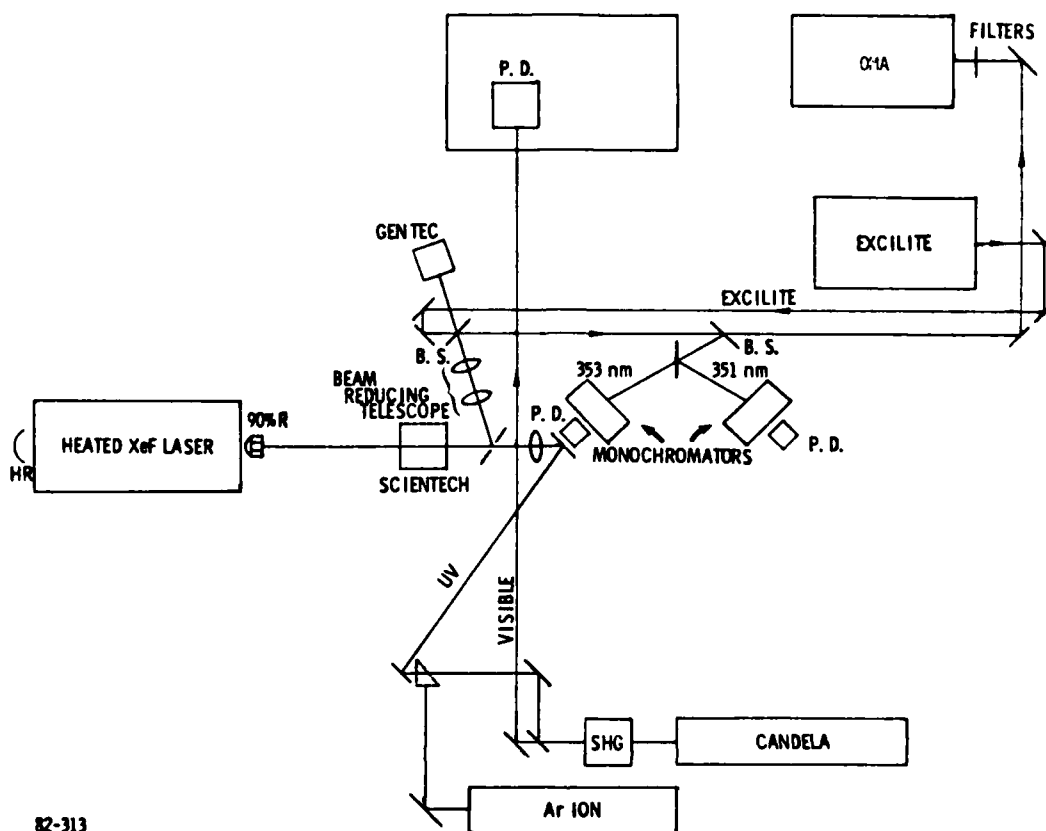


FIGURE 3.2-6 HOT INJECTION EXPERIMENTAL SCHEMATIC
FOR $M = 1.33$ UNSTABLE RESONATOR

being introduced into the cavity through a hole in the rear, the signal was injected through a partially reflecting output coupler. Again the tunable UV injection source was provided by the Candela dye laser-KDP doubling crystal system. An Excilite discharge pumped XeF laser and an argon ion laser were used as alignment beams. The fundamental of the Candela was used as a reference for temporal overlap of the SWAT laser pulse and the injection signal. Monochromators were again used as bandpass filters so that the temporal history of the 351 nm and 353 nm bands could be monitored. Output energies were measured on either a Scientec or GenTec pyroelectric energy meter and the output spectra were recorded on the spectrometer-OMA system.

The operating conditions for this experiment were:

T = 140°C
Ne = 2.7 amagats
Xe = 0.3%
NF₃ = 0.1%
J_{EB} = 5-6 A/cm²
V_{EB} = 390 kV

Injection ratio $\sim 7 \times 10^4$

Figures 3.2-7 through 3.2-9 show the results for the free running case, injection on the 351.2 nm line, and injection on the 353 nm line. A summary of the energy distribution among the lines is given in Table 3.2-2. For the free running case, the 353 nm line had slightly more energy and the 351.1 nm line had

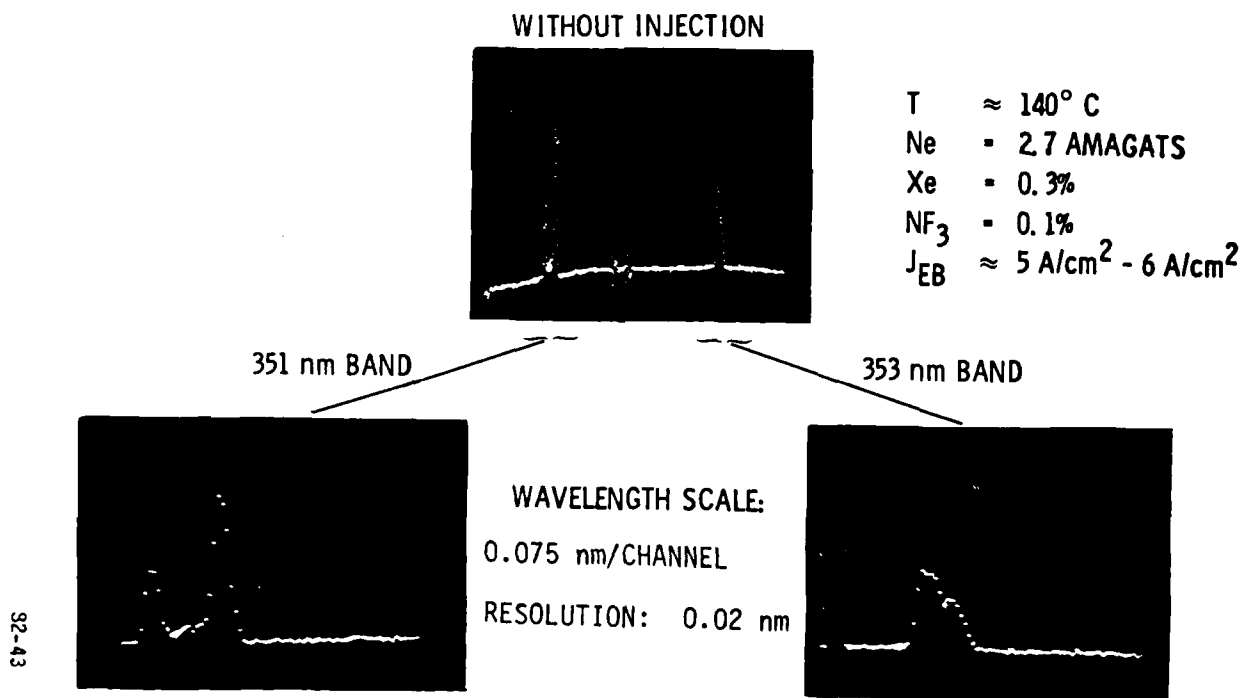


FIGURE 3.2-7 XeF LASER SPECTRUM AT 140°C WITH M = 1.33 RESONATOR

82-41

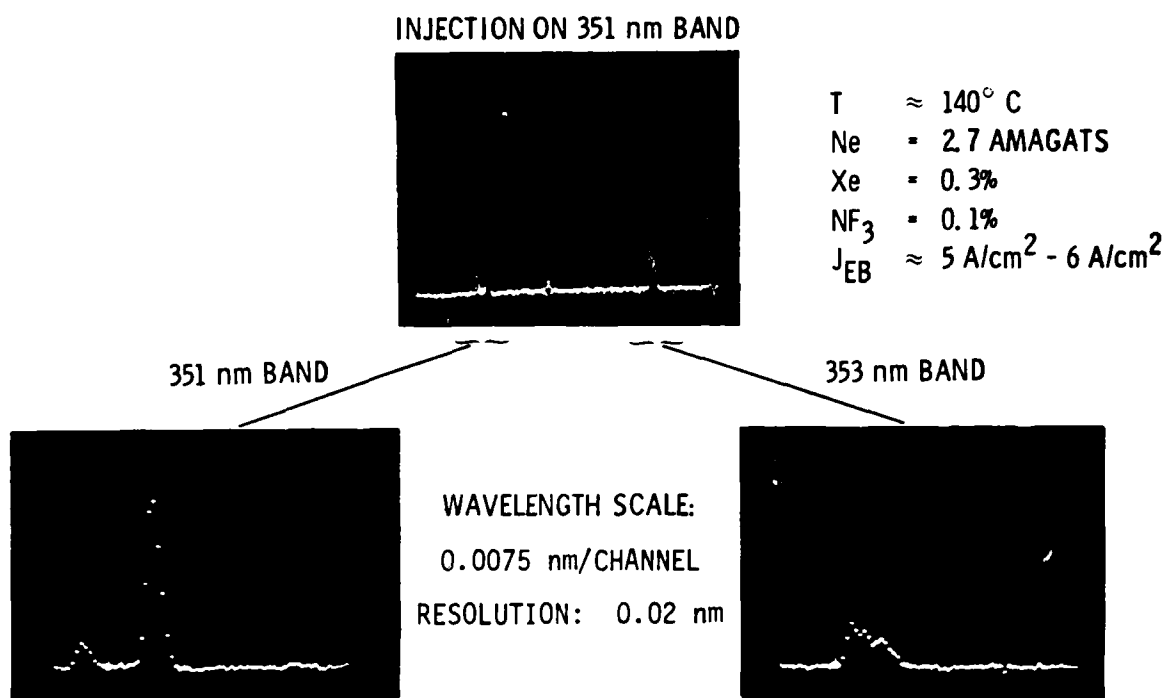


FIGURE 3.2-8 XeF LASER SPECTRUM AT 140°C WITH 351 nm INJECTION

82-42

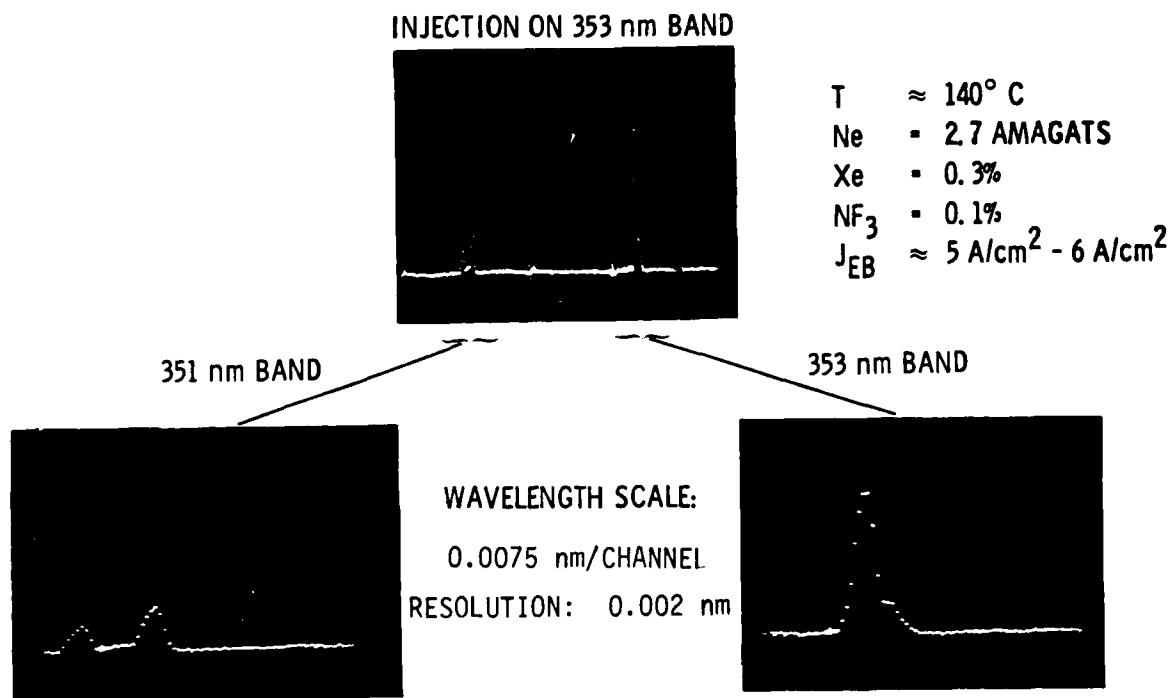


FIGURE 3.2-9 XeF LASER SPECTRUM AT 140°C WITH 353 nm INJECTION

TABLE 3.2-2 HEATED XeF LASER SPECTRAL DISTRIBUTION
WITH M = 1.33 RESONATOR

INJECTION SOURCE	EMISSION PEAK		
	351.1 nm	351.2 nm	353.2 nm
NO INJECTION	18%	42%	40%
INJECTION ON 351.2 nm PEAK	8% ($\Delta = -10\%$)	57% ($\Delta = +15\%$)	35% ($\Delta = -5\%$)
INJECTION ON 353.2 nm PEAK	10% ($\Delta = -8\%$)	18% ($\Delta = -24\%$)	72% ($\Delta = +32\%$)

slightly less energy than the free running case of the previous experiment. Injection on the 351.2 nm line caused a slightly greater funneling of energy into the 351.2 nm than before. However, injection on the 353 nm line had a much greater effect; 72% of the energy was extracted on the 353 nm band compared with 43% in the M = 2.33 experiment.

These results indicated that complete suppression of either one of the lasing lines may not be possible for a hot XeF laser. In the room temperature case, when the 351 nm line was not present in the free running case, injection locking extracts >90 % of the energy in a narrow line. When the laser is heated, neither line can be totally suppressed. Even in the M = 1.33 case, when the operating conditions (lower e-beam current density and lower temperature) favor 353 nm production, total suppression of the 351 nm band was not possible.

Figure 3.2-10 reveals the temporal histories of both the 351 nm and 353 nm bands which were typical for both the M = 2.33 and M = 1.33 experiments. When the laser was free running, both bands turned on nearly simultaneously. With injection on the 351 nm band, the 351 nm band advanced its turn-on while the 353 nm band turn-on was retarded. Conversely, with injection on the 353 nm band, the 351 nm band retarded its turn on, while the 353 nm band turn-on was advanced. The difference in turn on times in both cases was between 50

and 100 ns. The line which received the injection signal turned on sooner because it did not have to build up from noise. The line without the injection signal turned on later because the gain was reduced due to the earlier turn on of the other line.

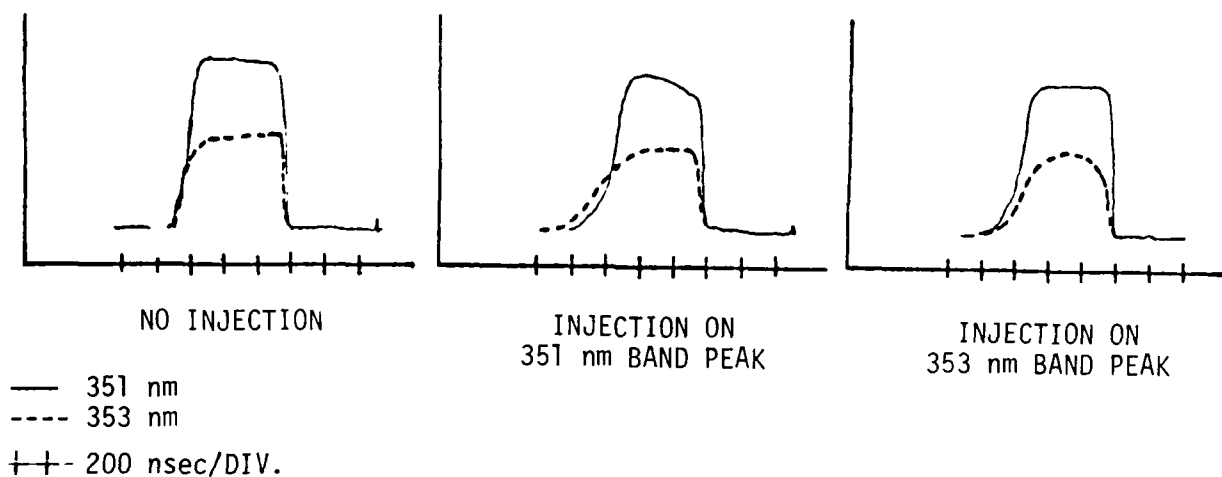


FIGURE 3.2-10 RELATIVE TIME HISTORY

The hot injection locking data strongly suggests that single quantum relaxation was not solely responsible for populating the B- and X-state manifolds. If it were, complete control of the laser should have been possible by injecting on the 351.2 nm line which accessed the $V'=1$ transition. This would have prevented the $V'=0$ state from being populated, and hence, prevented lasing on the 353.2 nm line. However, if multi-quantum relaxation were occurring, the $V'=0$ state would become populated even during injection on the 351.2 nm line. An injection locking code was developed to model the observed energy distribution and temporal evolution data. The B-state manifold model incorporated five levels ($V'=0$ to $V'=4$), multi-quantum relaxation, and quenching. The X-state manifold incorporated three levels ($V''=2$ to $V'=4$), multi-quantum relaxation, and dissociation. No C-state mixing or unstable resonator effects were used in the model. The code qualitatively predicted the relative shifts in turn-on times and energy distribution of the various lines. Upper state relaxation times was a critical parameter in the model.

3.3 XeF Gain Measurements

Temporally resolved gain measurements on the 353 nm line of XeF were recorded using the SWAT laser. Shown in Figure 3.3-1 is a schematic of the experimental setup which was used. As before, the grating tuned flash lamp pumped Candela dye laser coupled with a KDP doubling crystal provided a narrowband, tunable UV source. This UV source was beam split so that one beam acted as a reference while the other beam probed the SWAT gain medium. Both signals were detected by photodiodes enclosed in a screen box. The photodiode outputs were recorded on a dual channel transient digitizer which was housed in a screen room. The XeF laser gas was at room temperature for these measurements.

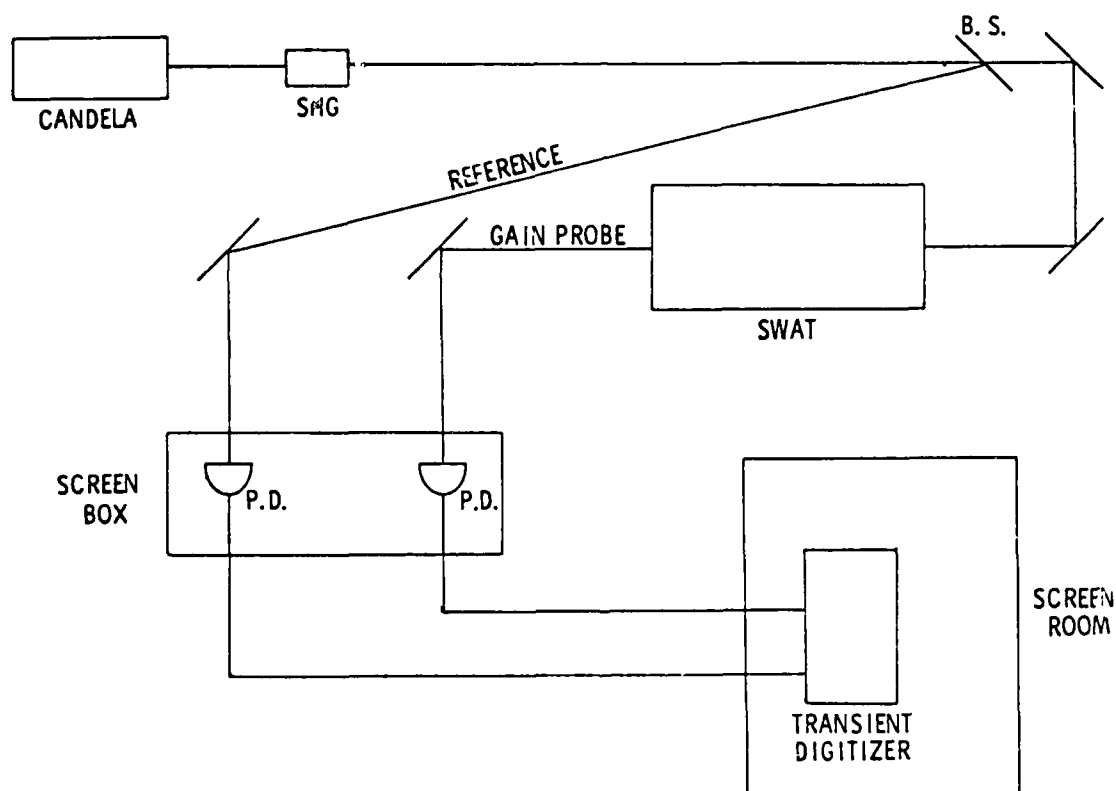


FIGURE 3.3-1 TEMPORALLY RESOLVED GAIN EXPERIMENT

First, the reference and gain probe signals were recorded by the transient digitizer without firing the e-beam. A software routine was then used to overlap the waveforms and scale the amplitudes such that the ratio of gain probe to reference was unity over most of the pulse width. Then, the waveforms were recorded when the e-beam was fired. The resulting ratio of gain probe to reference produced by the software routine provided a temporally resolved evolution of the gain.

The data for the gain on line center is presented in Figure 3.3-2. The data was recorded with the following experimental parameters.

NF_3	=	0.1%
Xe	=	0.3%
Ne	=	3 amagats
J_{EB}	=	9 A/cm ²
V_{EB}	=	390 kV

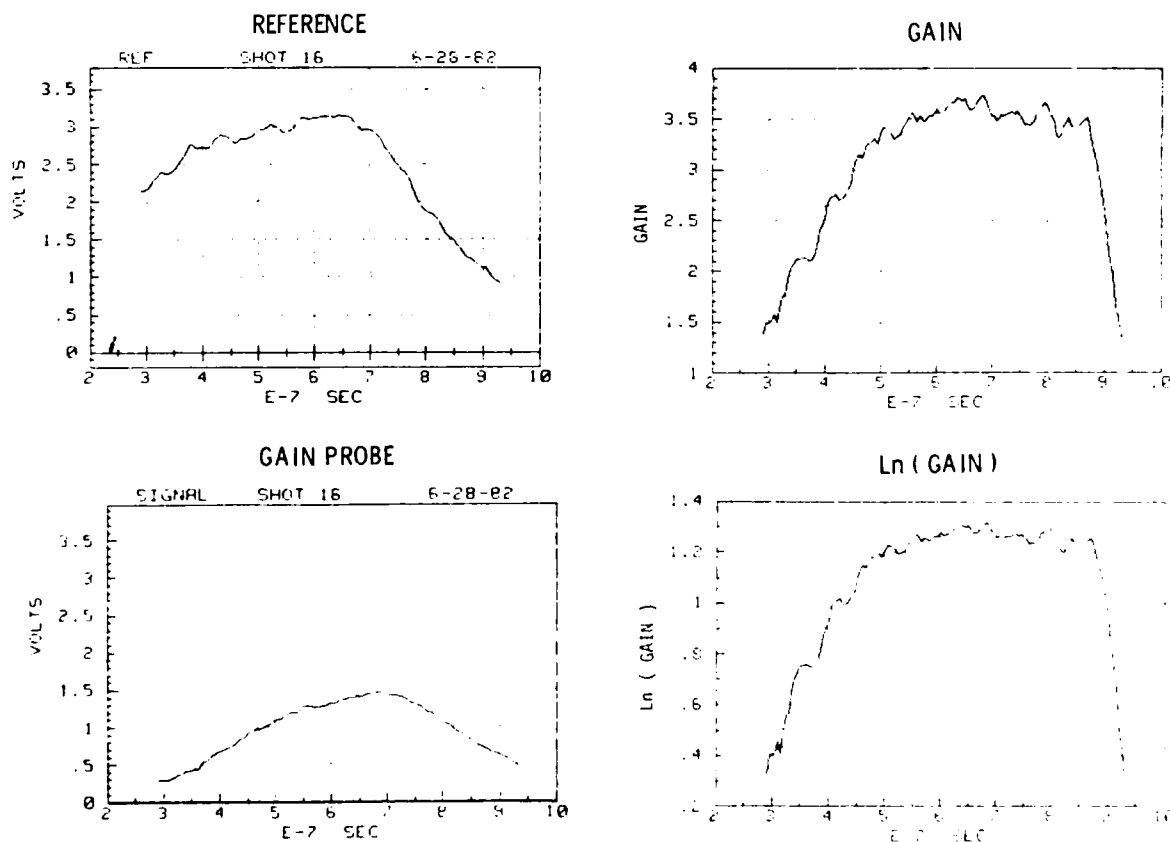


FIGURE 3.3-2 COLD XeF GAIN DATA

The upper and lower traces on the lefthand side are the raw data for the reference and gain probe respectively. The upper and lower traces on the righthand side are the gain and logarithmic gain. The logarithmic gain has a rise time of ~ 200 ns and reaches a steady state value of 1.25. Since the active region which was probed was one meter in length, the steady state gain was 1.25%/cm.

Steady state gain versus wavelength is plotted in Figure 3.3-3. The curve represented by Xe was the raw data which were recorded on one gas fill. Since the performance of the XeF degrades with the number of shots, the data points denoted by "•" were taken on a fresh gas fill and used to scale the raw data. This scaled curve is given by the +'. The gain dropped sharply on the blue side of the peak, but exhibited a long red tail similar to the free lasing spectrum.

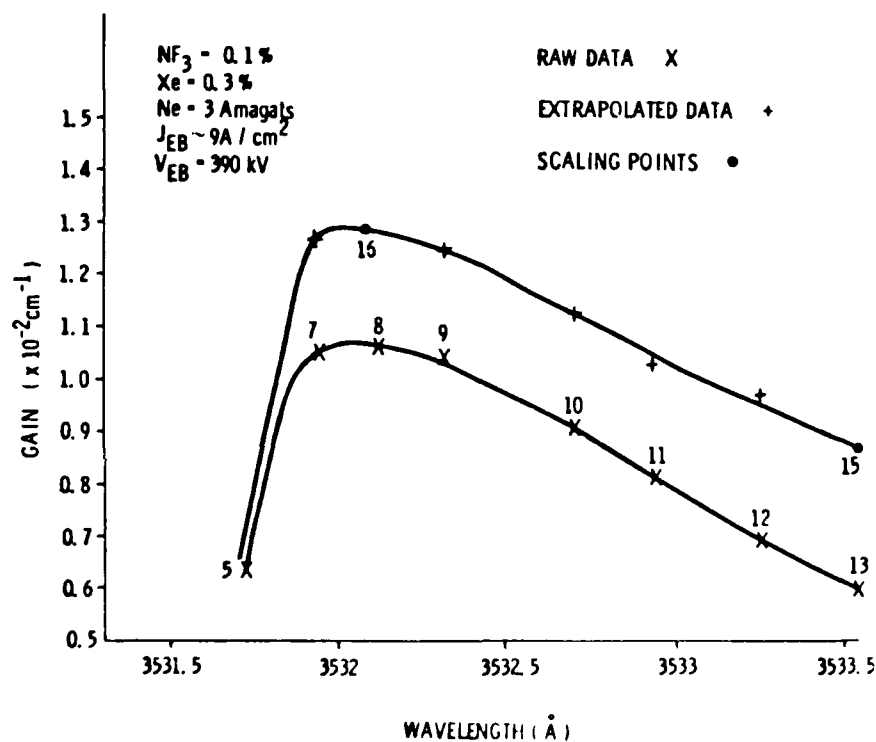


FIGURE 3.3-3 COLD XeF STEADY STATE GAIN VS. WAVELENGTH

4.0 REPETITIVELY-PULSED XeF LASER RAMAN CONVERTER

Experimental investigations on Raman conversion scaling to date have been limited to single-pulse demonstrations of energy, pulse length, and conversion efficiency. For high average power applications requiring good beam quality output, a number of technology issues concerning repetitively pulsed operation need to be addressed. Foremost of these issues specific to Raman converter are medium homogeneity of the Raman cell and optical quality requirements of the beam transport optics. In order to investigate these issues, a baseline experiment using an existing DARPA repetitively-pulsed XeF laser facility has been considered as a possible subscale demonstration. Data generated under this subscale experiment are intended to validate the basic design of a scalable, repetitively-pulsed Raman converter. Specifically, conversion efficiency and beam quality measurements with a flowing hydrogen Raman cell would provide a data base on which further scale-up analysis and engineering design can be founded.

Under this contract, a design analysis for a subscale demonstration experiment was carried out. The analysis consisted of the following elements.

- Overall laser/Raman converter system integration
- Repetitively-pulsed XeF laser injection locking
- Repetitively-pulsed Raman converter design

The analysis was based on nominal operating parameters of a DARPA/Maxwell electron-beam excited XeF laser. The output of this laser is anticipated to yield 7 to 10 J pulses of one microsecond duration at a nominal repetition rate of 25 Hz. The pulse energy and duration are comparable to the single-pulse experiments at NRTC performed under a previous DARPA contract (N00014-80-C-0442), in which 43% power conversion was demonstrated using 353 nm XeF pump radiation to generate second Stokes output at 500 nm. Therefore, the proposed repetitively pulsed subscale experiment represents an extension of the recent Raman scaling experiments to a modest average power levels with primary emphasis on beam quality issues.

The overall subscale experiment is described in Section 4.1 in terms of laser/Raman converter system integration, DARPA/MLI facility modification,

and test plan. Section 4.2 discusses the necessary XeF laser injection locking to achieve spectral bandwidth and polarization requirements, and presents test results of a repetitively pulsed laser injection source. Section 4.3 presents Raman converter design analyses including flow and acoustics considerations for achieving requisite medium homogeneity in the Raman cell.

4.1 Overall System Description and Test Plan

The objective of the proposed repetitively-pulsed XeF laser Raman conversion is to quantify the effect of flow inhomogeneity in the Raman cell on the output conversion efficiency and beam quality. The converter configuration is based on an oscillator-amplifier scheme using sequential Raman shifting into the blue-green starting from the ultraviolet XeF (353 nm) pump radiation. For the Raman medium, flowing hydrogen gas at a pressure near 6 atmospheres at room temperature is used to form two 8 m long, rectangular channels. Figure 4.1-1 shows a schematic of the experimental layout in which the two flow channels are used as the oscillator and amplifier sections.

The Raman oscillator is a single-pass superfluorescent multiple-order Stokes generator with primary outputs in the first and second Stokes components. A focusing geometry, which is optimized for good beam quality output, followed by a spatial filter provides near diffraction-limited Stokes injection radiation into the amplifier. The amplifier pump beam which contains about 90% of the laser output (off of beam splitter BS) is combined with the injection Stokes beams at a dielectric mirror (BC) that reflects 353 nm and transmits the first (414 nm) and second (550 nm) Stokes wavelengths.

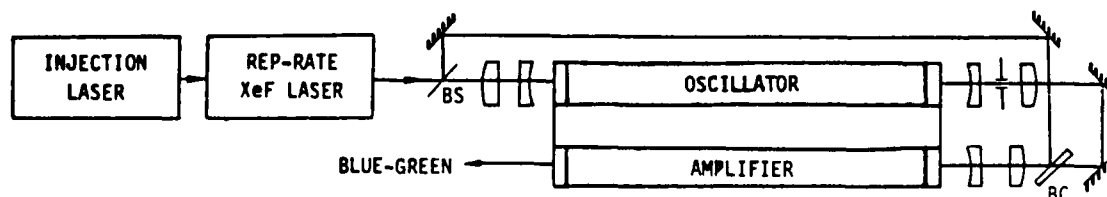


FIGURE 4.1-1 REP-PULSED XeF LASER INJECTION-LOCKING/RAMAN CONVERSION
OVERALL SYSTEM SCHEMATIC

In the Raman amplifier, the injected first Stokes (S_1) radiation is amplified by the XeF beam initially. As the beams propagate into the middle part of the cell, most of the XeF radiation is converted into S_1 , which provides amplification of the second Stokes (S_2) beam. Conversion from S_1 into S_2 occurs in the latter half of the cell, resulting in a dominant output in the second Stokes component.

In order to realize a high conversion efficiency into blue-green, the XeF laser must satisfy certain operating requirements. These include laser beam quality, frequency bandwidth, polarization, pulse shape, and output power. Linearly polarized pump and Stokes fields in parallel yield the maximum interaction via stimulated Raman scattering by H_2 molecules. Injection locking of the laser with an external polarized laser controls the polarization. A narrow frequency bandwidth also provided by injection locking, relaxes the spectral (temporal) correlation tolerance to achieve optimum Raman gain. This is a practical consideration in addition to the narrow spectral bandwidth requirement of the blue-green output for SLC applications. Further details of injection locking are given in Section 4.2.

In order to characterize the laser beam quality, flow, and acoustics diagnostic measurements on the existing DARPA/MLI laser cavity have been carried out by Poseidon Research under a subcontract. The results indicate a need for a major upgrade of the flow loop design and acoustics suppression as discussed in more detail in Appendix A. The modified laser cavity is expected to meet the operating specifications as listed in Table 4.1-2.

TABLE 4.1-1 XeF LASER SPECIFICATIONS

LASER PARAMETER	SPECIFICATION	UNITS
Energy	7-10	J
Pulse Length	1	μ S
Peak Power	7-10	MW
Rep-Rate	25	Hz
Duration	10	sec
Wavelength	353.2	nm
Bandwidth	0.4-4	cm^{-1}
Beam Quality	$\leq 2x$	D.L.
Beam Profile	Uniform Square	--

Based on these operating parameters, a point design of a Raman converter yielded specifications listed in Table 4.1-3.

TABLE 4.1-2 H₂ RAMAN CONVERTER SPECIFICATIONS

RAMAN CONVERTER PARAMETER	SPECIFICATION	UNIT
OSCILLATOR		
Pump Input	1	J
Cell Length	8	m
H ₂ Density	6	amagats
Beam Fluence	5	J/cm ²
AMPLIFIER		
Pump Input	6 - 9	J
Stokes Injection	0.02	J
Cell Length	8	m
H ₂ Density	6	amagats
Medium Optical Quality	2 x	D.L.
Beam Fluence	5	J/cm ²
Fresnel Number	~70	--
Pump Beam Quality	≤ 5 x	D.L.
Stokes Injection Beam Quality	≤ 2 x	D.L.

The requirement on pump beam quality of 5 x D.L. (diffraction-limited) or better allows for phase distortions due to beam transport optics and propagation from the XeF laser to the Raman converter. This beam quality budget also satisfies a Fresnel number scaling constraint which yields an allowable beam quality of about 8 x D.L.

The specification of medium optical quality has a baseline figure of 2x diffraction limit. This is a variable for parametric measurements of the dependence of flow uniformity on Raman conversion efficiency and beam quality. Both near-field and far-field beam measurements are included in a test plan. The near-field data provides spatial intensity variations which could result from local refractive index inhomogeneities and diffraction (scintillation) of the pump and Stokes beams. The far-field beam measurements can determine the Strehl ratio.

4.2 Rep-pulsed XeF Injection Laser

The requirements for the DARPA/MLI rep-pulsed XeF injection locking source have been identified and are presented in this section. A simple model has been used to estimate the minimum injection energy level and temporal pulse-length. The additional requirements for wavelength control, frequency bandwidth, polarization and rep rate allow only a well controlled discharge XeF laser as a viable alternative. Various resonator configurations have been tried and the experimental results are presented. Finally, a recommended injection laser design is given.

An estimate of the minimum injection intensity may be obtained using a ramp-to-flat-top model of the XeF gain pulse, shown in Figure 4.2-1. A simple integration of the net gain during the pump pulse results in an expression which relates the ratio of output to injection intensities (prior to gain saturation) to laser parameters:

$$\ln G = \left(\frac{C \tau_R}{L} \right) \left(g_0^{th} \ell \right) \left[N \left(\bar{t} - \frac{1 + \bar{\tau}_D^2}{2} \right) - \bar{t} + \bar{\tau}_D \right]$$

where

- τ_R = gain ramp-up time (other times normalized to τ_R)
- L = main resonator length
- g_0^{th} = laser gain coefficient to sustain cw oscillation
- ℓ = gain length
- N = number times CW pump threshold
- \bar{t} = time normalized to τ_R
- $\bar{\tau}_D$ = time delay of injection pulse relative to start of gain ramp, normalized to τ_R

In addition, the CW threshold gain is given by

$$g_0^{th} \ell = \alpha \ell + \frac{M}{R}$$

where α is the medium's loss coefficient, M is the unstable resonator magnification, and R is the effective mirror reflectivity. If we now take $\alpha = .005 \text{ cm}^{-1}$, $R = 1$, $\ell = 50 \text{ cm}$, $L = 75 \text{ cm}$, $M = 2$, $\tau_R = 100 \text{ ns}$, $N = 1.5$, $\bar{t} = 1.5$, $\bar{\tau}_D = 1/N$

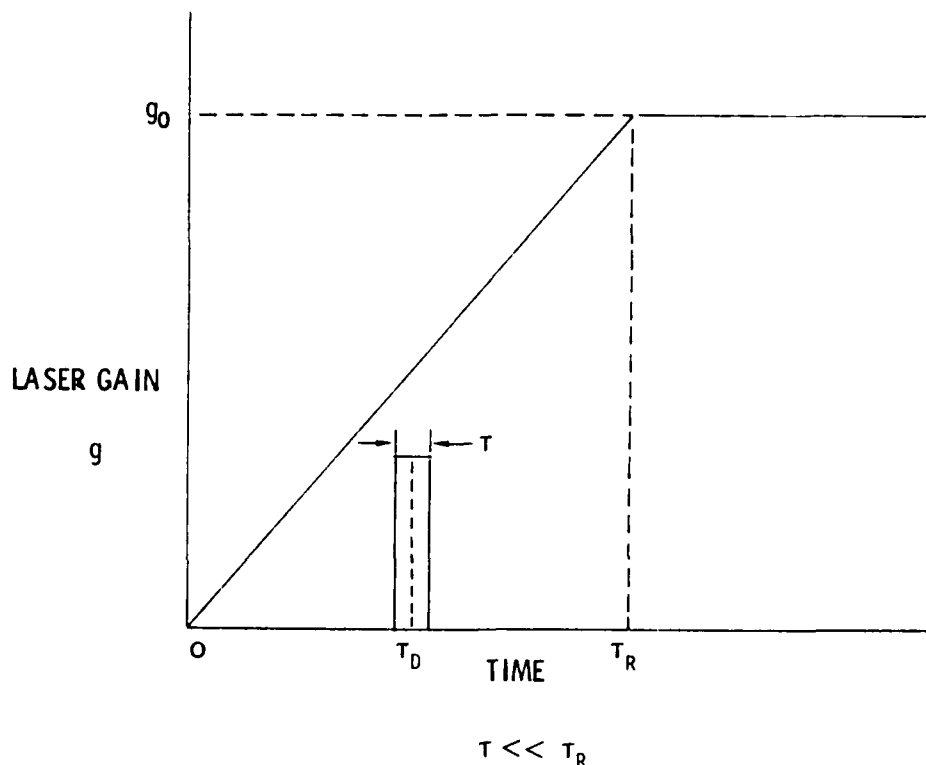


FIGURE 4.2-1 SHORT PULSE INJECTION
GAIN TEMPORAL PROFILE MODEL

(inject when net gain goes positive), then the necessary injection intensity is 10^{-5} the output intensity, I_0 . If we include a safety factor of 10 and use an output intensity of 200 kW/cm^2 , then the necessary injection intensity is 20 W/cm^2 . If the injection is made only into the diffraction channel of the unstable resonator, the necessary power is 5 W. This is consistent with the results of Bigio *et al*, [BS82], who demonstrated injection locking at 351 nm with a CW laser.

The required pulselength for the injection source is simply that it must fill a resonator roundtrip of $2L/C$, or 5 ns for a 75 cm cavity. The necessary injection energy inside the resonator is then 2.5 nJ. This allows a considerable amount of freedom to prepare a good quality, narrowband injection pulse. For design purposes, we chose a minimum energy of $1 \mu\text{J}$ in the resonator.

Wavelength and bandwidth control are additional requirements of the injection source. Mission requirements currently call for a wavelength bandwidth $\Delta\lambda$ greater than .1 Å, corresponding to a frequency bandwidth $\Delta\nu > .8 \text{ cm}^{-1}$. In contrast, a smaller $\Delta\nu$ eases temporal matching of the Raman oscillator and amplifier arms. Therefore, the frequency bandwidth design point is 1 cm^{-1} .

Raman frequency conversion in hydrogen requires a polarized pump source, so the injection laser must be greater than 95% linearly polarized.

Finally, the injection source must have a pulse repetition frequency greater than 25 Hz to meet the XeF laser pulse repetition frequency.

The candidates for the injection source were narrowed rapidly. Only dye and excimer lasers may oscillate at the required wavelength 353 nm, but available dye lasers do not possess the necessary repetition rate. Since a short injection pulse is permitted with no reduction of locking efficiency, the clear choice is a discharge excimer (XeF) laser which has been engineered to provide a good quality beam with the required bandwidth.

Two resonator designs have been implemented to test and optimize performance. The first is a TEM_{00} resonator with an internal telescope (Figure 2a). The

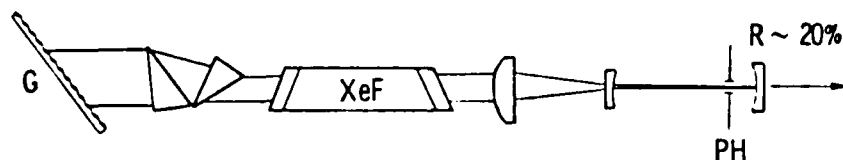


FIGURE 4.2-2a INJECTION LASER CAVITY CONFIGURATION

section between the telescope and the concave mirror forms the diffraction channel and is spatially filtered by the pinhole PH. This is expanded by the telescope (X 10), amplified in the gain medium, and then linearly expanded again by the prism beam expander (X 6) before reflecting from the diffraction grating in Littrow configuration. For polarization control (in addition to the prism Brewster surfaces) an intracavity linear polarizer may be used. A primary consideration in the design of this resonator is to minimize cavity length, since the discharge current pulse is quite narrow.

The second resonator design is an oscillator/amplifier configuration shown in Figure 2b. A stable resonator is set up between the concave output coupler and the diffraction grating. A prism expander of higher power than the previous case must be used if the same frequency bandwidth is to be obtained. A portion of the beam transmitted through the output coupler concave surface is then reflected back through the amplifying medium, and this useful output is picked off on the other side. Pulse energies of $1 \mu\text{J}$ have been reliably obtained with good beam quality in a 1 cm^{-1} bandwidth. A larger gain medium is needed here if the amplified beam is not to be clipped. A Lambda-Physik EMG-101 was used in this experiment, but for the repetition rates required for the DARPA/Maxwell system, the Lumonics TE-430-2 would be satisfactory.

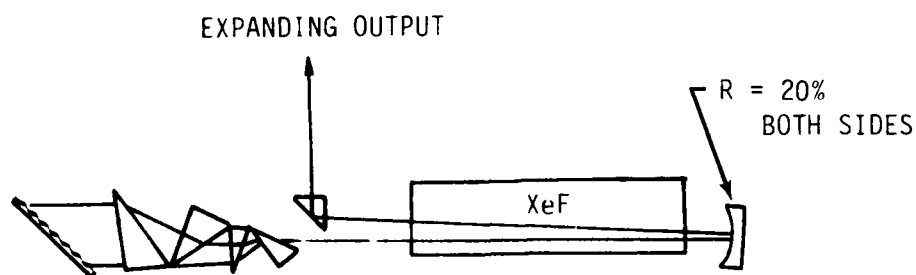


FIGURE 4.2-2b INJECTION LASER CAVITY CONFIGURATION

One feature common to both designs is the characteristically short pulsewidth of these discharge lasers. If the length of the primary laser resonator (DARPA/Maxwell) increases to, say, 1.5 meter the injection pulse must be stretched to 10-15 ns. One method of handling this difficulty is to stack two short pulses using a delay line. Another method is to adjust the injection laser gas mix to stretch the pulse. In general, we found that the pulse could be lengthened by using a mixture which was leaner in Xe and NF_3 than that which provided peak energy performance. For the 25 cm gain length of the Mathematical Sciences Northwest Excilite 401, an NF_3 :Xe:Ne mixture of 0.25%:1%:98.75% with a fill pressure of 40 psia produced a 15 ns pulse with a flat top, but at reduced energy (~ 0.1 mJ). The same technique was tried on the Excilite 402, but the longer gain region of this laser apparently caused an even leaner mixture to be necessary (.05%:.07%:99%). If this method is to be used, a short gain region is preferred.

The recommended design for the injection laser of the DARPA/Maxwell facility depends to a large degree on which commercial injection laser is chosen. One desirable feature of this laser is that it have a short gain length. The number of passes through the frequency selection component is then maximized and the output bandwidth is narrowed. The gain bore diameter usually scales down with the length. This makes the oscillator/amplifier configuration more difficult since there will be interference between the two sections, and an output beam with a hole in it is not acceptable for injection locking. In addition, the gain of the amplifier arm may be insufficient if the discharge length is too short. Therefore, to optimally use the oscillator/amplifier approach a large bore laser with a gain region ~ 60 cm long and a longer discharge pulse is necessary. At the present time, commercial lasers of this type may have repetition rates up to 50 Hz (e.g., Lumonics TE 861).

If a small bore 100 Hz laser is all that is available, then the telescopic resonator is the preferred setup, where considerable care is to be taken in minimizing cavity length and optical losses. The choice of a grating is important; a 600 ℓ/mm 54° blazed grating is recommended. Also, care should be taken in aligning the expansion prisms to minimize feedback reflections. The telescope collimation adjustment is also sensitive. It should be performed using ~ 350 nm light to avoid setup errors due to dispersion.

The above considerations lead to a recommendation for the construction of an ideal injection laser. Such a laser should have a 2 cm bore diameter and a 50-70 cm gain length. Its most important feature would be a long discharge time, 30-50 ns. If such a laser were available, it would greatly simplify the implementation of an injection laser for the DARPA/Maxwell system.

4.3 Repetitively Pulsed Raman Converter Design

The high beam quality requirement for high average power applications leads to a flowing medium for Raman cell. A need for the flow has been identified through calculations on the effect of energy deposition in the Raman medium. It is found that transverse thermal gradients can lead to phase shifts large enough to defocus or distort beams in the cell if the heat is not removed between pulses.

The geometries of the flow channel and energy deposition profile in the Raman medium are quite different from those of lasers. Thus flow homogeneity management and acoustic wave damping considerations must be treated appropriately. In order to address these issues in detail, a subcontract was awarded to Poseidon Research with an objective of generating a preliminary design of a flowing hydrogen cell. The detailed discussions on the trade-off analysis and the cell design are given in Appendices B and C, respectively. A brief summary of the analysis and design are presented in the following sections.

4.3.1 Energy Deposition and Acoustics

The beam geometry of the oscillator and amplifier sections are schematically shown in Figure 4.3-1. The energy deposited in each beam path initially appears as excitation of the hydrogen $V=1$ level. This is subsequently converted into thermal energy by gas collisions. Direct vibration-translation (V-T) energy transfer from H_2 ($V=1$) is slow because of the large energy mismatch between H_2 ($V=1$) and thermal energies. Jeffers, Hilden, and Bauer [JHB 73] have calculated the relaxation of H_2 ($V=1$) by examining both V-T and V-V processes. Beginning with a distribution with 1% of the H_2 in $V=1$ and the remainder in Boltzmann equilibrium at 300K, they find that V-V processes populate levels as high as $V=12$ on time scales of 1 to 10 μs . For these higher levels, V-T relaxation is much more rapid. After about 10 μs , V-T processes dominate

and quench all levels to room temperature in approximately 10^{-3} sec. DeMartini and Ducing [DD 66] have measured the relaxation of H_2 ($V=1$) produced by stimulated Raman scattering in a room temperature gas. They find a quenching time constant τ given by

$$P\tau = (1.06 \pm 0.1) \times 10^{-3} \text{ atm-sec.}$$

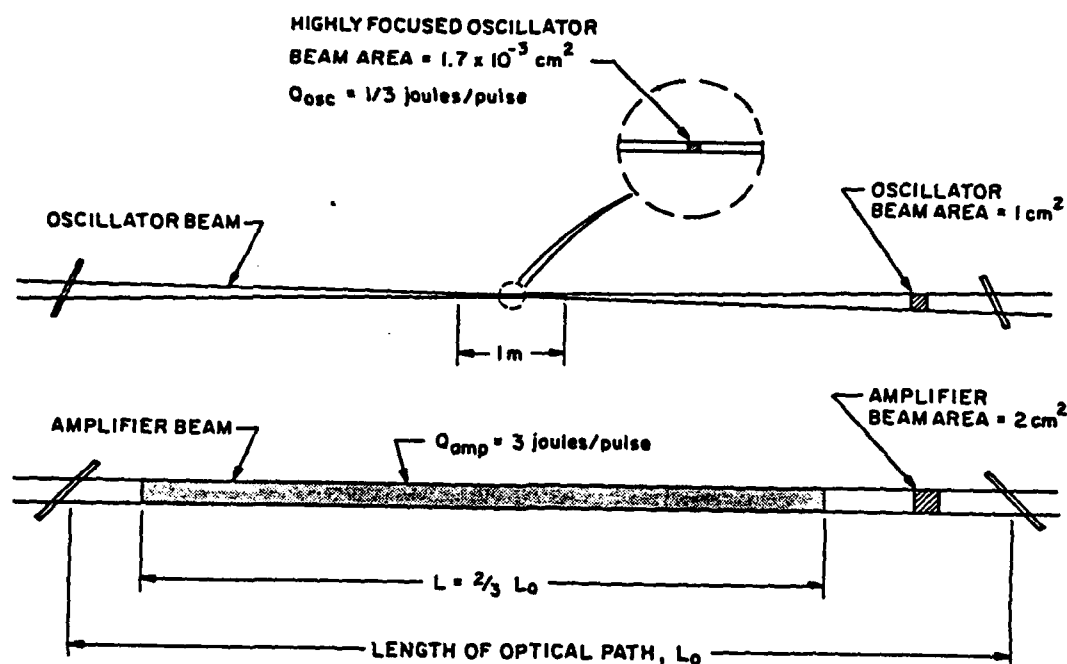


FIGURE 4.3-1 ILLUSTRATION OF BEAM ENERGY DEPOSITION IN RAMAN CELL

Thus, for a Raman amplifier operating between 1 to 10 atmospheres, the $V=1$ level will be quenched in 0.1 to 1 ms. This indicates that all excited H_2 molecules are relaxed between pulses if the pulse repetition rate is less than 1 kHz.

The V - T relaxation results in a local temperature increase followed by an increase in pressure. The heated volume then relaxes back to its original pressure, with a loss of energy equal to the work done. As it expands, acoustic waves are produced and energy propagates into the surroundings. This acoustic energy is expressed as E_a given by

$$E_a = \frac{\gamma}{\gamma-1} P_0 V_0 \left\{ \left(1 + \frac{1}{\gamma} \frac{\Delta P}{P_0} \right) - \left(1 + \frac{\Delta P}{P_0} \right)^{1/\gamma} \right\}$$

where P_0 and V_0 are the initial pressure and volume, respectively, and ΔP is the pressure increase. The ratio of specific heats, γ , for H_2 is 1.41 [Ma67]. (See Appendix B for derivation).

The heat deposited in the gas, Q , can be written as

$$Q = \frac{P_0 V_0}{\gamma - 1} \cdot \frac{\Delta P}{P_0}$$

by recognizing that an initial relative temperature change due to heat release is equal to the relative pressure change. A fraction of the heat that goes into the acoustic energy is the acoustic efficiency $\eta = E_a/Q$.

In the present design of the beam geometries inside the cell, the energy deposited in the oscillator section is about 0.33 J in a thin cylindrical volume approximately defined by a beam area of $1.7 \times 10^{-3} \text{ cm}^2$ by 1 m length. In contrast, the energy deposition in the amplifier section is a function of position, that also depends on Stokes injection and amplifier gain.

For a uniform planewave pump beam profile, the energy deposition per unit volume ($\dot{U} = Q/V_0$) per unit time increment is given by

$$\dot{U} = g_1 I_0^2 (\epsilon_0 \epsilon_1 + \epsilon_1 \epsilon_2) \frac{\omega_R}{\omega_1}$$

where

$$I_0 = I_0(Z = 0, t)$$

$$\epsilon_n \equiv I_n(Z, t)/I_0(Z = 0, t)$$

and I_0 is assumed to be a slowly varying (pump) intensity function of time on a scale of transit times in the cell. As usual, g_1 is the first Stokes intensity gain coefficient, and ω_R/ω_1 is the ratio of Raman transition frequency to the first Stokes frequency. Based on this model, a simulation for the Raman amplifier is shown in Figure 4.3-2. The lower curves represent power conversion, ϵ_n , of the pump (P), first Stokes (S_1), and second Stokes (S_2) as a function of position in the cell. The origin of the normalized cell length corresponds to the input. The upper curve represents the value of a function $\epsilon_0 \epsilon_1 + \epsilon_1 \epsilon_2$, which is a relative measure of power density being deposited into the gas as a function of position. It is clear that primary power deposition occurs near

positions where adjacent Stokes orders have similar conversion values. Using the amplifier design parameters, the peak value of the deposited energy density is $4.5 \times 10^{-3} \text{ J/cm}^3$ where P and S_1 conversion curves intersect. The

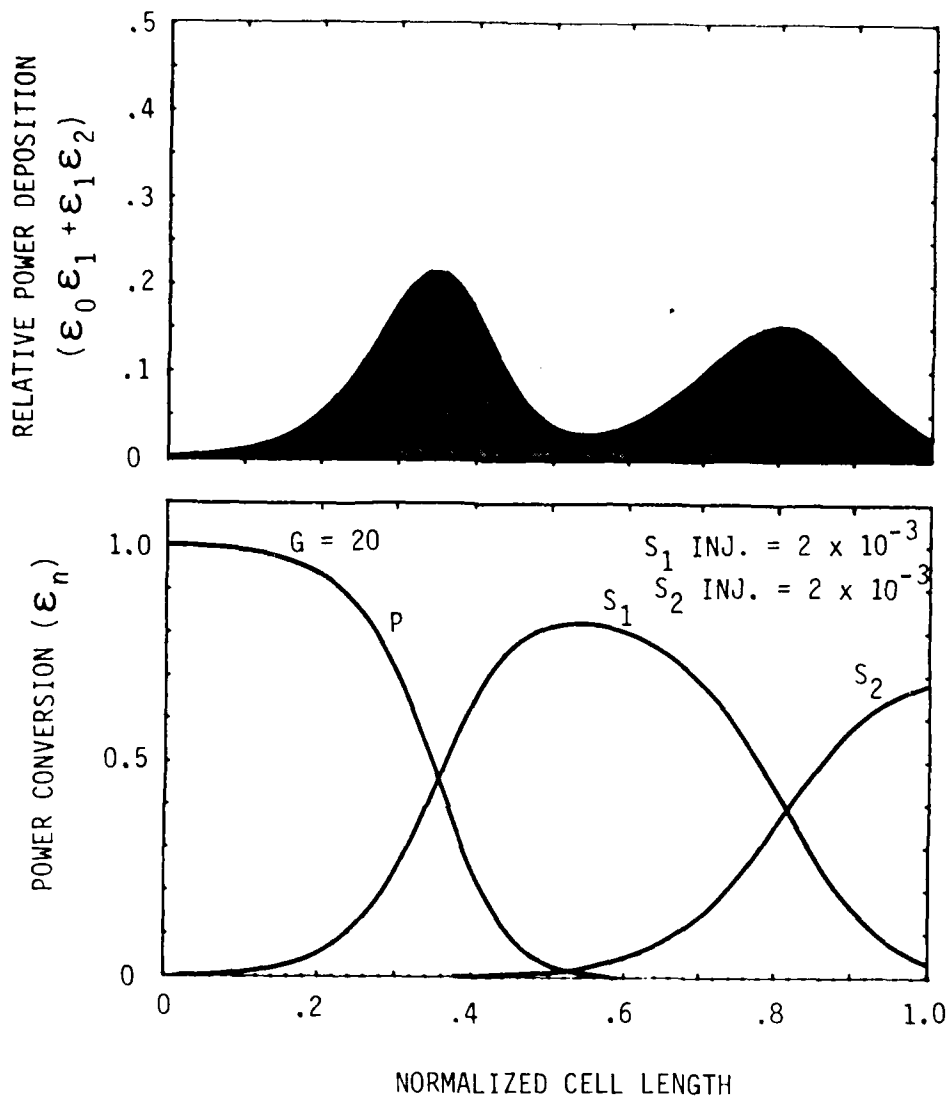


FIGURE 4.3-2 RAMAN AMPLIFIER POWER CONVERSION (LOWER CURVES) AND POWER DEPOSITION (UPPER CURVE) INTO GAS AS A FUNCTION OF POSITION IN AN 8m CELL. AMPLIFIER GAIN IS $G = 20$ WITH STOKES INJECTION LEVELS OF 0.2% FOR S_1 AND S_2 . RELATIVE TO A PUMP INPUT INTENSITY OF 5 MW/cm^2 .

total energy deposited into the gas is about 28% of the input pump energy, which yields 2.5 J for a 9 J input. Although this deposited energy is 7.6 times larger than that in the oscillator, the energy density is about two orders of magnitude smaller in the amplifier. This indicates that acoustic efficiency is much higher in the oscillator, and the acoustic energy radiated in the oscillator section can dominate over that generated in the amplifier.

Detailed analysis on acoustic disturbances by Poseidon Research shows that the oscillator indeed dominates the acoustic power spectrum in the absence of any attenuation. Further discussions in Appendix C address solutions to the acoustic attenuation problem in terms of appropriate muffler material and geometry. Their design analysis indicates that density nonuniformities arising from residual acoustic disturbances can be held to $(P'/P_o)_{rms}$ values near 5×10^{-7} . This $(P'/P_o)_{rms}$ value can be translated into rms phase distortion, ϕ_{rms} , using the relation

$$\phi_{rms} = 2 \pi N \frac{L}{\lambda} \beta \left(\frac{P_o}{P_s} \right) \left(\frac{P'}{P_o} \right)_{rms}$$

N is the number of passes through the cell ($N = 2$); L is the cell length. β is the Gladstone-Dale constant taken to be 1.45×10^{-4} for a wavelength λ of 353 nm in H_2 . (P_o/P_s) is the ratio of the operating density to the density at STP, and hence is essentially the pressure in atmospheres. Evaluating the above relation using the Raman converter design parameters yields a value of $\phi_{rms} = 0.12$ radian.

By defining the divergence of the beam or "beam quality (BQ)," one can relate ϕ_{rms} to BQ according to

$$BQ = (1 - \phi_{rms}^2)^{-1/2}$$

This yields a value of $BQ = 1.01 \times D.L.$ (diffraction-limited) using $\phi_{rms} = 0.12$ radian. Since the design objective for the beam quality through the cell is given as $1.2 \times D.L.$, ϕ_{rms} values up to 0.55 radian may be acceptable. Therefore, the muffler design appears to be adequate to suppress $(P'/P_o)_{rms}$ values with a considerable margin.

4.3.2 Flow Design

The oscillator and amplifier beams are arranged parallel in a single flow cavity as illustrated in Figure 4.3-3. The flow direction is selected to be along the vertical dimension as a result of trade-off analysis on muffler designs. A schematic of the flow cell cross section is shown in Figure 4.3-4. A fan drives the flow from an upstream plenum into a downstream plenum. Note that the working area is a small portion of the flow channel made up of the dissipative material for acoustics attenuation.

The random turbulent disturbances in the flow are an important source of density perturbation in the Raman medium. The allowable random density disturbances are predicted to be larger than the ordered disturbances (e.g., acoustics) by a factor \sqrt{Ne} , where Ne is the number of eddies along the optical path, L . In the present flow geometry, $Ne = L/h$, where h is the height of the cavity. Thus, in order to achieve $\phi_{rms} \leq 0.55$ radian, the allowable $(P'/P_o)_{rms}^{random}$ is about 4×10^{-5} .

According to analysis by Poseidon Research (Appendix C), there are two sources of random free-stream density fluctuations: (1) adiabatic density fluctuations produced by turbulent velocity fluctuations, and (2) isobaric density perturbations caused by temperature fluctuations. The first source is found to be negligible in the present design (i.e., $(P'/P_o)_{rms} \sim 10^{-8}$). However, uniformity is $\Delta T = 0.12K$ under room temperature operation. This temperature tolerance is the most restrictive design constraint; it is also recognized that ΔT requirement must be treated with great care in any subsequent design.

The present flow loop design basically consists of an upstream and downstream plenum, a fan, and a heat exchanger. Temperature variations in this loop can arise from entropy waves and heat exchangers. The former can be generated as a result of acoustic waves impinging on the heat exchanger, and the magnitude of the effect is estimated to yield $\Delta T/T \sim 10^{-7}$ or $(P'/P_o)_{rms} \sim 10^{-8}$. Temperature rise due to heat exchangers themselves are calculated to be $0.03K$ under appropriate cooling conditions (see Appendix C). Thus, $(P'/P_o)_{rms} = 1 \times 10^{-5}$, which is well below the requirement, is considered feasible with a modest heat exchanger power requirement.

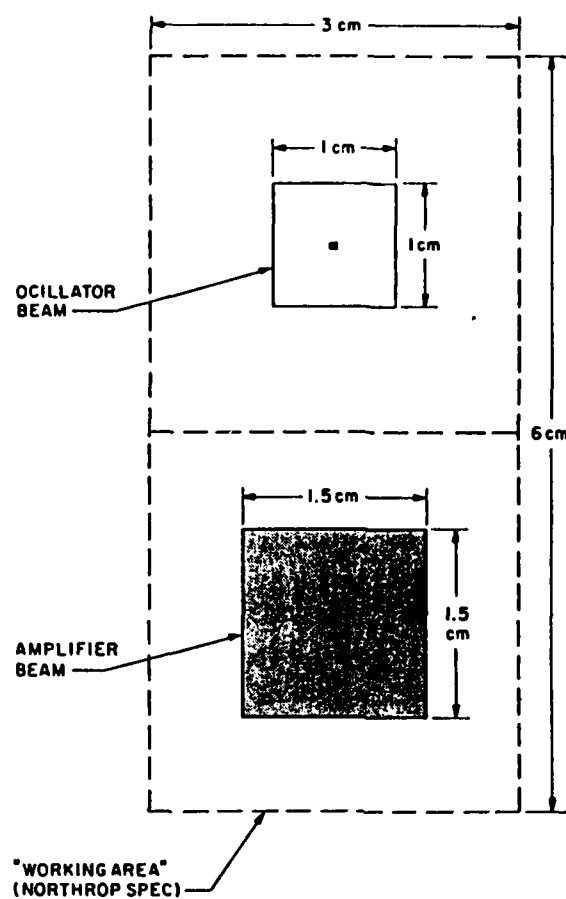


FIGURE 4.3-3 CROSS SECTION OF RAMAN CELL CAVITY

In summary, the detailed analyses and trade-off studies on flow and acoustics issues, principally performed by Poseidon Research, predict feasibility of constructing a prototype flowing hydrogen cell for repetitively pulsed Raman conversion experiment. The flow loop design has been carried out through preliminary design, including identification of key components such as muffler material. The cell fabrication and testing may be pursued in the subsequent technology programs.

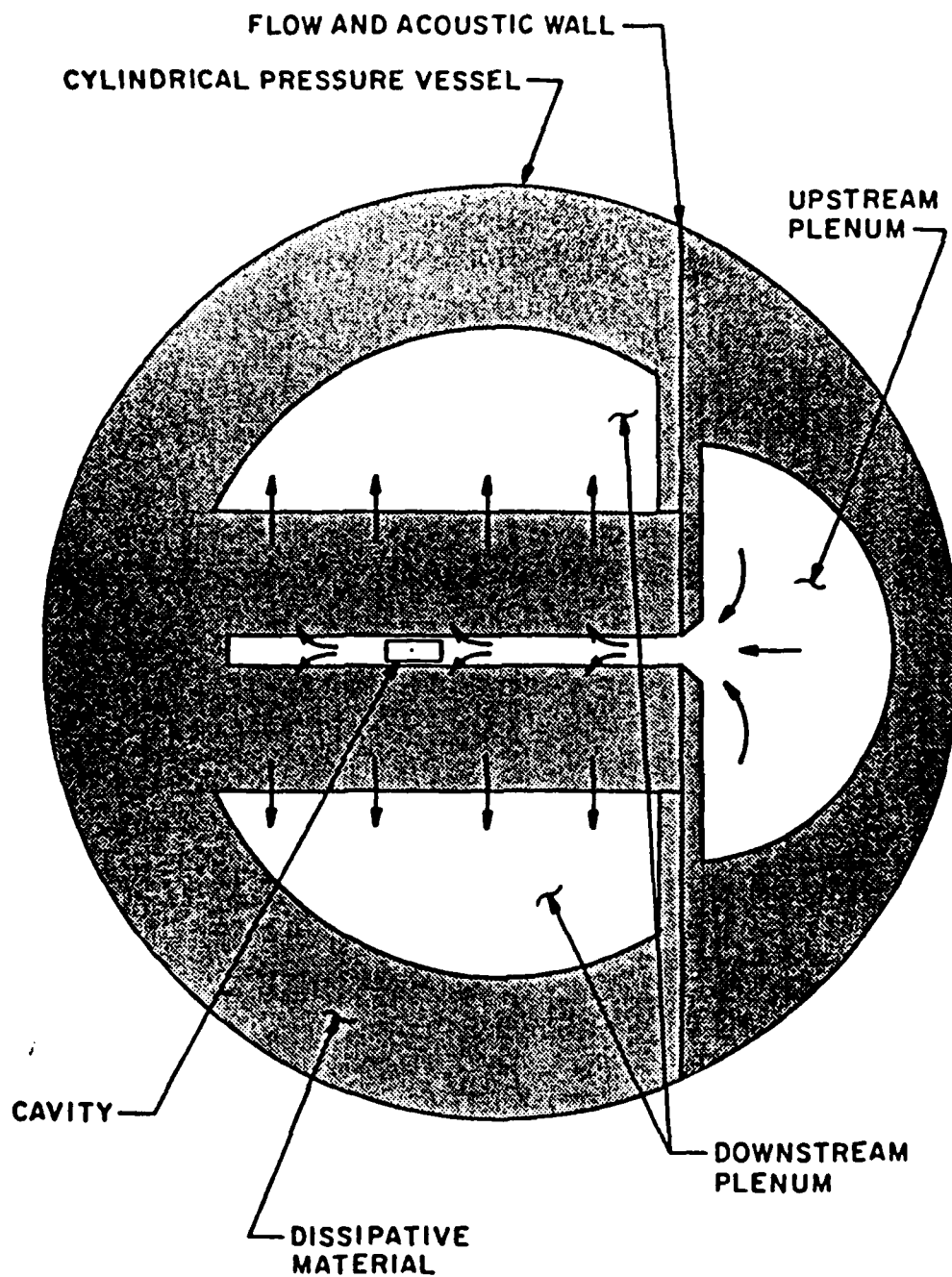


FIGURE 4.3-4 · FLOW DESIGN SCHEMATIC CROSS SECTION

5.0 RAMAN CONVERTER SCALING STUDIES

This section contains results of analytical and experimental investigations relevant to scaling of Raman converters to higher energies and good beam quality. Section 5.1 discusses Stokes injection level requirements in terms of suppressing competing effects which can reduce conversion efficiency and/or beam quality. This requirement is found to translate directly into power scaling of Raman amplifiers. Section 5.2 presents the elements of Raman amplifier modeling which includes both temporal (bandwidth) and spatial (beam quality) effects, as well as physical effects such as linear and Raman-induced refractive index dispersion in the Raman medium. Computer code simulations based on the model are given to illustrate some of the important aspects of Raman amplifier output beam quality; namely, the beam cleanup property and the conditions under which it is feasible. Section 5.3 summarizes the results of a Raman amplifier experiment which demonstrated the beam cleanup phenomenon at low Fresnel numbers.

5.1 Stokes Injection Analysis

The key design parameters governing the performance of Raman converters using the oscillator-amplifier scheme are the injected Stokes intensity and amplifier gain. For efficient conversion, the gain must be chosen such that the injected Stokes beam is amplified well into pump depletion without competing effects. These undesirable effects include superfluorescence, parasitics, and four-wave mixing interactions. Conditions that are necessary to suppress these effects are discussed in this section in terms of Stokes injection level limitations. The requirement of spectral correlation to optimize gain is also discussed for the case of broadband pump laser spectra.

5.1.1 Superfluorescence

Superfluorescence occurs in stimulated Raman scattering when the gain is sufficiently large to amplify Stokes radiation emitted by spontaneous Raman scattering (sprs). Theoretical treatment of this phenomena has been described using quantum electrodynamics [MR81] as well as phenomenological approaches [EB79]. Using the latter approach, the intensity growth of spontaneous Raman scattering can be given by

$$\frac{dI_s}{dz} = \int_{\Omega} N \frac{d\sigma}{d\Omega} I_p d\Omega \quad (5.1)$$

where N is the number density, $\frac{d\sigma}{d\Omega}$ is the differential Stokes scattering cross section; I_p is the pump intensity. Integration over solid angles depends on the geometry of the amplifier; this may be approximated by a gain region bounded by beam area, A , and length, L . The angular dependence of $\frac{d\sigma}{d\Omega}$ is well known [P1 34] and is nearly constant for small solid angles in the forward scattering direction. This, eq. (5.1) simplifies to

$$\frac{dI_s}{dz} \approx N \left(\frac{d\sigma}{d\Omega} \right)_{\theta=0} I_p \Delta\Omega \quad (5.2)$$

where $\Delta\Omega = A/L^2$ is the solid angle accessible to stimulated Raman gain over the length of the amplifier pumped by a large Fresnel number beam (i.e. $A/\lambda L \gg 1$).

The effective seed radiation at the Stokes frequency can be estimated from eq. (5.2) by integrating over an e-folding length, given by

$$\ell = (gI_p)^{-1} \quad (5.3)$$

where g is the intensity gain coefficient of the Stokes radiation.

The result yields an effective input Stokes intensity given by

$$I_s \approx \frac{NA}{gL^2} \left(\frac{d\sigma}{d\Omega} \right)_{\theta=0} \quad (5.4)$$

The effective input level due to spontaneous Raman scattering can now be expressed as

$$\tau_{\text{sprs}} \equiv \frac{I_s}{I_p} \approx \frac{gNP}{G^2} \left(\frac{d\sigma}{d\Omega} \right)_{\theta=0} \quad (5.5)$$

where P is the pump beam power, and G is the integrated small signal gain parameter defined by

$$G = gI_p L \quad (5.6)$$

The effective Stokes input level as given by eq. (5.5) can lead to uncontrolled amplification with beam divergences on the order of $\Delta\Omega$, which may be much larger than the desired beam divergence. In order to suppress this effect, the amplifier gain and the injected Stokes level must be chosen to deplete the pump radiation well before the spontaneous Stokes radiation can be amplified to any significant levels. In the case of a first Stokes amplifier, the necessary gain to achieve 50% photon conversion in the saturated regime is given by

$$G_{\text{sat}} = \frac{\ln(1/\eta_{\text{inj}})}{1 + \eta_{\text{inj}}(u_p u_s)} \quad (5.7)$$

where η_{inj} is the injected Stokes intensity level relative to the undepleted pump intensity. For small values of η_{inj} , eq. (5.7) reduces to

$$\eta_{\text{inj}} \approx e^{-G_{\text{sat}}}; (\eta_{\text{inj}} \ll 1) \quad (5.8)$$

Therefore, for a given value of gain, a minimum requirement exists for the Stokes injection level to achieve efficient conversion. This minimum level, given by (5.8), must also be much larger than the spontaneous Raman intensity level to suppress superfluorescence. Figure 5.1-1 shows a plot of Stokes input level as a function of gain for saturated amplification and spontaneous Raman scattering in H_2 gas at a pump wavelength of 351 nm. The curves are calculated using $\frac{d\sigma}{d\Omega} = 9 \times 10^{-30} \text{ cm}^2/\text{sr}$ [BB83] and $N(J=1) = 1.1 \times 10^{20} \text{ cm}^{-3}$ and $g = 5 \times 10^{-9} \text{ cm}^2/\text{w}$ corresponding to normal hydrogen gas at 6 amagats.

It is evident that at power levels of 10^8 W or less the condition $\eta_{\text{inj}} \gg \eta_{\text{spr}}$ is satisfied for $G < 25$. Above this gain η_{spr} can exceed η_{inj} , and superfluorescence may dominate the Stokes output. Hence, lower gains and appropriate injection levels provide the preferred operating conditions for high conversion efficiency with low divergence Stokes beam.

5.1.2 Parasitics

Parasitics represent another phenomenon that can lead to uncontrolled Stokes amplification with large beam divergences. A likely mechanism for parasitics in

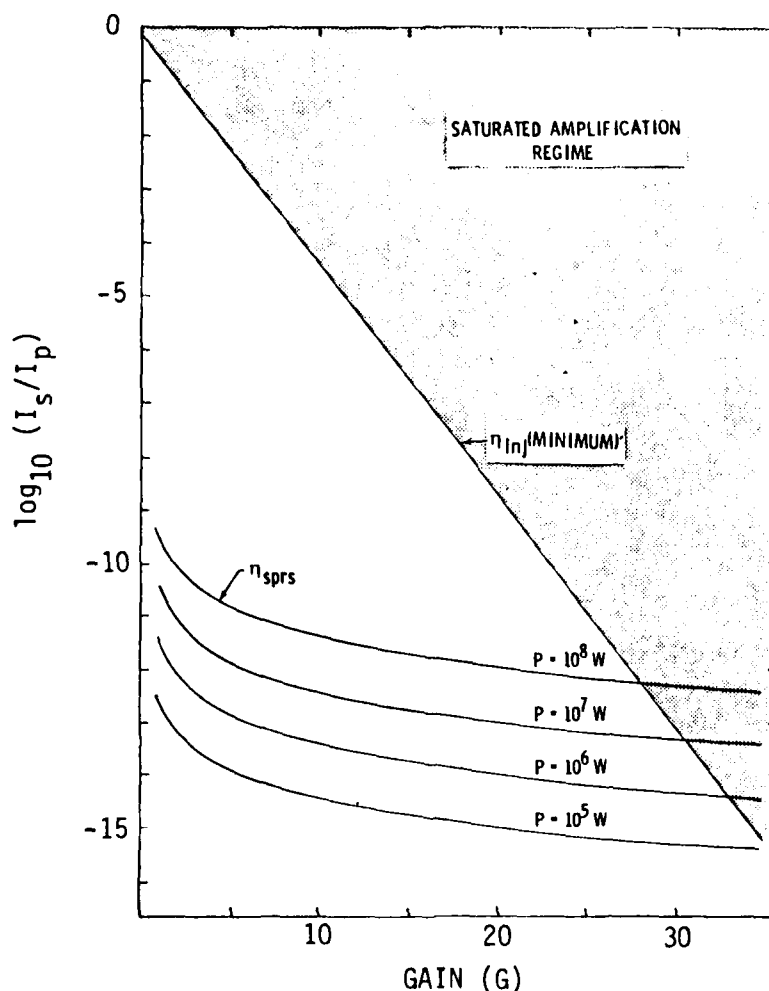


FIGURE 5.1-1 STOKES INPUT LEVEL VS. GAIN FOR SATURATED AMPLIFICATION AND SPONTANEOUS RAMAN SCATTERING

a Raman amplifier is the feedback of amplified Stokes radiation appearing at the input as effective noise. This feedback may be generated as a result of back-scattering of Stokes radiations at the output cell window and other optics. Upon reflections inside the cell, the backscattered radiation may be scattered again in the forward direction, thereby contributing to a divergent component of Stokes beam in the cell. If this contribution is not suppressed and/or if adequate injection level is not provided, parasitics may increase the beam divergence substantially.

In order to estimate the feedback levels, consider a Raman cell made of two windows and a long cylindrical tube of aperture A and length L . Each of the windows is assumed to scatter incident radiation with an efficiency $\frac{d\phi}{d\Omega}$ into a differential solid angle. The backscattered Stokes power due to the output window is given by

$$\frac{dP_{bs}}{d\Omega} = I_s^{OUTPUT} \times \frac{d\phi}{d\Omega} dA \quad (5.9)$$

If reflections inside the tube are suppressed by a suitable wall material, then the feedback radiation reaching the input window is approximately given by:

$$\frac{\Delta P_{bs}}{A} \approx A I_s^{OUTPUT} \times \frac{d\phi}{d\Omega} \Delta \Omega \quad (5.10)$$

where $\Delta \Omega$ is an effective solid angle. This approximation neglects backward Raman amplification which is valid for vibrational Raman shifting in H_2 at visible and UV wavelengths because of a large asymmetry of forward and backward gain coefficients. If the same scattering process is assumed for the input window, then the effective Stokes input in the forward direction is given by

$$I_s^{NOISE} \approx \frac{\Delta P_{bs}}{A} \frac{d\phi}{d\Omega} \Delta \Omega \quad (5.11)$$

Since the output Stokes intensity can be nearly the quantum ratio times the input pump intensity in an efficient converter, equations 5.10 and 5.11 may be combined to yield

$$\tau_{iNOISE} \equiv \frac{I_s^{NOISE}}{I_p} \approx \frac{\omega_s}{\omega_p} \left(\frac{d\phi}{d\Omega} \right)^2 (\Delta \Omega)^2 \quad (5.12)$$

Thus, numerical values of τ_{iNOISE} depend strongly on the scattering efficiency and geometry. High-quality transparent glass substrates polished to rms roughness of about 20 ~ 30 Å typically yield scattering efficiencies on the order of 1% in the UV to visible region [Ho 81], as shown in Figure 5.1-2. If the scattered light is assumed to be isotropically radiated, then $d\phi/d\Omega$ has a numerical value on the order of $10^{-3}/\text{sr}$.

The geometry of the amplifier can be expressed in terms of the Fresnel number, $N_F = A/\lambda L$. Thus, the scattering solid angle is approximately given by $\Delta \Omega = N_F(\lambda/L)$. A substitution into eq. (5.12) yields

$$\tau_{iNOISE} \sim 10^{-6} \times \left(\frac{\lambda}{L} \right)^2 N_F^2 \quad (5.13)$$

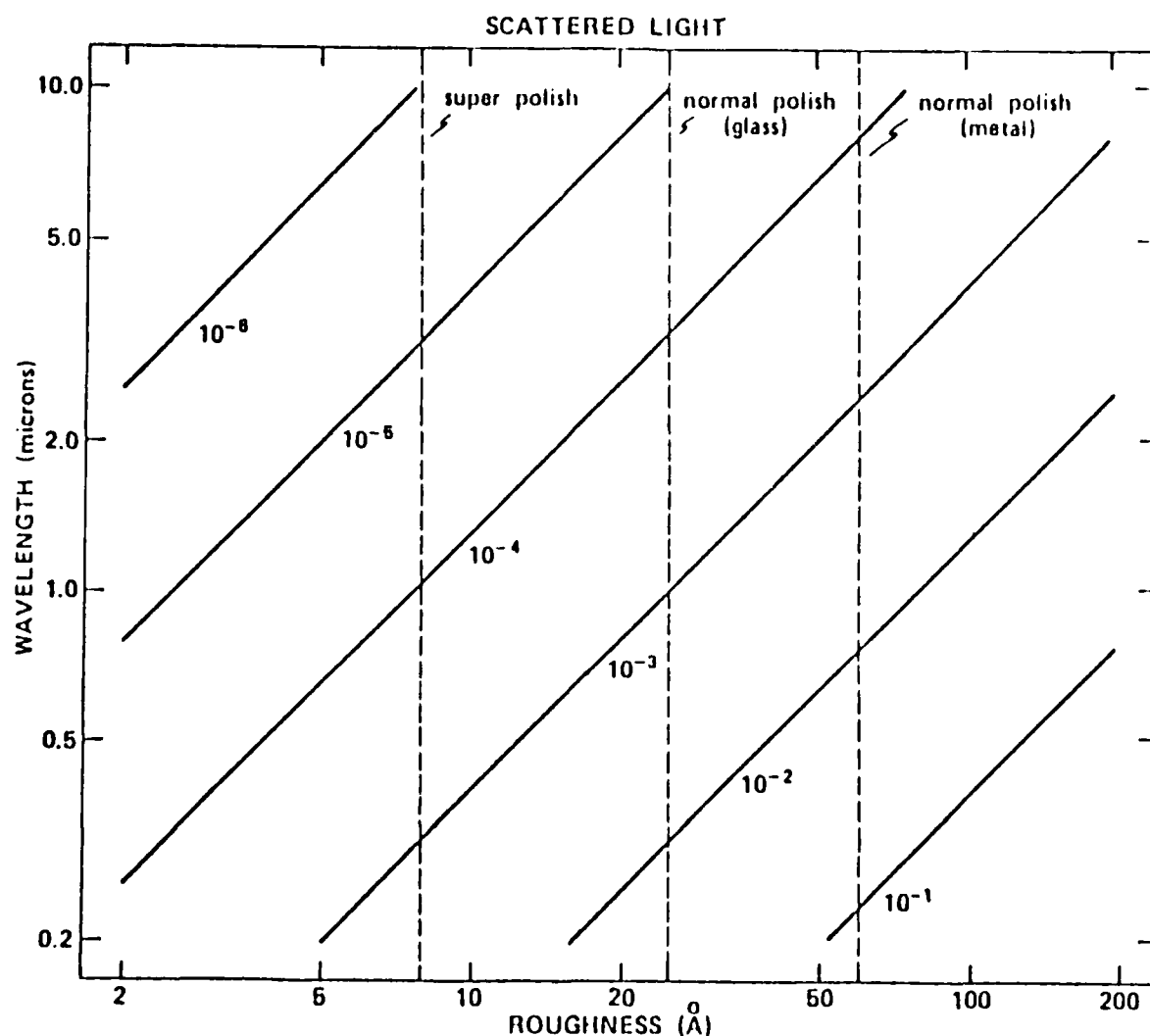


FIGURE 5.1-2 SCATTERING BY OPTICAL SUBSTRATES VS. RMS SURFACE ROUGHNESS
AT VARIOUS WAVELENGTHS

This expression is plotted in Figure 5.1-3 for various N_F at values of λ/L which are typical of Raman amplifiers being considered. Evidently, the effective input Stokes noise due to diffuse backscattering from windows and/or optics becomes important if the injected Stokes levels are much smaller than 10^{-10} . This criterion is roughly comparable to the superfluorescence suppression requirement described in the previous section.

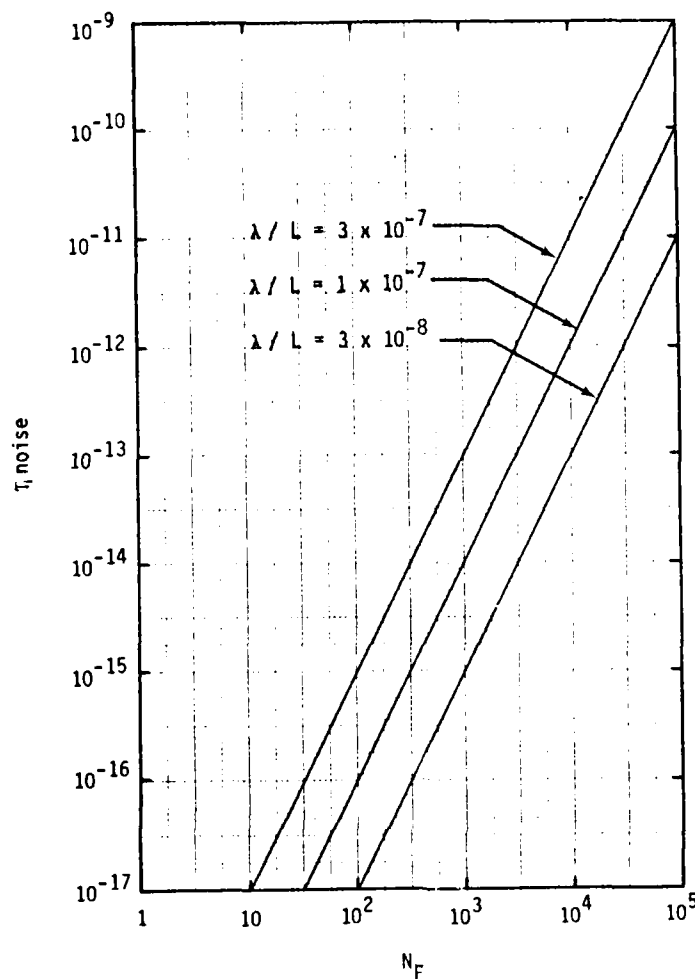


FIGURE 5.1-3 PARASITICS STOKES INPUT LEVEL VS. FRESNEL NUMBER
FOR ISOTROPIC SCATTERING EFFICIENCY OF 1%

5.1.3 Four-Wave Mixing

One of the ways in which four-wave mixing affects Raman amplifier conversion efficiency of higher Stokes order is to generate seed radiation that can compete with the injected Stokes radiation. The seed radiation may have a beam divergence exceeding that of the injected Stokes beam. This can potentially lead to uncontrolled output if the mixing-generated seed is amplified substantially before the pump radiation is converted into a collimated Stokes output. Therefore, the intensity of the seed radiation generated by four-wave mixing determines one of the minimum injection intensity requirements to control conversion efficiency and beam divergence.

The intensity of the seed radiation due to four-wave mixing can be calculated from a set of coupled plane-wave field equations governing the pump (E_0) and the first two Stokes orders (E_1 and E_2) under steady-state conditions [MK69].

$$\frac{dE_0}{dZ} = -\frac{g_0}{4\eta_i} |E_1|^2 E_0 + E_1^2 E_2^* e^{i\Delta k Z} \quad (5.14)$$

$$\frac{dE_1}{dZ} = \frac{g_1}{4\eta_i} |E_0|^2 E_1 - |E_2|^2 E_1 \quad (5.15)$$

$$\frac{dE_2}{dZ} = \frac{g_2}{4\eta_i} |E_1|^2 E_2 + E_0^* E_1^2 e^{-i\Delta k Z} \quad (5.16)$$

where $g_{0,1,2}$ are intensity gain coefficients, and η_i is the impedance of free space. There exists a wave vector mismatch, Δk , due to dispersion of the Raman medium, and it is defined by

$$\Delta k \equiv k_0 - 2k_1 + k_2 \quad (5.17)$$

with

$$k_i = \frac{n_i \omega_i}{c} \quad (5.18)$$

where n_i is the refractive index at frequency ω_i . For H_2 at 1 amagat, the index of refraction (for $\lambda > 250$ nm) is given by [Ka 64]

$$n = 1 + \frac{0.91992 \times 10^{27}}{1.01305 \times 10^{31} - \omega^2} + \frac{0.75379 \times 10^{27}}{1.66813 \times 10^{31} - \omega^2} \quad (5.19)$$

Using this formula, the calculated coherence length, $L_c \equiv |\pi/\Delta k|$, for the second Stokes of the XeF (353 nm) wavelength is 16.1 cm at 1 amagat. Since typical operating densities are in the range of 1 to 20 amagats, four-wave mixing interaction occurs over lengths much longer than L_c ; this leads to an oscillating power flow from the pump field to the second Stokes field and vice versa. Figure 5.1-4 shows a computer simulation based on equations 5.14-5.16. The second Stokes (S_2) conversion efficiency is plotted as a function of $G \equiv g_1 I_0 Z$, where Z ranges from 0 to 12 m. The coherence length is assumed to be 2.5 cm which corresponds to

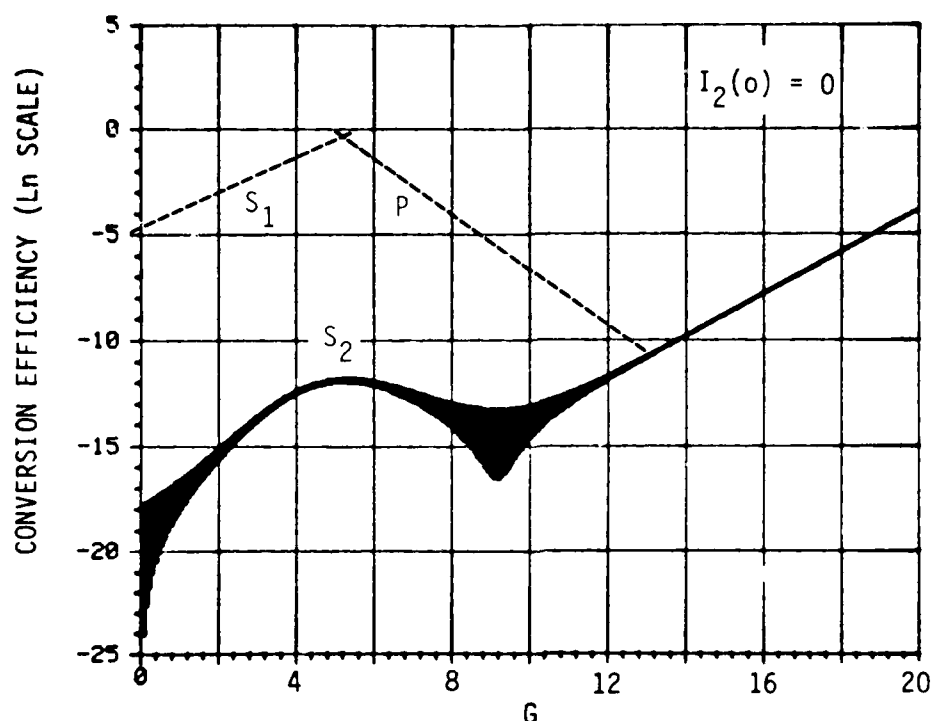


FIGURE 5.1-4 S_2 BUILDUP WITH NO INJECTION

an operating density of 6.5 amagats. An S_1 injection level of 1% is used, but S_2 injection level is set to zero in Figure 5.1-4. Thus, S_2 is generated entirely by four-wave mixing and shows the expected oscillatory behavior indicated by the shaded regions. The oscillation amplitude decreases as the S_2 intensity increases toward $G \approx 5$. This local maximum occurs as the product of the pump and S_1 fields maximizes; beyond this gain the pump is depleted significantly by S_1 , and S_2 conversion decreases as the oscillation amplitude becomes larger. However, as G increases still further, the S_2 intensity increases due to the stimulated Raman term in eq. (5.16). This indicates that four-wave mixing introduces an effective S_2 input level on the order of e^{-15} .

The conversion efficiency of S_2 in the presence of both injection radiation and four-wave mixing interaction is illustrated in Figures 5.1-5 and 5.1-6. All other conditions are the same as in Figure 5.1-4. In Figure 5.1-5, an S_2 injection level of 10^{-5} is used, which leads to an oscillatory growth of the S_2 intensity for gains up to about 8. In this region, four-wave mixing is superimposed over an exponential growth due to stimulated Raman gain.

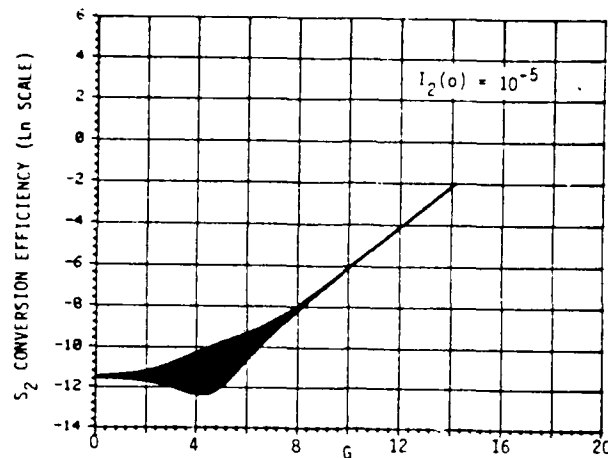


FIGURE 5.1-5 S_2 BUILDUP WITH 10^{-5} INJECTION

Figure 5.1-6 illustrates an S_2 growth essentially governed by stimulated Raman gain with an injection level of 10^{-3} . Note that the oscillatory growth is greatly reduced with a higher injection level, which indicates that four-wave mixing contribution to the amplified S_2 beam decreases as injection levels are increased.

A necessary condition on the injection level to suppress four-wave mixing contribution can be derived from the peak mixing efficiency given by

$$\epsilon_2^{\text{MIX}} = \left[\frac{G}{2\pi} \left(\frac{u_2}{u_1} \right) \left(\frac{L_c}{L} \right) \right]^2 \quad (5.20)$$

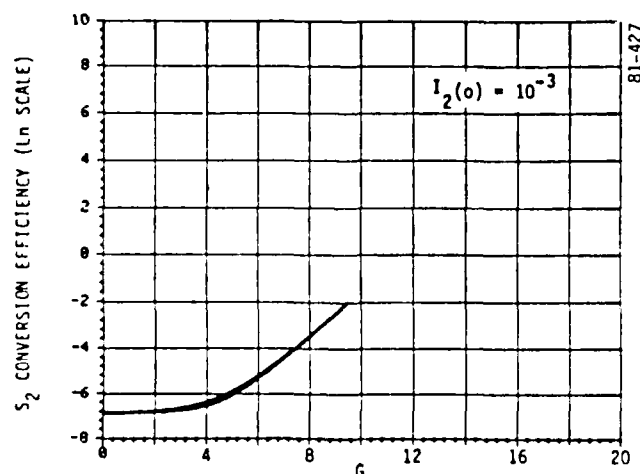


FIGURE 5.1-6 S_2 BUILDUP WITH 10^{-3} INJECTION

Using the parameters of Figure 5.1-4, the calculated value of ϵ_2^{MIX} is 3×10^{-5} . If an injection level comparable to ϵ_2^{MIX} is used, the expected S_2 intensity growth would be similar to that of Figure 5.1-5. Thus injection levels much higher than ϵ_2^{MIX} are necessary; Figure 5.1-6 suggests that a factor of one to two orders of magnitude may be required.

The discussion of four-wave mixing up to now has involved only a colinear geometry in which all waves propagate in the same direction. In practice, real beams have finite divergence and the possibility of angular phase matching should be considered, as it defines acceptable beam divergence and/or beam crossing angle. Figure 5.1-7 shows a wave vector diagram for a collimated S_1 beam interacting with

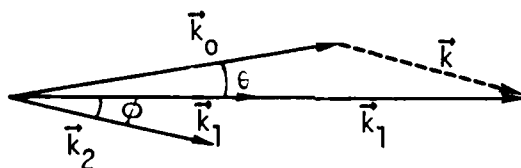


FIGURE 5.1-7 WAVEVECTOR DIAGRAM FOR FOUR-WAVE MIXING

a pump beam at an angle θ . The generated polarization vector \vec{k} is given by $2\vec{k}_1 - \vec{k}_0$. The S_2 wave vector is assumed to make an angle ϕ with the S_1 beam.

Angular phase matching (i.e., $\vec{k} = \vec{k}_2$) occurs if the following momentum conservation relations are satisfied:

$$k_0 \cos \theta + k_2 \cos \phi = 2k \quad (5.21)$$

and

$$k_0 \sin \theta - k_2 \sin \phi = 0 \quad (5.22)$$

For small angles,

$$\phi \approx \sqrt{\frac{k_0}{k_2}} \sqrt{\frac{2\Delta k}{k_2 + k_0}} \quad (5.23)$$

and

$$\theta = \sqrt{\frac{k_2}{k_0}} \sqrt{\frac{2\Delta k}{k_2 + k_0}} \quad (5.24)$$

For the case of XeF (353 nm) pump wavelength and $L_c = 2.5$ cm, the phase matching angle, θ_{PM} , is approximately 2.4 mrad. This means that the injected S_1 and pump beams have to be overlapped with each other at angles much smaller than the θ_{PM} value; otherwise, phase matching enables significant build up of the second Stokes beam propagating at an angle $\phi_{PM} \approx 3.4$ mrad. Equally important are the beam divergence angles of the pump and S_1 radiation as they may also lead to phase matched S_2 mixing.

Under conditions where $\theta \ll \theta_{PM}$ is satisfied, four-wave mixing is not phase matched, and there is no unique angle for the S_2 beam direction. Using the wave vector diagram of Figure 5.1-7, the residual mismatch can be expressed as

$$\Delta k_z \approx \Delta k + \frac{1}{2}k_0 \theta^2 + \frac{1}{2}k_2 \phi^2 \quad (5.25)$$

In the case of collimated beams ($\theta = 0$), the angle ϕ_c for which the mismatch is twice Δk is given by

$$\phi_c \approx \sqrt{\frac{2\Delta k}{k_2}} = \sqrt{\frac{\lambda_2}{L_c}} \quad (5.26)$$

Using $L_c = 2.5$ cm, $\phi_c = 4.47$ mrad; therefore, the divergence of S_2 radiation due to phase mismatched four-wave mixing interaction can greatly exceed the input beam divergence.

5.1.4 Spectral Correlation

Raman amplifiers pumped by broadband lasers impose an additional requirement on the injected Stokes radiation with respect to phase correlation of the spectral modes of the Stokes field with those of the pump field. Under conditions where chromatic dispersion is negligible, a correlation value of unity yields a Raman gain which is equal to the monochromatic case. However, if the correlation is not unity, then the amplification is nonexponential for low gains until the individual Stokes longitudinal modes are brought into correlation (phase-locking) with those of the pump wave. Once this phase-locking is established, the usual exponential amplification results thereafter at higher gains.

A manifestation of the spectral correlation effect was observed in our earlier experiment [SLK80], in which a single pump laser was used to drive an oscillator and an amplifier. The degree of Stokes injection phase correlation was varied by means of an optical delay line. When the optical delay was chosen to match the arrival of the pump and the injected Stokes waves at the amplifier input an exponential amplification was observed. This demonstrated that under proper temporal correlation broadband Raman amplifiers can operate with an effective gain which is equal to the monochromatic value. Furthermore, the results indicated that the Stokes spectrum generated by a broadband pump spectrum in a superfluorescent oscillator can be nearly proportional to the pump spectrum (translated by the Raman frequency shift) with the proper phase relationship. Extensive theoretical analyses followed these experimental results to investigate the effects of broadband spectra under various conditions of interest for practical applications. The details of the analyses are presented in the next section (5.2); however, an important point relevant to Stokes injection analysis is that not only the Stokes intensity, but also the spectral correlation, affect the amplifier performance. Thus, in the case of broadband Raman converters employing an amplifier stage, Stokes injection radiation generated from an oscillator pumped by the same laser optimizes the injection condition. In contrast, injection radiation derived from other sources, such as tunable dye lasers, may satisfy the frequency and intensity requirements but may lack spectral correlation with the pump laser. The use of these sources requires additional Raman gains (e.g., higher pump intensities and/or longer lengths) to establish spectral correlation via phase-locking phenomena. Such schemes may be acceptable provided that the increased gain does not violate the Stokes injection requirements discussed in the previous sections.

5.2 Raman Amplifier Modeling

The Raman gain depends on both the temporal and spatial properties of the pump and Stokes radiation. The effect of the temporal properties (bandwidth) will be discussed first. This will be followed by a discussion of the effect of the spatial properties (beam quality). Dispersive effects, both linear and non-linear types, are also treated.

5.2.1 Temporal Effects (Bandwidth)

A considerable amount of insight into the effects of the temporal properties of the laser and Stokes radiation on the Raman gain can be obtained using a single-Stokes-order, plane-wave analysis. For the case of high Fresnel number Raman amplifiers, the coupling between the spatial and temporal domains can be kept small, and a plane wave analysis is a good approximation. However, this decoupling is not possible for Raman oscillators. These coupling effects will be pointed out and discussed as they are encountered in the analysis.

Temporal phenomena can be most easily studied in the temporal frequency domain, by expanding the pump and Stokes fields in the longitudinal modes of the pump laser. The system of equations governing the slowly varying envelopes of the pump and Stokes waves is [SLK80]:

$$\frac{\partial v_j}{\partial x} = \frac{G}{2} \sum_n \sum_k \frac{v_k u_{k-n}^* u_{j-n}}{1 + i \frac{2n\gamma}{\Gamma}} \exp[i(k-j)\gamma z], \quad (5.27)$$

$$\frac{\partial u_j}{\partial x} = -\frac{G}{2} \sum_n \sum_k \frac{u_k v_{k-n}^* v_{j-n}}{1 + i \frac{2n\gamma}{\Gamma}} \exp[i(j-k)\gamma z], \quad (5.28)$$

where u_j and v_j are the amplitudes of the pump and Stokes modes, respectively, Γ is the homogeneously broadened linewidth, and γ is the mode spacing. The

propagation coordinate x is normalized to the cell length, L , and $G = gI_{L0}L$ where g is the monochromatic gain coefficient and I_{L0} is the incident pump intensity. The effect of dephasing collisions is fully taken into account in this formalism through the Lorentzian lineshape. Doppler broadening or other types of inhomogeneous broadening are not considered a good approximation for the pressures of interest. This is shown clearly in Figure 5.2-1 which shows the measured Raman susceptibility at 2.5 atmospheres (room temperature) together with a Lorentzian fit [Ow78]. The parameter $\nu = 1/v_p - 1/v_s$, where v_p and v_s are the group velocities of the pump and Stokes waves, characterizes the dispersion of the medium. Dispersive effects can be neglected when the maximum value of the phase shift is less than π , i.e.

$$\Delta\omega_L \nu L < \pi \quad (5.29)$$

or

$$\Delta\nu_L < \frac{1}{2L(v_s - v_L)/c}$$

For H_2 gas and a pump wavelength of 351 nm, $(v_s - v_L)/c \approx 8.6 \times 10^{-6} \times p$, where p is the pressure in amagats. For example, at a pressure of 6 amagats and for a 12 m long cell, Eq. 5.29 yields $\Delta\nu_L < 8 \text{ cm}^{-1}$. If the blue-green bandwidth is chosen to be 0.4 cm^{-1} (corresponding to 0.1 \AA), the XeF bandwidth must be limited to this value also since bandwidth is preserved in the Raman shifting process. Therefore, group velocity dispersion may be neglected and the phase factors in Eq. 5.27,28 can be set equal to unity. Results of numerical simulations below will verify this statement.

In what follows, the laser modes are assumed to be uncorrelated and uniformly distributed between $-\pi$ and π . It has been shown, both theoretically and experimentally [SLK80], that the Stokes gain is maximized when the injected-Stokes spectrum is proportional to the pump spectrum (temporal matching). With these initial conditions, and when $\gamma \gg \Gamma$, the broadband Stokes gain is equal to the monochromatic value, both for saturated and unsaturated conditions. The assumption $\gamma \gg \Gamma$ is commonly made [Tr79, SLK80, Fl81], because it is the only case where closed form solutions can be obtained. However, this assumption is in general invalid for an H_2 converter operating near room temperature at a pressure of several atmospheres. Under those operating conditions, the H_2 Raman linewidth is a few hundred MHz wide [Ow78] while the

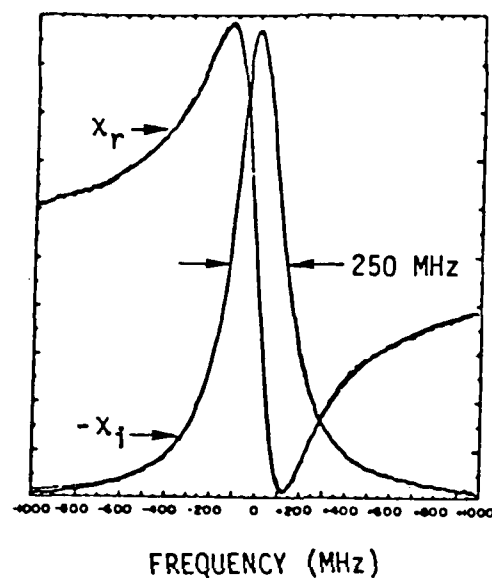


FIGURE 5.2-1 Real and imaginary spectra of x_3^{1111} in the vicinity of the $Q_{01}(1)$ mode of H_2 at the motionally narrowed linewidth minimum. The spectrum is overlaid with the Lorentzian lineshapes shown by the dotted curves. The $\text{Re } x_3^{1111}$ spectrum has been shifted upward by approximately a half scale for convenient display. $p = 2.5 \text{ atm}$. $T = 23 \text{ C}$

mode spacing is on the order of 150 MHz (1 m resonator) or less. Therefore, $\Gamma \geq \gamma$ and terms with $n \neq 0$ also contribute. However, as the laser bandwidth and the number of modes become very large, the correlation represented by the summation over k approaches a δ -function, thereby decreasing the contribution of the $n \neq 0$ terms, irrespective of whether $\gamma > \Gamma$ is satisfied or not. This will be shown more clearly below.

As was mentioned above, when the pump and Stokes spectra are δ -correlated, the broadband Raman gain is equal to its monochromatic value. In the general case, in the small signal regime, the gain is larger than the monochromatic value. Long [Lo79] has calculated the expectation value and standard deviation of the gain as a function of γ, Γ and $\Delta\omega_L$. The results of his analysis are shown in Figure 5.2-2. Note that, as $\Delta\omega_L/\Gamma \rightarrow \infty$, the average gain approaches the monochromatic value while the standard deviation goes to zero. This corresponds to the limit of δ -correlated pump and Stokes spectra, as was mentioned above.

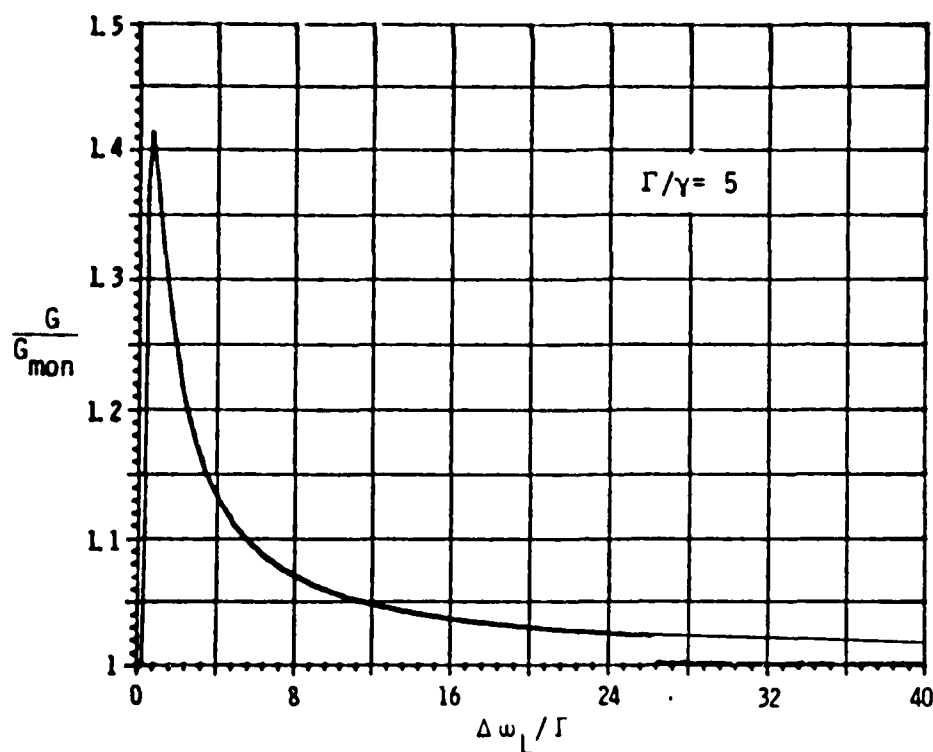


FIGURE 5.2-2 FORWARD RAMAN GAIN, NORMALIZED TO ITS MONOCHROMATIC VALUE, VERSUS LASER BANDWIDTH/MOLECULAR LINEWIDTH

Recent studies [SL81] have shown that these results are not valid in the saturated gain regime. An example for a relatively low number of laser modes is shown in Figure 5.2-3. Shown is the Stokes growth both for broadband and monochromatic conditions. Note that while the broadband gain exceeds the monochromatic value in the unsaturated regime, the relationship is reversed in the region of strong depletion. This gain reduction effect is explained by the loss of correlation between the pump and Stokes fields, and can be clarified by looking at two limiting cases. When $\gamma > 1$, the molecular vibration cannot follow the fast variations of the driving force (\propto Stokes field \times pump field) and the vibration has a (nearly) constant steady state amplitude ($n=0$ term only). In this case, for initially correlated pump and Stokes fields, the polarizations at the pump and Stokes frequencies are proportional to these fields, and the waveforms are amplified (depleted) without distortion. In the opposite limit when $\Delta\omega_L \ll 1$, the molecular vibration can instantaneously follow the fluctuations in the driving force. In this limit, the

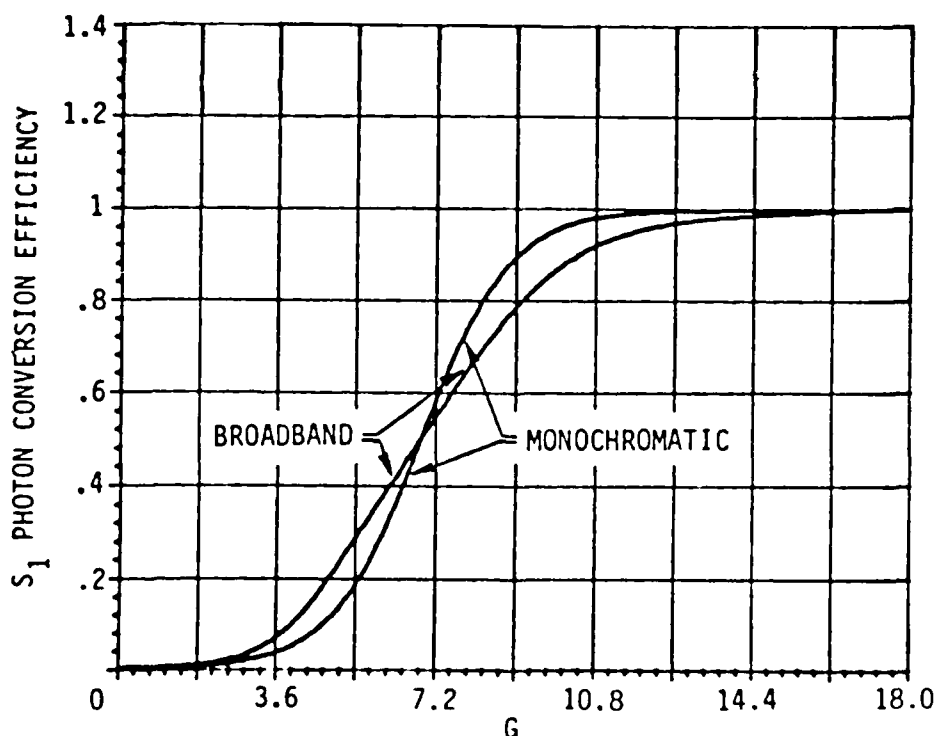


FIGURE 5.2-3 CONVERSION EFFICIENCY FOR BROADBAND AND MONOCHROMATIC PUMPING. $I_1(0) = 10^{-3}$, $\Delta\omega_L/\gamma = 51$, $\Gamma/\gamma = 5$, $L = 12$ m, $p = 6$ amagat, $\Delta\omega_L = 0.4$ cm $^{-1}$

Raman gain is proportional to the instantaneous pump intensity, and the "highest peaks" in the pump waveform will be converted preferentially, thereby modifying the pump spectrum. As the depletion becomes complete, the Stokes waveform will still closely resemble the initial pump waveform because of power conservation, while the depleted pump waveform becomes totally uncorrelated to its initial shape and the amplified Stokes waveform. The general case has some of the aspects of both limiting cases. In particular, the amplified Stokes waveform (spectrum) closely resembles the initial pump waveform (spectrum), while the pump spectrum gets distorted to some degree, thereby reducing the gain.

The number of modes in the example of Figure 5.2-3 was chosen fairly low to illustrate the behavior discussed above. A representative example corresponding to a laser bandwidth of 0.4 cm^{-1} (0.1 \AA in BG) and Raman linewidth of 0.012 cm^{-1} (room temperature, 6 atm) is shown in Figure 5.2-4. The gain under

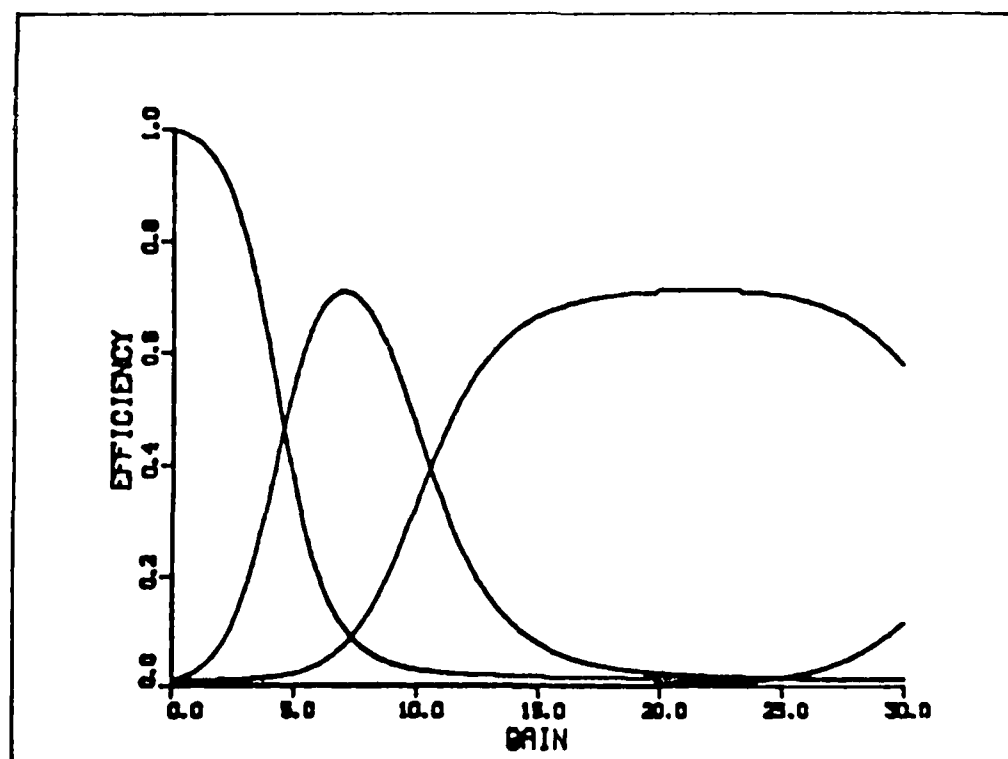


FIGURE 5.2-4 POWER CONVERSION EFFICIENCY FOR SECOND STOKES BROADBAND CONVERTER. GAUSSIAN PUMP SPECTRUM $\Delta\omega_L/\gamma = 160$, $\Gamma/\gamma = 5$, $I_1(0) = I_2(0) = 10^{-2}$, $I_3(0) = 10^{-5}$

these conditions closely approaches the monochromatic value. Finally, Figure 5.2-5 illustrates the effect of dispersion. In this case the pump and Stokes field lose correlation because of their different phase velocities, thereby reducing the gain.

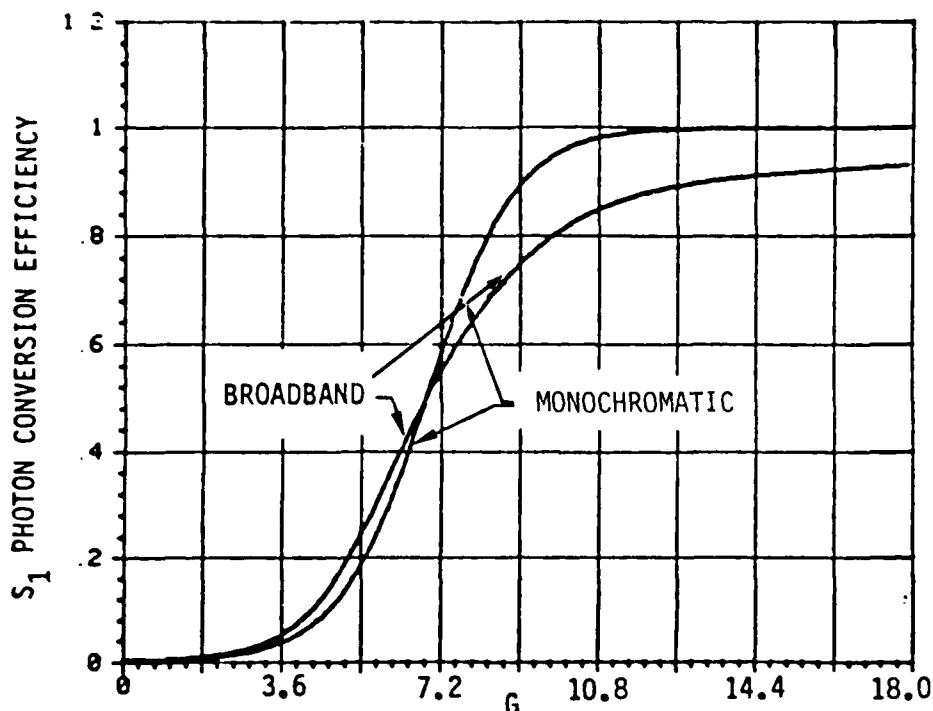


FIGURE 5.2-5 CONVERSION EFFICIENCY OF BROADBAND, DISPERSIVE CONVERTER.

$$I_1(0) = 10^{-3}, \Delta\omega_L/\gamma = 51, \Gamma/\gamma = 5, L = 12 \text{ m}, p = 15 \text{ amagat}, \\ \Delta\omega_L = 10 \text{ cm}^{-1}$$

5.2.2 Spatial Effects (Beam Quality)

The Raman gain is also a function of the angular spectra of the interacting beams. This can best be illustrated using a k-vector diagram as shown in Figure 5.2-6. Consider the amplification of a (nearly) plane wave Stokes beam by an aberrated pump with divergence θ_p . For all k-vector combinations to contribute to the Raman gain, the worst case phase shift between the Stokes field and polarization caused by the off-axis pump wave must be limited

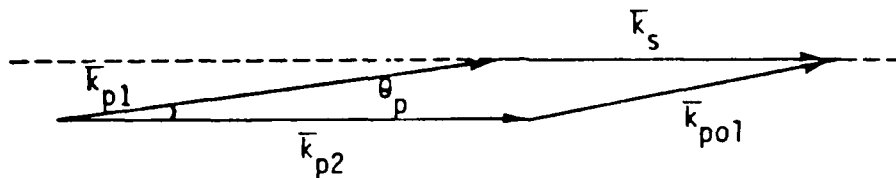


FIGURE 5.2-6 K-VECTOR DIAGRAM FOR AMPLIFICATION OF PLANE WAVE STOKES BY PUMP BEAM WITH DIVERGENCE θ_p . $\bar{k}_{p1,2}$ ARE PUMP VECTORS, \bar{k}_s IS STOKES VECTOR, AND \bar{k}_{po1} = STOKES POLARIZATION VECTOR

to π ; i.e.,

$$\frac{k_p \theta_p^2 L}{2} < \pi. \quad (5.30)$$

This can be rewritten as

$$\theta_p < \sqrt{\frac{\lambda_p}{L}} \quad (5.31)$$

or

$$\frac{\theta_p}{\lambda/D} < \sqrt{N_F} \quad (5.32)$$

where the Fresnel number N_F has been defined as $N_F = D^2/(\lambda_p L)$. This phase-matching condition ensures that the coherence length for the mixing process is longer than the cell length. The gain breakpoint predicted by Eq. 5.32 is in good agreement with more detailed calculations by Kung [Ku81]. For the case of plane wave Stokes injection, the angle given by Eq. 5.32 corresponds approximately to the point where the gain has dropped to 75% of its peak value according to his calculations.

The gain of a Raman amplifier is also reduced when the beam is not collimated over the entire cell length. The collimation condition can be written as

$$\theta < D/L \quad (5.33)$$

or

$$\frac{\theta}{\lambda/D} < N_F \quad (5.34)$$

This condition is less stringent than the phase-matching condition Eq. 5.32.

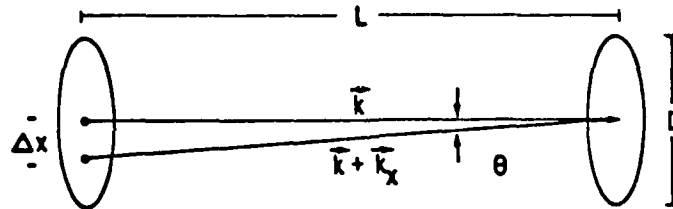
A third limit on the beam divergence relates to the temporal properties of the radiation. To maintain temporal correlation between the pump and Stokes waveforms, also for off-axis waves, the difference in propagation distance for on- and off-axis waves (Figure 5.2-7) must be within the tolerance given by the temporal matching criterion [SLK80], i.e.

$$\frac{L\theta_p^2}{2} < \frac{1}{\Delta\nu} \quad (5.35)$$

or

$$\frac{\theta_p}{\lambda_p/D} < \sqrt{\frac{N_F}{\Delta\lambda/\lambda}} \quad (5.36)$$

where $\Delta\lambda/\lambda$ is the fractional laser bandwidth. Since this number is much less than unity, condition Eq. 5.36 is much less stringent than Eqs. 5.32 and 5.34.



$$\text{TIME SLIP: } \Delta t = \frac{\Delta x^2}{2Lc} = \frac{L\theta^2}{2c}$$

FIGURE 5.2-7 GEOMETRY SHOWING TEMPORAL CORRELATION
REQUIREMENTS FOR DIVERGENT BEAMS

These analyses and modeling efforts have led to the development of computer codes which take into account the spatial and spectral properties of the interacting fields; i.e., arbitrary beam profiles (intensity and phase) and longitudinal mode spectra can be specified. The physical effects taken into account include Raman gain and dispersion, four-wave mixing, linear dispersion and diffraction. Aberrations in the optical elements and the Raman medium can be included as well. Models developed at NRTC allow a complete three dimensional (X,Y,Z) simulation of monochromatic converters, while polychromatic converters can be analyzed with a model which incorporates one transverse dimension (X,Z,T).

An important property of Raman amplifiers is their capability, under certain conditions, to provide beam "clean-up"; i.e., a weak, nearly diffraction-limited Stokes beam can be amplified with very low distortion and near quantum-limited conversion efficiency, by a strongly aberrated pump beam. As discussed earlier, one parameter regime where this occurs is when the aberrations on the pump beam are such that the number of times this beam is diffraction-limited is less than the square root of the amplifier Fresnel number. This Fresnel number is given by $A/\lambda L$ where A is the beam area and L is the length over which the conversion occurs (\approx the amplifier length). An example of a simulation which demonstrates this property is shown in Figures 5.2-8 through 5.2-12. The intensity profile of the pump beam, which is generated in an unstable resonator, is shown in Figure 5.2-8. The beam size is $4 \times 4 \text{ cm}^2$ and the resonator magnification is 2. The far field pattern of this beam, for the case of a flat phasefront, is shown in Figure 5.2-9. An aberration plate is introduced producing the phasefront shown in Figure 5.2-10. The far field pattern of the resulting aberrated pump beam is shown in Figure 5.2-11. The injected Stokes beam has a plane phasefront. The amplifier length is 10 m and the small signal gain e^{10} . The key output of the simulation is the far field pattern of the amplified Stokes beam shown in Figure 5.2-12. Note that this profile is very close to that of the unaberrated pump beam of Figure 5.2-9, demonstrating the beam clean-up property. More quantitatively, the beam quality derived from the Strehl ratio is $1.03 \times$ diffraction-limited.

The regime for beam "clean-up" specified above is not the only operating regime. Another regime of interest is where the beam quality is even much worse than

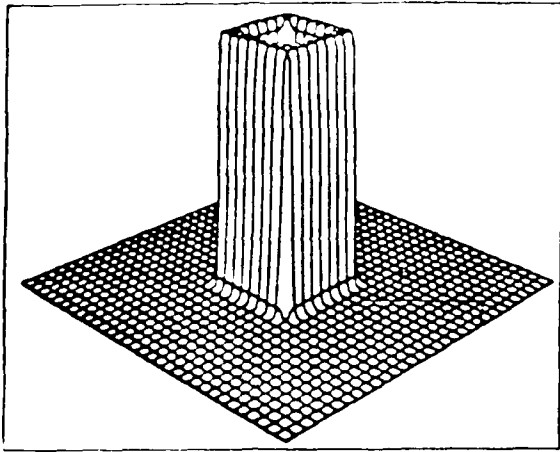


FIGURE 5.2-8 APODIZED BEAM

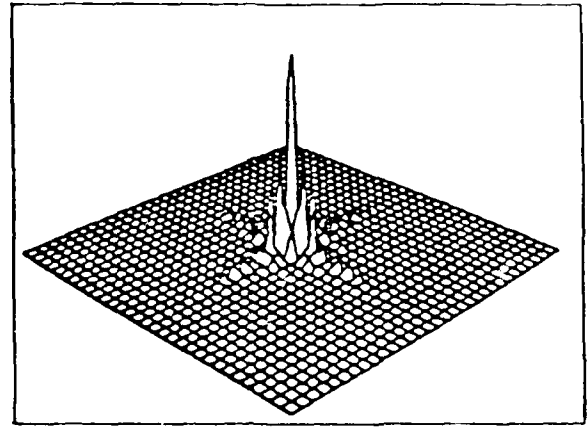


FIGURE 5.2-9 FAR-FIELD OF APODIZED BEAM

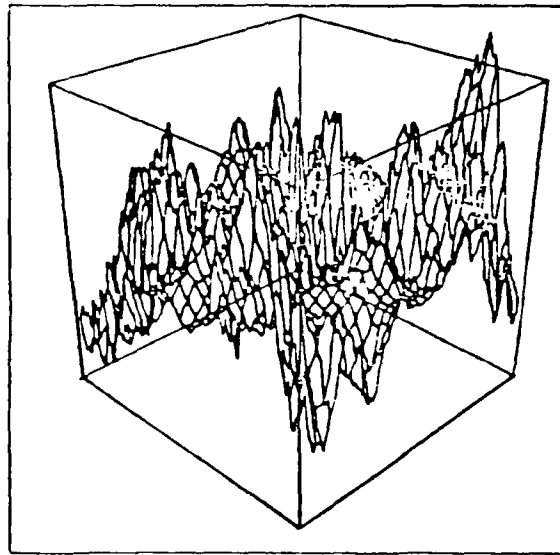


FIGURE 5.2-10 PHASE FRONT ABERRATION DUE TO TURBULENT MEDIUM

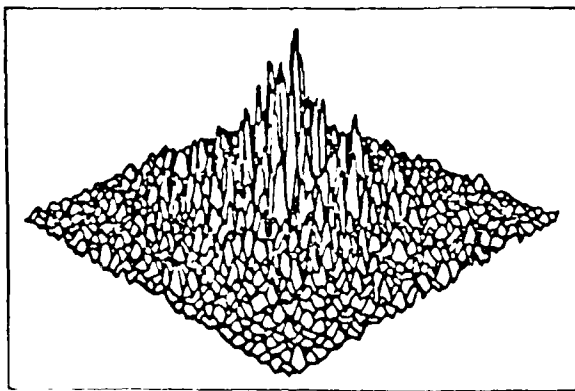


FIGURE 5.2-11 FAR-FIELD OF ABERRATED BEAM

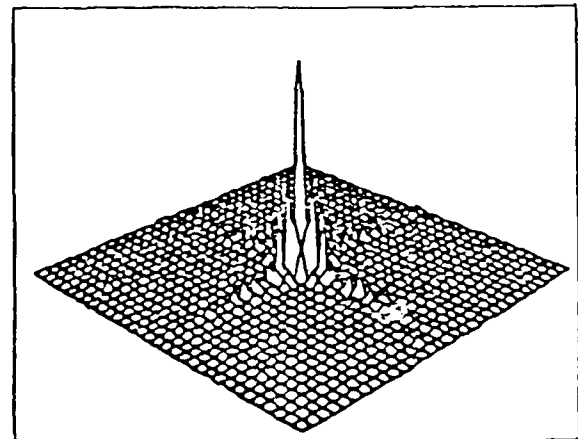


FIGURE 5.2-12 FAR-FIELD PROFILE OF STOKES OUTPUT

considered above, but still good enough to avoid a considerable beam area increase over the amplifier length. Under certain conditions, low distortion amplification can be obtained in this regime as well, due to an "intensity averaging" effect.

5.2.3 Raman (nonlinear) Dispersion

According to Eqs. 5.27 and 5.28, the polarization at each Stokes and pump mode will, in general, have an inphase, as well as, a quadrature component, resulting in phase accumulation through the converter. The phase shift will be zero if

- Dispersion is absent
- Only the $n = 0$ term is important in the summation over n (i.e., $\lambda \gg \Gamma$ or δ -correlated waveforms) in Eqs.
- The injected Stokes spectrum is proportional to the pump spectrum (temporal matching)

With these assumptions, the Stokes equation can be written as:

$$\frac{dv_j}{dx} = \frac{G_s}{2} u_j \sum_k v_k u_k^* \quad (5.37)$$

Substituting $v_k = u_k^* (v/u)$ and $u_j = v_j^* (u/v)$ yields:

$$\frac{dv_j}{dx} = \frac{G_s}{2} v_j \sum_k |u_k|^2 \quad (5.38)$$

showing that no phase is collected.

When the above conditions are not satisfied, usually because the second one is violated, the Stokes and pump waves will accumulate phase as they travel through the converter. The r.m.s. value of this phase shift in the small signal regime has been calculated by Long [Lo81]. It is plotted versus the ratio of laser to Raman linewidth in Figure 5.2-13. Notice that the shift is largest for a small number of modes, but asymptotically disappears as $\Delta\omega_L/\Gamma \rightarrow \infty$, corresponding to δ -correlated spectra.

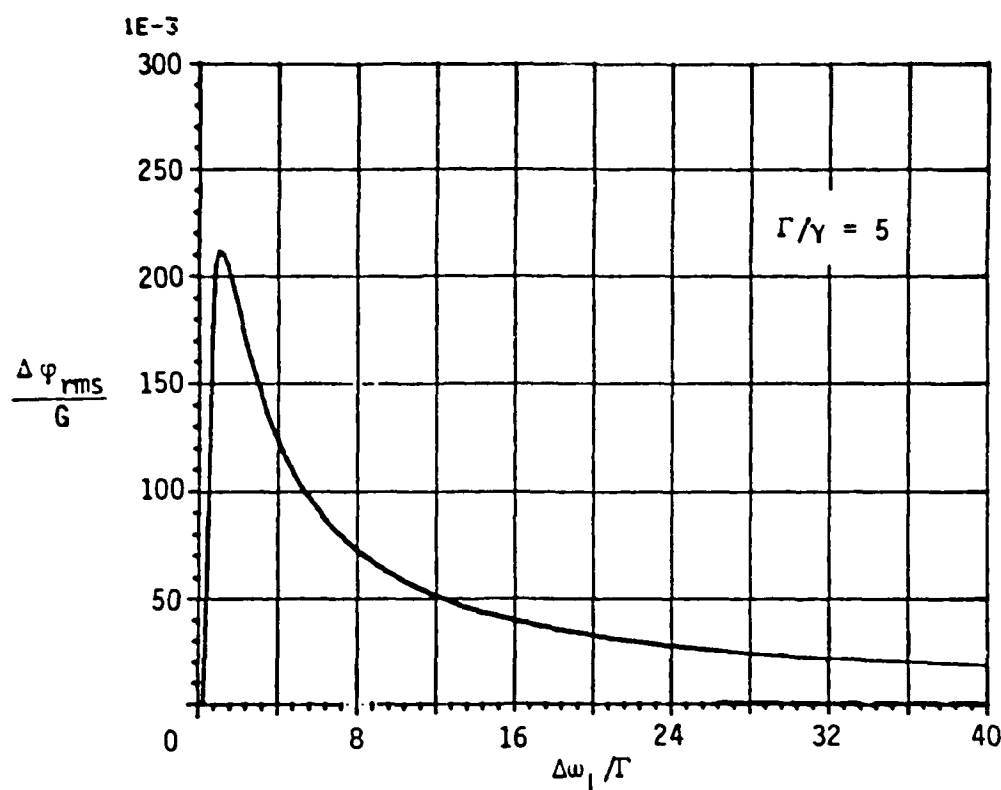


FIGURE 5.2-13 RMS INTENSITY-AVERAGED PHASE INCREMENT
IN SMALL-SIGNAL REGIME

These non-linear phase shifts represent a case of coupling between the temporal and spatial domains. Because they are intensity dependent, they lead to wave-front errors if the pump intensity profile is nonuniform. In Raman oscillators, which build up from noise, shifts of several radians can be accumulated in the small-signal regime. These shifts lead to beam focusing or defocusing, depending on the sign of the shift. As an example, in the case of defocusing, the beam area at the cell exit can be shown to increase by a factor of 2 when $\phi \approx b/(2L)$ where b is the confocal parameter of the pump beam and L the cell length. For a typical value of $b/L \approx 0.1$, this yields $\phi \approx 0.05$. Since this value is much smaller than the actual shifts encountered, strong (de-focusing) effects are present in oscillators.

In Raman amplifiers, the saturated value of the phase shifts is important. Figure 5.2-14 shows the r.m.s. value of the accumulated Stokes phase obtained with a computer simulation of Eqs. 5.27 and 5.28. The number of laser modes was 51 and the number of modes under the Raman linewidth 5 in this simulation. The r.m.s. value corresponds to an average over modes for the given example.

Notice how the phase increases to some maximum value and then decreases in the saturated regime. As an example, when G decreases from 18 to 13.5, corresponding to a 25 percent $\Delta I/I$ variation, the differential phase shift is .02 radians $\approx \lambda / 300$. Figure 5.2-15 shows the corresponding phase spectrum at the amplifier exit. Notice that the magnitude of the shift is relatively constant across the spectrum. The small average slope is due to dispersion.

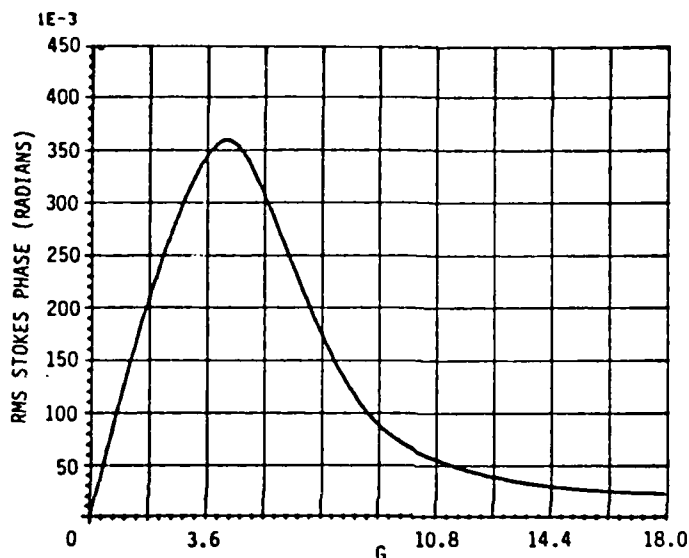


FIGURE 5.2-14 RMS STOKES PHASE SHIFT IN DEPLETION REGIME

$$I_1(0) = 10^{-3}, \Delta\omega_L/\gamma = 51, \Gamma/\gamma = 5, L = 12 \text{ m}, \\ p = 6 \text{ amagat}, \Delta\omega_L = 0.4 \text{ cm}^{-1}$$

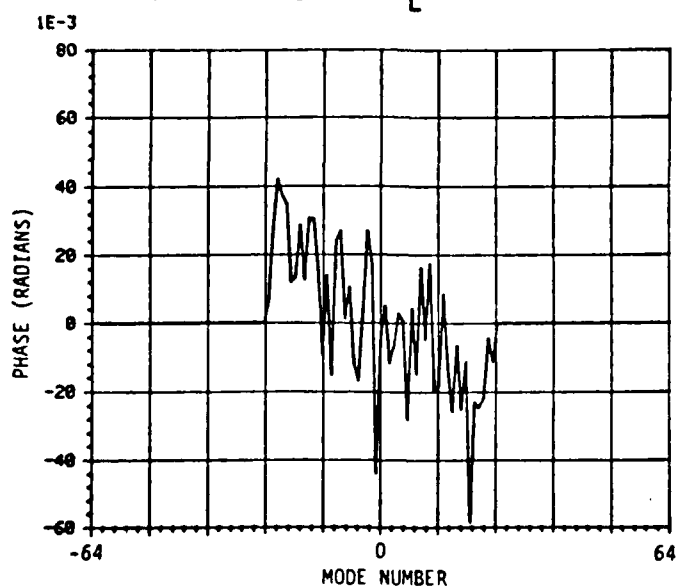


FIGURE 5.2-15 SPECTRUM OF ACCUMULATED STOKES PHASE.
(SAME CONDITIONS AS FIGURE 5.2-9)

Finally, Figures 5.2-16 and 5.2-17 illustrate the effect of dispersion. Dispersion is important in this example because of the higher pressure and laser bandwidth. Notice how the average Stokes phase in Figure 5.2-18 has a linear frequency dependence, corresponding to a shift in the time domain. This is in agreement with theoretical results [ZM78].

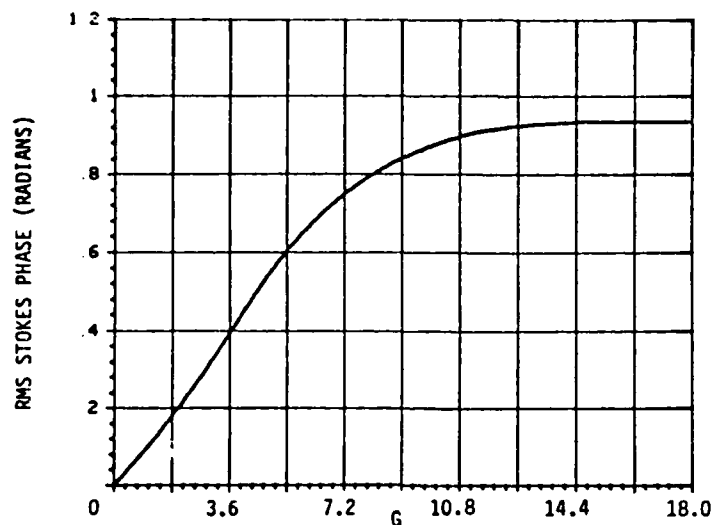


FIGURE 5.2-16 RMS STOKES PHASE SHIFT IN DEPLETION REGIME FOR DISPERSIVE CONVERTER $I_1(0) = 10^{-3}$, $\Delta\omega_L/\gamma = 51$, $\Gamma/\gamma = 5$, $L = 12$ m, $p = 15$ amagats, $\Delta\omega_L = 10$ cm $^{-1}$

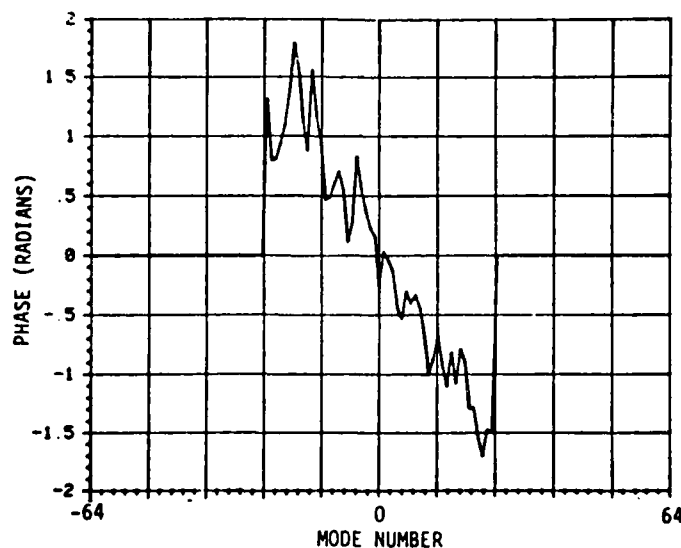


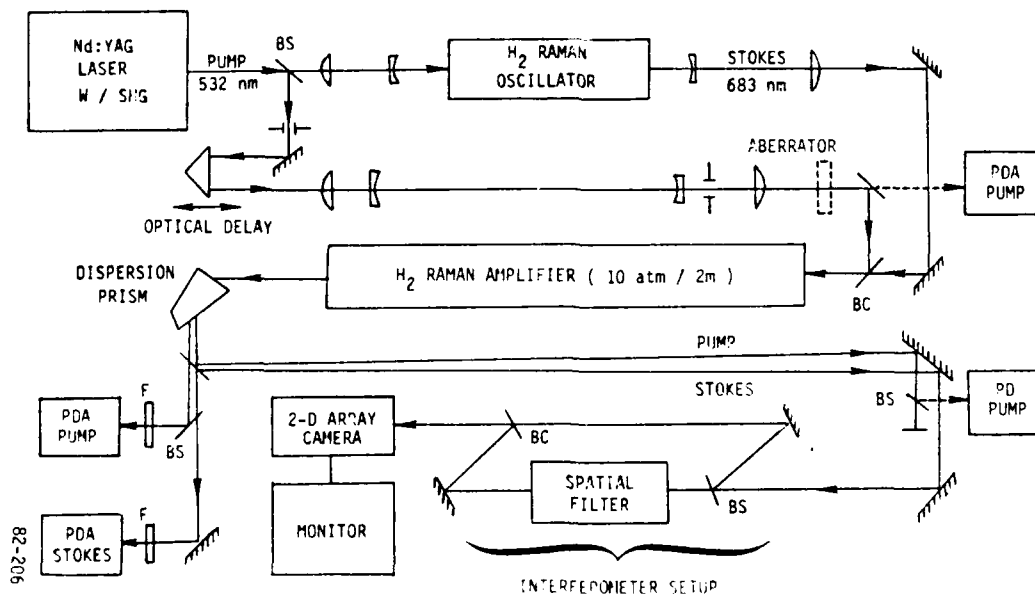
FIGURE 5.2-17 SPECTRUM OF ACCUMULATED STOKES PHASE FOR DISPERSIVE CONVERTER (SAME CONDITIONS AS FIGURE 5.2-11)

5.3 Broadband Raman Amplifier Experiment with Aberrated Pump Beam

The possibility of amplifying good-beam-quality Stokes radiation in a Raman amplifier pumped by an aberrated laser beam has been investigated experimentally. The initial experiments utilized a broadband laser with relatively small beams due to peak power limitations of the laser. Thus, the objective of the investigation was to observe the effects of an aberrated broadband pump beam in a relatively low Fresnel number Raman amplifier. The experimental apparatus and the preliminary results are presented in the following sections.

5.3.1 Experimental Apparatus

The pump laser used for the experiments is a frequency-doubled Nd:YAG laser operating at 532 nm (bandwidth $\approx 0.86 \text{ cm}^{-1}$) with about 8 ns pulse length. The output of this laser was split into two beams to drive a Raman oscillator and a Raman amplifier, as schematically shown in Figure 5.3-1. The oscillator consisted of a 1 m long H_2 cell with fused silica windows and several lenses to focus the input pump beam and to recollimate a nearly diffraction-limited first Stokes output at 683 nm. A pair of high reflectance dielectric mirrors steered the Stokes beam to a third dielectric mirror which transmitted approximately 80% of the radiation.



(PDA = PHOTODIODE ARRAY; PD = PHOTODIODE DETECTOR; F = FILTERS; BS = BEAM SPLITTER)

FIGURE 5.3-1 RAMAN CONVERSION WITH CLEAN/ABERRATED PUMP BEAM
EXPERIMENTAL SCHEMATIC

This mirror was coated to reflect 99% of the pump radiation at 532 nm in order to operate as a beam combiner for the amplifier pump and injected Stokes beams. The combined beams were overlapped temporally by an optical delay and spatially in a colinear geometry over the 2 m long amplifier cell filled with 10 atm of H_2 .

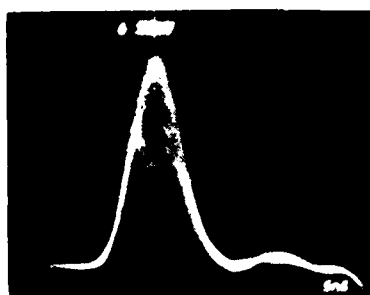
In order to study the effects of aberrated pump beam on the amplified Stokes beam, the pump beam was initially cleaned up using a beam reducing telescope and a far field aperture. Upon beam expansion and recollimation, the pump beam was passed through several types of aberrators. Glass microscope slides etched in hydrofluoric acid and plexiglass (lucite) plates were found to provide suitable aberrations without breaking up the beam completely.

The diagnostics consisted of linear photodiode arrays for beam profile measurement, a P-I-N photodiode for pulse shape measurement, and an interferometer to quantify the near-field wavefront aberration. The interferometer was set up in a self referencing configuration in which a fraction of the beam to be analyzed was spatially filtered to yield a plane wave reference beam. This reference beam was then combined with the rest of the sampled beam to generate interference fringes which were imaged onto a two dimensional CID array camera (GE Model TN 2500). The array consisted of 244 by 248 pixels, each measuring $36 \mu m$ by $46 \mu m$. The camera output was displayed on a monitor, and the fringe pattern was recorded on a Polaroid film for off-line analysis. A Zygo interference fringe analyzer (ZAPP) was utilized to convert the fringe data into optical path difference (OPD) contours and peak-to-valley and rms phase measurements.

5.3.2 Stokes Beam Quality Measurements

Initial measurements of amplified Stokes beam quality were performed without any aberrators. The pump beam was collimated with an effective calculated confocal parameter of about 80 m. Pulse energy at the amplifier cell entrance was typically 12 mJ which yielded a calculated small signal gain of 8.5 in the amplifier.

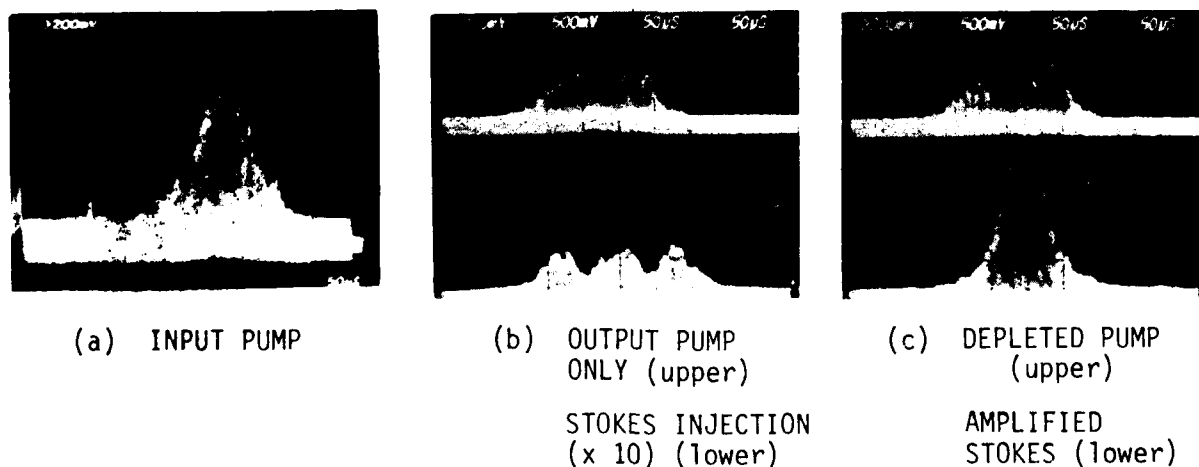
The Stokes injection level was adjusted to partially deplete the pump pulse as shown in Figure 5.3-2. This permitted observation of any changes in the conversion efficiency with aberrated pump beams. It should be noted that pump depletion reached nearly 100% over the central part of the pulse at higher injection levels.



(5 ns/div.)

FIGURE 5.3-2 PUMP AND DEPLETED PUMP PULSES

The spatial conversion efficiency data are shown in Figure 5.3-3a, b, c, which represent pulse-integrated beam profiles near the center of the beam. The data qualitatively indicate that the pump beam is collimated in the amplifier (Note: Jagged features are caused by color glass filters to attenuate intensity). A comparison of the depleted pump profile and the output pump without Stokes injection shows that the high-intensity center portion of the beam is converted efficiently as expected. This is evident in the amplified Stokes beam size.



(a) INPUT PUMP

(b) OUTPUT PUMP
ONLY (upper)

(c) DEPLETED PUMP
(upper)

STOKES INJECTION
(x 10) (lower)

AMPLIFIED
STOKES (lower)

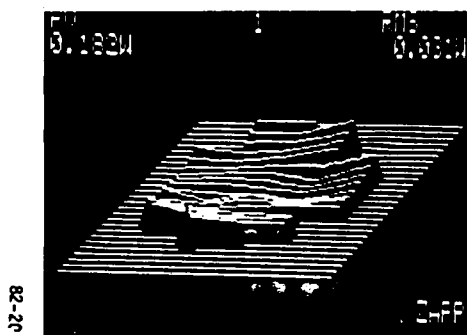
FIGURE 5.3-3 RAMAN AMPLIFIER CONVERSION WITH GOOD QUALITY
PUMP AND STOKES BEAMS

The choice of aberrators for the pump beam was made by testing several candidates using the interferometer operating with 532 nm. Figure 5.3-4 shows a typical interferogram of a pair of etched microscope glass slides 0.3 cm thick. A ZAPP

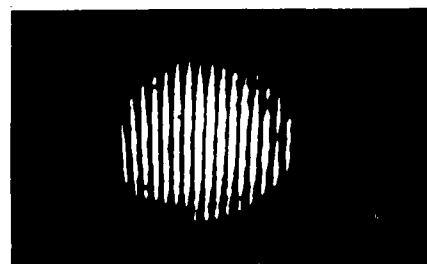
analysis indicates a peak-to-valley (P-V) variation of 0.182 waves at $\lambda = 632.8$ nm, which translates to a P-V phase variation of 1.63 rad. for the pump beam. A plexiglass plate 1.25 cm thick was also tested, and the results are shown in Figure 5.3-5. In this case, the P-V value was 1.63 rad. for the pump beam. For both aberrators the sampled region is approximately 5 mm in diameter, and the same region was used to intercept the pump beam.



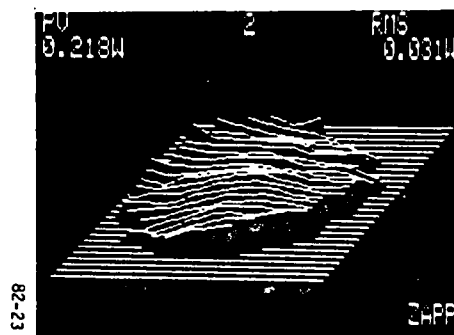
(a) INTERFEROGRAM



(b) OPTICAL PATH DIFFERENCE
CONTOUR



(a) INTERFEROGRAM



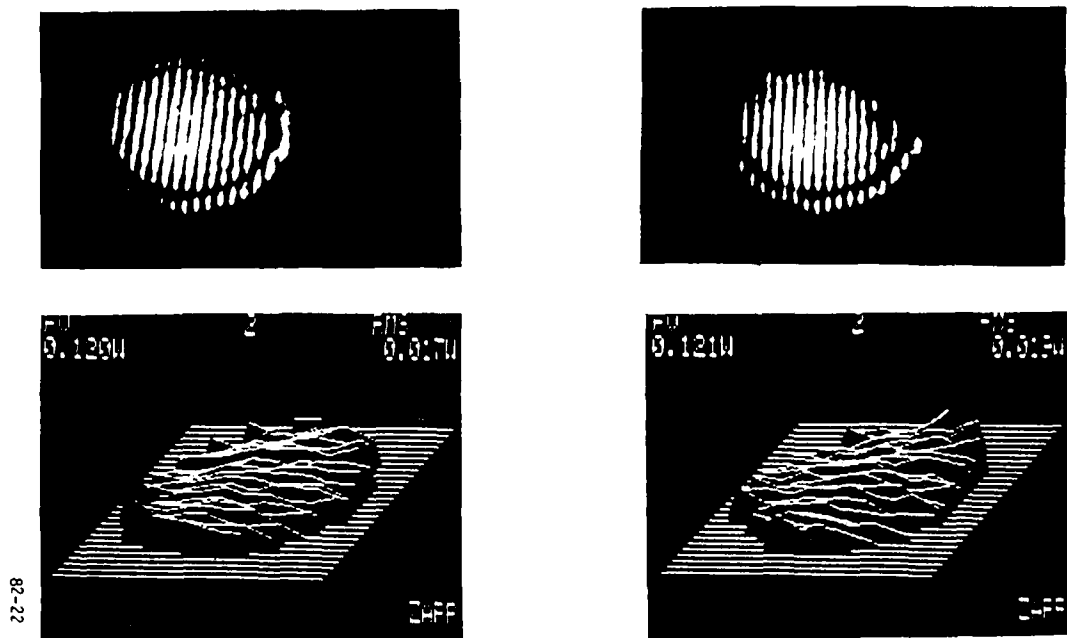
(b) OPTICAL PATH DIFFERENCE
CONTOUR

FIGURE 5.3-4 ABERRATOR: ETCHED MICROSCOPE
GLASS SLIDES 0.3 cm THICK

FIGURE 5.3-5 ABERRATOR: PLEXIGLASS
PLATE 1.25 cm THICK

The amplified Stokes beam wavefront data are presented in Figures 5.3-6 and 5.3-7 for the two different cases of aberrators. A certain background P-V variation and rms values are present in the interferograms, due to local OPD variations caused by the interferometer setup and associated beam steering optics. The background OPD for the case of no aberrator are different in Figure 5.3-6 and 5.3-7 because of adjustments made in between changing the aberrators. Therefore, the measurement of significance is the change in OPD with or

without aberrator. For both aberrators the OPD changes are very small, being equivalent to the reproducibility of ZAPP analysis. In fact, a close examination reveals that the two-dimensional OPD contours are nearly preserved for both cases. These data indicate that a Stokes beam can be amplified by stimulated Raman scattering of an aberrated pump beam under appropriate conditions.

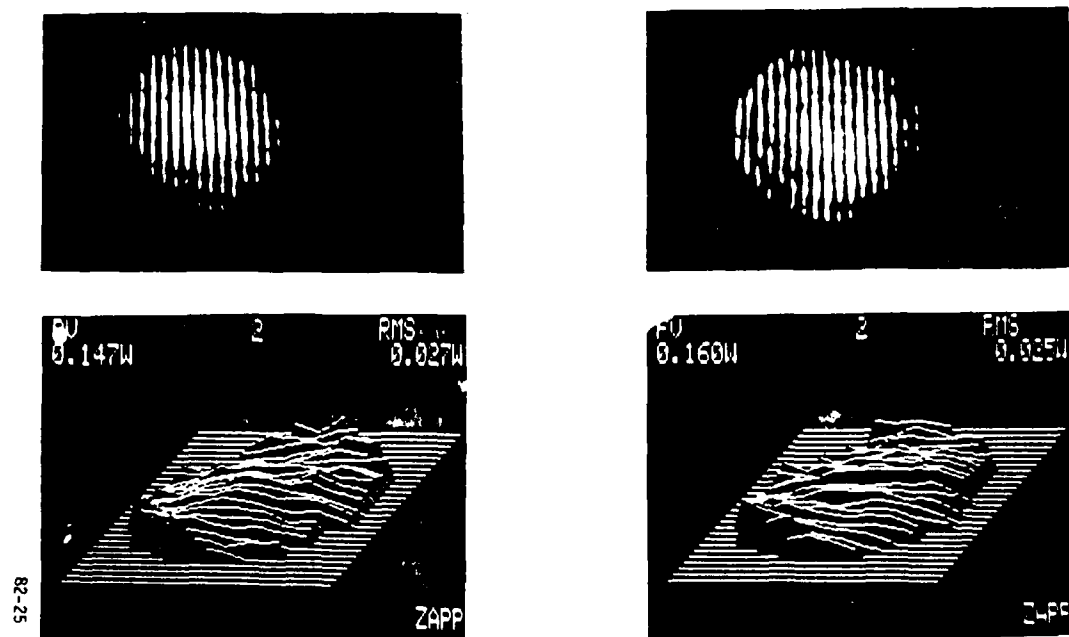


(a) WITHOUT ABERRATOR

(b) WITH ABERRATOR

(ABERRATOR: ETCHED MICROSCOPE SLIDES)

FIGURE 5.3-6 AMPLIFIED STOKES BEAM INTERFEROGRAM AND PHASE FRONT ANALYSIS



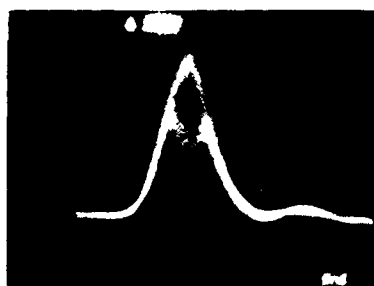
(a) WITHOUT ABERRATOR

(b) WITH ABERRATOR

(ABERRATOR: PLEXIGLASS PLATE 1.25 cm)

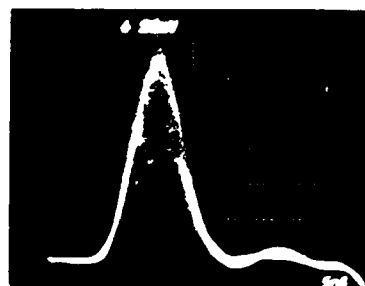
FIGURE 5.3-7 AMPLIFIED STOKES BEAM INTERFEROGRAM AND PHASE FRONT ANALYSIS

The conversion efficiency of Stokes amplification with aberrated pump beams was monitored by measuring pump depletion as before. In each case, the pump depletion was slightly less than that without an aberrator. Figures 5.3-8 and 5.3-9 show the pump pulses with and without Stokes injection for the two aberrators. The reduced pump depletion can be explained as a result of lower pump intensities in the amplifier caused by Fresnel reflection losses of the aberrators. Thus, conversion efficiency does not appear to change under aberrated pump beam conditions. These data are preliminary, and further investigation is being considered for future work.



(5 ns/div.)

FIGURE 5.3-8 PUMP AND DEPLETED PUMP PULSES
WITH ABERRATOR: ETCHED MICRO-
SCOPE SLIDES
PUMP ENERGY = 11 mJ



(5 ns/div.)

FIGURE 5.3-9 PUMP AND DEPLETED PUMP PULSES
WITH ABERRATOR: PLEXIGLASS
PLATE
PUMP ENERGY = 11 mJ

6.0 CONCLUSIONS

The analytical and experimental investigations reported here have been performed in order to advance the understandings obtained in the previous program and to address technical issues relevant to high average power operations envisioned for a ground-based SLC system.

Specific areas investigated included (1) experimental work supported by modeling on injection locking of a heated XeF laser, (2) elements of repetitively-pulsed XeF laser Raman converter systems, and (3) scaling studies of Raman amplifiers in regard to conversion efficiency and beam quality.

The main objective of the heated XeF laser injection locking experiment was to measure the degree of energy extraction in a single line under conditions in which the free-running output emits two separate bands near 351 and 353 nm. Interest in this measurement arose from the observed increase in the laser efficiency at elevated temperatures. Results obtained from the present experiments indicate that it is difficult to injection lock the laser output to a single line while suppressing the unlocked band emission from lasing. Modeling of the XeF kinetics suggests that the upper laser level may involve a detailed description of vibrational population distribution and coupling rates to account for the observed spectral output.

The analysis of repetitively pulsed Raman converter consisted of preliminary designs for an XeF laser injection locking source, e-beam XeF laser beam quality management, and a hydrogen Raman cell with a closed-cycle flow loop and acoustic suppression. The injection laser is needed to define the laser bandwidth and polarization, and the laser beam quality control is required to achieve the requisite pump beam quality for the Raman converter to operate efficiently. The flow and acoustics management is necessary to operate good beam quality Raman converters at moderate to high average power levels. The design analysis for the flow and acoustics management was performed by Poseidon Research under a subcontract work. Preliminary designs incorporate flow geometries and muffler configurations that are quite distinct from those of the laser cavities. Since heat deposition and chemical compatibility problems are generally more relaxed in a Raman converter as compared with

typical high power lasers, material selection and engineering appear to be less demanding in a Raman converter. However, requirements of good beam quality output from a long Raman cell call for density and temperature non-uniformities that are much less than those demonstrated in conventional flow loops. Further technological development in this area is needed to achieve the beam quality goals for SLC applications.

The extension of the Raman converter scaling studies addressed Stokes conversion efficiency and beam quality dependence on pump and Stokes radiation as well as Raman medium. The Stokes injection requirements have been analyzed in further detail to take into account the effects of superfluorescence, parasitic oscillation, four-wave mixing, and spectral correlation. It is found that a certain minimum injection intensity is needed to control a Raman amplifier, thereby establishing a scaling factor for maximum amplification. Raman amplifier modeling has been refined considerably to include important temporal and spatial effects of the pump and Stokes radiation fields. Dispersive effects have also been incorporated in this new formulation in a systematic way to investigate the magnitude of group velocity (linear) dispersion and Raman induced (nonlinear) dispersions. Computer codes based on these models which include three-dimensional wave propagation have been generated to yield simulation of various cases of interest. One important and practical case is amplification of a low-intensity, good-beam-quality Stokes radiation by an aberrated pump beam. Under certain conditions, the output Stokes beam could be generated with much better beam quality than that of the pump beam, demonstrating a "beam clean-up" feature of a Raman amplifier. Implementing such features in actual devices is of considerable value, since pump laser beam quality requirement is decoupled from the Raman shifted output. An experimental verification of the beam cleanup property of the Raman amplifier has been carried out, and the preliminary measurements have demonstrated positive results.

The analytical and modeling advances and progress in experimental verification made under this program represent significant milestones towards a conceptual development of scalable, high average power UV excimer Raman converters with good beam quality and conversion efficiency into the blue-green region.

7.0 REFERENCES

- [BB83] W. K. Bischel and G. Black, paper TuB3, OSA Topical Meeting on Excimer Lasers, Jan. 10-12, 1983
- [BD78] R. Burnham and N. Djeu, Opt. Lett., 3, 215 (1978)
- [BS82] I. J. Bigio, M. Slatkine, Opt. Lett., 7, pp. 19-21 (1982)
- [Ch79] L. Champagne, Appl. Phys. Lett., 35, 516 (1979)
- [DD66] R. DeMartini and J. Ducing, Phys. Rev. Lett., 17, 117 (1966)
- [EB79] J. Eggleston and R. L. Byer, IEEE J. Quant. Electron QE-15, 648 (1979)
- [Fl81] A. Flusberg, Opt. Commun., 38, 427 (1981)
- [GZ78] A. Z. Grasiuk and I. G. Zubarev, Appl. Phys., 17, 211-232 (1978)
- [HMJ79] J. C. Hsia, J. A. Mangano, J. H. Jacob, and M. Rokni, Appl. Phys. Lett., 34, 208 (1979)
- [Ho81] S. Holmes, NRTC, private communication (1981)
- [JHB73] P. Jeffers, D. Hilden, and S. H. Bauer, Phys. Lett., 20, 525 (1973)
- [Ka64] M. Karplus, J. Chem. Phys., 41, 880 (1964)
- [KS79] H. Komine and E. A. Stappaerts, Opt. Lett., 4, 398 (1979)
- [KSB81] H. Komine, E. A. Stappaerts, S. J. Brosnan, and J. B. West, DARPA CONTRACT N00014-80-C-0442, Final Technical Report (NRTC82-2R) (1981)
- [KSB82] H. Komine, E. A. Stappaerts, S. J. Brosnan, and J. B. West, Appl. Phys. Lett., 40, 551 (1982)
- [Ku81] R. T. V. Kung, WJSA, Presentation at NRL, unpublished (1981)
- [Lo70] W. H. Long, Jr. DOE advanced Laser Meeting, W35A 78-6 Sr-12 (1979)
- [Lo81] W. H. Long, Jr., NRTC internal report to be published (1981)
- [LSB79] T. R. Loree, R. C. Sze, D. L. Barker, and P. B. Scott, IEEE J. Quant. Electron., QE-15, 337 (1979)
- [Ma67] B. H. Mahan, University Chemistry, p. 59 (Addison-Wesley Publishing Co., Reading Mass., 1967)
- [MK69] M. Maier and W. Kaiser, Phys. Rev. 177, 580 (1969)

AD-A130 382

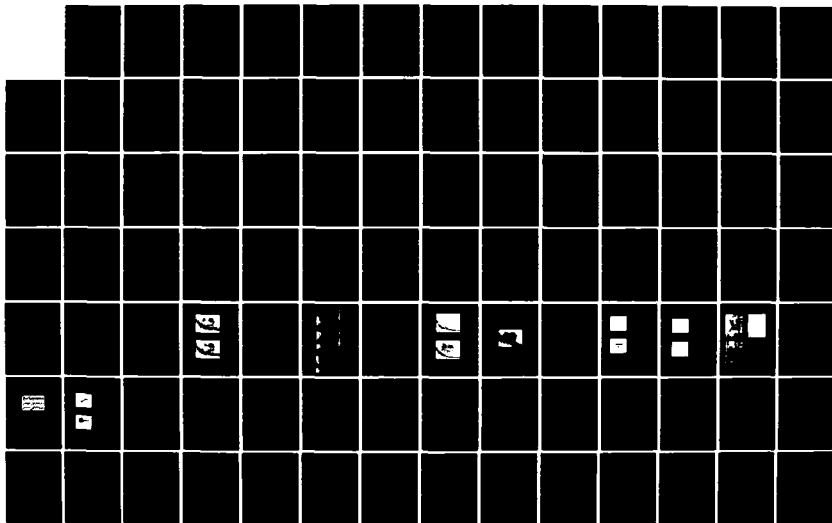
SCALING STUDIES OF EFFICIENT RAMAN CONVERTERS(U)
NORTHROP RESEARCH AND TECHNOLOGY CENTER PALOS VERDES
PENINSULA CA H KOMINE ET AL. 01 JUL 83 NRTC-83-89R
N00014-81-C-0637

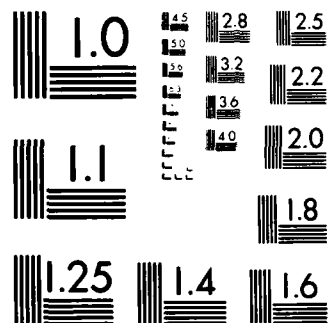
2/3

UNCLASSIFIED

F/G 20/6

NL





MICROCOPY RESOLUTION TEST CHART
NATIONAL BUREAU OF STANDARDS-1963-A

- [MR81] J. Mostowski and R. G. Raymer, Opt. Commun. 36, 237-240 (1981)
- [Ow80] A. Owyong, Opt. Lett., 2, 91 (1978)
- [PL34] G. Placzek, Handbuck der Radiologie, ed. by E. Marx, (Leipzig, Akademische Verlagsgesellschaft VI., 2, 209-374, 1934); translation by A. Werbin, Lawrence Radiation Laboratory, University of California, Livermore, report no. UCRL, Trans. No. 526(L), (1959)
- [SL81] E. A. Stappaerts, W. H. Long, Jr., NRTC internal report to be published (1981)
- [SLK80] E. A. Stappaerts, W. H. Long, Jr., and H. Komine, Opt. Lett1, 5, 4 (1980) and references contained therein
- [Tr79] W. R. Trutna, Y. K. Park, and R. L. Byer, IEEE J. Quant. Electron. QE-15, 648 (1979)
- [VKM75] B. V. Venkin, L. L. Kalyuk, and D. I. Malees, Sov. J. Quant. Electron. 5, 1348 (1975)
- [WKS81] J. B. West, H. Komine, and E. A. Stappaerts, J. Appl. Phys., 52, 5383 (1981)
- [ZM78] I. G. Zubarev and S. J. Mikhalov, Sov. J.Q.E., 8, 1338 (1978)

Poseidon Research Note No.84

**CONCEPTUAL DESIGN FOR THE
UPGRADE OF THE DARPA/MAXWELL
REP-RATED XeF LASER**

by

Patrick M. Hurdle

December 1981

Prepared for
Northrop Corporation
Research and Technology Center
One Research Park
Palos Verdes Peninsula, California 90274
Req. No. 51088

Table of Contents

	<u>Page</u>
1. Introduction.....	1
2. Laser Cavity Diagnostics.....	2
3. Medium Homogeneity.....	4
3.1 $\Delta\rho/\rho$ Requirement.....	4
3.2 Random Density Fluctuations.....	8
3.3 Ordered Density Fluctuations.....	12
3.4 100 Hz Operation.....	17
4. Conceptual Design.....	18
5. Conclusions.....	27
6. References.....	29
Appendix A: Poseidon Research Note No. 78.....	30

1. Introduction

This technical note is the final report for Task II for Northrop Corporation Research and Technology Center Req. No. 51088. The majority of the information presented in this document has been presented in briefing form to Northrop Corporation Research and Technology Center.

In order to conduct successful Raman conversion experiments at Maxwell Laboratories, it is necessary that the DARPA/Maxwell rep-rated XeF laser provides an output beam quality of two or better. The objectives of this work were, first, to analyze the medium homogeneity of the existing DARPA/Maxwell rep-rated XeF laser and secondly, to formulate a conceptual design, which will provide the required beam quality. Initially, it was hoped that the conceptual design would consist of making minor modifications to the existing system. Upon completion of the diagnostic tests on the present system, it was realized that it would be impossible to meet the required beam quality by modifying the existing rep-rated XeF laser.

Section 2 of this document presents the conclusion of the diagnostic tests conducted on the present DARPA/Maxwell rep-rated XeF laser. These conclusions are based on Poseidon Research Note No. 78. (Appendix A of this document) submitted to Northrop Corporation Research and Technology Center in August 1981. The issue of medium homogeneity is discussed in Section 3. Based on the results of Section 3, a conceptual design was formulated. This design is presented in Section 4. The conclusions are given in Section 5.

2. Laser Cavity Diagnostics

Extensive tests were conducted on the existing DARPA/Maxwell rep-rated XeF laser. The initial tests were made on the baseline flow. These included heat exchanger pressure drop, compressor pressure rise, mean velocity profiles in the laser cavity, turbulence intensity profile in the laser cavity, temperature fluctuations in the laser cavity, and sound pressure level measurements in the flow duct and laser cavity. For e-beam operation, the amplitude, frequency, and decay time for longitudinal waves generated in the laser cavity were measured. In addition, the presence of transverse waves in the cavity was investigated using two probe transducers simultaneously.

As previously mentioned, the description and results of these tests were submitted to Northrop Research and Technology Center in August 1981, (see Appendix A). Therefore in this section only the main results of the analysis will be stated. These are:

1. The vibrations, caused by the operation of the centrifugal compressor, are excessively high and are the major contributor to the flow system noise.
2. The placement of vaned diffuser between the nozzle and the laser cavity provides poor flow uniformity in the cavity.
3. The heat exchanger construction is unsatisfactory, since the flow can by-pass some of the heat exchanger elements.
4. Since there is no absorption material incorporated in the circulator, strong acoustic oscillations reside in the laser cavity for a period exceeding 50 msec after e-beam firing.

5. The rectangular flow ducts are for the most part unsatisfactory from a safety and reliability stand point.
6. The system does not reach a steady-state temperature.

Based on these results, Poseidon Research reported to the Defense Advanced Research Projects Agency, Northrop Research and Technology Center, and Maxwell Laboratories that it would be impossible for the DARPA/Maxwell rep-rated XeF laser to meet the required beam quality by simply adding acoustic damping material to the present configuration. Poseidon Research recommended that the circulator be completely redesigned. Of the existing hardware, only the blower with modification would be employed in the proposed new circulator.

3. Medium Homogeneity

The specifications for the DARPA/Maxwell rep-rated XeF laser are shown in Table 1. The primary method of operation will be a burst mode with the laser operating at 25 Hz for 10 seconds. During this operation the XeF laser must output a beam whose quality is two-time diffraction limited or better. It is possible that for certain operations the pulse-repetition frequency of the laser will be increased to 100 Hz. For these cases it is not necessary that the output beam meets the stringent requirement of two-time diffraction limited, but it is necessary that the beam quality can be predicted prior to the construction of the new circulator. Therefore, even though the point design for the conceptual design was done for a pulse-repetition frequency of 25 Hz, the effect of operating the system at 100 Hz was also examined.

3.1. $\frac{\Delta\rho}{\rho}$ Requirement

As previously mentioned, the beam quality required for the design point is two-time diffraction limited. A number of mechanisms contribute to the beam quality. These mechanisms with the exception of the medium homogeneity are given in Table 2. The value for these mechanisms were generated by the personnel from Maxwell Laboratories.

Table 2. Mechanisms Contributing to Beam Quality

Resonator Mirrors	1.04
Windows	1.00
Steering Mirrors	1.12
Medium Pumping	1.04

Table 1. Specifications for the DARPA/Maxwell
Rep-rated XeF Laser

Cavity Dimensions	
L_o - optical axis - meter (in.)	0.61 (24)
L_f - flow axis - meter (in.) (including nonactive region)	0.11 (4.31) (0.51) (20)
L_e - e-beam axis - meter (in.)	0.11 (4.31)
Diluent	Neon
Operating Pressure - atmosphere	4
Operating Temperature - °K	300
Energy Loading - J/l	150
Pulse Repetition Frequency - Hz	10
Operation with degradation of B.Q.	100
Beam Quality	2 × D.L.
Flow Loop Pressure Drop - Pascal (psi)	1.52×10^4 (2.2)
Operating Mode	Burst
Operating Time - sec.	10
Minimum Time Between Runs - min.	30

The total effect of these mechanisms results in a beam quality of 1.21 time diffraction limited. Therefore, the beam quality allocated for the medium homogeneity is 1.65.

The effect of the medium homogeneity on the beam quality is given by

$$B.Q. = \text{Exp} \left\{ 2\pi^{3/2} \left[\beta \frac{\rho}{\rho_s} \frac{\Delta\rho}{\rho} \frac{L_o}{\lambda} \right]^2 \left[\log_m \left(\frac{D}{r} \right) + \frac{3(m-1)m^2 + m^3 - 1}{3(m-1)(m^2-1)} \right] \right\} \quad (1)$$

Solving for the required medium homogeneity, $\Delta\rho/\rho$, we have

$$\frac{\Delta\rho}{\rho} = \frac{\left[\ln B.Q. \right]^{1/2}}{\left(2\pi^{3/2} \right)^{1/2} \beta \frac{\rho}{\rho_s} \frac{L_o}{\lambda} \left[\log_m \left(\frac{D}{r} \right) + \frac{3(m-1)m^2 + m^3 - 1}{3(m-1)(m^2-1)} \right]^{1/2}} \quad (2)$$

To calculate the required $\Delta\rho/\rho$ for the point design, the values employed for the various parameters are given in Table 3. Solving equation (2), the result gives

$$\frac{\Delta\rho}{\rho} = 2.5 \times 10^{-4} \quad (3)$$

The circulator will be designed to provide a $\Delta\rho/\rho$ of 1×10^{-4} , thereby giving a safety factor of 2.5.

Table 3. Values Employed for Calculating $\Delta\rho/\rho$.

B.Q. - Beam Quality	1.65
β - Gladstone-Dale constant time the standard density	6.7×10^{-5}
ρ/ρ_s - Operating density divided by the standard density	3.64
L_o - Length of optical axis	0.61 m
λ - Wavelength of laser output	3.53×10^{-7} m
D - Diameter of optical window	0.11 m
ℓ - Eddy length scale in flow direction	0.028 m
m - Magnification	2

The medium homogeneity is given by

$$\frac{\Delta\rho}{\rho} = \left[\left(\frac{\Delta\rho_r}{\rho} \right)^2 + \left(\frac{\Delta\rho_o}{\rho} \right)^2 \right]^{1/2}, \quad (4)$$

where $\Delta\rho_r/\rho$ is the rms random density fluctuations and $\Delta\rho_o/\rho$ is the rms ordered density fluctuations.

The flush factor is defined as

$$F = \frac{U_c}{PRF \cdot L_f}, \quad (5)$$

where U_c is the flow velocity in the cavity, PRF is the pulse-repetition frequency, and L_f is the cavity dimension in the flow direction. For typical energy deposition in e-beam-pumped laser, experimental data show that a flush factor of 2.5 will allow ample time for clearance of the thermal slug from the laser cavity, taking into account the tail of the energy deposition at the edges of the cavity. Therefore, the flow velocity, U_c , in the laser cavity is

$$U_c = (25\text{Hz}) (0.11 \text{ m}) (2.5) = 6.88 \text{ m/sec} \quad (6)$$

3.2 Random Density Fluctuations

The medium homogeneity for random disturbances is given as

$$\frac{\Delta\rho_r}{\rho} = \left[\left(\frac{\Delta\rho_v}{\rho} \right)^2 + \left(\frac{\Delta\rho_T}{\rho} \right)^2 \right]^{1/2}, \quad (7)$$

where $\Delta\rho_v/\rho$ is the rms density fluctuations due to turbulence, and $\Delta\rho_T/\rho$ is the rms density fluctuations due to temperature fluctuations.

To examine the effect of turbulence on the medium homogeneity, it is necessary to examine the boundary layers in the acoustic muffler upstream of the laser cavity. Due to the perforated wall construction of this muffler, one can assume rough-wall boundary layers. Therefore, the boundary layers grow approximately linearly with the distance downstream from their origin (i.e., the turbulence management system). Now due to the low flow velocity required for a system flush factor of 2.5 the design for the circulator will not employ a contraction section. Therefore, at the entrance to the laser cavity the mean square turbulence intensity is given by (Poseidon Research Report No. 21)

$$\overline{\left(\frac{u'}{u_c}\right)^2} = 1.885 \times 10^{-4} \left(\frac{2L}{D_H}\right)^{0.953}, \quad (8)$$

where L is the total length of the muffler and the nonactive region of the cavity, and D_H is the hydraulic diameter. This is defined as

$$D_H = \frac{4A}{P}, \quad (9)$$

where A is the cross-sectional area of the muffler, and P is the perimeter.

Based on the above formulation, the mean square turbulence intensity is

$$\begin{aligned} \overline{\left(\frac{u'}{u_c}\right)^2} &= 1.885 \times 10^{-4} \left(\frac{2.49}{0.19}\right)^{0.953} \\ &= 2.19 \times 10^{-3} \end{aligned} \quad (10)$$

This corresponds to a turbulence intensity of 4.6 percent.

Now the pressure fluctuations corresponding to the velocity fluctuations is given by

$$\Delta p = 0.7 \rho (u')^2, \quad (11)$$

where Δp is the rms pressure fluctuations, and u' is the rms velocity fluctuations. To calculate the density fluctuations resulting from these pressure fluctuations, we assume that the process is adiabatic, and therefore,

$$\Delta \rho_v = \Delta p / a^2, \quad (12)$$

where ' a ' is the speed of sound. Therefore

$$\frac{\Delta \rho_v}{\rho} = 0.7 M_c^2 \left(\frac{u'}{u} \right)_c^2, \quad (13)$$

where M_c is the Mach number in the cavity, and $(u'/u)_c$ is the turbulence intensity in the laser cavity. Therefore,

$$\frac{\Delta \rho_v}{\rho} = 0.7 (.015)^2 (2.19 \times 10^{-3})^2 = 3.5 \times 10^{-7}. \quad (14)$$

This is negligible compared to the overall allocation of $\Delta \rho / \rho$ of 1×10^{-4} . If, in addition, we take in consideration that there are a number of uncorrelated eddies along the optical axis of the laser cavity, the $\Delta \rho_v / \rho$ value is further reduced by the square root of this number.

The second mechanism which contributes to random density fluctuations is temperature fluctuations in the gas stream. The assumption is that this process is isobaric, therefore,

$$\frac{\Delta \rho_T}{\rho} = \frac{T'}{T_g} \quad , \quad (15)$$

where T' is the rms temperature fluctuations and T_g is the mean gas temperature in the circulator.

Reynolds' analogy between turbulent momentum and heat transport states that

$$\frac{T'}{(T_w - T_g)} = \frac{u'}{u} \quad , \quad (16)$$

where T_w is the wall temperature, and u'/u is the turbulence intensity. Combining equations (15) and (16), we have

$$\frac{\Delta \rho_T}{\rho} = \frac{T_w - T_g}{T_g} \frac{u'}{u} \quad . \quad (17)$$

If we allow half of the medium homogeneity budget to random disturbances, and since the disturbances due to turbulence is negligible, we have

$$\frac{\Delta \rho_T}{\rho} = 7.1 \times 10^{-5} \quad . \quad (18)$$

Letting the operating temperature, T_g , equal 300°K and using the values for u'/u and $\Delta \rho/\rho$ from equations (10) and (18) respectively, we have

$$\begin{aligned} (T_w - T_g) &= 300 (7.1 \times 10^{-5}) (4.68 \times 10^{-2})^{-1} \\ &= 0.46^\circ\text{K} \end{aligned} \quad (19)$$

By letting the system come to a steady state and with a certain amount of insulation on the outerskin of the upstream muffler portion of the circulator, there should be no problems in achieving a temperature difference between the wall and the gas of less than 0.46°K .

3.3 Ordered Density Fluctuations

It is anticipated that an energy loading of 150 Joules per liter will take place in the laser cavity when the e-beam is fired. Of the 150 J/l, optical abstraction will account for 2 Joules. The remaining energy will result in a sudden temperature rise in the cavity defined by

$$\Delta T_c = \frac{\Delta E_{\text{total}} - \Delta E_{\text{optical}}}{C_v} \quad (20)$$

For the diluent gas Neon, the overtemperature rise will be 73°K . Since this action takes place almost instantaneously, the process can be considered isochoric, and, therefore, the overpressure in the cavity is

$$\frac{\Delta p_c}{p_c} = \frac{\Delta T_c}{T_c} \quad (21)$$

Since the operating pressure is four atmosphere, the overpressure will be 9.83×10^4 Pa (0.97 atmosphere). Immediately afterwards shock waves and expansion fans propagate upstream and downstream of the laser cavity. The temperature inside the cavity relaxes to

$$\Delta T = T_c \left[\left(\frac{T_c + \Delta T_c}{T_c} \right)^{1/\gamma} - 1 \right], \quad (22)$$

and this temperature slug convects downstream. For the design condition the temperature of this slug is 341.7°K.

The acoustic waves and their by-products generated by this process produce the ordered density fluctuations. This is given as

$$\frac{\Delta \rho_o}{\rho} = \left[\left(\frac{\Delta \rho_L}{\rho} \right)^2 + \left(\frac{\Delta \rho_T}{\rho} \right)^2 + \left(\frac{\Delta \rho_E}{\rho} \right)^2 \right]^{1/2}, \quad (23)$$

where $\Delta \rho_L/\rho$ is the density fluctuations due to longitudinal acoustic waves, $\Delta \rho_T/\rho$ is due to transverse wave, and $\Delta \rho_E/\rho$ is the result of entropy waves.

3.3.1 Longitudinal Acoustic Waves

Longitudinal acoustic waves is the term given to the shock waves and expansion fans propagating upstream and downstream with their wave front approximately normal to the flow axis of the circulator.

The peak pressure of the shock wave propagating upstream and downstream will be equal to one-half the initial overpressure in the cavity. Therefore the shock strength will be 4.91×10^4 Pa. The acoustic energy residing in these two shock waves will have to be dissipated in the upstream and downstream mufflers. For dissipative mufflers Sabine (Beranek, 1960) formulated an empirical formula for acoustic attenuation:

$$A = 12.6 \bar{\alpha}^{1.4} \frac{P}{S} \text{ dB/ft} \quad , \quad (24)$$

where $\bar{\alpha}$ is the average sound absorption coefficient of the muffler packing material, P is the acoustically lined perimeter of the duct in inches, and S is the cross-sectional open area of the duct in square inches.

If we assume an average sound absorption, $\bar{\alpha}$, of 0.8, the attenuation in one pass is

$$A = 12.6 \bar{\alpha}^{1.4} \frac{P}{S} L = 33.9 \text{ dB} \quad , \quad (25)$$

where L , the length of the upstream muffler, is chosen to be 2.44 m (8 ft), and P/S , based on the assumption that only two sides of the duct are lined with acoustic material, is 0.46. On reaching the end of the upstream muffler the peak pressure in the shock wave is reduced to 9.92×10^2 Pa. If we assumed that at the end of the muffler the shock wave was totally reflected downstream toward the cavity, it would again be attenuated by 33.9 dB prior to entering the laser cavity. This would result in shock wave having a peak pressure of 20.02 Pa at the entrance to the cavity. This peak pressure would correspond to a $\Delta p_L / \rho$ of 2.96×10^{-5} . This value is below the required $\Delta p / \rho$ of 7.07×10^{-5} . Since only a partial reflection will occur, the value

of $\Delta p_L / \rho$ of 2.96×10^{-5} is extremely conservative. As will be seen in the next section, the length of the upstream acoustic muffler is primarily dictated to minimize the generation of entropy waves.

For the longitudinal acoustic waves propagating downstream, the same process will take place. Since entropy waves convect with the flow, it is not necessary to worry about the generation of these waves downstream of the cavity. In addition, any temperature disturbance, generated downstream of the cavity, will be subjected to a heat exchanger system prior to entering the laser cavity. Therefore, the length of the downstream muffler need only be designed to provide sufficient acoustic attenuation.

3.3.2 Entropy Waves

When the upstream propagating shock wave comes into contact with the turbulence management system, entropy waves are generated. These waves result from the attenuation of the shock wave as it propagates through the turbulence management section. The density fluctuations resulting from these waves are given by

$$\frac{\Delta \rho_E}{\rho} = \left(\frac{\gamma - 1}{\gamma} \right) M C_D \frac{\Delta p}{p}, \quad (26)$$

where M is the Mach number of the flow at the entrance to the turbulence management system, and C_D is the drag coefficient of the turbulence management screens. The term, $\Delta p/p$, is the ratio of the overpressure to the ambient pressure of the shock wave at the end of the upstream acoustic muffler just prior to the entrance of the turbulence management system. For screens, the drag coefficient,

C_D , is dependent upon Reynolds number. For the Reynolds number regime of interest, the drag coefficient is defined as (Cornell, 1958)

$$C_D = \frac{1 - A_f/A}{(A_f/A)^2} \frac{6}{R_d^{1/3}}, \quad (27)$$

where A_f/A is the percentage open area of the screen, and R_d is the Reynolds number of the screen. For the configuration envisioned for the proposed circulator, C_D will equal 3.7. Therefore, since $\Delta p/p$ at the end of the upstream acoustic muffler is projected to be 2.45×10^{-3} , $\Delta p_E/p$ will be 5.5×10^{-5} .

3.3.3 Transverse Acoustic Waves

When energy is deposited in the laser cavity, the deposition is not perfectly uniform. This lack of uniformity results in standing acoustic waves being generated in the cavity in directions transverse to the flow axis. Standing waves generated along the optical axis do not affect the beam quality of the laser. This is not true for the standing waves formed along the e-beam axis. These are extremely detrimental to the beam quality and must be cleared prior to the system being reactivated. If left unattended these acoustic disturbances will reside in the laser cavity for an excessive period of time. For example, in the present DARPA/Maxwell Rep-rated XeF Laser, these transverse waves have been observed to reside in the cavity for periods exceeding 50 msec with very little degradation of their amplitudes.

The proposed circulator design will employ a dissipative acoustic muffler positioned opposite of the e-beam to squelch these standing waves. For the design operating frequency of 25 Hz, the number of

acoustic transits of the cavity in the e-beam direction will be 80. The peak-overpressure for these standing waves is at most 20 percent of the initial overpressure in the cavity, therefore initially $\Delta p_T/p$ is at most 4.86×10^{-2} . If we assume an extremely conservative attenuation rate of 1 dB (~ 11 percent) of the amplitude of this transverse disturbance per acoustic transit, after 80 transits the $\Delta p_T/p$ will be 4.86×10^{-6} . The density disturbances, $\Delta \rho_T/\rho$, due to this mechanism will be 2.92×10^{-6} . This number is negligible in comparison to a $\Delta \rho_0/\rho$ of 7.07×10^{-5} allowed for ordered density fluctuations.

3.4 100 Hz Operation

When operating the system at 100 Hz, the primary factor affecting the medium homogeneity will be the increase in the Mach number of the flow. In order to keep the flush factor constant, the flow velocity will be increased to 27.5 m/sec (Mach number ~ 0.06). Since the turbulence intensity (u'/u_c) will remain constant, the effect on the density fluctuations due to random disturbance will remain essentially constant. The primary effect will be on the generation of entropy waves. The $\Delta \rho_E/\rho$ will be increased by a factor of at least 2.5. In addition, by including the additional heat, which will be generated in the muffler packing material to absorb the added acoustic energy, it is anticipated that for 100 Hz operation the total $\Delta \rho/\rho$ will be 5×10^{-4} or less.

4. Conceptual Design

The conceptual design for the circulator for the DARPA/Maxwell rep-rated XeF laser is based on the technical approach described in the preceding sections. The conceptual design is shown in figures 1 through 6. The key features of this design are as follows:

1. Upstream and downstream acoustic mufflers will be positioned adjacent to the laser cavity. The internal cross-section area of these mufflers will be identical to that of the laser cavity (4.31 in \times 24 in). The sides corresponding to the 24 inch dimension will consist of perforated aluminum plates backed by acoustic absorbing material. This material will be composed of aluminum screens and will have a thickness of 4 inches. These mufflers will be housed in cylindrical pipes having an internal diameter of 24.4 inches.
2. Opposite of the e-beam foil, there will be an acoustic muffler composed of a perforated aluminum plate backed by aluminum screen material. In addition, active cooling will be incorporated in the muffler backing material, in order to remove any heat generated by energy deposition from the e-beam into this material. Active cooling will be extremely important when operating the system at a frequency of 100 Hz.
3. A turbulence management section will be located directly upstream of the upstream acoustic muffler. This unit will be composed of aluminum honeycomb and aluminum screens. In addition, it will handle the transition of the flow

from cylindrical to rectangular, since the return duct of the circulator will be composed of cylindrical pipes.

4. A gas-bypass system will be included in the three acoustic mufflers (upstream, cavity, and downstream). The by-pass system will be employed between runs, to stabilize the temperature of the acoustic packing material with the gas flow.
5. A heat exchanger will be located between the pump and the turbulence management system. At the present time we are planning on using the existing heat exchangers with modifications.
6. The pump to drive the circulator will be the pump presently being employed. This pump will have to be modified to handle the increase in operating pressures. This unit will be mounted in a manner which will minimize vibration coupling.
7. The return ducts will be composed of 16 inch internal diameter cylindrical pipes. The transition to the rectangular inner channel will take place just before the turbulence management section and just after the downstream acoustic muffler.
8. The elements between the heat exchanger and the cavity will be thermally insulated from the environment. This is to ensure that this portion of the circulator will rapidly attain thermal equilibrium with the gas flow.
9. The flow axis through the laser cavity will be oriented in the vertical direction.

10. The system will be structurally mounted in a manner allowing access to the laser cavity and e-beam without the necessity to remove any additional hardware such as upstream and downstream acoustic mufflers.
11. Instrumentation ports will be positioned throughout the circulator to monitor temperature and pressure.

Figures 1 and 2 show the conceptual drawings for a system which can employ a drift region approximately 12 inches in length. This will allow the use of cylindrical shaped, outer-shell mufflers. If it is necessary to employ a shorter length drift region, a rectangular outer-shell geometry will have to be employed for a short segment of the acoustic mufflers immediately upstream and downstream of the laser cavity, as shown in figures 3 and 4.

A sketch of the cavity/muffler interface is shown in figure 5. The muffler packing material for the cavity muffler has been pulled back from the perforated plate. The active cooling elements, which will be employed for the cavity mufflers, are not shown in this sketch. This figure also shows the near cavity muffler configuration, if it is necessary to employ the shorter length drift region. A cross-section of the turbulence management system is shown in figure 6.

AW 5726

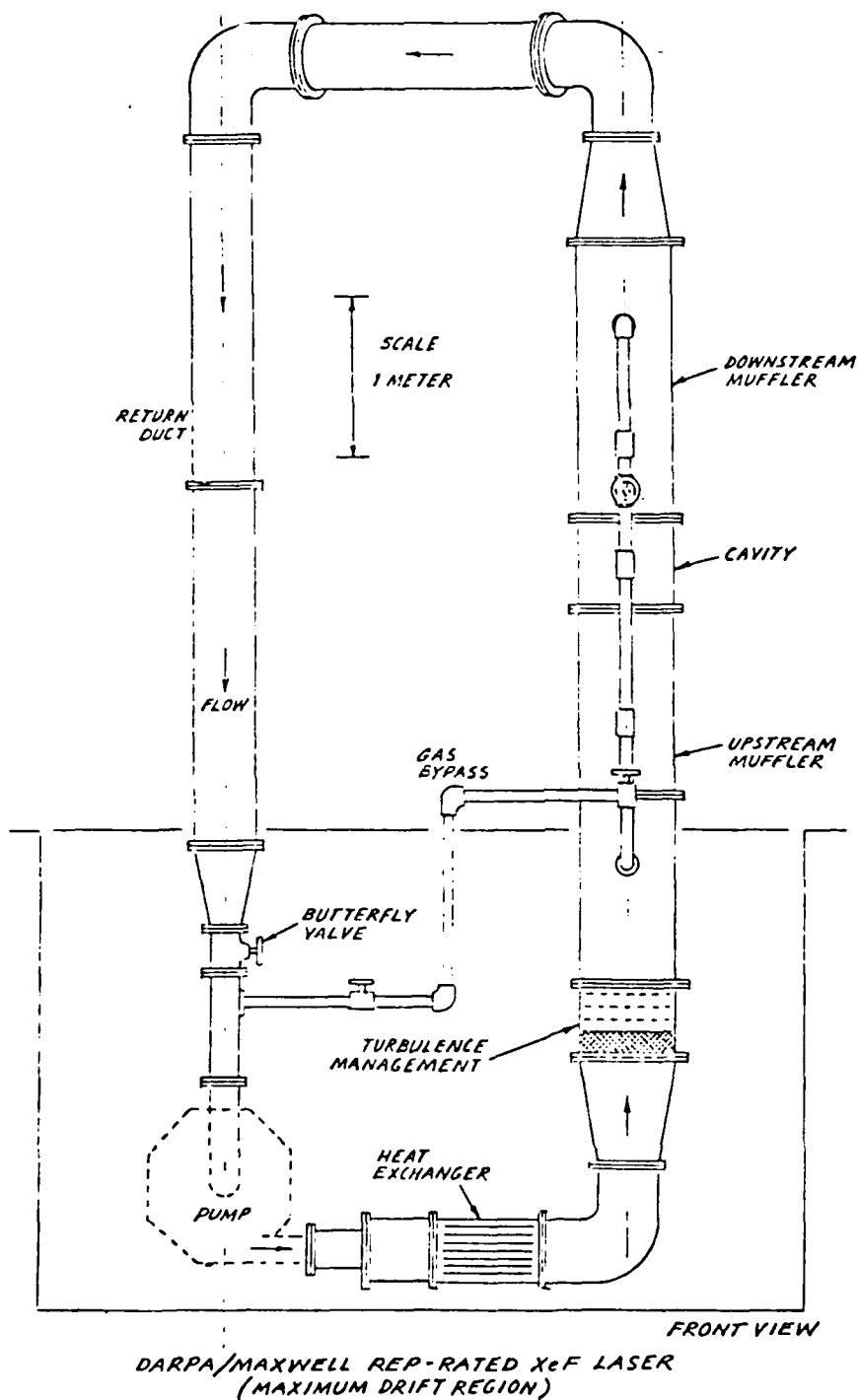
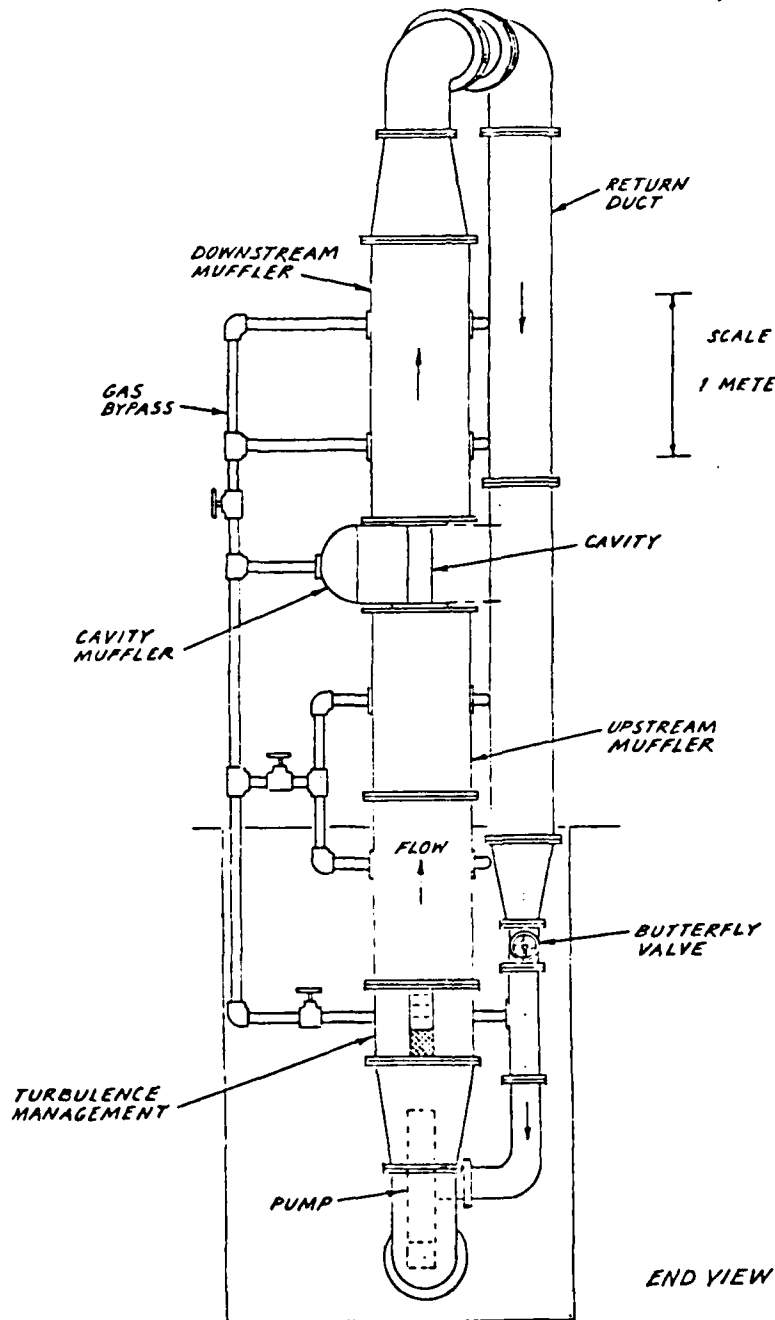


Figure 1.

AW3725



DARPA/MAXWELL REP-RATED XeF LASER
(MAXIMUM DRIFT REGION)

Figure 2.

4W3724

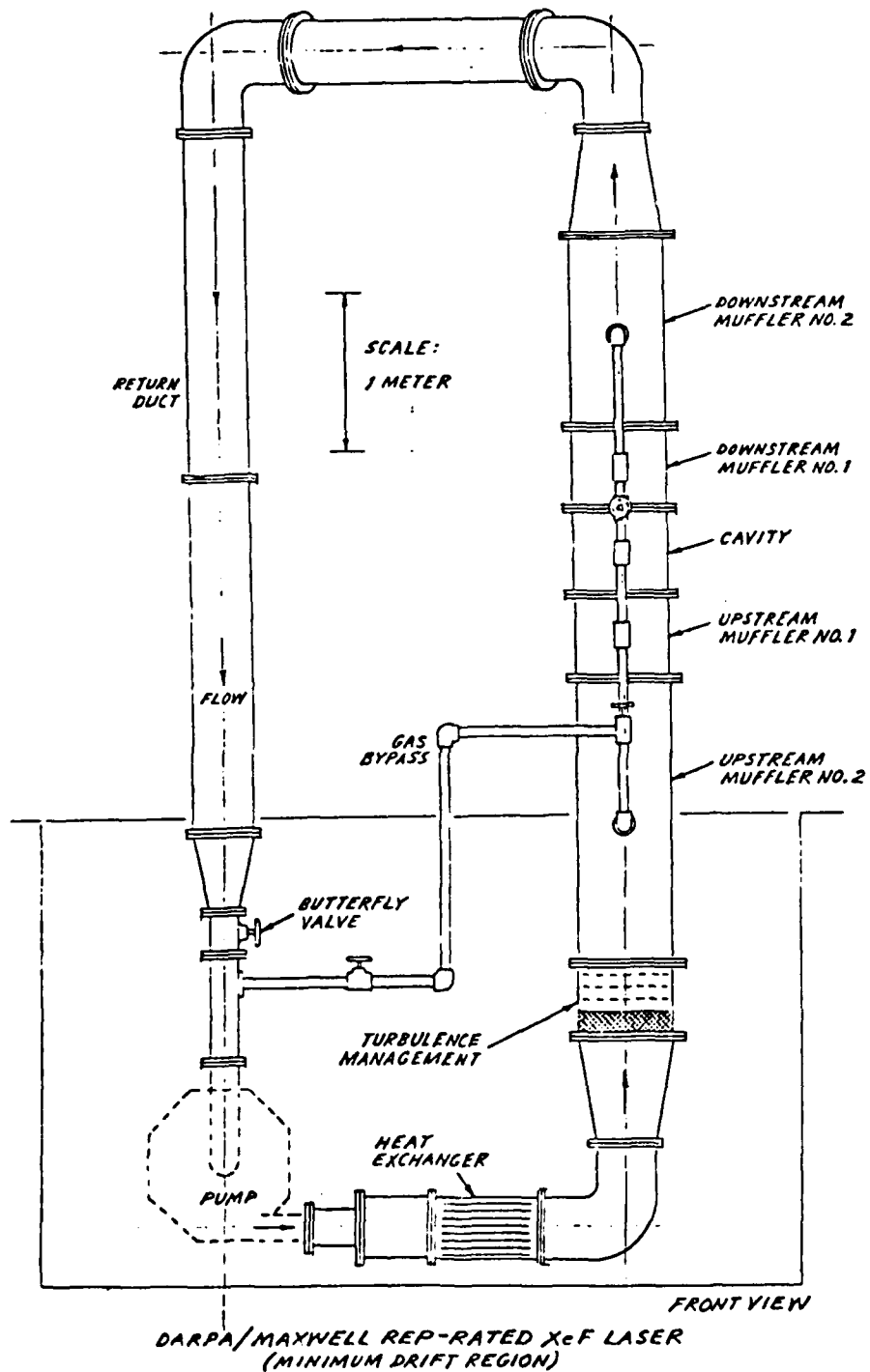
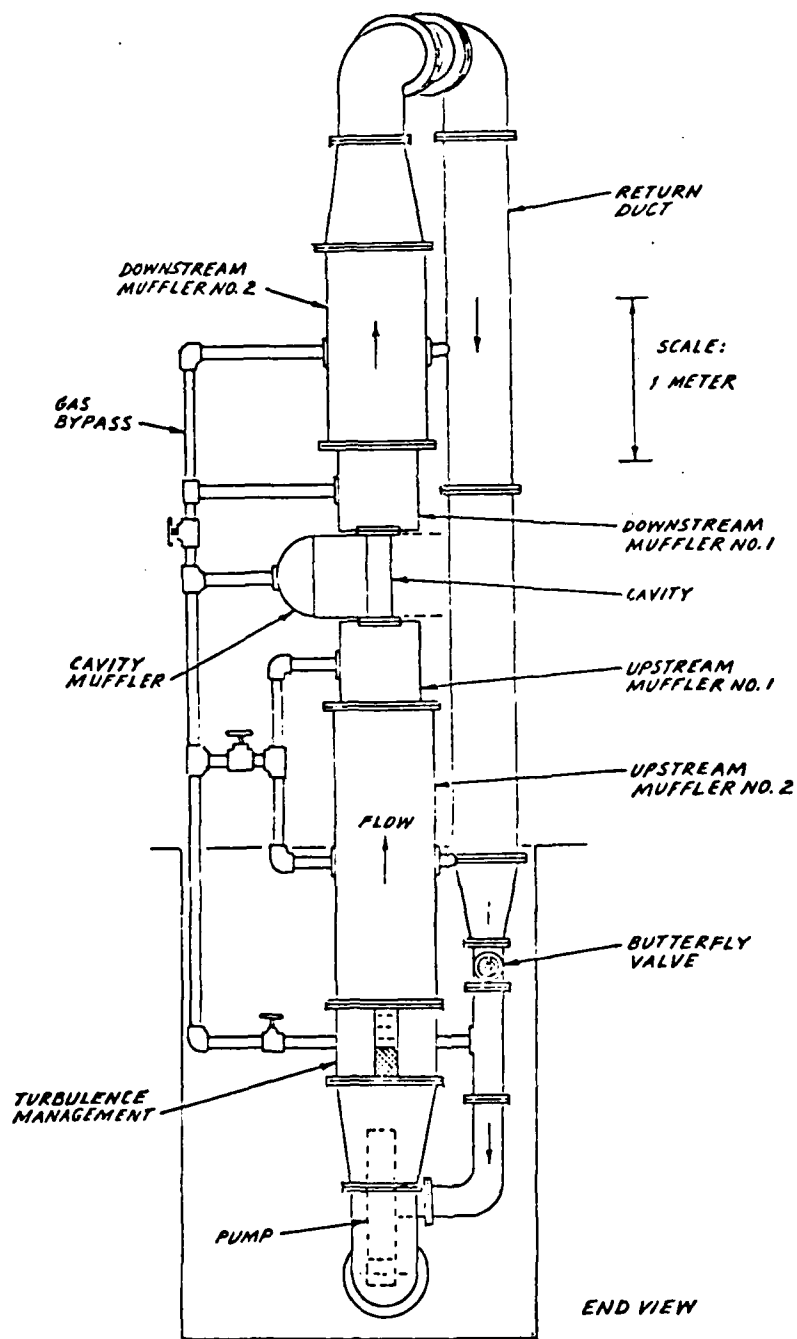


Figure 3.

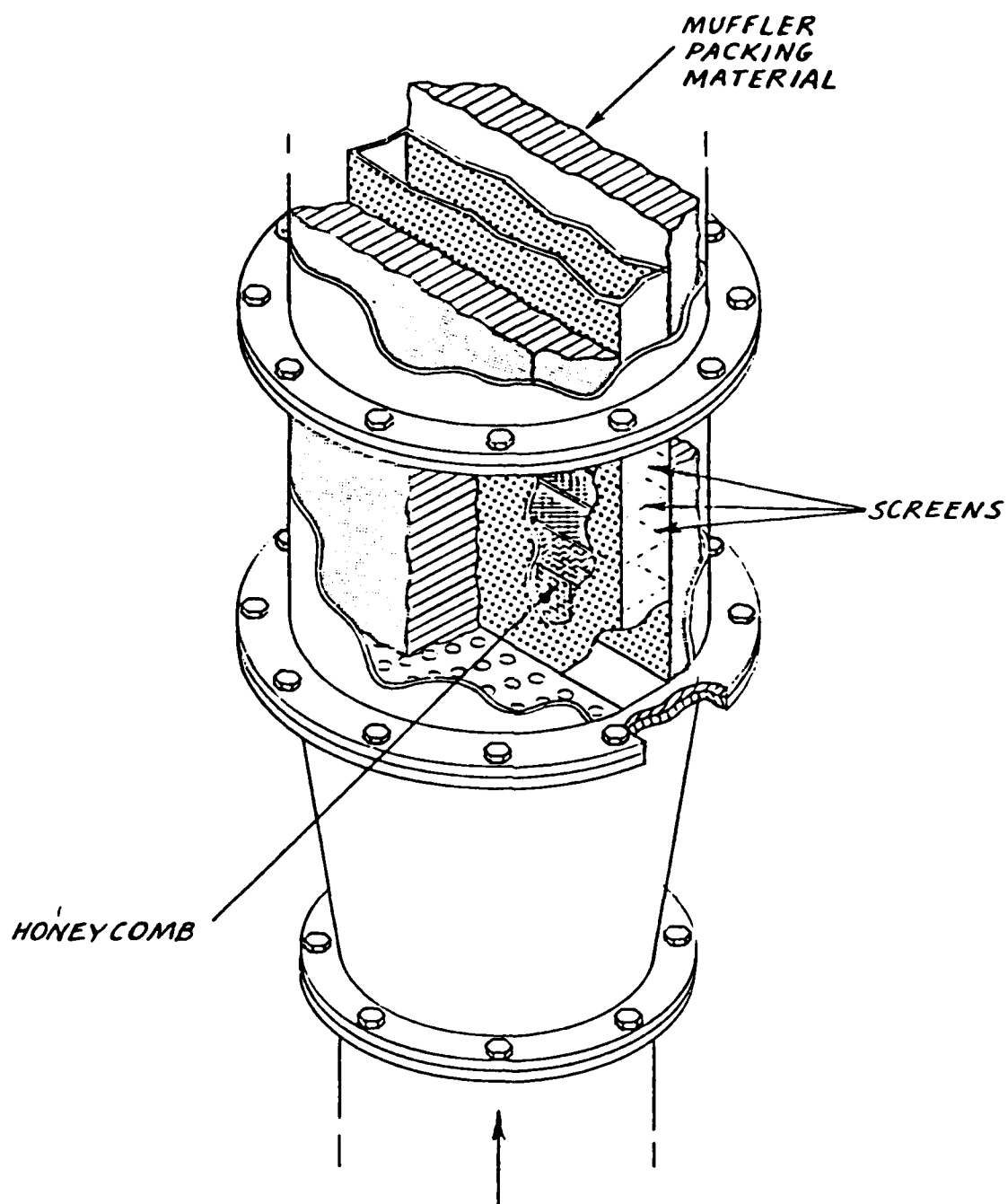
Aw 5723



DARPA/MAXWELL REP-RATED XeF LASER
(MINIMUM DRIFT REGION)

Figure 4.

AW3721



TURBULENCE MANAGEMENT SYSTEM

Figure 5.

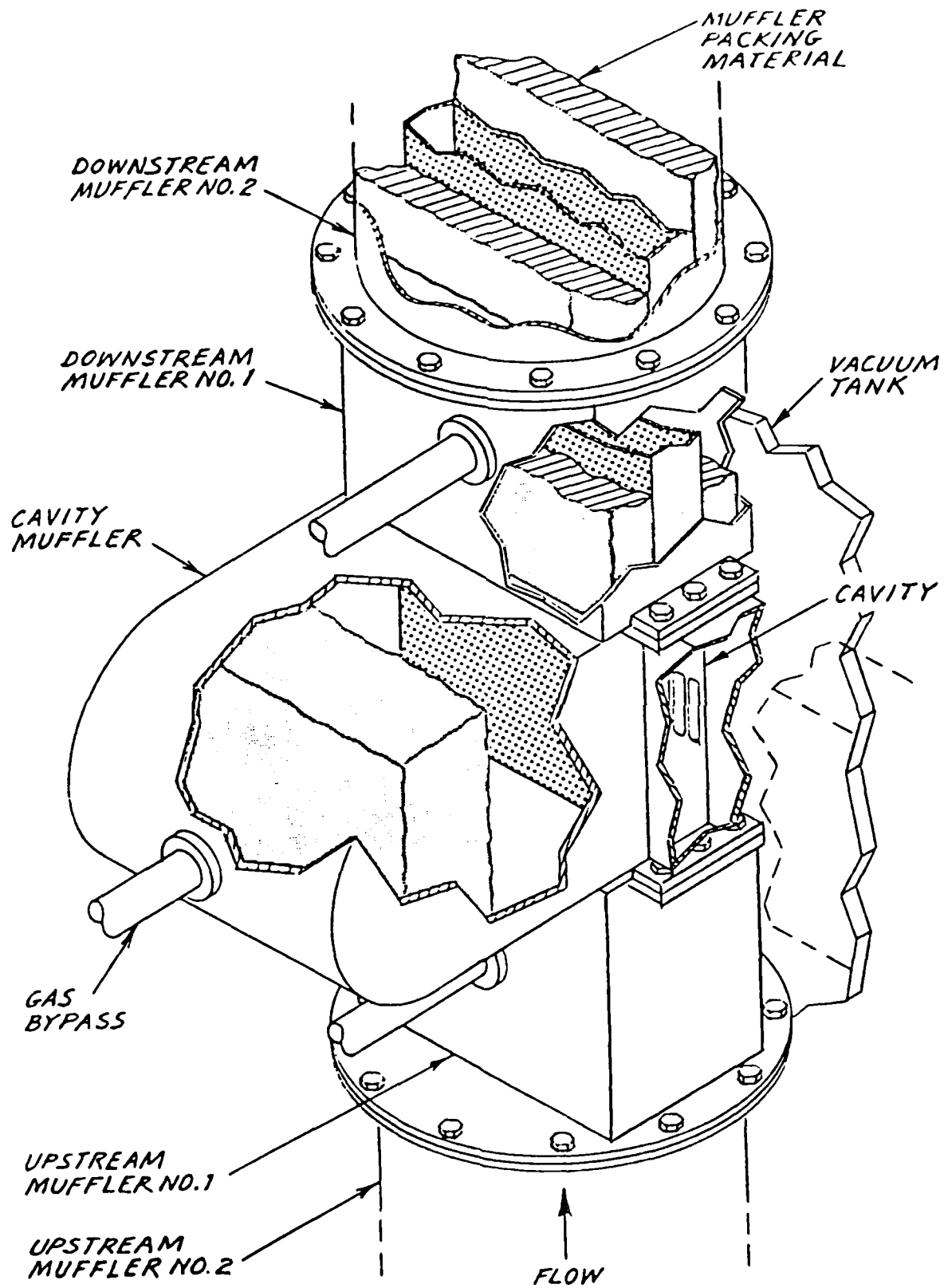


Figure 6.

5. Conclusions

Based on the results of the diagnostic tests conducted on the DARPA/Maxwell Rep-rated XeF laser, it was decided that a beam quality of two-time diffraction limited could not be attained by simply modifying the existing system. Therefore, the decision was made to formulate a conceptual design, which would provide the required beam quality for the desired mode of operation, in the simplest fashion without any constraints from any of the existing hardware.

After subtracting the contributions from resonator mirrors, windows, steering mirrors and medium pumping, a beam quality of 1.65-time diffraction limited was allocated to the medium homogeneity. This beam quality requires a $\Delta\rho/\rho$ of 2.5×10^{-4} . Therefore, in order to provide a safety factor, the conceptual design was formulated to provide a $\Delta\rho/\rho$ of 1×10^{-4} . Typical operations will consist of operating the system in a burst mode with a repetition frequency of 25 Hz. In some cases, this frequency will be increased to 100 Hz. When this occurs, the medium homogeneity will degrade to 5×10^{-4} . This will result in a beam quality of 9.1-time diffraction limited. This number is based on the assumption that the other mechanisms contributing to beam quality remain constant when the frequency is increased from 25 Hz to 100 Hz.

The design chosen is a constant area duct with upstream and downstream acoustic mufflers. In addition, an acoustic muffler is positioned on the opposite wall of the e-beam in the laser cavity. The purpose of this muffler is to absorb transverse waves created in the laser cavity due to nonuniform energy deposition. A turbulence management system will be positioned just upstream of the upstream acoustic muffler. A gas-bypass flow system is included in the mufflers to cool the acoustic muffler packing material between test runs. A heat exchanger will be

placed between the pump and the turbulence management system. The outer shells of the elements of the system located between the heat exchanger and the laser cavity will be thermally insulated. The system will have its flow axis oriented in the vertical direction.

Preliminary pricing estimates were done for the conceptual design. This costing was done assuming the program would be completed in three phases. The first phase would be the engineering design phase at a cost of approximately \$72K. The fabrication phase would be approximately \$380K. The final phase would be the installation and testing of the system at an estimated cost of \$100K.

Upon completion, this proposed laser circulator would provide an excellent test bed for Raman cell conversion experiments and, also, for testing uniform energy deposition of rep-rated e-beams.

6. References

Beranck, L. L. 1954 *Acoustic*. New York: McGraw-Hill.

Cornell, W. G. 1958 Loses in flow normal to plane screens.
Transactions of the American Society of Mechanical Engineers 80 No. 4,
pp. 791-799.

Hogge, H. D., Crow, S. C., Morris, J. H. and Hurdle, P. M. 1979
Modeling and simulation of flow and acoustics in pulsed excimer lasers.
Poseidon Research No. 21.

APPENDIX A

Poseidon Research Note No. 78

Evaluation of the Flow and Acoustic
Properties of the Maxwell Close-Cycle
Pulsed Excimer Laser Flow System

by

Dennis R. Regan and Timothy N. Turner

August 1981

Table of Contents

	<u>Page</u>
1. Introduction.....	1
2. Baseline Flow Measurement Results.....	2
3. E-beam Acoustics and Thermal Slug Temperature Signature Measurements.....	9
4. Conclusions.....	16

1. Introduction

An evaluation of the flow and acoustic properties of the Maxwell Laboratories closed-cycle pulsed excimer laser system was investigated experimentally at the Maxwell facility in San Diego, California during the period of 22 June 1981 to 2 July 1981. The baseline flow and acoustic measurements included heat exchanger pressure drop, compressor pressure rise, mean cavity velocity profile, cavity turbulence intensity profile, cavity temperature fluctuation intensity, thermal slug temperature signature and the flow duct and cavity sound pressure levels and spectra. The e-beam acoustics included measurements of the amplitude, frequency and decay time of longitudinal waves generated within the laser cavity by e-beam deposition. The presence of transverse waves in the cavity was also investigated using a dual probe-tube set-up.

A diagram of the Maxwell closed-cycle wind tunnel is displayed in figure 1. The flow loop is powered by a single-stage 1000 CFM belt-driven centrifugal compressor powered by a 25 hp three-phase electric motor. A butterfly valve at the pump inlet allows the pump speed to be varied. All 90° elbows are equipped with vanes to reduce flow separation and swirl. The nozzle is two-dimensional and has a contraction ratio of approximately five. Note that a vaned two-dimensional diffuser is placed between the nozzle outlet and the laser cavity in order to physically match the nozzle to the cavity; an arrangement that all but eliminates the benefits of using a nozzle upstream of the cavity.

Much of the rectangular shaped ducting used in the Maxwell closed-cycle wind tunnel was originally designed to withstand internal pressures ranging from zero to atmospheric pressure. Maxwell Labs has been currently operating this system at pressures exceeding two atmospheres absolute (30 psia). A failure of a weld in one of the rectangular duct sections did occur during pressurization. The weld failure appeared to be due to fatigue caused by repeated expansion and contraction of the duct walls.

2. Baseline Flow Measurement Results

The results of the baseline flow measurements indicate that several design deficiencies of the closed-cycle wind tunnel exist and should be corrected in order to obtain higher beam quality with continuous flow loop operation.

For example, during the heat exchanger pressure drop measurement it was learned that only one of the three heat exchangers was shrouded so that the duct flow would be forced through the tube-fin core. The other two heat exchangers were not shrouded and as a result some of the flow bypasses the heat exchanger cores. In addition, coolant water was not supplied to the heat exchanger cores and as a result the closed-cycle wind tunnel never attained steady state operation during these tests.

The pressure drop across the heat exchanger core was measured using an oil manometer calibrated in inches H_2O . During these and all other measurements the pump head was monitored using a mercury (Hg) manometer.

The heat exchanger pressure drop measurements for a total pressure of 30 psia (Argon gas) are summarized in figure 2 for one, two and three heat exchanger core sections in series for throttle settings of 50 percent, 75 percent, and 100 percent. Note that after these latter measurements were made it was discovered that the shrouded Number 1 heat exchanger core (normally placed downstream closest to the cavity) was reversed such that heat exchanger cores Number 2 and Number 3 were downstream closest to the cavity. For the remainder of the flow and acoustic tests, the heat exchanger core positions were reversed to coincide with the usual arrangement used by Maxwell Labs.

Figure 2 shows that because of the ability of the flow to bypass heat exchanger cores Number 2 and Number 3 the pressure drop does not scale with the total length of the heat exchanger core. An estimate of

the heat exchanger pressure drop for several shrouded heat exchanger cores can be made by multiplying the pressure drop measured with the single shrouded heat exchanger core by the total number of cores in the flow duct.

During the heat exchanger pressure drop measurements it was noticed that the pressure rise across the centrifugal compressor decreased with time. This decrease in pump pressure head corresponded with an increase in system pressure and temperature as heat was not being removed from the closed-cycle flow system. The exact reason for the decrease in the pump pressure head is not fully understood at this time, but could be due to a decrease in compressor efficiency caused by an increase in fan blade boundary layer thickness caused in turn by the increase in gas temperature.

The mean velocity profile in the laser cavity was measured using both a Prandtl type pitot-static probe and a hot-film anemometer. During these measurements all three heat exchanger cores were inserted in the flow duct and the flow loop was pressurized with argon gas to 30 psia.

The results of the pitot probe scan is displayed in figure 3 for the full throttle condition normally used by Maxwell. The mean velocity has been normalized to the centerline value of $U(0) = 62.55$ m/sec. The transverse pitot probe position X is normalized with respect to the cavity width $W = .38$ m (15 in), so that $2X/W = 0, -1, +1$ is the center of the flow channel, left wall and right wall positions respectively.

The pitot probe measurements show that variations in mean velocity approaching twenty percent occur in the laser cavity. These latter variations in mean velocity are caused by the vaned diffuser ahead of the cavity entrance. The dip in the mean velocity profile at $2X/W = -0.3$ is caused by the wake produced by one of the upstream cavity diffuser vanes.

The hot-film anemometer was also used to measure mean velocity profile as well as the rms turbulence intensity profile in the laser cavity. The hot-film probe was calibrated for argon gas at $p = 30$ psia using the pitot-static probe. The hot-film instrumentation consists of a Disa 55M01 main frame with a Disa constant temperature 55M11 anemometer bridge and a Disa 55R11 single sensor hot-film probe. The operating hot-film resistance ratio was 1.55. A HP-3400A true rms voltmeter was used in conjunction with the hot-film probe calibration curve to determine the rms turbulence intensity. In order to reduce the effects of increasing gas temperature on the hot-film probe calibration, all flow measurement points were made after allowing the gas temperature from the previous run to cool to near room temperature.

The mean velocity and rms turbulent velocity profiles for the laser cavity are displayed in figure 4 for a centerline velocity $\bar{U}(0) = 63.34$ m/sec. Note that the shape of the normalized mean velocity profile as measured by the hot-film anemometer and pitot-static probe differ, especially towards the cavity side wall. These latter discrepancies are most likely caused by the increased sensitivity of the hot-film anemometer probe to flow direction as compared to a Prandtl type pitot-static probe, which is relatively insensitive to flow direction for flow angles $\theta \leq 15^\circ$. There are two other effects that will cause an apparent increase in the velocity measured by a Prandtl type pitot-static probe over a hot-film anemometer probe: an additional contribution to the dynamic pressure due to free-stream turbulence and an apparent increase in dynamic pressure when the angle between the probe axis and the flow exceeds 15 degrees. Because of these latter effects, it is felt that the mean velocity profile measured using the hot-film anemometer is more representative of the axial component of the cavity flow velocity than those measurements made with the pitot-static probe. The agreement between the mean velocity profiles measured near the cavity centerline indicate that the flow is essentially axial in nature.

The turbulence intensity profile displayed in figure 4 shows that as one progresses from the center of the laser cavity toward the wall the rms turbulence intensity decreases reaching a minimum of $u'/\bar{U}(0) = 0.033$ at $2X/W = -0.6$ and then increases to $u'/\bar{U}(0) = 0.09$. It is likely that in the wall boundary layer located between $0.95 \leq |2X/W| \leq 1.0$ the rms turbulence intensities would exceed ten percent. The peak in the rms turbulence intensity between $2X/W = -0.75$ and $2X/W = -0.9$ is most likely caused by a thick shear layer associated with the diverging walls of the vaned diffuser upstream of the nozzle. Clearly, a substantial improvement in the mean velocity profile and as well as a reduction in turbulence intensity would result from eliminating the vaned diffuser and matching the nozzle directly to the laser cavity.

The spectrum of the turbulent velocity fluctuations measured with a Tektronix 3L5 spectrum analyzer at $2X/W = -0.15$ in the laser cavity is displayed in figure 5 for a centerline velocity $\bar{U}(0) \approx 61.0$ m/sec. These spectrums represent the one dimensional spectrum function for longitudinal (axial) velocity fluctuations. For frozen flow (eddy convection velocity equal to mean flow velocity) the longitudinal eddy scale length ℓ is related to the mean flow speed \bar{U} and the eddy passage frequency f by

$$\ell \sim \bar{U}/f \quad . \quad (2.1.1)$$

The velocity fluctuation spectrum displayed in figure 5 indicates that strong velocity fluctuations with eddy scale lengths $\ell \approx 5 - 6$ cm exist in the flow. Weaker velocity fluctuations with longitudinal eddy scale lengths $\ell \sim 0.5$ cm are also observed for eddy passage frequencies $f > 9$ kHz in the laser cavity at $2X/W = -0.15$.

The sound pressure level (SPL) measured in the flow duct upstream of the heat exchangers is displayed in figure 6. A B&K 4138 condenser microphone fitted with a vented aerodynamic nose cone was used to measure the static pressure fluctuations inside the duct. The axis of the microphone nose cone was oriented parallel to the flow using a right-angle stem fitted directly to a B&K 2615 cathode follower. The output of the cathode follower was in turn fed into a B&K 2603 wide-band amplifier. The entire microphone amplifier system was calibrated using a B&K 4220 pistonphone that generated a sound pressure level of 124 dB re 0.0002 d/cm^2 .

The results of the flow duct sound level measurements displayed in figure 6 shows that when the Maxwell flow loop is first turned on (cold start) the measured SPL increases with throttle setting, as might be expected, reaching a maximum of about 153 dB. However, as time progressed the measured SPL decreased substantially as indicated by the dash lines in figure 6. This same effect was also observed in the noise spectrums measured with the Tektronix 3L5 spectrum analyzer shown in figure 7 for different running times. Measurements made outside the laser cavity show that the SPL is about 105 dB on the linear weighting scale. Thus, one would expect the SPL inside the cavity to be at least 20 - 30 dB higher than the SPL outside the cavity under "no vibration" conditions.

One explanation for the behavior of the noise level measured by the duct microphone as a function of time is that flow system vibration is contributing significantly to the overall SPL measurement. Indeed, one can easily detect that vibration is present in the system by simply placing ones hand on the flow ducting. The source of the vibration is the centrifugal compressor-motor system. According the Maxwell personnel, the centrifugal compressor sounds different to their ears after it has been running continuously for a few minutes. Therefore, it seems likely that the centrifugal pump is causing excessive flow system vibration

when first starting up and that the vibration decreases with time. The noise spectrums shown in figure 7 also shows that as time progresses, the low-frequency noise components decrease in intensity while coherent high-frequency spectral components increase in intensity.

Noise level measurements made with a flush-mounted microphone in the laser cavity are displayed in figure 8 along with noise spectra shown in figure 9. The flush-mounted cavity microphone tests were conducted at a pressure of 20 psia (instead of 30 psia) because of microphone cavity bleed problems. These latter measurements show a nearly constant noise level regardless of throttle setting. This indicates that the flush-mounted cavity microphone is not responding to turbulent boundary layer pressure fluctuations, which increase with the square of the flow velocity. Furthermore, the measured noise level in excess of 150 dB re 0.0002 d/cm^2 is too high to be accounted for solely by boundary layer pressure fluctuations. For example, a rms turbulent velocity fluctuation intensity of fifteen percent in the boundary layer would produce an SPL of 133 dB for a centerline flow speed $\bar{U} = 60.0 \text{ m/sec}$ at 20 psia at full throttle. The measurably higher noise levels obtained with the flush-mounted cavity microphone along with the insensitivity to throttle setting (flow speed) suggests that the cavity vibration noise level is overriding the noise level associated with turbulent boundary layer pressure fluctuations. Note that the noise spectra shown in figure 9, measured with the flush-mounted cavity microphone, does contain coherent spectral components that would be expected to be associated with vibration rather than from random turbulent boundary layer pressure fluctuations.

The temperature fluctuation intensity was measured in the laser cavity at $2X/W = -0.6$ for the full throttle condition using a five-micron tungsten wire temperature sensing element. A Disa 55M01 main frame and a Disa 55M20 temperature bridge were used in conjunction with

the temperature sensing element. The results of the cavity temperature fluctuation measurements are displayed in Table 1. At the $2X/W = -0.6$ position in the laser cavity it was found that the rms temperature fluctuation intensity $t'/\bar{T} \approx 10^{-3}$. The temperature fluctuation spectrum, displayed in figure 10, shows that the strongest temperature fluctuations are below 400 Hz. Note that the five-micron wire temperature sensing element most likely has a frequency response that does not extend beyond 2 kHz. The relatively large temperature fluctuation intensities measured in the laser cavity would be substantially reduced by activating the heat exchangers and insulating the duct walls.

3. E-Beam Acoustics and Thermal Slug Temperature Signature Measurements

The generation of longitudinal and transverse shock and acoustic waves within the laser cavity by e-beam deposition was investigated using two B&K 4138 microphones. In order to reduce interference from x-ray and electromagnetic pulse (EMP) effects, the two microphones were connected to separate insulated (alumina) probe tubes that were three feet in length, as shown in figure 11. These probe tubes were located in one of the laser cavity sidewalls and were positioned such that transverse waves reflecting between the e-beam foil and cover plate would produce out of phase signals while longitudinal waves would produce in phase signals. Using the latter scheme, the microphone signals could be fed into an electronic subtraction circuit to study transverse waves (in phase longitudinal wave signals would be nulled out). As shown in figure 11, an additional twelve feet of copper tubing is attached to each microphone probe tube at the junction between the microphone and the alumina tubing. The ends of the copper tubes are sealed and provide an additional 24 ms of time between wave reflections at the tube ends and the microphones.

The electronic signal processing consisted of a real time display of each individual microphone channel using a Tektronix 459A scope with a dual-beam plug-in amplifier and scope camera. The scope was externally triggered 5.3 ms before the e-beam was fired. The signals from the microphone channels were also recorded on magnetic tape using a four channel HP 3964A tape recorder operating in the direct mode at 15 i.p.s. The bandwidth of the HP 3964A ranged from 70 Hz to 60 kHz.

A temperature probe was also used to measure the temperature of the thermal slug convected downstream produced by e-beam deposition. The temperature sensing element was a Disa 55R11 film probe and was

located 12 inches downstream of the laser cavity in the center of the diffuser duct. The frequency response of the film probe to temperature fluctuations extends out to several hundred Hertz. The film temperature probe was connected to the Disa 55M01 main frame and Disa 55M20 temperature bridge. The bridge output was monitored in real time using a Tektronix 464A scope and scope camera. The temperature bridge output was also fed into one channel of the HP 3964A tape recorder.

The e-beam apparatus was operated in both single and multiple shot modes. Normally, a flow system pressure of 30 psia is used to ensure proper cavity energy loading. However, in the following tests the argon gas pressure had to be reduced to one atmosphere because of microphone cavity bleed problems. Therefore, in reviewing the following data one should keep in mind that the cavity overpressures and overtemperatures reported here will be reduced compared to their normal levels at a system pressure of 30 psia.

The microphone and cathode followers were checked for spurious signals resulting from the EMP generated by the e-beam apparatus by removing the probe tubes from the cavity and sealing the tube entrance to reduce unwanted noise pickup. A photograph of the EMP pulse picked up by both microphone circuits is displayed in Run #18 in figure 12. Note that the EMP signatures are not identical because different signal amplifiers were used for each microphone channel. The EMP pulse effect appears as a sharp negative step 5.3 ms from the beginning of the trace (the sync trigger pulse arrives 5.3 ms before the e-beam is fired) followed by a relatively slow return to normal. The low-frequency excursions caused by the e-beam EMP can be filtered out using a high-pass filter and, therefore, present no problem insofar as data reduction is concerned. The sharp negative spike will be present on all our data but will be displaced from the acoustic signals by the time it takes the acoustic waves to propagate down the 36 inch probe tubes (about 3 ms).

The nature of the longitudinal waves generated in the laser cavity by e-beam deposition are shown in Run #17 in figure 12. Note that in this and all subsequent photographs increasing pressure is in the negative (downward) direction. The Run #17 real time data shows the 5.3 ms delay between the arrival of the sync pulse and e-beam firing followed by an additional 3 ms delay for shock waves to propagate down the alumina probe tubes. The shock waves are found to have the characteristic sawtooth waveform. The bottom trace in Run #17 (channel "I" probe tube nearest the e-beam foil) shows a large overpressure while the top trace (channel "H" nearest the outside reflector plate opposite the e-beam foil) does not exhibit a similar overpressure. The reason for the lack of an initial overpressure signature for channel "H" is that the Ithaco signal conditioning amplifier is saturating because of the strong EMP effect produced by the e-beam apparatus. The Ithaco amplifier saturation effect can be observed in Run #20 of figure 13 when an inductor flashover prevented full e-beam output from occurring. With reduced e-beam output, hence EMP production, an initial overpressure spike was observed for channel "H" (top trace). Note that the overpressure spike is clipped at the same level usually observed for the EMP.

The microphone amplifier gains were adjusted so that a 1v rms amplifier output corresponded to a sound pressure level of 152 dB for channel "H" and 154 dB for channel "I" re 0.0002 d/cm^2 . Thus, the initial overpressure in the laser cavity is typically $\leq 170 \text{ dB}$ according to the channel "I" trace in Run #17 of figure 12. This particular e-beam pulse had a time duration of 0.8 us and a peak current intensity of 13.2 KA .

Once the initial overpressure occurs, shock waves reflect from cavity walls and any sudden expansion or contractions upstream or downstream of the cavity. Since the cavity width in the optical direction $L_o = 15 \text{ in.} = 38.1 \text{ cm}$, one would expect to observe oscillations at a

frequency f_o given by

$$f_o = C/L_o, \quad (3.1.1)$$

where C is the sound speed, for pressure waves reflected simultaneously from each cavity wall. For example, with a sound speed of 3.35×10^4 cm/sec for Argon gas at 50°C and $L_o = 38.1$ cm, one finds $f_o = 879$ Hz; in excellent agreement with the measured frequency of $f_o = 889$ Hz taken from data displayed in figures 13 and 14.

The decay time of the transverse waves (in the optical direction perpendicular to the flow) can be seen from figures 12 and 14, where sweep times of 5 ms/cm were used. The decay time appears to extend well beyond the acoustic round trip time of 24 ms for the twelve foot probe tube extensions. Note that the strength of the shock waves is still large at times of 20 - 30 ms after the initial overpressure, being typically about 140 dB re 0.0002 d/cm^2 .

The oscilloscope traces displayed in Run #17 of figure 14 show that the pressure waves detected by the probe tube microphone systems are in phase as they should be for waves passing back and forth in the flow direction and perpendicular to the flow direction along the optical axis. A pressure wave reflecting between the e-beam foil and the cover plate transverse to the flow will be detected out of phase since the probe tube orifices are in line with the direction of travel. Thus, if pressure waves transverse to both the flow and optical direction are present they may be observed by passing both probe tube channels through a differencing circuit to null out the strong pressure disturbances created by pressure waves transverse to the flow along the optical axis.

The setup for looking for pressure waves transverse to the flow and optical axis is displayed in figure 15. The previously recorded data was replayed on the HP 3964A tape recorder and the signals from the probe tube microphone channels were passed through individual Krohn-Hite 3202 filters operated in the high-pass mode ($f > 150$ Hz). The high-pass filter outputs were then fed into TSI 1063 electronic differencing circuit. The output of the differencing circuit was passed through another Krohn-Hite 3203 high-pass filter and then displayed on a Tektronix 551 oscilloscope equipped with a 1A1 plugin amplifiers. The scope was triggered using a sync signal recorded on one of the tape recorder channels during the data runs.

The results of the signal processing for a typical data run is displayed in figure 16. The triple trace photograph represents respectively the TSI 1063 differencer output (top trace), the output from microphone channel "H" (middle trace), and the output from microphone channel "I" (bottom trace). The data displayed in figure 16 is for the case where the system pressure was 14.7 psia and the throttle position was full open. A single e-beam pulse of duration 0.8 μ s was fired having a peak e-beam current of 14.9 KA. Note that the scope trace sensitivity is increased by a factor of ten for the differencing output channel as compared to the sensitivity for each individual probe tube microphone channel.

The fact that the probe tube microphone channels were not exactly balanced results in some pickup of pressure waves transverse to the flow and in line with the optical axis. In spite of the slightly unequal microphone channel outputs, a substantial cancellation of these latter pressure waves did occur and it was possible to look for the higher frequency waves transverse to both the flow and optical axis. The frequency of these waves should be at about 2000 Hz.

The results obtained thus far fail to show high-frequency transverse waves in the laser cavity. This indicates that if out of phase pressure waves transverse to both the flow and optical axis are present in the laser cavity they are at least 26 dB below the level of the lower frequency pressure waves transverse to the flow and parallel to the optical axis.

There are two other explanations as to the lack of observable high-frequency pressure waves transverse to both the flow and optical axis. The first explanation involves uniform e-beam loading between the e-beam foil and the reflector plate, while the second explanation involves simultaneous pressure wave reflections off both the foil and reflector plate. Uniform e-beam loading between the e-beam foil and the reflector plate would eliminate pressure gradients thereby eliminating pressure wave disturbances altogether. If the e-beam loading is uniform between the direction perpendicular to the flow and optical axis it means that the reflector plate opposite the e-beam foil is highly efficient in terms of reflecting secondary electrons back into the gas medium. The generation of simultaneous pressure waves off the foil and reflector plate would oscillate back and forth at a frequency of about 4400 Hz. Since the two probe tubes were placed equidistant from the cavity centerline, pressure waves reflecting simultaneously off the e-beam foil and reflector plate would produce in-phase signals at both microphones and the electronic differencing signal processing scheme will not work. It is interesting that weak in-phase, high-frequency (≈ 5000 Hz) signals can be observed in some of the probe tube microphone channel outputs.

The temperature signature of the thermal slug generated by e-beam deposition was determined using a film temperature sensing probe placed downstream of the cavity in the center of the diffuser. A Disa 55M01 main frame equipped with a Disa 55M20 temperature bridge was used in these measurements. The frequency response of the film probe is believed

to extend out to at least 400 Hz. The temperature bridge output was displayed in real time using a Tektronix 454A dual beam scope and recorded with the HP 3964A tape recorder.

The results of the thermal slug temperature signature measurements are displayed in figure 17 and Table 2. The scope traces in figure 17 show an increasing temperature in the negative (downward) direction. The film probe temperature sensitivity is $\Delta V/\Delta T = -0.2505 \text{ v}/^\circ\text{C}$ for these tests.

The data displayed in figure 17 shows that the hottest portion of the thermal slug arrives at the film probe about 9.7 ms after the e-beam is fired. Since the temperature probe is about 51 cm from the center of the e-beam foil, the average thermal slug convection velocity is $\bar{U}_c \approx 53 \text{ m/sec}$ as expected for the full throttle condition. The decay rate of the thermal slug temperature is considerably less than the initial rate of temperature increase indicating that a substantial portion of gas upstream of the cavity has been heated by the shock wave propagating upstream. A low intensity $f \sim 400 \text{ Hz}$ temperature oscillation is also observed in figure 17 that could be caused by a strong shock wave reflecting between the duct walls.

Table 2 shows a listing of the average and peak overtemperature measured in the center of the diffuser downstream of the cavity for Runs #5, #6, #10, #16, and #17. The system fill pressure for these tests was 14.7 psia; at least a factor of two below the usual system operating pressure. Doubling the system pressure would more than double the overtemperature because of the additional contribution to medium energy deposition made by secondary electrons emitted by x-ray bombardment of the tungsten coated reflector plate. Thus, a peak overtemperature of $\Delta T_{\text{max}} \approx 17.6^\circ\text{C}$ observed in these experiments may be expected to be significantly higher when the system fill pressure is increased to 30 psia.

4. Conclusions

Both the baseline flow and e-beam acoustic measurement program carried out on the Maxwell closed-cycle pulsed excimer laser wind tunnel have disclosed a number of areas that deserve attention for the upcoming modifications for achieving higher beam quality and longer running times. For example, the centrifugal compressor vibration appears to be excessively high to the extent that it is the major contributor to flow system noise. The heat exchanger arrangement is unsatisfactory and must be modified if long running times and system equilibrium is to be achieved. The placement of a vaned diffuser between the nozzle and laser optical cavity is an unsatisfactory arrangement insofar as achieving good flow uniformity, thin boundary layers and low turbulence and temperature fluctuation intensities are concerned. It is likely that a turbulence management section may also be needed ahead of the flow contraction to reduce swirl and turbulence scale lengths.

The rectangular flow ducting is for the most part unsatisfactory from a safety and reliability standpoint, since it was not originally designed to operate at a pressure of two atmospheres absolute. It is likely that certain portions of the flow system ducting will have to be insulated to further reduce temperature fluctuation intensities within the laser cavity.

The measurements of the decay time of shock waves in the laser cavity created by e-beam deposition indicates that the laser will most likely be relegated to low repetition rates. Therefore, methods to expedite the clearing of shock waves from the laser cavity will have to be adopted. The shock waves propagating out of the laser cavity will have to be attenuated using some kind of muffler arrangement in order to prevent excessively high sound pressure levels from building up in the flow system and laser cavity.

AW 3972

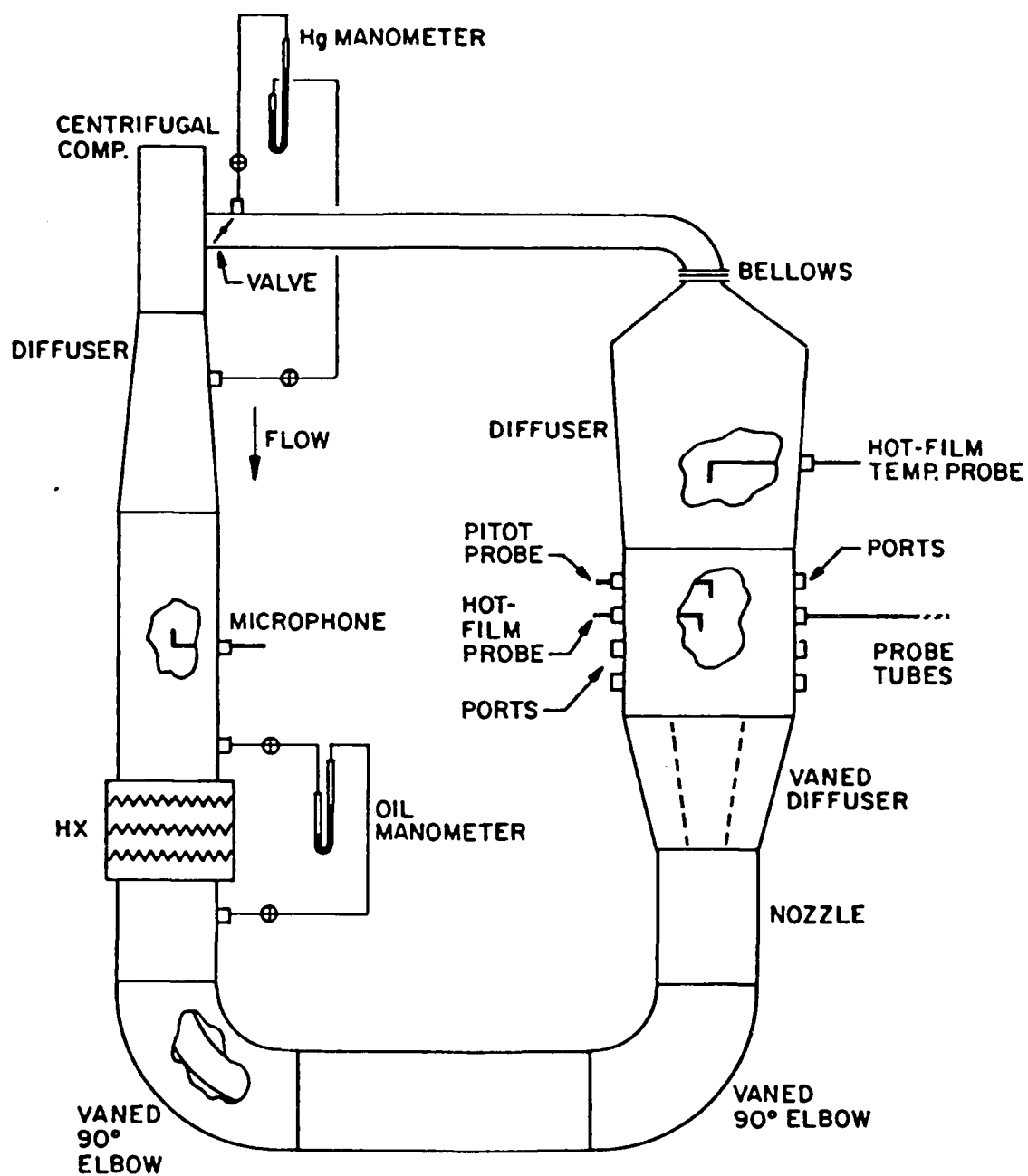


Figure 1. Maxwell closed-cycle wind tunnel.

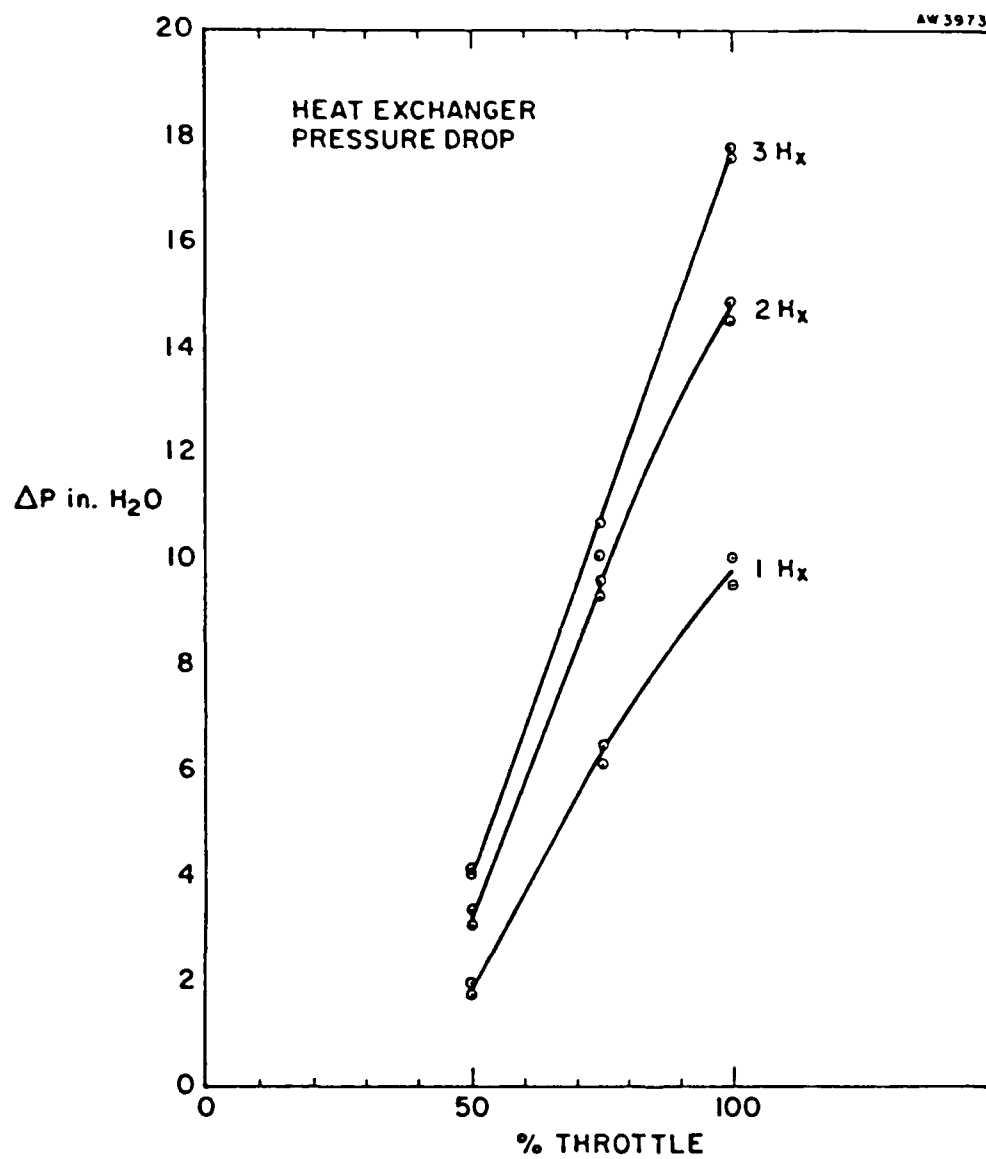


Figure 2. Heat exchanger pressure drop.

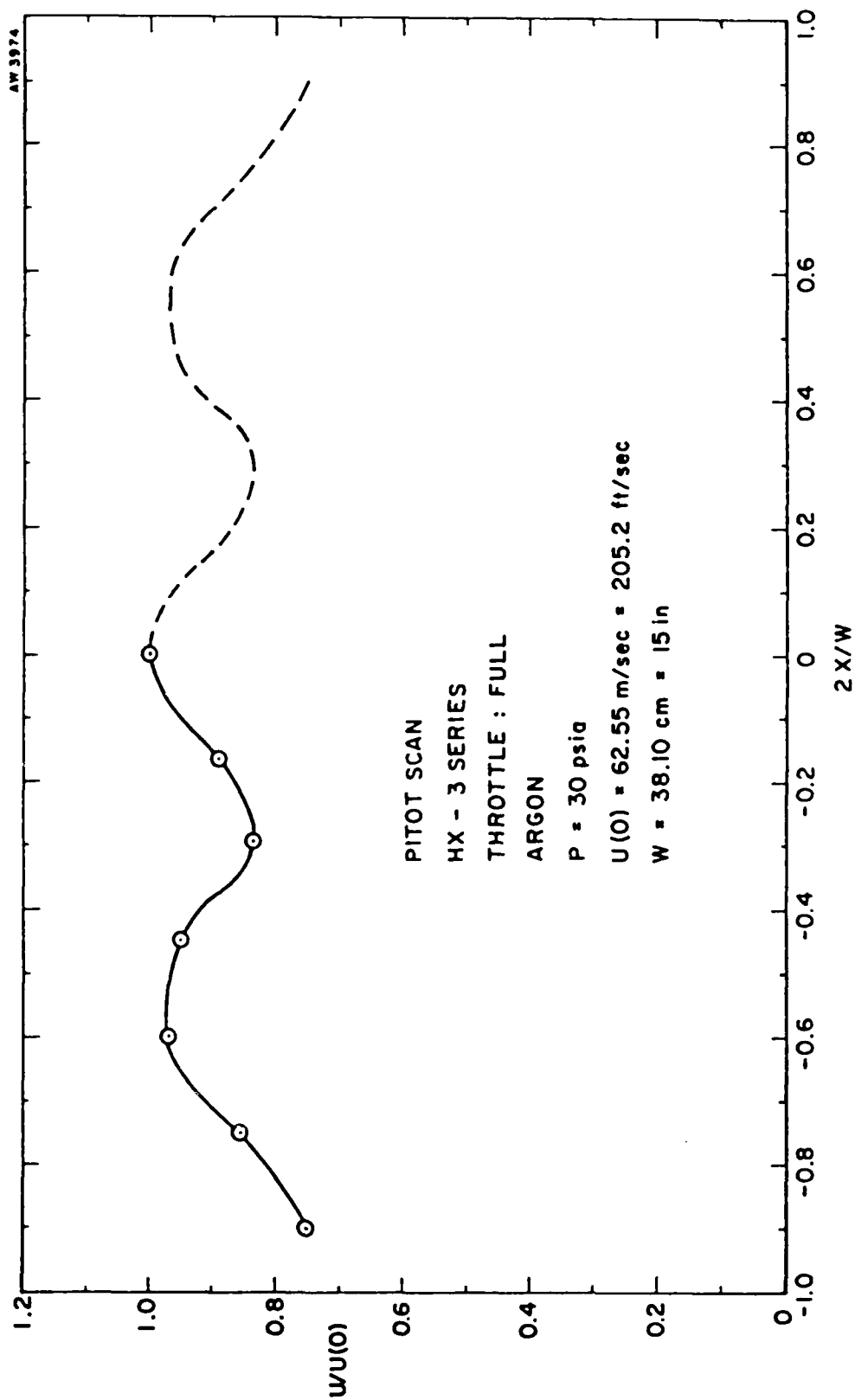


Figure 3. Pitot scan.

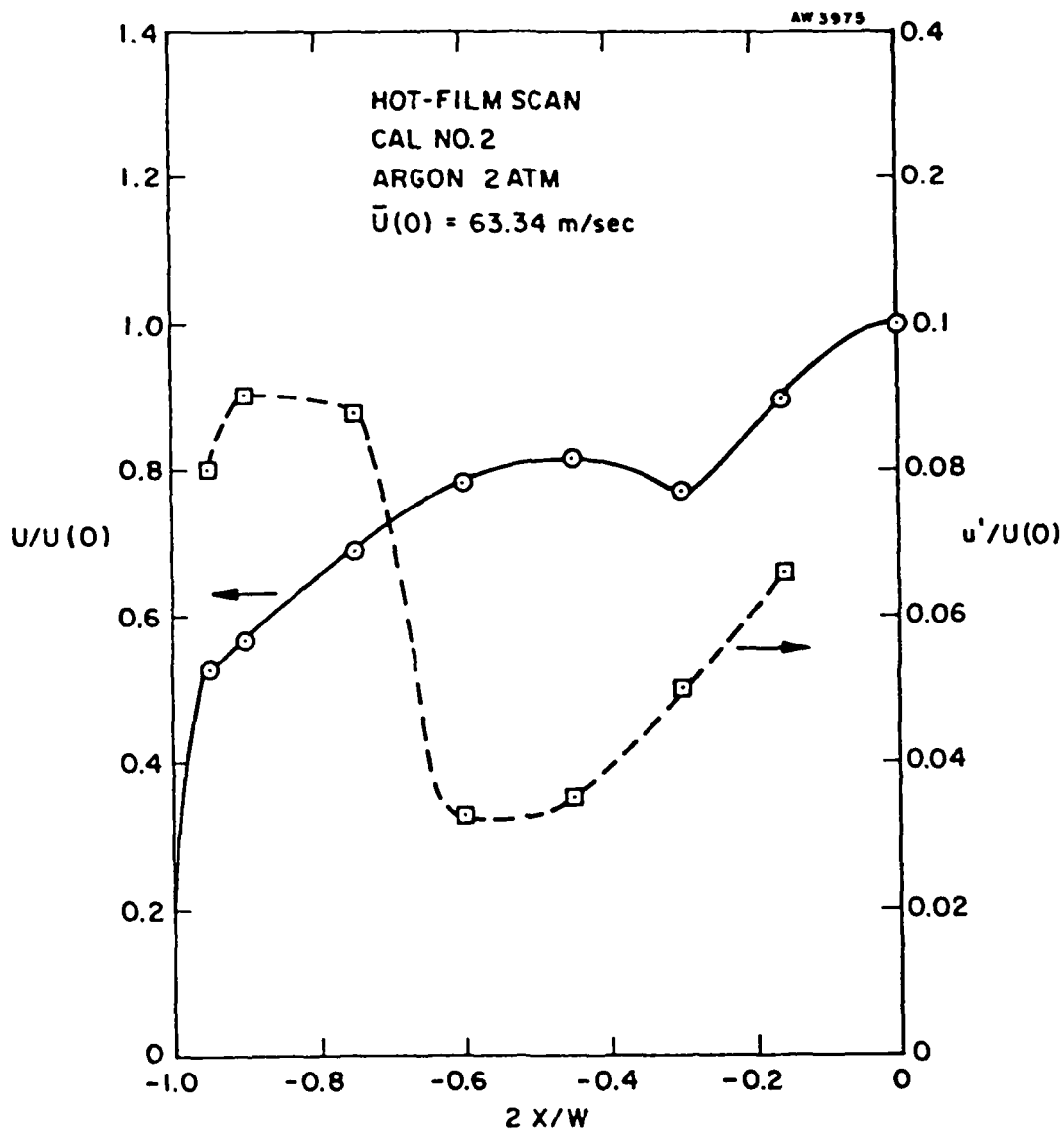
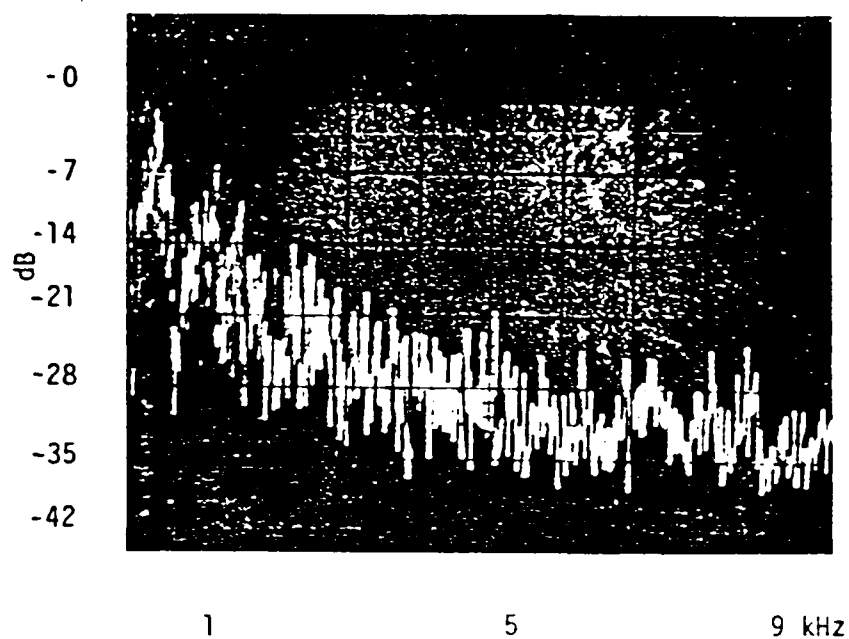
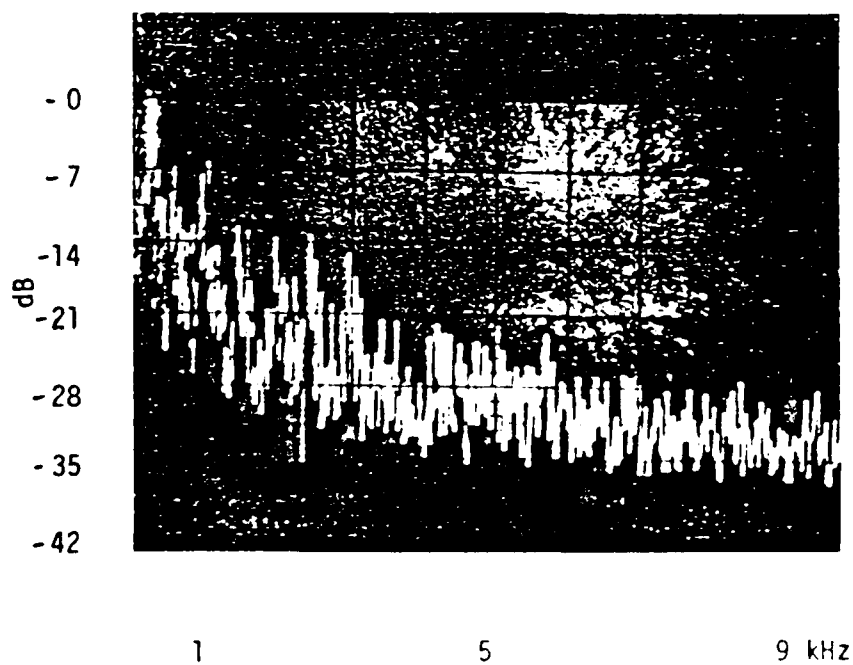


Figure 4. Hot-film scan.

6-25-81



RUN #2
B = 200 Hz
1 kHz/Div
5000 Hz CF
CH #1 Hot-film
FULL THROTTLE
2 ATM
EARLY TIME



RUN #8
FULL THROTTLE
LATE TIME

Figure 5. Velocity fluctuation spectra.

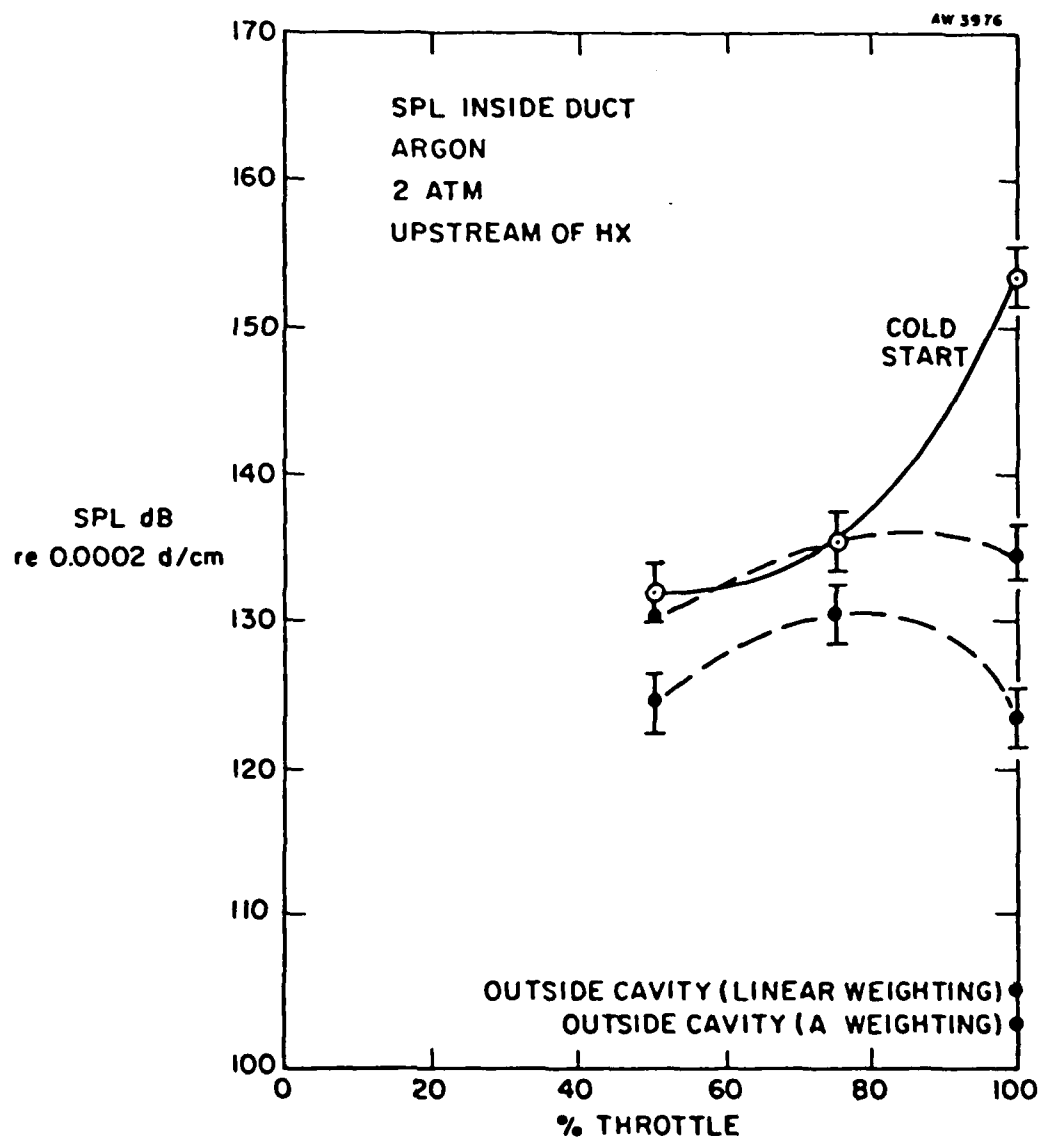
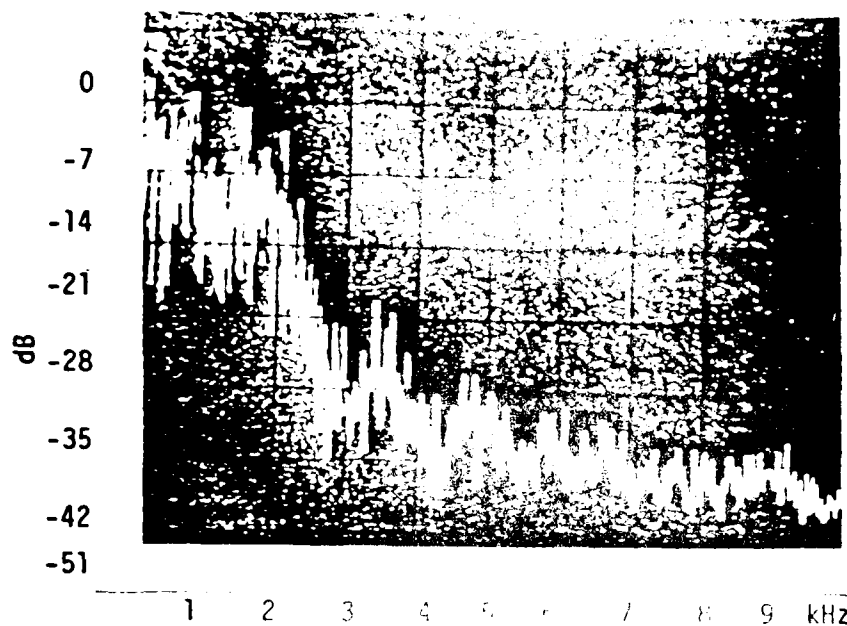


Figure 6. Duct sound pressure level.

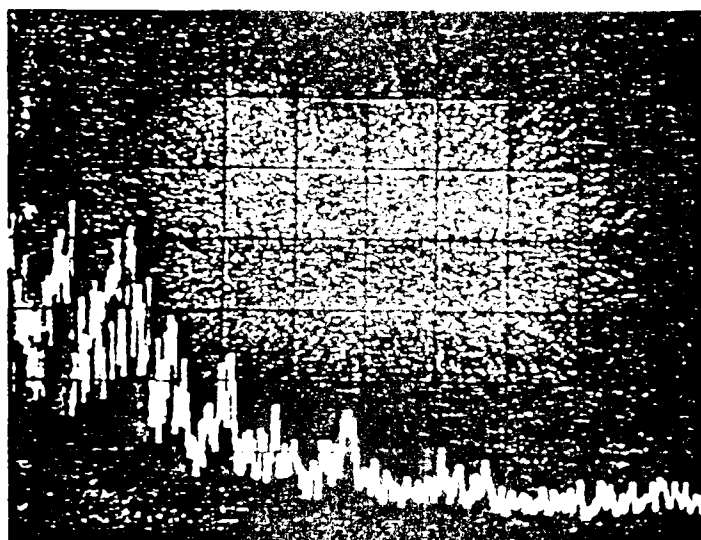


FULL THROTTLE

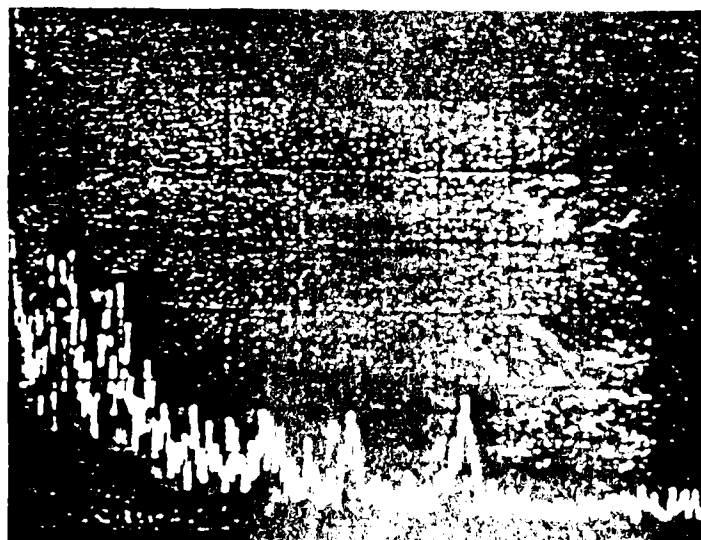
B = 200 Hz

RUN #2

EARLY TIME



RUN #6



RUN #8

LATE TIME

Figure 7. Flow duct acoustic spectra.

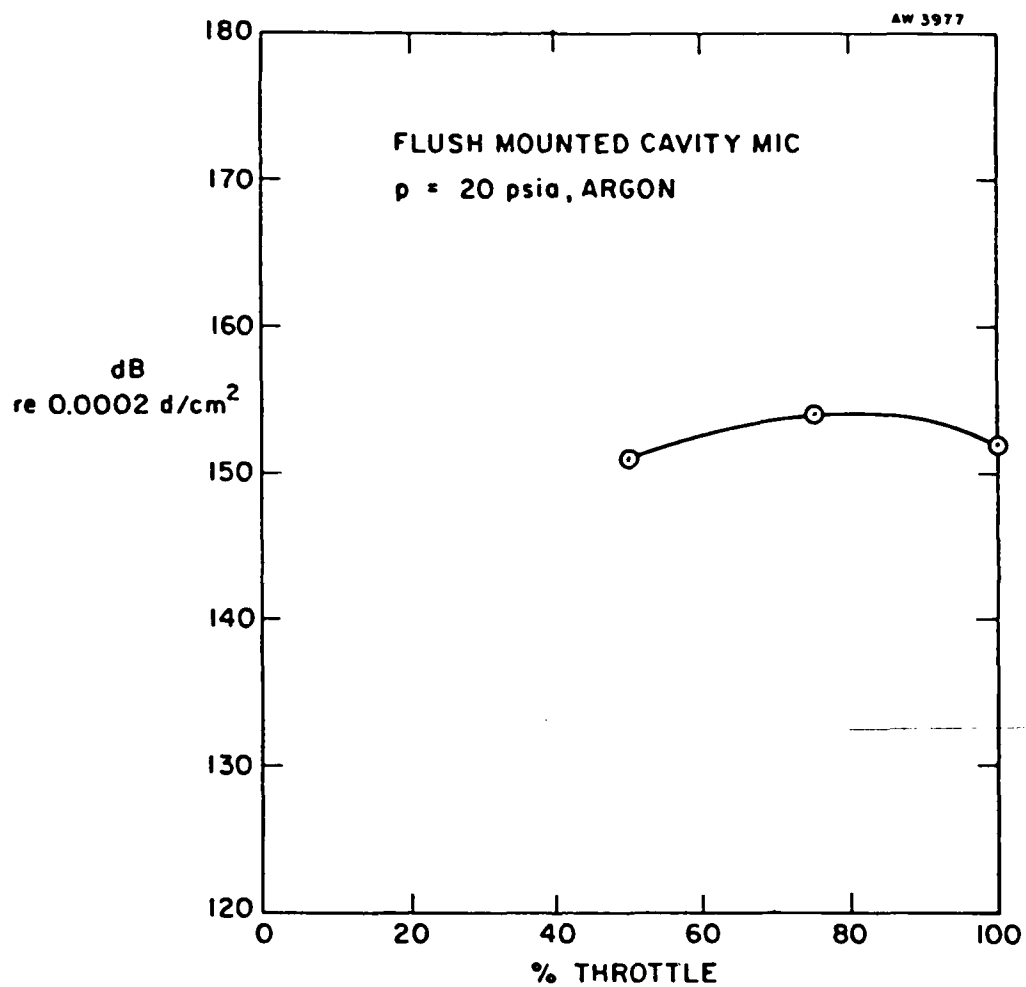


Figure 8. Flush-mounted cavity.

6-26-81

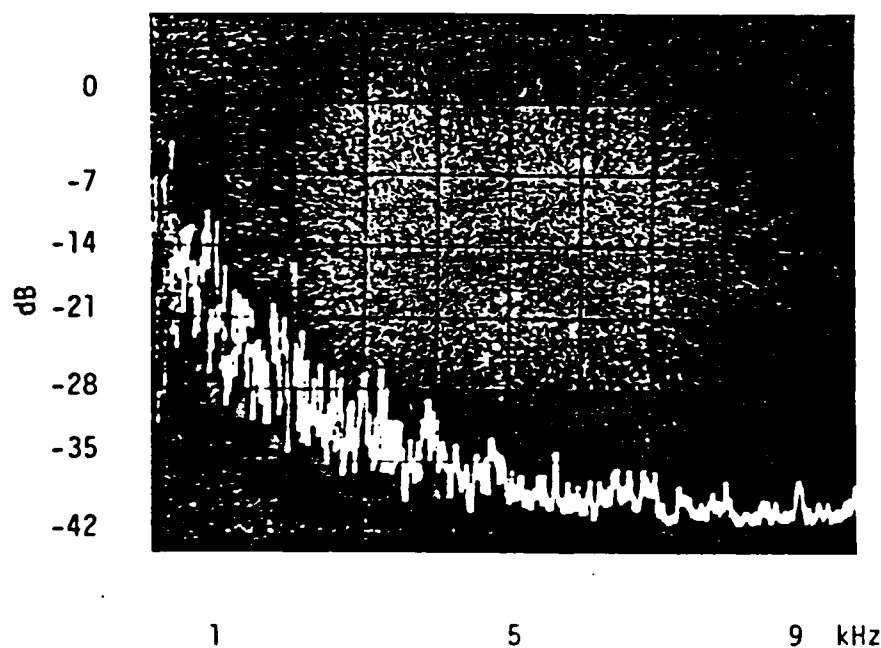
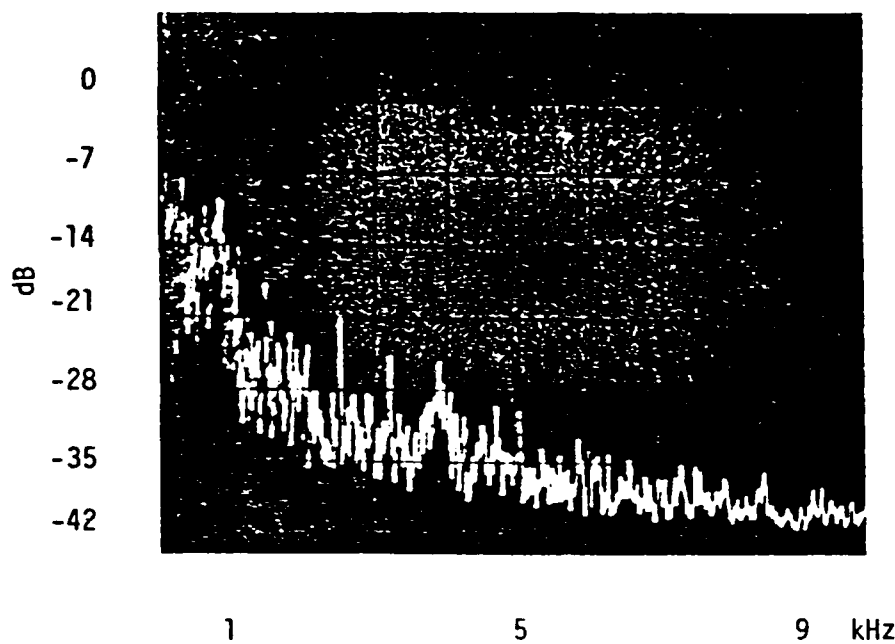


Figure 9. Flush-mounted cavity MIC spectra.

7-2-81

Run #22
Ch #1 5 μ Wire
200 Hz/Div
1 kHz CF
200 Hz/Div

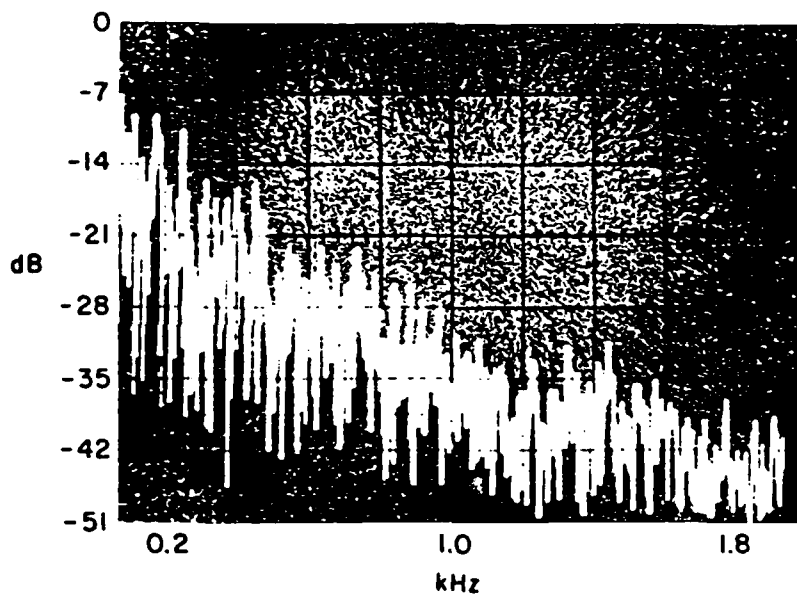


Figure 10. Temperature fluctuation spectra.

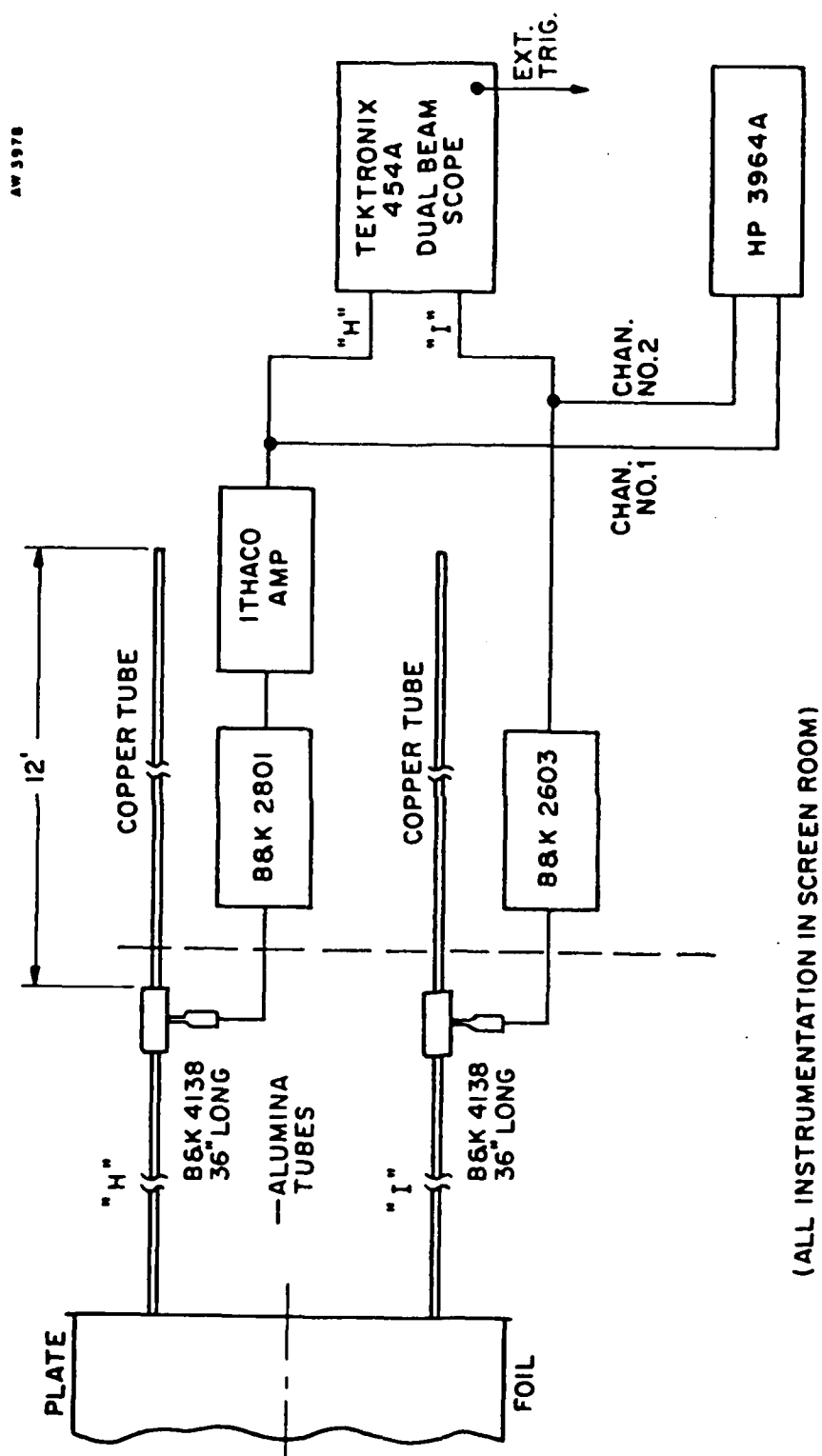
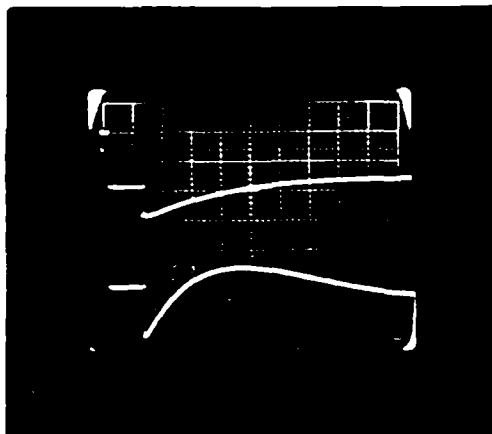
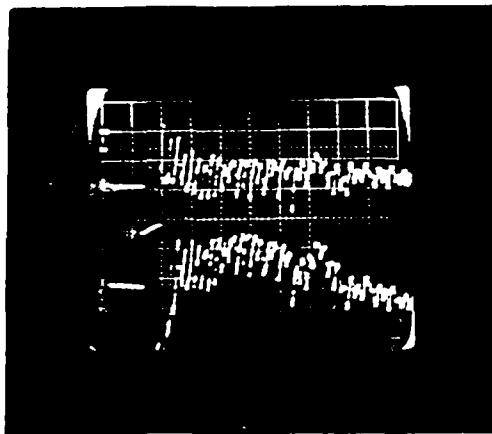


Figure 11. E-beam acoustics probe tube — microphone set-up.

7-1-81



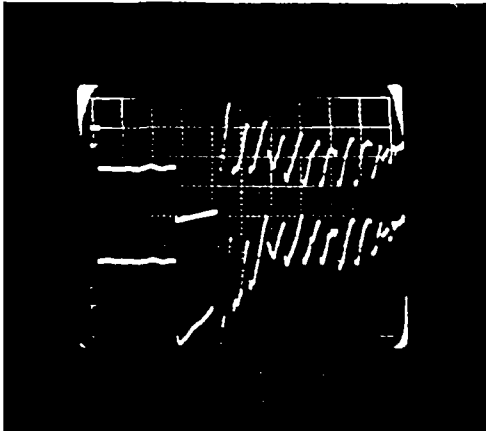
Run #18 EM Pulse Test
Probe tubes removed from cavity ports
Probe tubes sealed
5 v/cm, 5 ms/cm
Log 1205 - 1250
P = 14.7 psia Argon
Top trace: Ch "H"
BTM trace: Ch "I"
Real Time



Run #17 Real Time
E-beam 0.8 - 0.9 μ s pulse 5.3 ms
after SYNC
5 v/cm, 5 ms/cm
Log 1020 - 1065
Single shot, magnet on
Full throttle
P = 14.7 psia Argon
Top Trace: Ch "H" 1 vrms => 152 dB
BTM Trace: Ch "I" 1 vrms => 154 dB

Figure 12. EMP test and laser cavity acoustic signatures.

7-2-81



Run #19 Real Time

E-beam 0.8 - 0.9 μ s pulses

Rep-rate: 14.28 pps

5 v/cm, 2 ms/cm

Multiple shot, magnet on

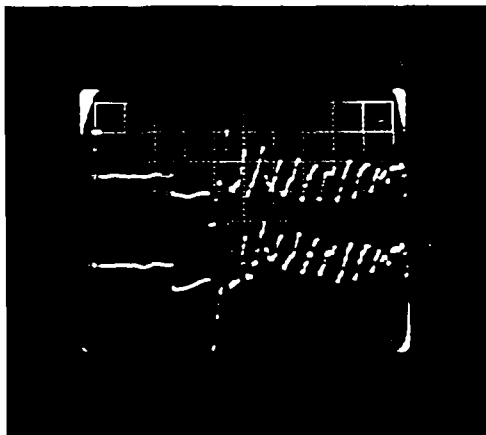
Full throttle

Top trace: Ch "H" 0.99 vrms \Rightarrow 154 dB
re 0.0002 d/cm²

BTM trace: Ch "I" 1.02 vrms \Rightarrow 154 dB

Log 1250 - 1305

P = 14.93 psia Argon



Run #20 Real Time

E-beam 0.8 - 0.9 μ s pulses

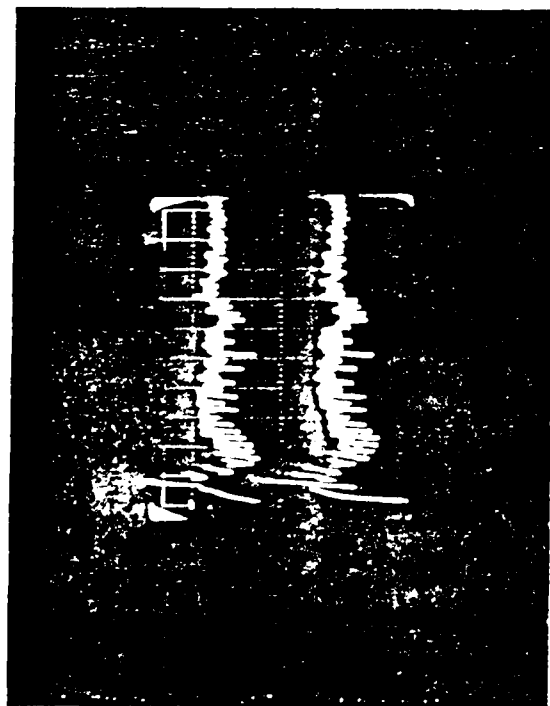
Aborted run: Inductor flashover

E-beam low

5 v/cm. 5 ms/cm

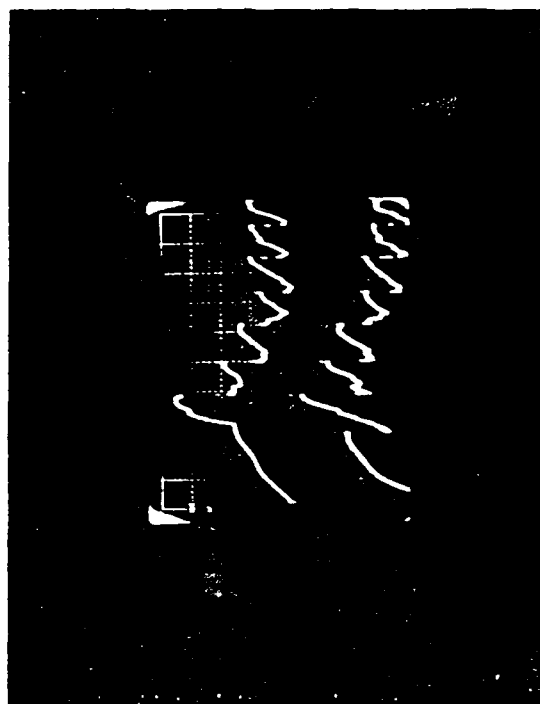
magnet on

Figure 13. Laser cavity acoustic signatures.



1 v/cm, 2 ms/cm

RUN #17 PLAY BACK
 E-BEAM 0.8 - 0.9 μ s PULSE
 1 v/cm, 5 ms/cm
 LOG 1020 - 1065
 SINGLE SHOT, MAGNET ON
 FULL THROTTLE
 P = 14.7 psia ARGON
 TOP TRACE: CH "H"
 BTM TRACE: CH "I"
 RINGING FREQUENCY: 889 Hz



1 v/cm, 1 ms/cm

Figure 14. Laser cavity acoustic signatures.

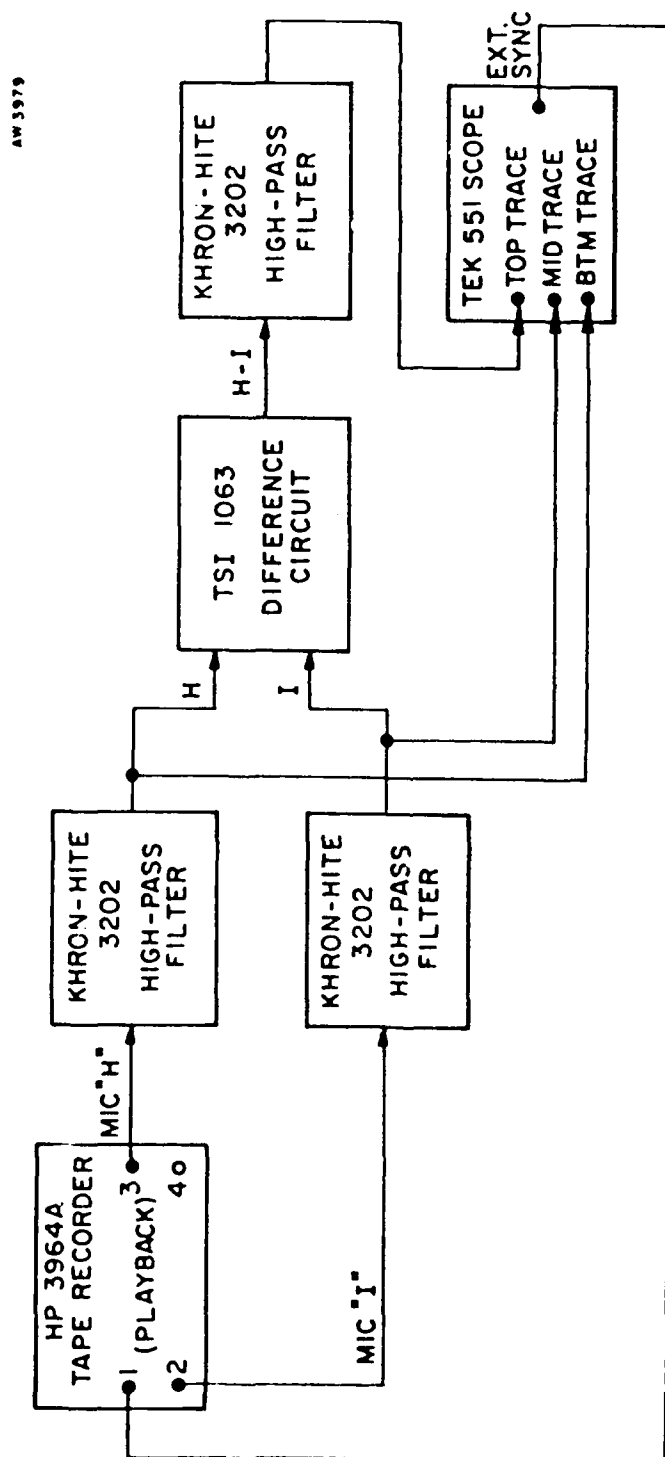
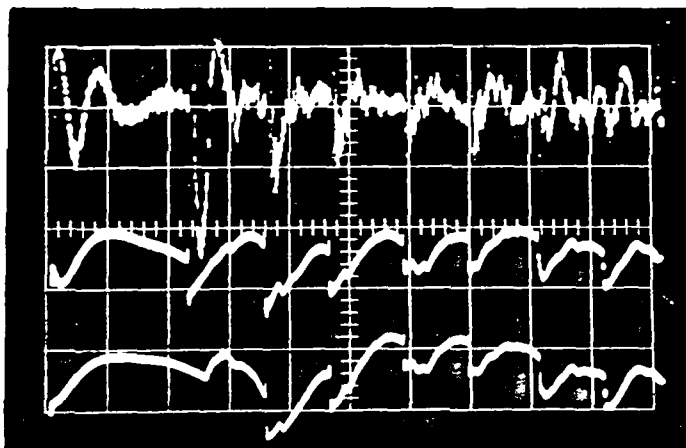


Figure 15. Transverse wave analysis set-up.

7-1-81

Run #16



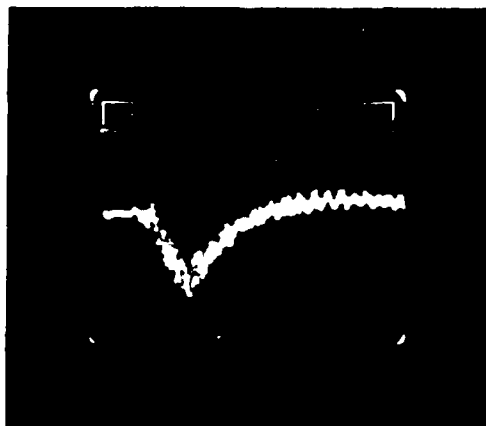
Top trace: 0.2 v/cm; 1 ms/cm
Channel "H" - Channel "I"
 $f > 1 \text{ kHz}$

Mid trace: 2 v/cm; 1 ms/cm
Channel "H"
 $f > 150 \text{ Hz}$

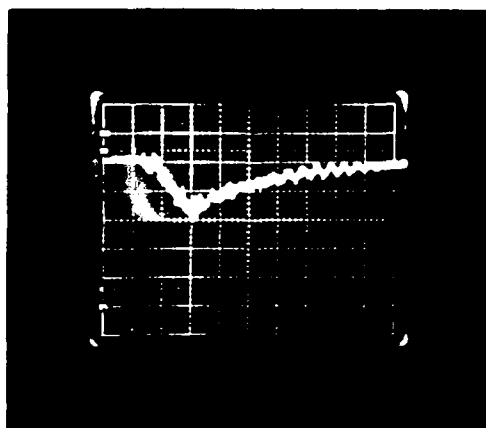
BTM trace: 2 v/cm; 1 ms/cm
Channel "I"
 $f > 150 \text{ Hz}$

Figure 16. Subtraction of probe-tube microphone channels "H" and "I".

7-1-81



Test #5
AC coupled
1 v/cm, 5 ms/cm
 $\bar{V} = 14.5$ v (No flow, $B = 0$)
Log 415 - 460
Full throttle
Magnet on ($B \neq 0$)
Single shot
 $P = 14.7$ psia, Argon



Run #6
DC coupled
2 v/cm, 5 ms/cm
 $V = 14.1$ v (No flow, $B = 0$)
Log 460 - 503
Full throttle
 $B \neq 0$
Single shot
 $P = 14.7$ psia, Argon

Note: The signal is a noisy pulse.

big temperature signatures.

Table 1. Cavity Temperature Fluctuations.

7-2-81

THROTTLE: FULL OPEN

P \approx 2 ATM; ARGON

PROBE POSITION: 2X/W = -0.6

RUN #21	$\bar{T} = 322.8^{\circ}\text{K}$	$t_{\text{rms}} = 0.31^{\circ}\text{K}$	$t_{\text{rms}}/\bar{T} = 9.6 \times 10^{-4}$
RUN #22	$\bar{T} = 325.8^{\circ}\text{K}$	$t_{\text{rms}} = 0.38^{\circ}\text{K}$	$t_{\text{rms}}/\bar{T} = 1.17 \times 10^{-3}$

Table 2. Thermal Slug Temperature Rise

DATA: 1 July 1981

THROTTLE: FULL OPEN

$U(0) \approx 6300$ cm/sec

SINGLE SHOT; 13.2 KA, 0.8 μ s e-beam pulse

ARGON GAS AT 14.7 psia

<u>RUN</u>	<u>P psia</u>	<u>PEAK $\Delta T^{\circ}C$</u>	<u>AVE $\Delta T^{\circ}C$</u>
5	14.7	11.2	8.8
6	14.7	16.0	12.0
10	14.7	17.6	15.2
16	14.7	16.0	13.6
17	14.7	12.8	10.4

Poseidon Research Memo No. 149

FLOWING RAMAN CELL EXPERIMENT DESIGN --
A TRADEOFF STUDY

December 1981

Table of Contents

1.	Introduction.....	1
2.	Conceptual Design.....	6
3.	Beam Quality and Medium Homogeneity.....	12
4.	Design Issues and Tradeoff Study.....	17
	4.1 Acoustics.....	17
	4.2 Baseline Flow.....	25
5.	Summary.....	28

To: Hiroshi Ehereni/Northrop

From: John Lewis

Date: December 1981

Subject: Flowing Raman Cell Experiment Design -- A Tradeoff Study

1. Introduction

The Northrop Raman cell experiment design, as schematically illustrated in figure 1, consists of two laser beams: one an amplifier beam and the other an oscillator beam. The amplifier beam has a nominally constant cross-sectional area of $A_{amp} = 2 \text{ cm}^2$ and a total thermal deposition of $Q_{amp} = 3 \text{ Joules/pulse}$. For the amplifier beam, the heat is deposited approximately uniformly along two-thirds of the length of the optical path, L_o . The oscillator beam is highly focused, with the initial cross-sectional area of 1 cm^2 becoming $A_{osc} = 1.7 \times 10^{-3} \text{ cm}^2$ in the region of thermal deposition. The heat that is deposited in the oscillator beam $Q_{osc} = 1/3 \text{ Joule/pulse}$ is deposited uniformly over a length of 1 m near the center of the cell. The baseline design calls for a repetition rate of 25 Hz and pure hydrogen as the operating gas within the cell.

An important design issue is the selection of the operating pressure, p_o , and the length of the optical path, L_o . Experiments at Northrop have demonstrated an optimum optical efficiency at $p_o = 6 \text{ atm}$ and $L_o = 8 \text{ m}$. Analysis shows that a similar efficiency can be maintained provided that the pressure and length of the optical path obey the formula

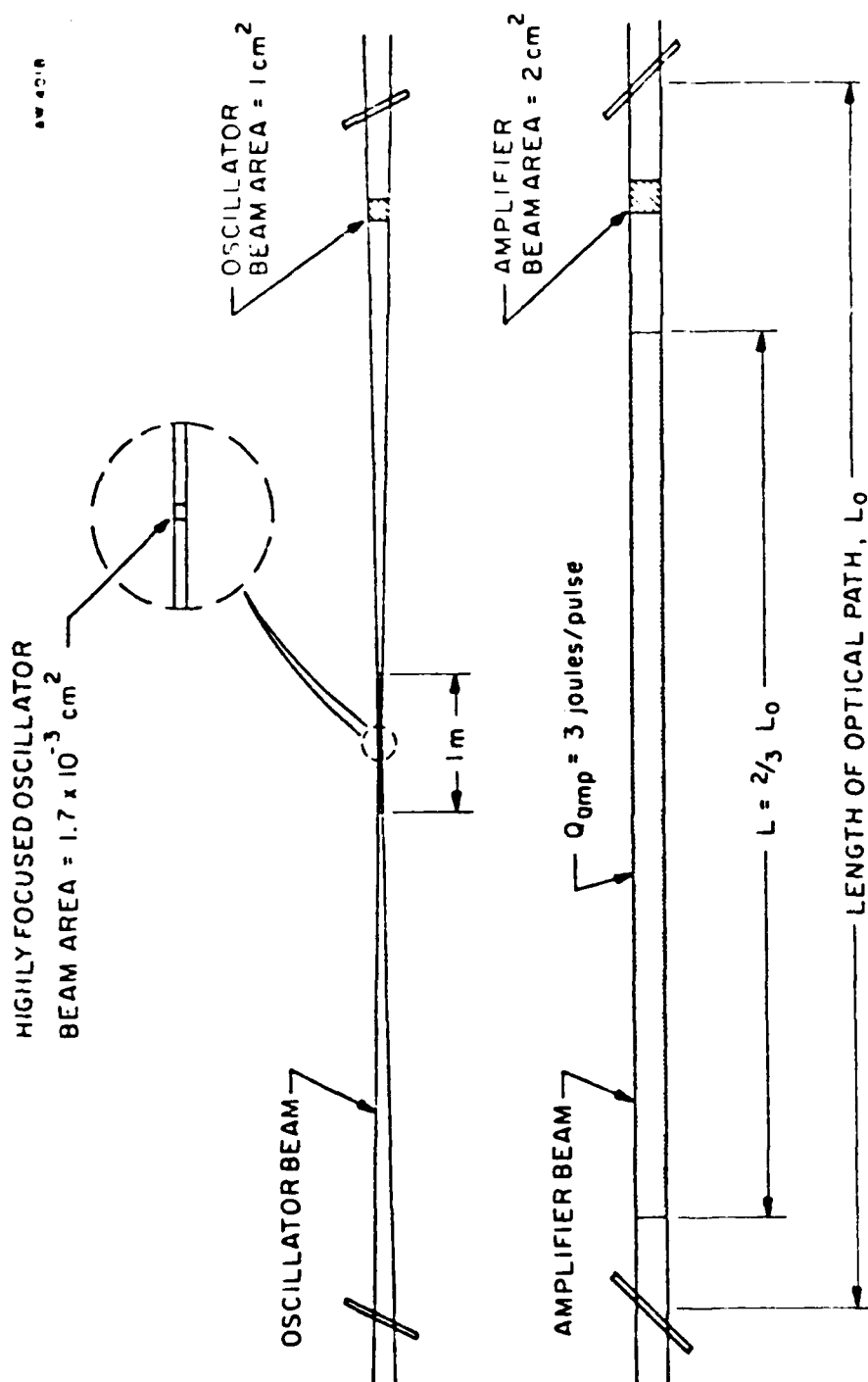


Figure 1. Schematic illustration of Northrop Raman cell design.

$$\frac{L_o}{L_{ref}} = 6.896 \left[1 + \left(\frac{P_{ref}}{P} \right)^2 \right], \quad (1)$$

where $P_{ref} = 2.4$ atm and $L_{ref} = 1$ m. A table of length versus pressure is listed below and shown in figure 2.

Table 1

$P_o = 1$ atm	$L_o = 46.6$ atm
2	16.8
3	11.3
4	9.4
5	8.5
6	8.0
8	7.5
10	7.3
∞	6.9

At pressures less than 2-3 atm, the length of the cell increases dramatically. This presents practical problems regarding laboratory space not to mention cost. For pressures greater than 6-8 atm, no significant reduction in length is achieved, and clearly cost will increase with increasing pressure. Even with these practical limitations, the design range of pressure is large, and the question is what additional technical issues can influence the final selection of the operating pressure and the length of the optical path. One obvious issue, beam quality, is the subject of this study.

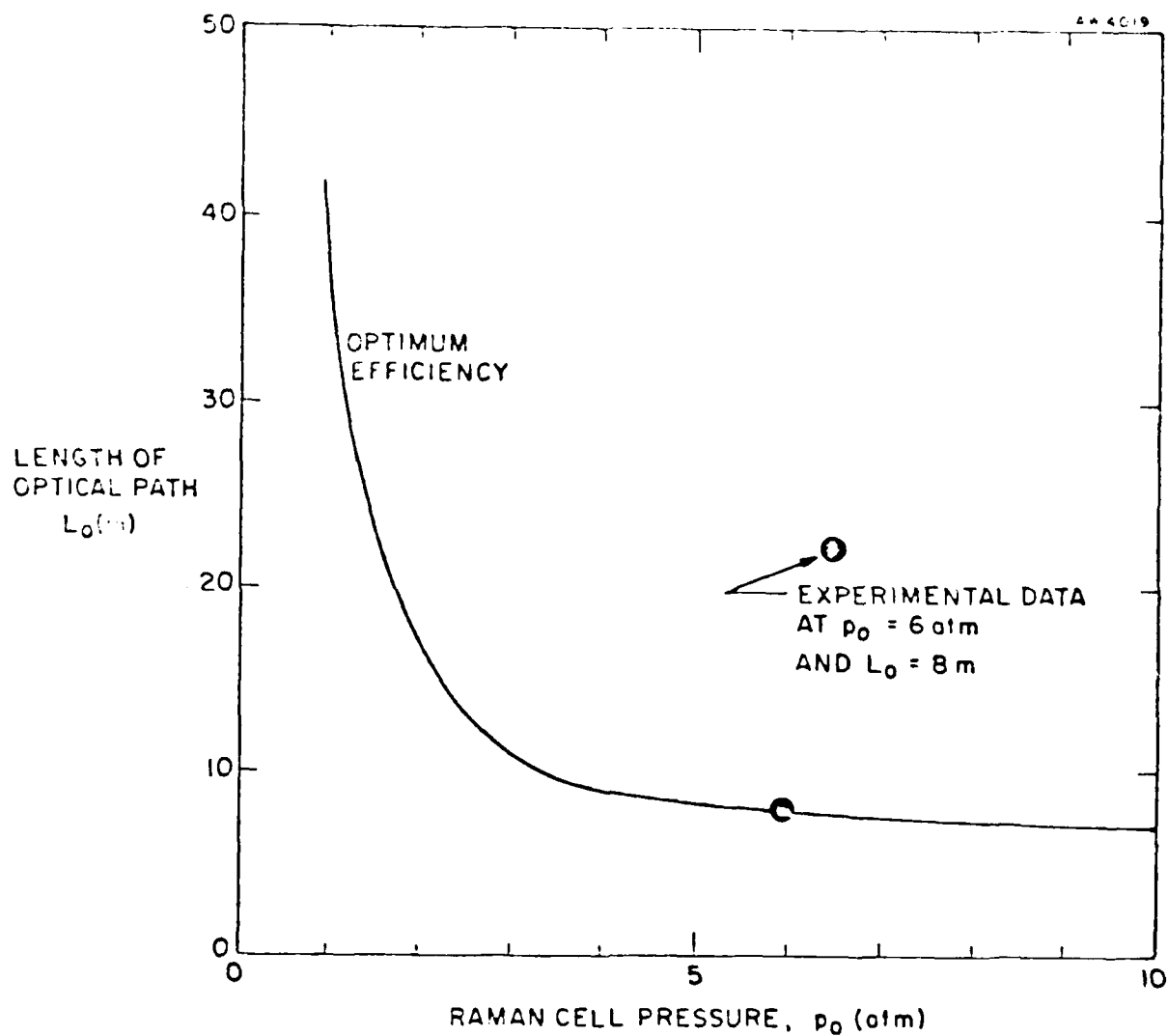


Figure 2. Northrop prediction of optimum design.

The purpose of this study is to select the optimum design subject to the above design constraints and using beam quality as a criterion. The approach is to begin with a conceptual design that has all of its essential features well enough defined to allow for a reasonable estimate of density homogeneity and thus beam quality. Next the operating pressure and the length of the optical path are varied in accordance with Northrop specifications, and an optimum design point selected based on beam quality. The conceptual design is presented in Section 2.

In Section 3, formulae for predicting the beam quality and estimates of required density homogeneity are presented. The controlling design issues are discussed in Section 4, including a careful analysis of acoustic efficiency that interestingly shows that the oscillator dominates the acoustic wave generation. Finally, the study is summarized in Section 5.

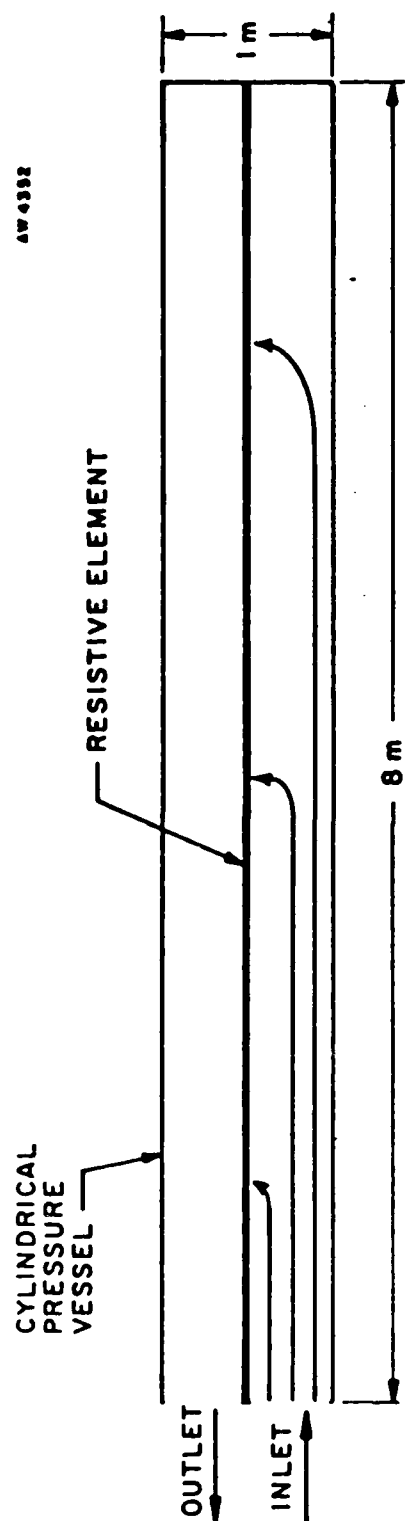


Figure 3. Flow design schematic.

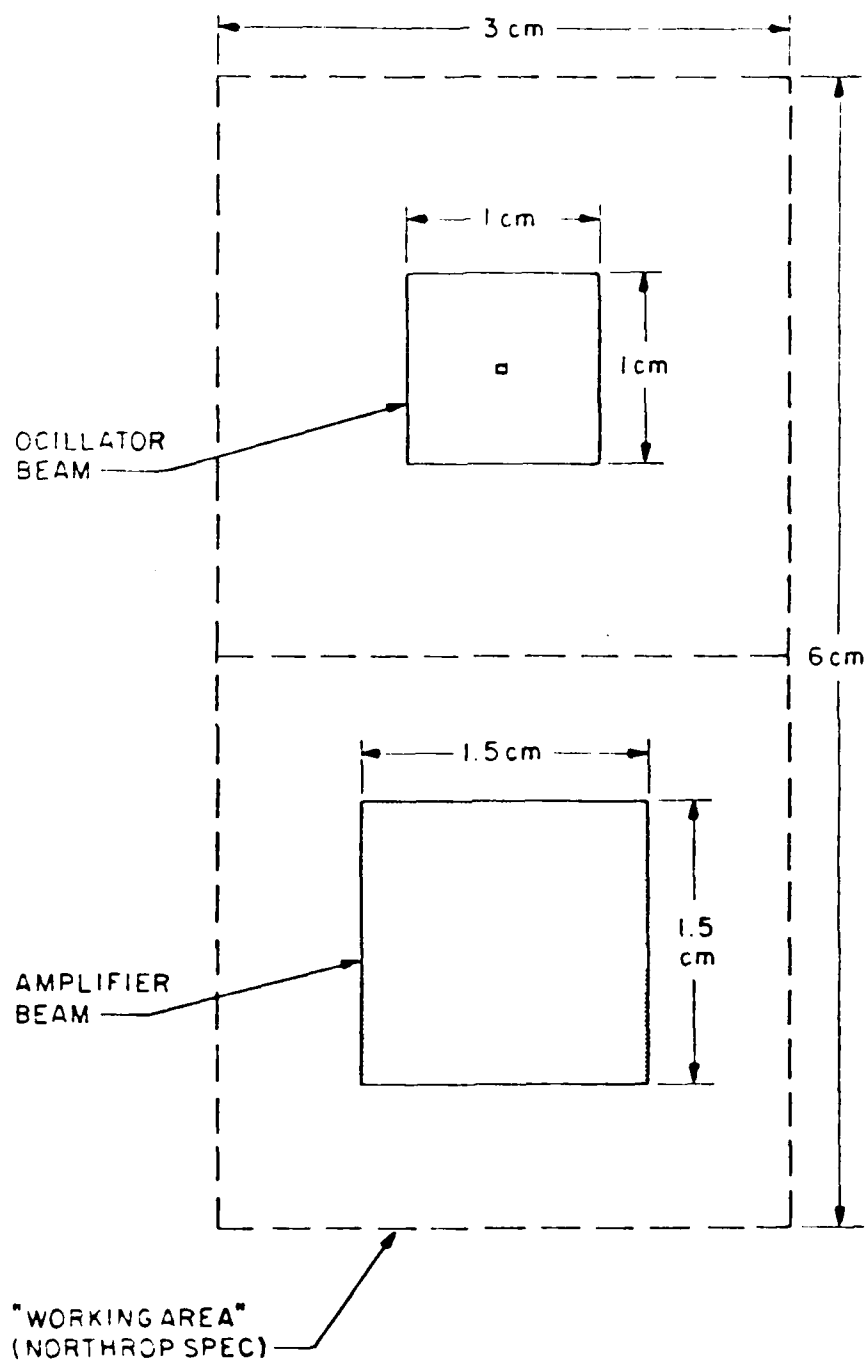


Figure 3. Cross section of laser beam cavity.

Clearly adiabatic turbulent fluctuations and acoustic attenuation should present no design difficulties.

Temperature fluctuations are a potentially important issue, and as we know from the work on the NeCL blue-green laser (see Poseidon Research Proposal No. 8112), the mufflers are a potential source of such disturbances. The design concept, as with the NeCL blue-green laser, is to cool the mufflers by forced convection as illustrated in figure 4. Since we need a strong pressure loss between the plenums in order to achieve flow uniformity along the very long optical path, the flow through the mufflers serves two purposes.

The complete conceptual design of the flowing Raman cell is illustrated in figure 5. It consists of a number of key elements that are described below. First, there is an upstream plenum. Its cross-sectional area will be chosen to be large enough to allow it to act largely as a settling chamber. Downstream (actually the direction is up so that natural convection is in the same direction as the forced flow) lies the laser cavity. It is surrounded by a muffler that is constructed of perforated walls and lined with an acoustic dissipative material, probably Pyral. Gas flows from the upstream plenum through the cavity, flushing out thermal pulses and also through the muffler packing material and thereby cooling it by forced convection as described earlier. A fan (which could be replaced by a centrifugal pump in the final design) serves to pull the gas from out of the downstream plenum and force it through a heat exchanger that must remove the total energy deposited by the laser beams.

Finally, the gas flows through a return duct back into the inlet of the upstream plenum. The fan and heat exchanger have been deliberately placed as far upstream of the cavity as possible in order to allow the maximum time for turbulent mixing of large scale temperature perturbations caused by the heat exchanger.

AW 4017

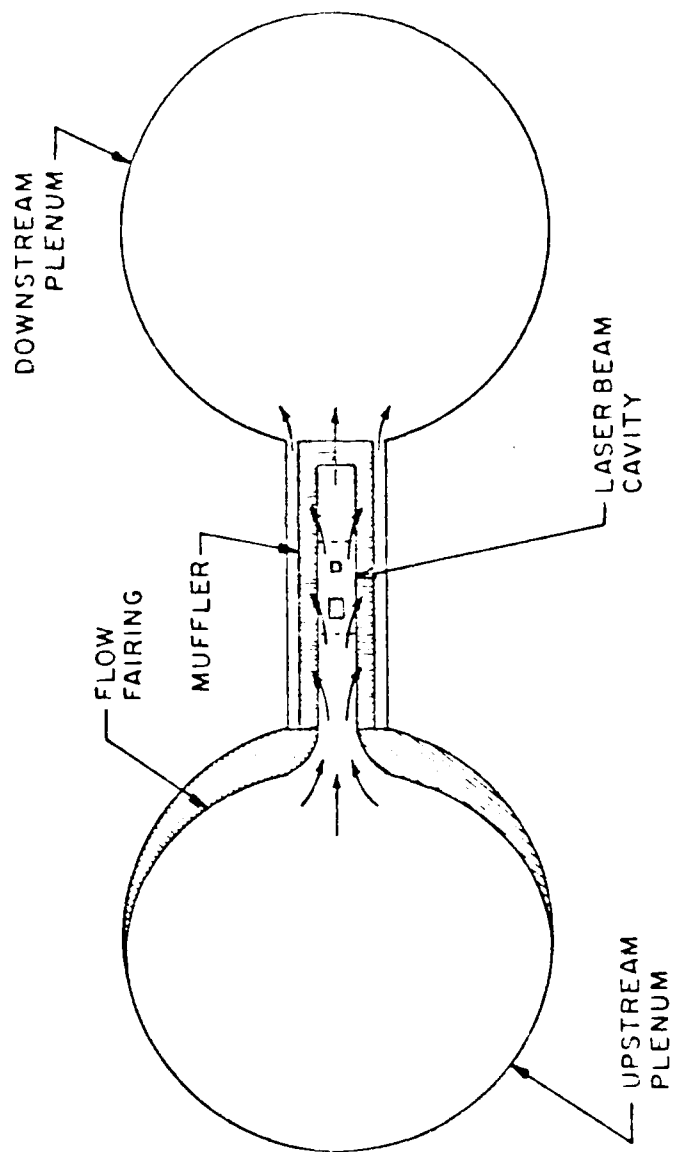
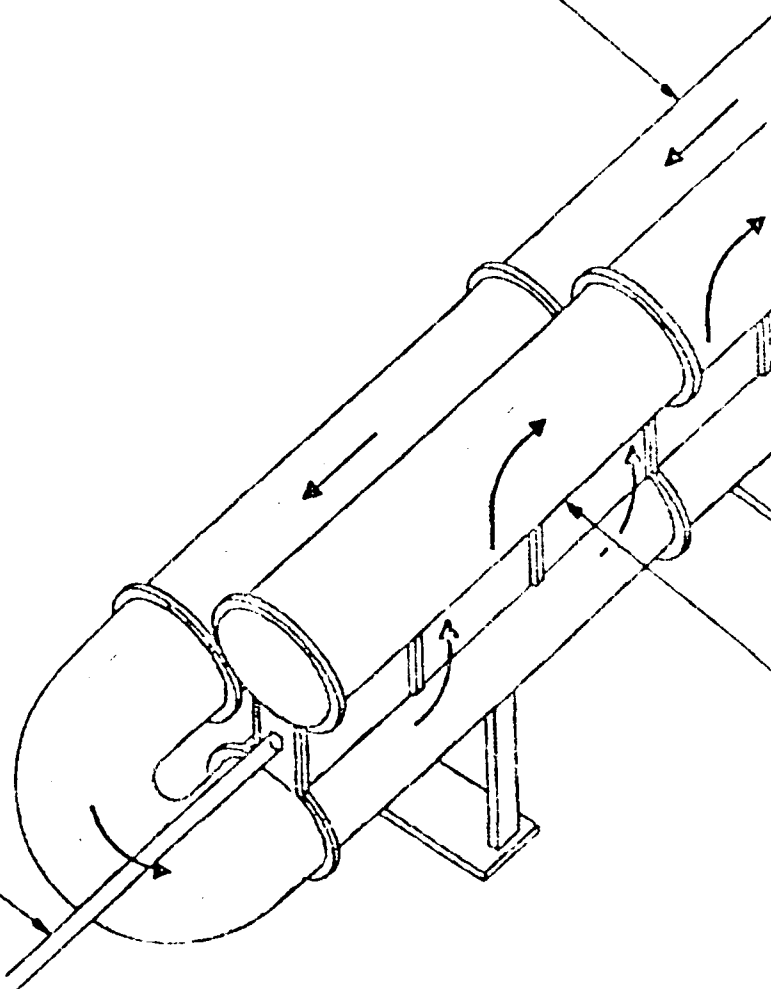


Figure 4. Cross section of muffler with illustration of flow system.

FLOW

RETURN DUCT

LASER BEAM



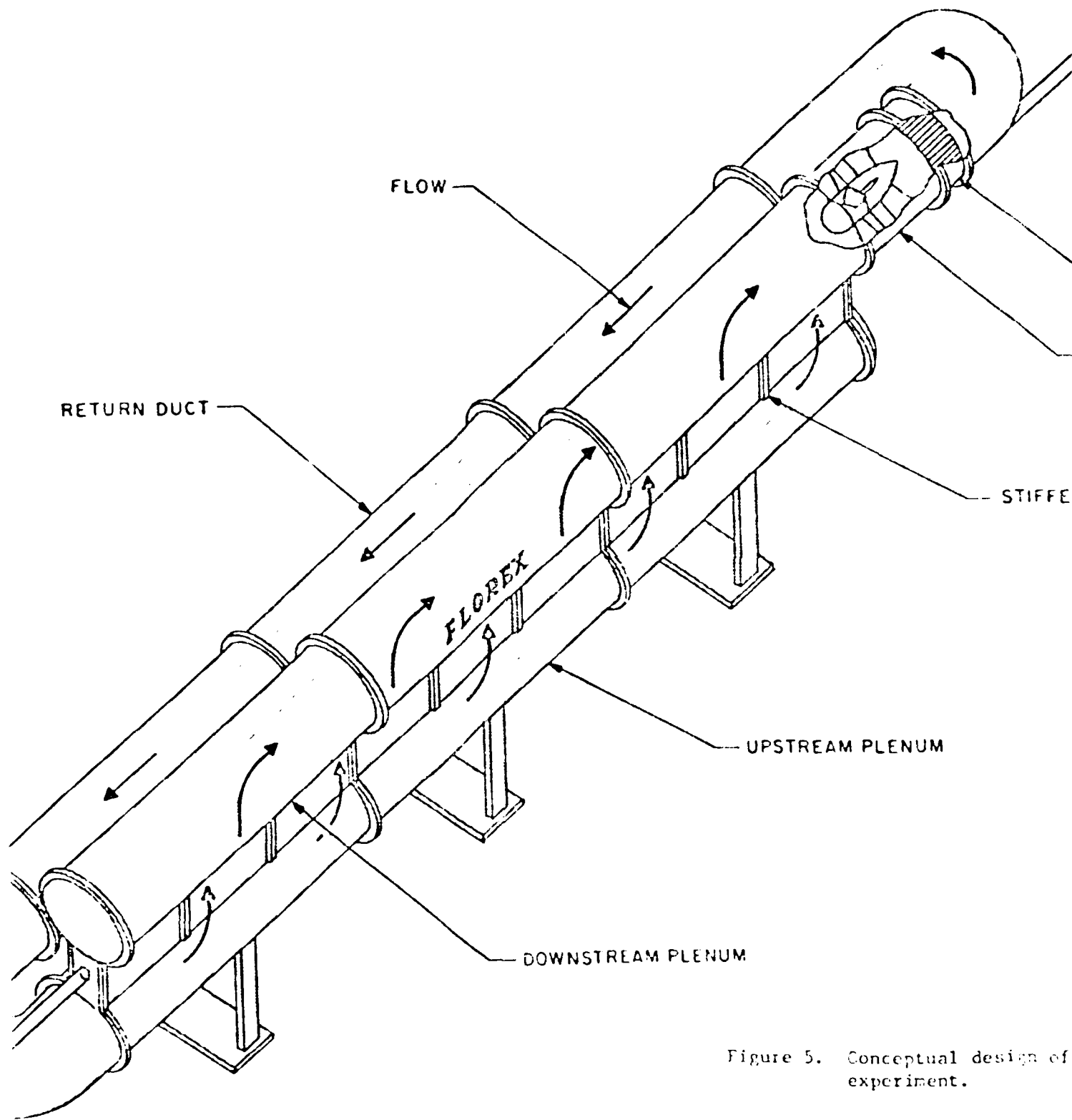


Figure 5. Conceptual design of experiment.

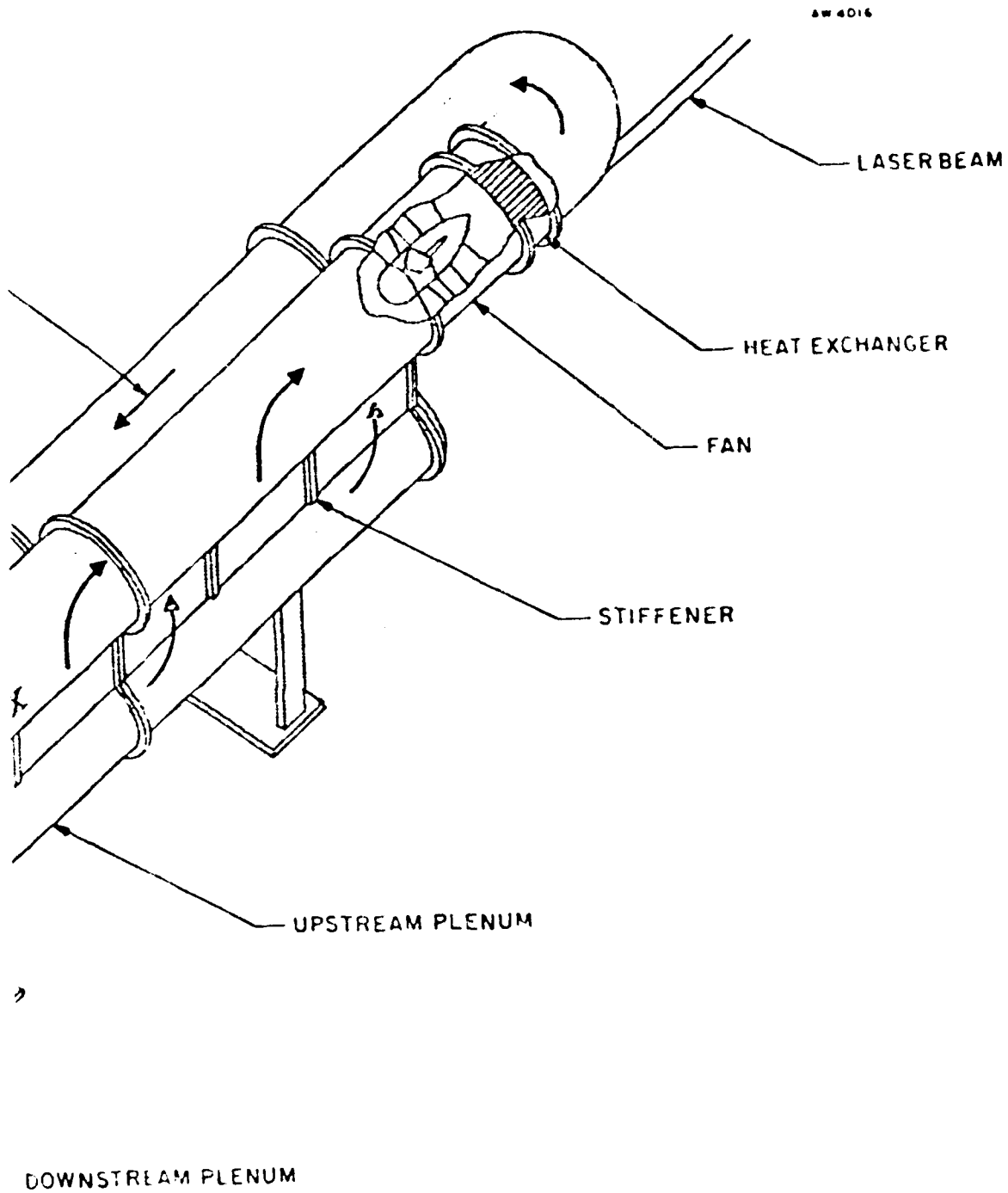


Figure 5. Conceptual design of DARPA/Northrop flowing Raman cell experiment.

These first two sections have served to introduce the problem and a conceptual design that can produce the required flow and acoustic control. In the following sections, we shall deal with the relevant design issues quantitatively, beginning in Section 3 with beam quality.

3. Beam Quality and Medium Homogeneity

A standard measure of beam quality is the far field intensity I , which depends on phase distortion ϕ at the output window according to the formula

$$\frac{I}{I_0} = \left| \frac{1}{A} \int e^{i\phi} dA \right|^2 \quad (2)$$

where I_0 refers to a diffraction limited beam and A is the cross-sectional area of the beam. For small phase variations,

$$\frac{I}{I_0} = 1 - \phi_{rms}^2 \quad (3)$$

and the divergence of the beam or "beam quality" BQ can be written as

$$BQ = \sqrt{\frac{I_0}{I}} = 1 + \frac{\phi_{rms}^2}{2} + \dots \quad (4)$$

This formula is not appropriate for large phase variations, and, as shown in Poseidon Research Proposal No. 8112, for $\phi_{rms} \gtrsim 1$,

$$BQ = 2 \phi_{rms} \quad (5)$$

These limits are shown in figure 6, with an educated guess at how they might merge.

Phase distortion is caused by variations of the index-of-refraction, which in turn is related to density perturbations according to the formula

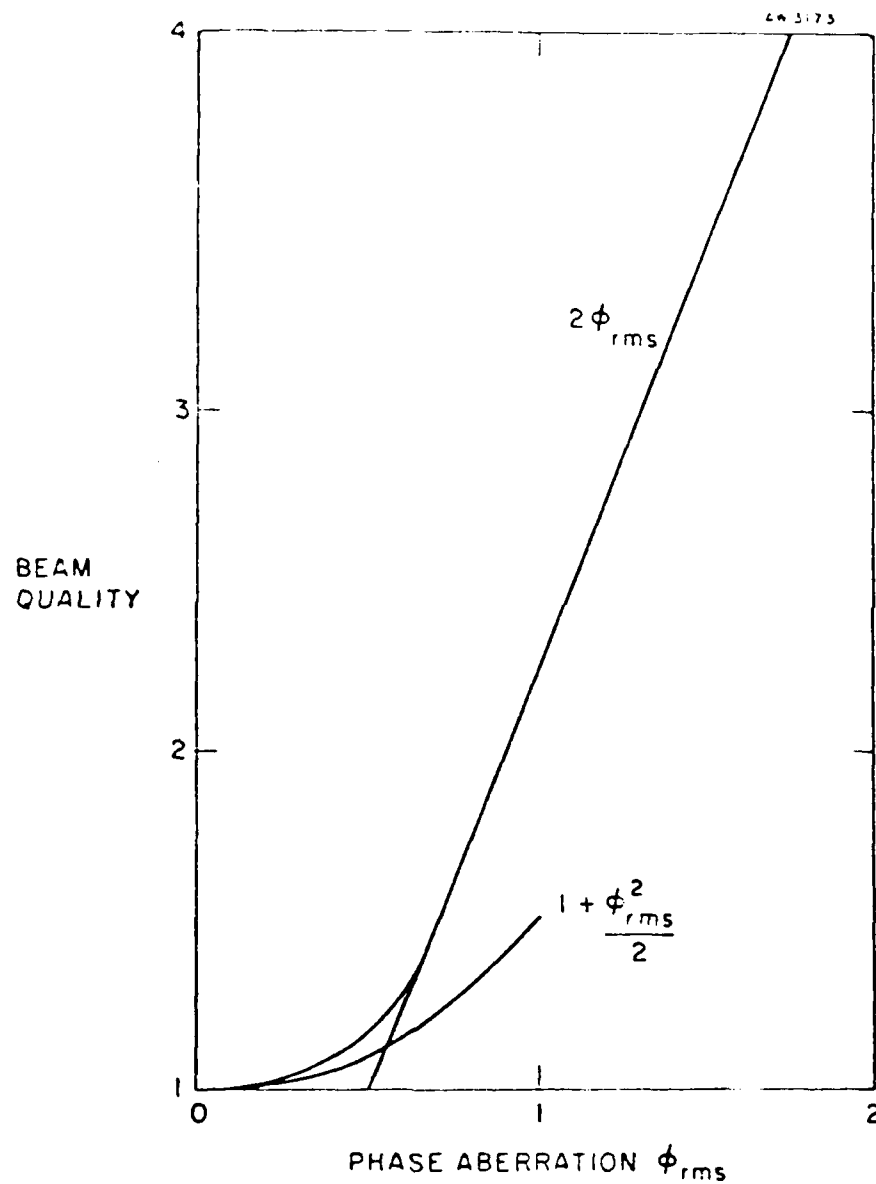


Figure 6. Beam quality dependence on phase aberration.

$$\phi_{\text{rms}} = 2\pi N \frac{L_o}{\lambda} \beta \frac{\rho_o}{\rho_s} \left(\frac{\rho'}{\rho_o} \right)_{\text{rms}} . \quad (6)$$

N is the number of passes through the cell, which for the Northrop design is 2, consisting of the oscillator beam and the amplifier beam each of which is subject to distortion. β is the Gladstone-Dale constant taken to be 1.45×10^{-4} for a wavelength λ of 353 nm. ρ_o/ρ_s is the ratio of the density to the density at standard temperature and pressure and hence is essentially the pressure p_o in atmospheres.

Clearly the density perturbation $(\rho'/\rho_o)_{\text{rms}}$ will in general depend on the pressure if not the length of the cell, and we shall quantify this dependence in the following section. Regardless it is interesting to evaluate the various density homogeneity requirements as a function of beam quality for a range of pressures and optical lengths satisfying the specification of equation (2).

These results are presented in figure 7 for both ordered acoustic disturbances and random turbulent disturbances. The allowable random density disturbances are predicted to be larger than the ordered disturbances by $\sqrt{n_e}$, where n_e is the number of eddies along the optical path and,

$$n_e = \frac{L_o}{h} , \quad (7)$$

where h is the height of the cavity.

For good beam quality, the requirement for ordered acoustic disturbances is $(\rho'/\rho_o)_{\text{rms}} \sim 10^{-6}$, considerably more restrictive than previous laser designs. Fortunately, as we will see in the following

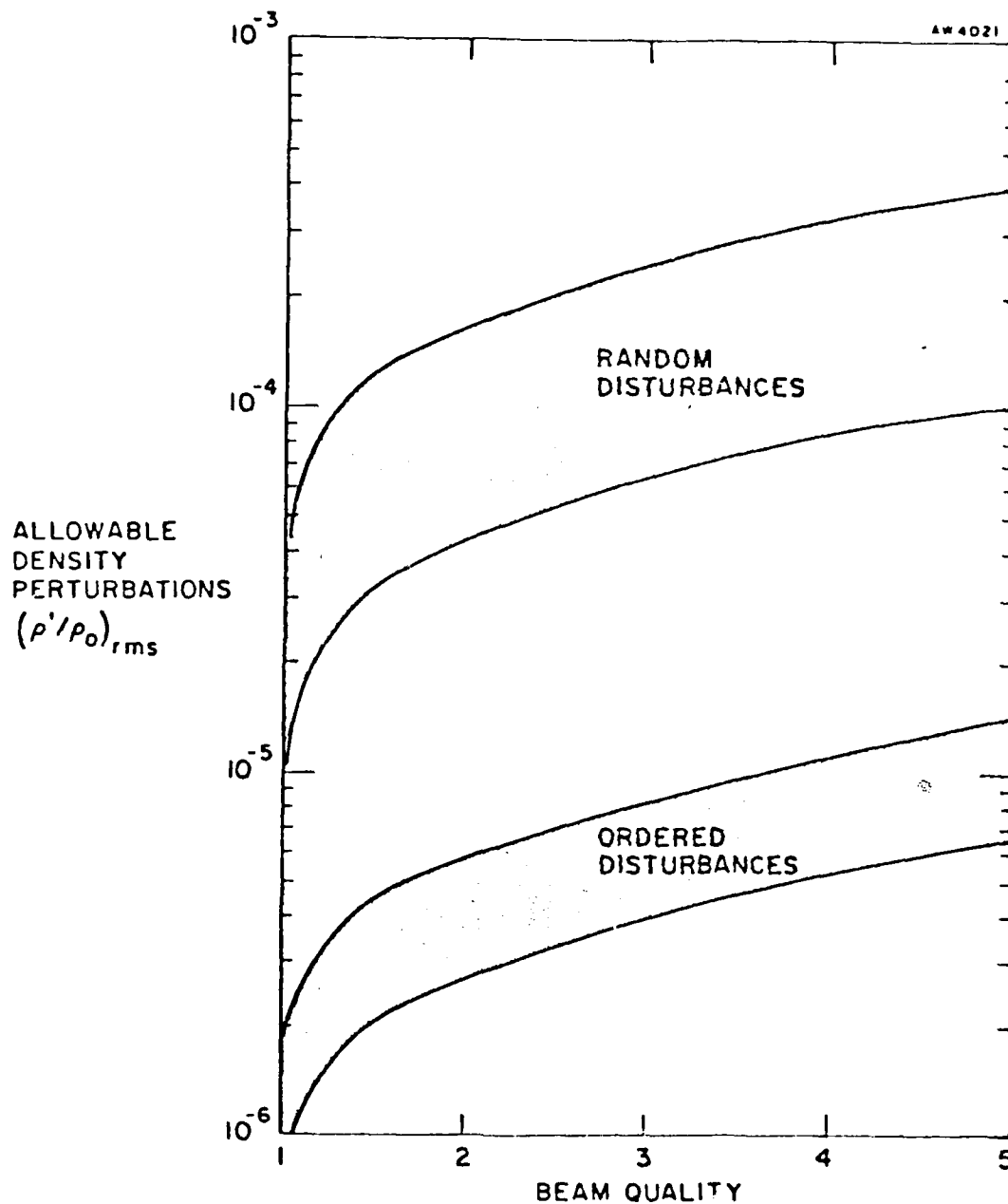


Figure 7. Range of allowable density perturbations as a function of beam quality for Northrop Raman cell design.

section, the amount of energy in acoustic disturbances is equally reduced and no serious design problem is encountered.

The much longer optical path and the accompanying large number of random eddies along it make the requirement for random turbulent disturbances much less restrictive, and $(\rho'/\rho_o)_{rms} \gtrsim 10^{-5}$.

The range of values shown in figure 7 represent a range of operating pressures for $p_o = 1$ atm to 10 atm, yet typical variability of allowable density perturbations for a given beam quality rarely exceeds a factor of 2, our first hint that the beam quality criterion may prove to be a soft design constraint.

4. Design Issues and Tradeoff Study

In this section, we address the controlling design issues beginning with a careful estimate of acoustic efficiency.

4.1 Acoustics

The physical problem that we wish to analyze is as follows. Heat is deposited into a fixed volume causing the temperature and pressure to increase. The heated volume then relaxes back to its original pressure, with a loss of energy equal to the work done. As it expands, acoustic waves are produced and energy propagates into the surroundings.

The initial rise in temperature is related to the heat addition as follows:

$$\rho_o V_o c_v (T_i - T_o) = Q \quad (8)$$

where ρ_o is the initial density, V_o is the initial volume, c_v is the specific heat at constant volume, T_i is the temperature after the heat is added, T_o is the initial temperature, and Q is the heat that is deposited in the gas. Introducing the initial pressure p_o , and solving for the temperature difference,

$$\frac{T_i - T_o}{T_o} \equiv \frac{\Delta T}{T_o} = (\gamma - 1) \frac{Q}{p_o V_o} \quad (9)$$

Since the density has not changed,

$$\frac{p_i - p_o}{p_o} \equiv \frac{\Delta p}{p_o} = \frac{\Delta T}{T_o} \quad (10)$$

The subsequent expansion is isentropic, and hence

$$\frac{V_f}{V_o} = \left(\frac{T_i}{T_f} \right)^{1/(\gamma-1)}, \quad (11)$$

$$\frac{P_f}{P_i} = \left(\frac{T_f}{T_i} \right)^{\gamma/(\gamma-1)}, \quad \text{and} \quad (12)$$

$$\frac{P_f}{P_i} = \left(\frac{V_o}{V_f} \right)^{\gamma}, \quad (13)$$

where $()_f$ refers to the final state and γ is the ratio of specific heats (*Elements of Gasdynamics*, Liepmann and Roshko).

Noting that the final pressure is the same as the initial pressure, the fraction of the initial energy deposition that remains in the form of the elevated temperature of the heated volume can be expressed as

$$\eta_T = \frac{E_f - E_o}{E_i - E_o} = \frac{\frac{T_f}{T_o} - 1}{\frac{T_i}{T_o} - 1} = \frac{\left(1 + \frac{\Delta P}{P_o} \right)^{1/\gamma} - 1}{\frac{\Delta P}{P_o}}. \quad (14)$$

As the initially heated gas expands, it loses energy that can be expressed as

$$\Delta E = - \int_{V_o}^{V_f} p \, dV. \quad (15)$$

Although the surrounding volume is large and its pressure does not rise significantly, nevertheless work is done on it and

$$\Delta E = + \int_0^{|\Delta V|} p_o \, dV . \quad (16)$$

The net overall energy must be unchanged and hence the energy that goes into acoustics is

$$\Delta E_a = \int_{V_o}^{V_f} (p - p_o) \, dV . \quad (17)$$

Substituting into equation (17) and performing the integral, we find that the work done by the piston, which is the energy that goes into acoustics, E_a , is

$$E_a = \frac{\gamma}{\gamma - 1} p_o V_o \left\{ \left(1 + \frac{1}{\gamma} \frac{\Delta p}{p_o} \right) - \left(1 + \frac{\Delta p}{p_o} \right)^{1/\gamma} \right\} . \quad (18)$$

From equations (9) and (10), it follows that

$$Q = \frac{p_o V_o}{\gamma - 1} \cdot \frac{\Delta p}{p_o} , \quad (19)$$

and the acoustic efficiency η_a becomes

$$\eta_a = \frac{W_A}{Q} = \frac{\left(1 + \frac{1}{\gamma} \frac{\Delta p}{p_o} \right) - \left(1 + \frac{\Delta p}{p_o} \right)^{1/\gamma}}{\frac{1}{\gamma} \frac{\Delta p}{p_o}} . \quad (20)$$

It is interesting to note that in the limit as $\Delta p/p_o \rightarrow 0$,

$$w_a = \frac{p_o v_o}{2\gamma} \left(\frac{\Delta p}{p_o} \right)^2. \quad (21)$$

The total energy, kinetic plus potential, contained in a one-dimensional acoustic pulse of length ℓ_w and strength Δp_w is

$$E_a = \frac{\Delta p_w^2}{\rho_o a_o^2} A \ell_w \quad (22)$$

(*Vibration and Sound*, Morse). Equating the two it follows that

$$\left(\frac{\Delta p_w}{p_o} \right)^2 = \frac{1}{2} \left(\frac{\ell_o}{\ell_w} \right) \left(\frac{\Delta p}{p_o} \right)^2. \quad (23)$$

Simple ray tracing for an initial pulse of ℓ_o implies that $\ell_w = 2 \ell_o^*$, and

$$\frac{\Delta p_w}{p_o} = \frac{1}{2} \left(\frac{\Delta p}{p_o} \right), \quad (24)$$

the old and familiar result that is to be expected in the acoustic limit.

* $2 \ell_o$ is the length of a symmetric one-dimensional laser cavity problem.

AD-A130 382

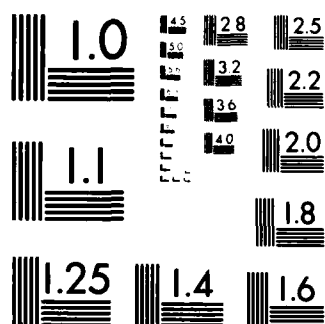
SCALING STUDIES OF EFFICIENT RAMAN CONVERTERS(U)
NORTHROP RESEARCH AND TECHNOLOGY CENTER PALOS VERDES
PENINSULA CA H KONINE ET AL. 01 JUL 83 NRTC-83-08R
N00014-81-C-0637 F/G 20/6

3/3

UNCLASSIFIED

F/G 20/6

NL



MICROCOPY RESOLUTION TEST CHART
NATIONAL BUREAU OF STANDARDS-1963-A

Northrop Design

For the oscillator beam, the energy per unit volume is independent of the operating pressure, with $Q_{osc} = 1/3$ Joule/pulse and $V_o = 0.17 \text{ cm}^3$. The initial overpressure and the acoustic efficiency does depend on pressure, with the acoustic energy modestly decreasing with initial pressure (see Table 2).

Table 2

$p_o = 2 \text{ atm}$	$\Delta p/p_o = 3.87$	$E_a = 0.030 \text{ Joules}$
$= 3$	$= 2.58$	$= 0.064$
$= 4$	$= 1.94$	$= 0.054$
$= 5$	$= 1.55$	$= 0.047$
$= 6$	$= 1.29$	$= 0.041$
$= 8$	$= 0.97$	$= 0.034$
$= 10$	$= 0.77$	$= 0.028$

The amplifier beam has a constant energy $Q_{amp} = 3$ Joules/pulse, but its volume increases linearly with the optical path length L_o . Despite the order-of-magnitude larger energy, the much larger volume of the amplifier beam results in the much lower overpressure and acoustic energies shown in Table 3.

Clearly, the acoustic field will be dominated by the oscillator. Note that while the oscillator heat deposition is confined to a length of 1 m in the center of the cell, the waves once in the plenum will spread and hence the entire length of the beams will be affected.

Table 3

$p_o = 2 \text{ atm}$	$L_o = 16.83 \text{ m}$	$\Delta p/p_o = 0.00264$	$E_a = 0.00113 \text{ Joules}$
$= 3$	$= 11.31$	$= 0.00260$	$= 0.00112$
$= 4$	$= 9.38$	$= 0.00236$	$= 0.00101$
$= 5$	$= 8.48$	$= 0.00210$	$= 0.00090$
$= 6$	$= 8.00$	$= 0.00184$	$= 0.00079$
$= 8$	$= 7.52$	$= 0.00147$	$= 0.00063$
$= 10$	$= 7.29$	$= 0.0012$	$= 0.00052$

Acoustic Attenuation

Were it not for the peculiar geometry of the Raman cell, even the most modest acoustic attenuation would completely kill off the acoustic waves because of the large number of acoustic transit times that exist between pulses. However, after the acoustic wave enters the upstream plenum, they will reflect in a complicated manner and one cannot be assured of complete attenuation. A conservative estimate can be made in the following manner. One half of the initial energy per pulse reaches the plenum after being attenuated on one pass through the muffler. The other one half passes through three times the length and can be neglected. When the device is in dynamic equilibrium, this rate of energy deposition must be balanced by the average intensity of the energy reentering the cavity; energy which suffers one additional attenuation pass through the muffler. This physical model can be expressed as

$$\underbrace{\frac{E_a}{2} \cdot \frac{1}{t_c} \cdot e^{-2\beta L_m/h}}_{\text{energy/sec into plenum}} = \underbrace{\frac{\Delta p_{\text{plenum}}^2}{\rho a_o^2} \cdot h L_o \cdot a_o}_{\text{flux of energy leaving the plenum and entering the cavity}} \quad (25)$$

Solving for the density perturbation after a final attenuation, we find that

$$\left(\frac{\Delta\rho}{\rho_o}\right)_{\text{cavity}}^2 = \frac{1}{2\gamma} \cdot \frac{E_a}{p_o V_c} \cdot \frac{L_m}{a_o t_c} \cdot e^{-2\beta L_m/h} \quad (26)$$

where V_c is the volume of the entire muffler cavity, L_m is the total length of the muffler, and β is the muffler attenuation coefficient that can be taken as 0.35 (*Noise Reduction*, Beranek). The density perturbation and the phase aberration, calculated from Equation (5), are presented below.

Table 4

$p_o = 2 \text{ atm}$	$L_o = 16.83 \text{ m}$	$(\Delta\rho/\rho_o)_{\text{cavity}} = 2.2 \times 10^{-6}$	$\phi_{\text{rms}} = 0.38$
= 3	= 11.31	= 2.0	= 0.35
= 4	= 9.38	= 1.7	= 0.33
= 5	= 8.48	= 1.5	= 0.33
= 6	= 8.00	= 1.3	= 0.32
= 8	= 7.52	= 1.1	= 0.33
= 10	= 7.29	= 0.9	= 0.33

As can be seen there is a slight preference for the $p_o = 6 \text{ atm}$, $L_o = 8 \text{ m}$ design. However, a variation of muffler length of as little as $\Delta L_m/h = 0.5$ corrects the widest variation of phase aberration over the entire range shown.

Two conclusions can be drawn. First, insofar as acoustic disturbances are concerned, the beam will be nearly diffraction limited ($BQ \sim 1.05$). Second, beam quality in this circumstance does not present any real constraint on the optical design.

Poseidon Research Memo No. 149

These conclusions are, as stated, applicable only for ordered acoustic disturbances. The effect of random turbulent fluctuations are evaluated below

4.2 Baseline Flow

There are two sources of random free-stream density fluctuations: 1) adiabatic density fluctuations produced by turbulent velocity fluctuations, and 2) isobaric density perturbations caused by temperature fluctuations.

For adiabatic disturbances,

$$\left(\frac{\rho'}{\rho_0}\right)_{\text{rms}} \sim 0.7 M_c^2 \left(\frac{u'}{U}\right)_{\text{rms}}^2 \quad (27)$$

where M_c is the cavity Mach number and u'/U is the fractional turbulent velocity fluctuations in the cavity. For the Northrop Raman cell, $M_c \sim 10^{-3}$, $u'/U \sim 10^{-1}$, and $(\rho'/\rho_0)_{\text{rms}} \sim 10^{-8}$. Clearly, adiabatic fluctuations are irrelevant to our design.

The final source of disturbance to be evaluated is density fluctuations caused by temperature fluctuations. Following Prandtl's hypothesis,

$$\frac{\rho'}{\rho_0} \sim \left(\frac{\Delta T}{T_0}\right) \frac{u'}{U_0} \quad (28)$$

Recalling that $(\rho'/\rho_0)_{\text{allowable}} \sim 10^{-5}$, we find that the requirement on ΔT is 300×10^{-4} or 0.03°C . This is clearly the most restrictive design constraint of the system and it must be treated with great care in any subsequent design.

In addition to wall temperature variations, which can be controlled by external insulation, the primary sources of temperature variations will be entropy waves and large-scale temperature variability caused

by heat exchanger temperature nonuniformity. In anticipation of this issue, the conceptual design presented in Section 2 has the heat exchanger placed as far upstream of the cavity as possible, in order to allow for turbulent mixing.

Entropy "waves", which are no more than thermal disturbances, will be created when acoustic waves from the upstream plenum impinge on the heat exchanger. The magnitude of these disturbances can be estimated from the formula,

$$\frac{\Delta T}{T} = \frac{\gamma - 1}{\gamma} C_{D_L} M_L \left(\frac{\Delta p}{p_o} \right)_{\text{incident}} \quad (29)$$

where C_{D_L} is the local drag coefficient of the screen and can be taken as ~ 1 . M_L is the local Mach number, which for the Raman cell is $\sim 10^{-3}$, $(\Delta p/p_o)_{\text{incident}} = (\Delta p/p_o)_{\text{plenum}} \sim 10^{-4}$ and hence $\Delta T/T \sim 10^{-7}$, which independent of turbulent mixing poses no problems.

This leaves temperature variations emanating from the heat exchanger as our last design issue. Without extraordinary precautions one can expect $\Delta T_{\text{HX}} \sim 1^\circ$. Hence, in the absence of turbulent mixing, the density variations

$$\frac{\rho'}{\rho_o} \sim \left(\frac{\Delta T}{T} \right) \left(\frac{u'}{U} \right) = 3 \times 10^{-4}.$$

This final issue is clearly an important design problem, although turbulent mixing in the return duct, which is the length of the optical path, should readily reduce the levels to acceptable tolerances. Interestingly, here the choice of pressure could influence the phase aberration at least within a factor of 2. Referring to equation (6) and noting that

ΔT over the heat exchanger is a function of the heat removal and not the local pressure, we find that the Northrop design criteria (equation (1)) leads to a minimum random temperature fluctuation at

$p_o = p_{ref} = 2.4$ atm. Between $p_o = 2$ and 5 atm the variation is only 25 percent, but at $p_o = 10$ atm the phase aberration will have doubled.

Thus, this design criteria is seen to favor the lower pressures

$p_o \lesssim 5$ atm.

5. Summary

The Northrop Raman optimal design criteria has been translated into a conceptual design for the flow and acoustics module, and this design has been analyzed in terms of the impact of various design points on beam quality. The conclusions are that:

1. For a nearly diffraction limited beam, the allowable density perturbations are

$$\left(\frac{\rho'}{\rho_o}\right)_{\text{rms}} \sim 10^{-6} \quad \text{ordered acoustics}$$

$$\left(\frac{\rho'}{\rho_o}\right)_{\text{rms}} \gtrsim 10^{-5} \quad \text{random turbulence}$$

2. The oscillator dominates the acoustic field because of its highly focussed beam and the resulting higher overpressure and higher acoustic efficiency.
3. The upstream plenum will have a more or less steady random acoustic field with $\Delta p/p_o \sim 10^{-4}$.
4. The effect of the operating pressure on phase aberrations caused by acoustic disturbances is trivial.
5. Random adiabatic density perturbations $(\rho'/\rho_o)_{\text{rms}} \sim 10^{-8}$ and have no influence on the design.
6. Random temperature fluctuations are probably the most important flow and acoustics issue, and they will be dominated by large-scale temperature variations emanating from the heat exchanger.

7. The design has a weak preference for pressures in the range
 $p_o = 2$ to 5 atm.
8. Regardless of pressure, it is expected that flow and acoustics
will allow a nearly diffraction-limited beam to remain so.
9. Selection of a design point cannot readily be made on the basis
of beam quality.



POSEIDON RESEARCH

Proposal No. 8219

**A PROPOSAL FOR
THE DESIGN AND FABRICATION
OF A FLOW SYSTEM FOR THE
DARPA / NRTC HYDROGEN RAMAN CELL**

by

John E. Lewis

August 1982

**Prepared for
Northrop Research and Technology Center**

Table of Contents

1.	Introduction.....	2
2.	Design Concept.....	5
3.	Design Issues.....	9
	3.1 Flow Uniformity.....	9
	3.2 Acoustic Attenuation.....	14
	3.3 Random Disturbances.....	24
	3.4 Heat Exchanger and Power Requirements.....	26
4.	References.....	29

List of Figures

	Page
1. Illustration of NRTC Raman cell optical design.....	3
2. Cross section of Raman cell cavity.....	4
3. Flow design schematic.....	6
4. Flow design schematic cross section.....	7
5. Acoustic design schematic cross section.....	8
6. Flow uniformity calculations.....	12
7. Power requirements for various flow systems.....	13
8. Power spectrum of initial acoustic disturbance of NRTC Raman cell design.....	15
9. Transmitted acoustic intensity as a function of wave number...	16
10. Dissipation of acoustic intensity as a function of wave number.....	17
11. Illustration of open channel muffler.....	19
12. Effect of open channel on acoustic attenuation.....	20
13. Effects of finite aperture and viscosity (25 Hz).....	21

Poseidon Research Proposal No. 8219

	Page
14. Power spectrum decay caused by various design elements.....	23
15. Coolant reservoir.....	28

1. Introduction

This proposal is addressed to the design and fabrication of a flow system for the DARPA/NRTC hydrogen Raman cell. The specifications defined by Northrop are as follows:

Gas	-- hydrogen
Temperature	-- $T_o = 300^\circ\text{K}$
Pressure	-- $p_o = 6 \text{ atm}$
Cell length	-- $L_o = 8 \text{ m}$
Beam quality	-- $BQ \leq 1.2$
Pump energy	-- 10 J/pulse
Rep rate	-- 25 Hz

The optical design consists of two beams that are schematically illustrated in figure 1. The amplifier beam has a constant cross section of approximately 2 cm^2 . Thirty percent of the pump energy or 3 J/pulse is deposited in the gas in the form of heat, and this thermal deposition occurs more or less uniformly over a distance along the beam equal to two-thirds of the length of the optical path. The oscillator beam is quite different. The thermal energy deposition is only 1/3 J/pulse but the beam is highly focused. Its initial cross-sectional area of 1 cm^2 focuses down to $1.7 \times 10^{-3} \text{ cm}^2$, with the length of thermal deposition equal to 1 m.

The cross section of the working area of the laser beam cavity as specified by Northrop is shown in figure 2. The center line of the two beams are 3 cm apart, and the working area is 3 cm x 6 cm.

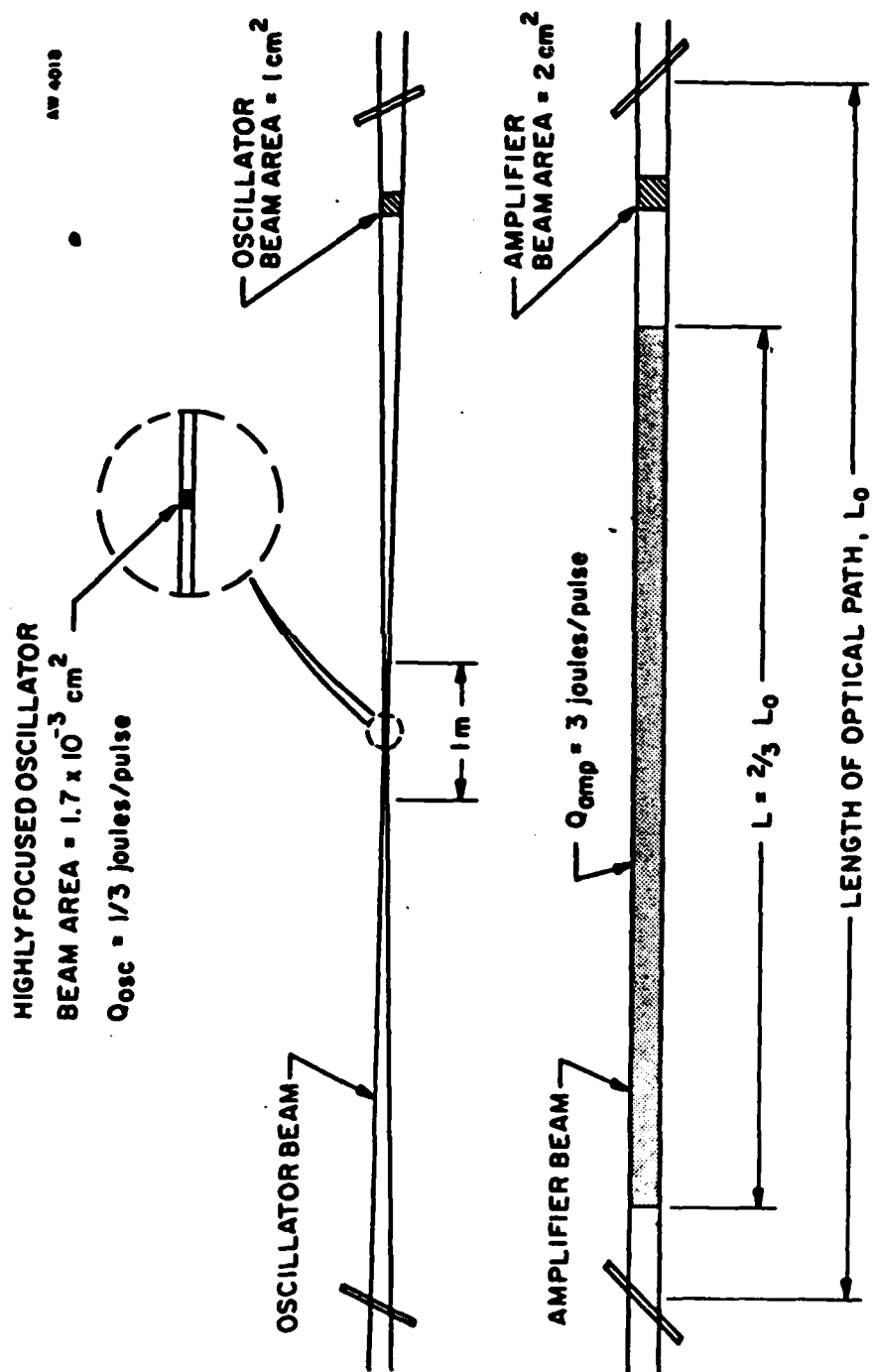


Figure 1. Illustration of NRTC Raman cell optical design.

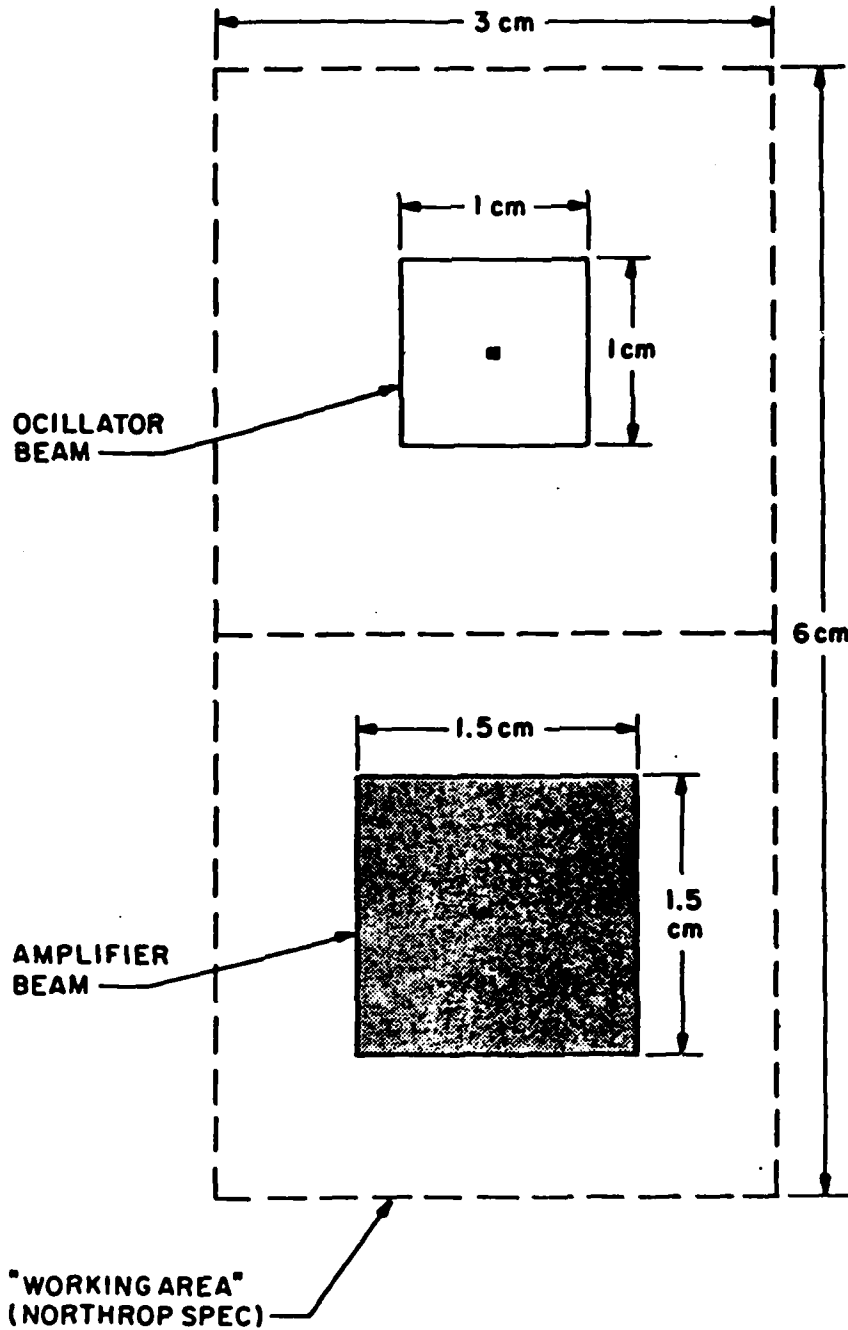


Figure 2. Cross section of Raman cell cavity.

2. Design Concept

The design concept consists of two primary elements: the flow system and the acoustic design. The flow system is required to clear thermal remnants from the working area before the next pulse, and the long aspect ratio of the optical design represents a unique problem of flow uniformity that will be treated quantitatively in the following section. The basic idea is shown in figure 3. A cylindrical pressure vessel 1 m in diameter and 8 m long is separated into an inlet chamber and an outlet chamber. A resistive element allows the chambers to act primarily as settling chambers with nearly uniform flow between them along its length. A cross section of the flow design is shown in figure 4. The two chambers are separated by an impermeable flow and acoustic wall. Gas flows from the upstream plenum to two downstream plenums through a dissipative material that acts as the previously described resistive element. The resistivity of the design can be changed either by increasing the thickness of the material or by increasing the density of the material. The acoustic design concept is illustrated in figure 5. Since the speed of sound is high and the rep rate is low, it is desirable to allow the acoustic waves to freely radiate into the dissipative material making multiple transits in the downstream plenum before the next pulse. The upstream plenum is focused to minimize residual acoustic energy. Dissipative material here is not necessary and could give rise to random thermal fluctuations that would degrade the beam quality of the device.

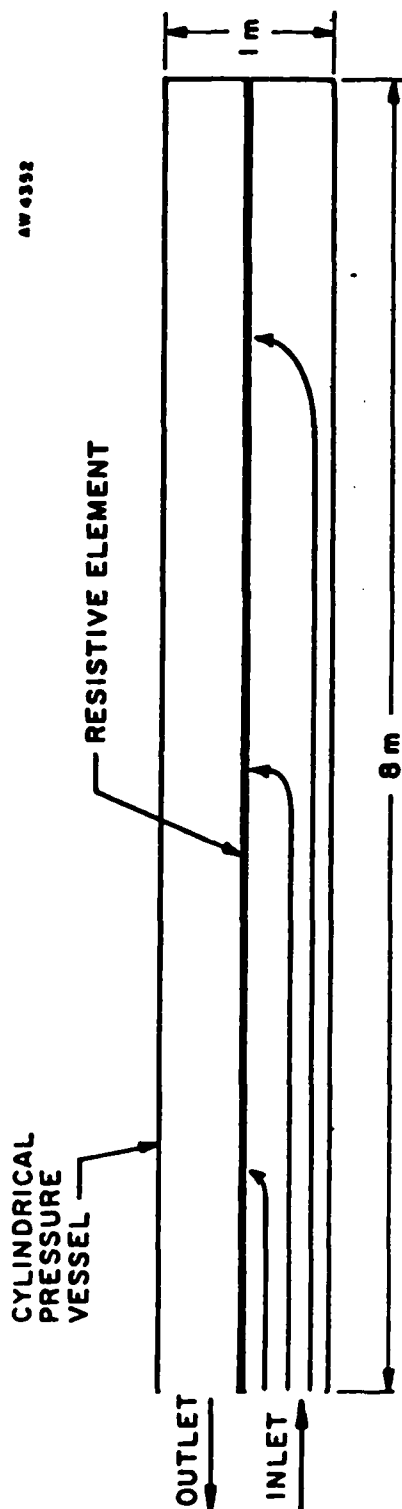


Figure 3. Flow design schematic.

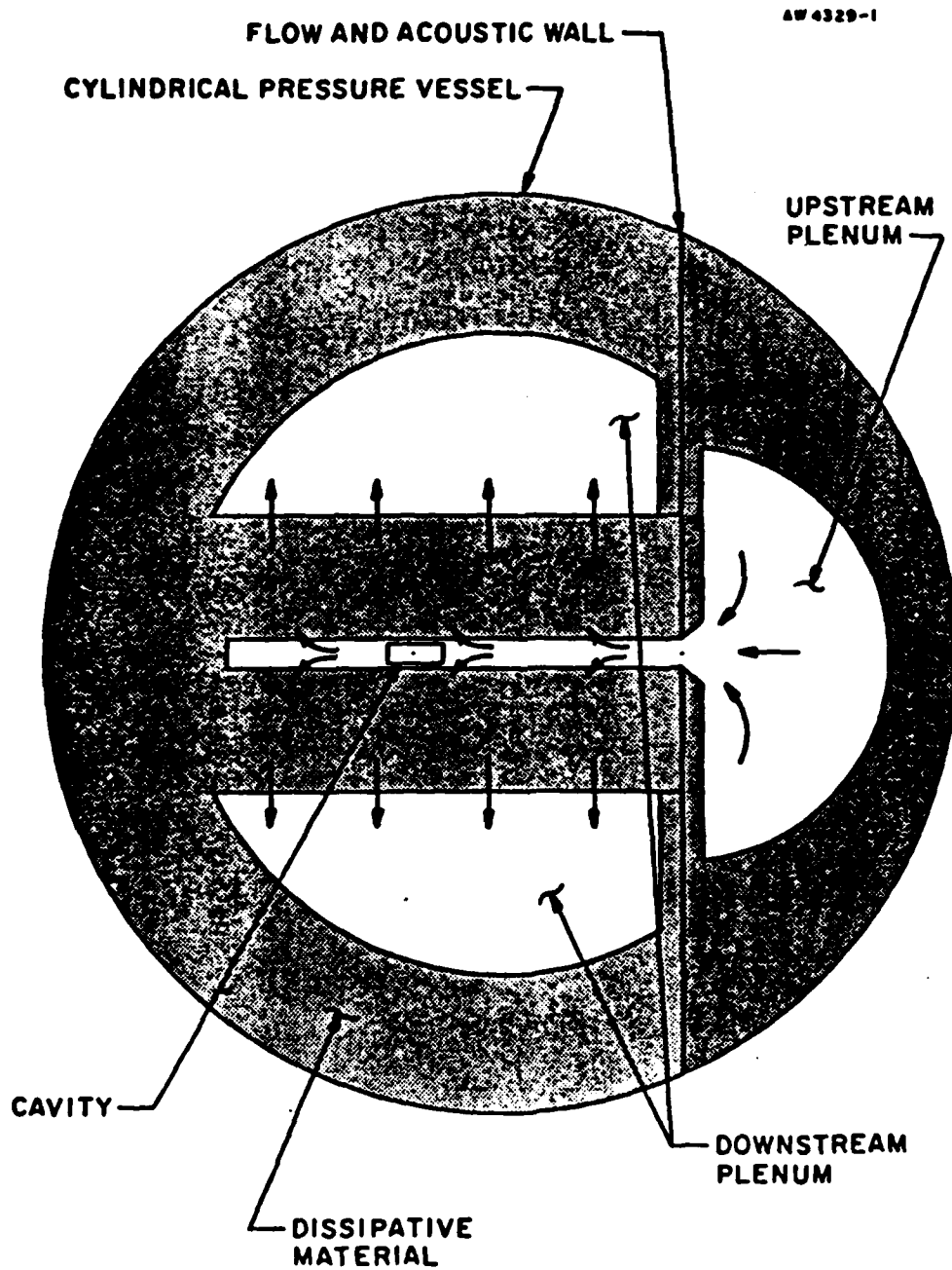


Figure 4. Flow design schematic cross section.

AW 4329

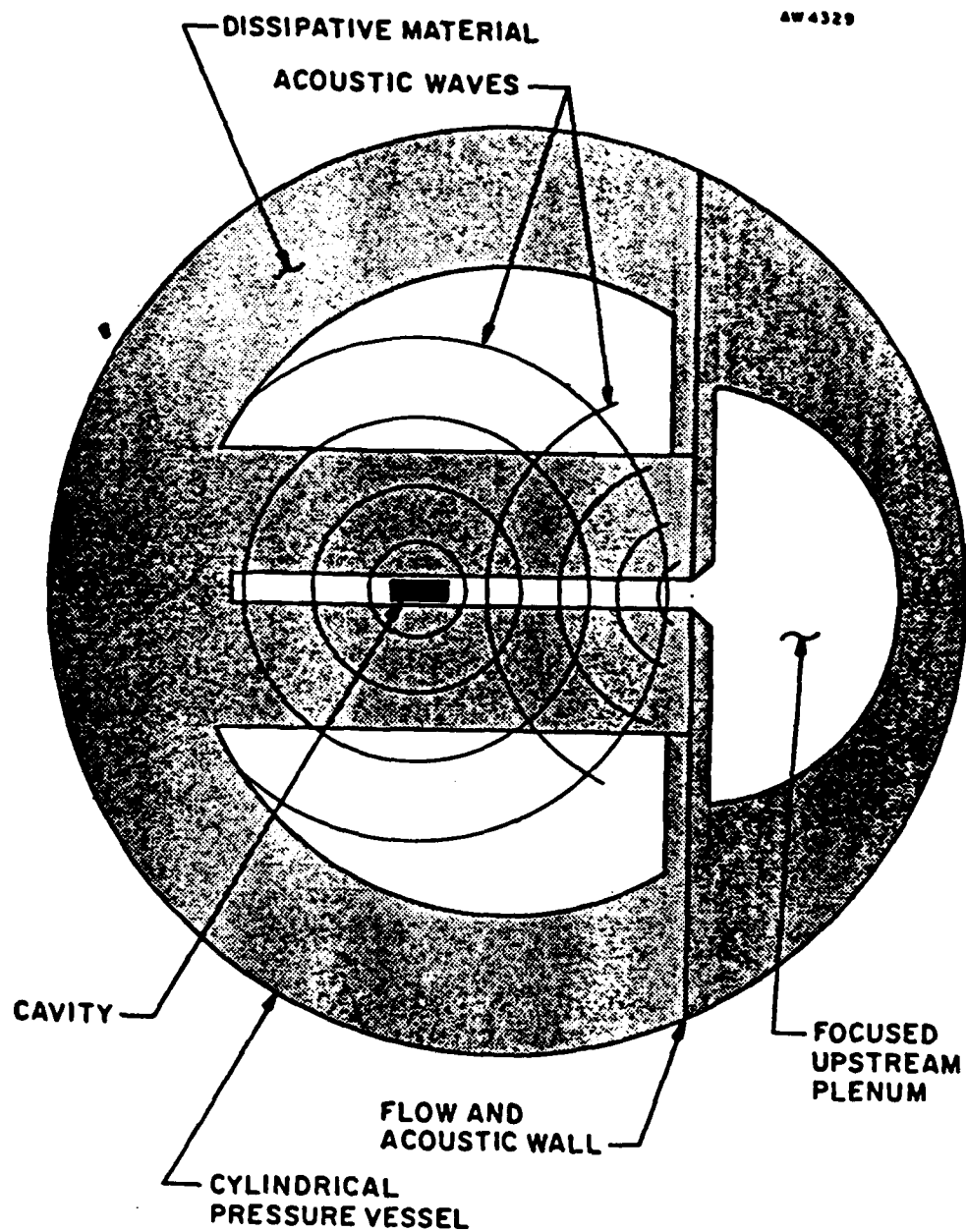


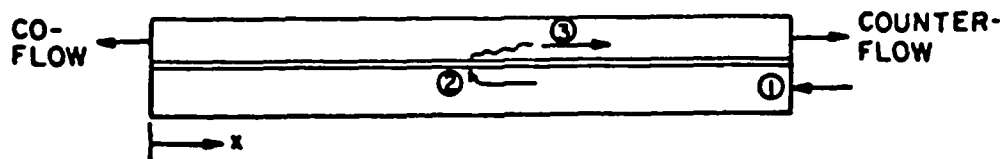
Figure 5. Acoustic design schematic cross section.

3. Design Issues

In this section the major technical issues and design element analyses are presented.

3.1 Flow Uniformity

Design selections of co-flow *versus* counter-flow (see schematic below) and the choice of resistive material requires a prediction of flow uniformity.



The modeling used for this purpose is as follows.

The flow in the upstream plenum is governed by

$$A_1 \frac{du_1}{dx} = hv_2, \quad (1)$$

$$A_1 \frac{d}{dx} (p_1 + \rho u_1^2) = \rho u_1 v_2 h + \tau_1 c_1, \quad (2)$$

where A_1 is the cross-sectional area of the upstream plenum, u_1 is the axial velocity, h is the height of the working area, v_2 is the cross flow velocity at the entrance to the muffler, p_1 is the upstream pressure, ρ is the density, τ_1 is the turbulent shear stress, and c_1 is the circumference of the upstream plenum.

The pressure at the inlet of the muffler p_2 is modified by the contraction and

$$p_2 + \frac{1}{2} \rho (u_1^2 + v_2^2) = p_1 + \frac{1}{2} \rho u_1^2 . \quad (3)$$

The downstream pressure p_3 also follows Bernoulli's equation, but is modified by the loss caused by the dissipative material as indicated

$$p_3 + \frac{1}{2} \rho v_3^2 = p_2 + \frac{1}{2} \rho v_2^2 - \Delta P , \quad (4)$$

$$\Delta P = K \Delta_m v_3 . \quad (5)$$

K is the dissipative constant and Δ_m is the thickness of the material.

The flow in the downstream plenum is governed by

$$A_3 \frac{du_3}{dx} = (-1)^{j+1} h v_3 , \quad (6)$$

$$A_3 \frac{d}{dx} (p_3 + \rho u_3^2) = (-1)^{j+1} \tau_3 c_3 , \quad (7)$$

where $j = 0$ refers to co-flow and $j = -1$ refers to counter-flow. The definition of terms are obvious. The major assumption here is that the axial momentum has been suppressed by the dissipative material.

These equations can be reduced to two equations for u_1 and v_2 with the controlling nondimensional parameters $K \Delta_m / \rho u_0$ and A_1 / A_3 . The results of calculations performed for 4-lb Pyrel* are shown in

* A commercially available dissipative material that has been successfully used in the Poseidon laser simulation facility.

figure 6, where the fractional flow variation in the cavity $v_{\max} - v_{\min}$ is plotted versus the area ratio A_1/A_3 for various muffler thicknesses and both co-flow and counter-flow. The results show that the best design is counter-flow with an area ratio of $A_1/A_3 \approx 0.5$. On the other hand, none of the variability is particularly high, and in fact the proper design criteria is what power is required for maintaining a minimum flush factor. In figure 7, the power required is plotted versus the area ratio, again for co-flow and counter-flow and for various muffler thicknesses. The conclusion is that so long as the area ratio is less than 1.0 either flow direction is acceptable. The choice of muffler packing material thickness is dictated by the acoustic design, with only the constraint that $K\Delta_m/\rho U_0 \ll 1$. (This is the condition that is required to suppress the downstream axial momentum.)

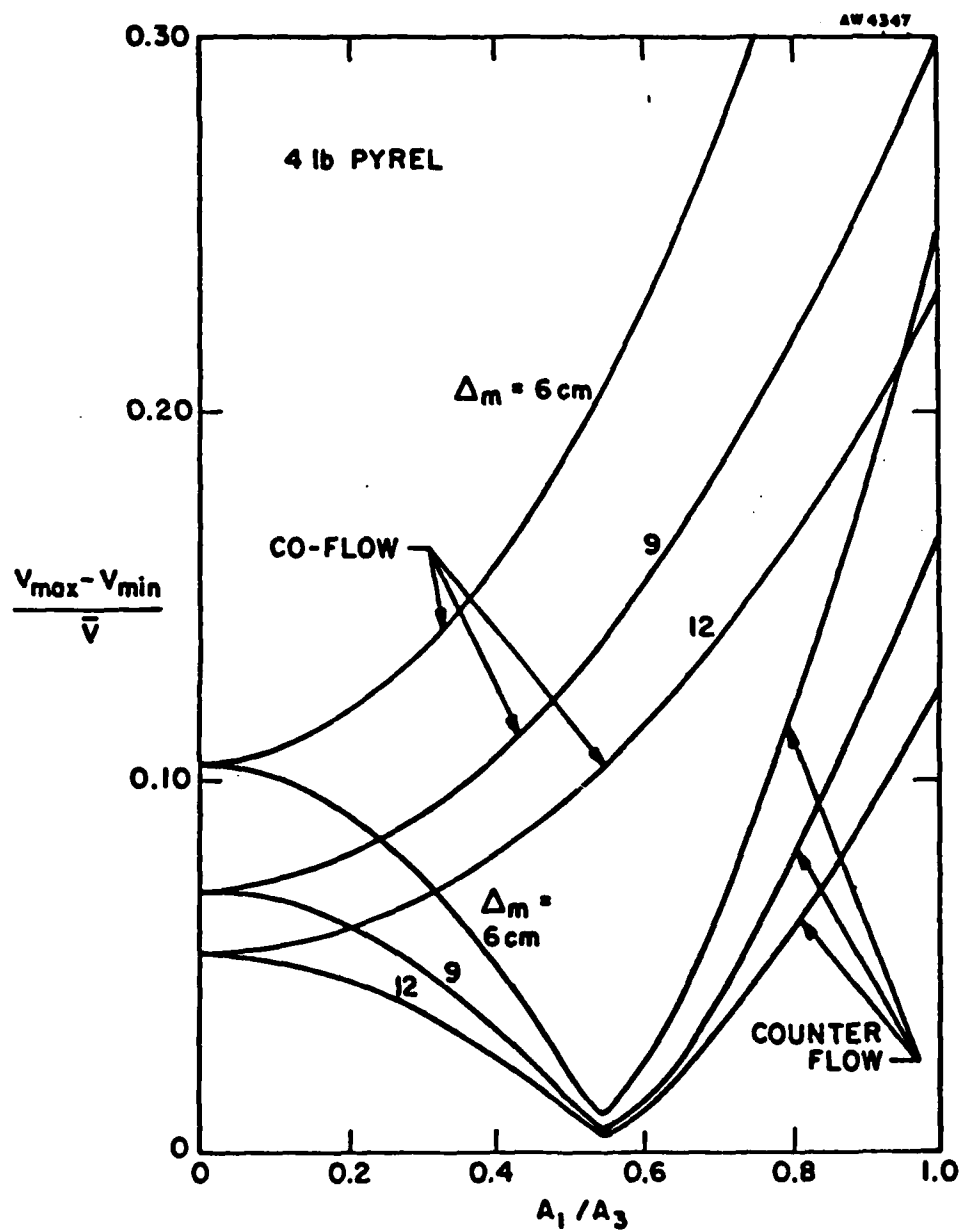


Figure 6. Flow uniformity calculations.

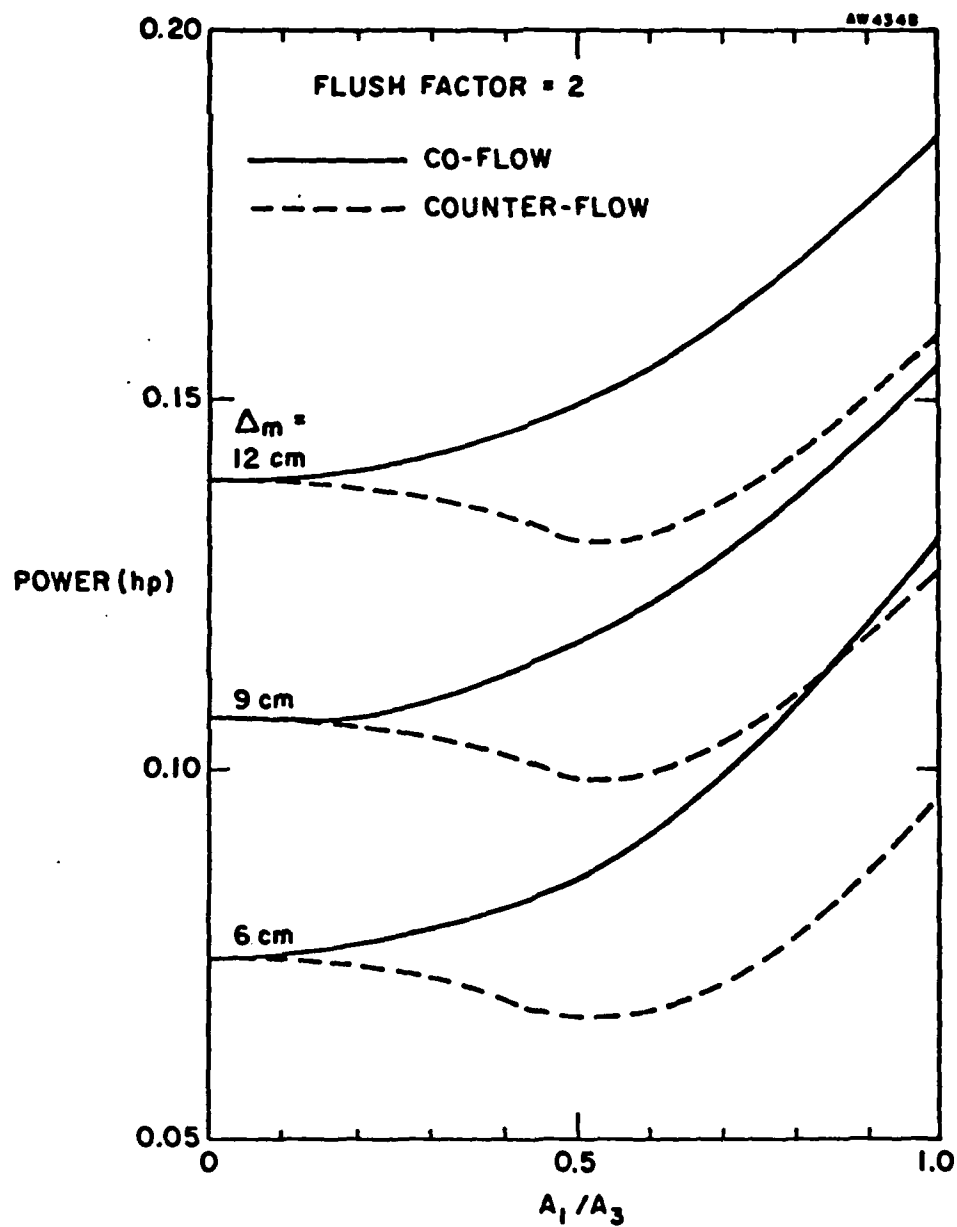


Figure 7. Power requirements for various flow systems.

3.2 Acoustic Attenuation

From the experiments of Morris, *et al.* (1980) and Wright and Medendorp (1967), the acoustic disturbance is expected to be an "N-wave" with a wavelength λ and acoustic energy E_a given in Table 1 (see Poseidon Research Memo No. 149).

Table 1

	λ (cm)	E_a (J/pulse)
Oscillator	0.1	4.1×10^{-2}
Amplifier	1.5	7.9×10^{-4}

The combined power spectrum of the initial acoustic disturbance for the NRTC Raman cell design is shown in figure 8 as a function of kh , where k is the wave number and h is the height of the channel. Without any attenuation, the oscillator clearly dominates at a $kh \sim 100$. The reason as explained in Poseidon Research Memo No. 149 is that the acoustic efficiency of the amplifier is so low.

In order that the acoustic design that was presented in Section 2 be functional, it is necessary that the dissipative material both transmit and attenuate the acoustic wave.

The solution for the transmitted acoustic energy of a plane wave incident on a dissipative material is presented in figure 9. It can be seen that for a practical range of $kh/\rho_0 a_0 = 0.23 \rightarrow 1.0$, transmission is nearly 100 percent for $kh \geq 1$. In figure 10, the nondimensional attenuation coefficient $k_1 h$, where k_1 is the imaginary component of the wave number, is presented as a function of kh . For

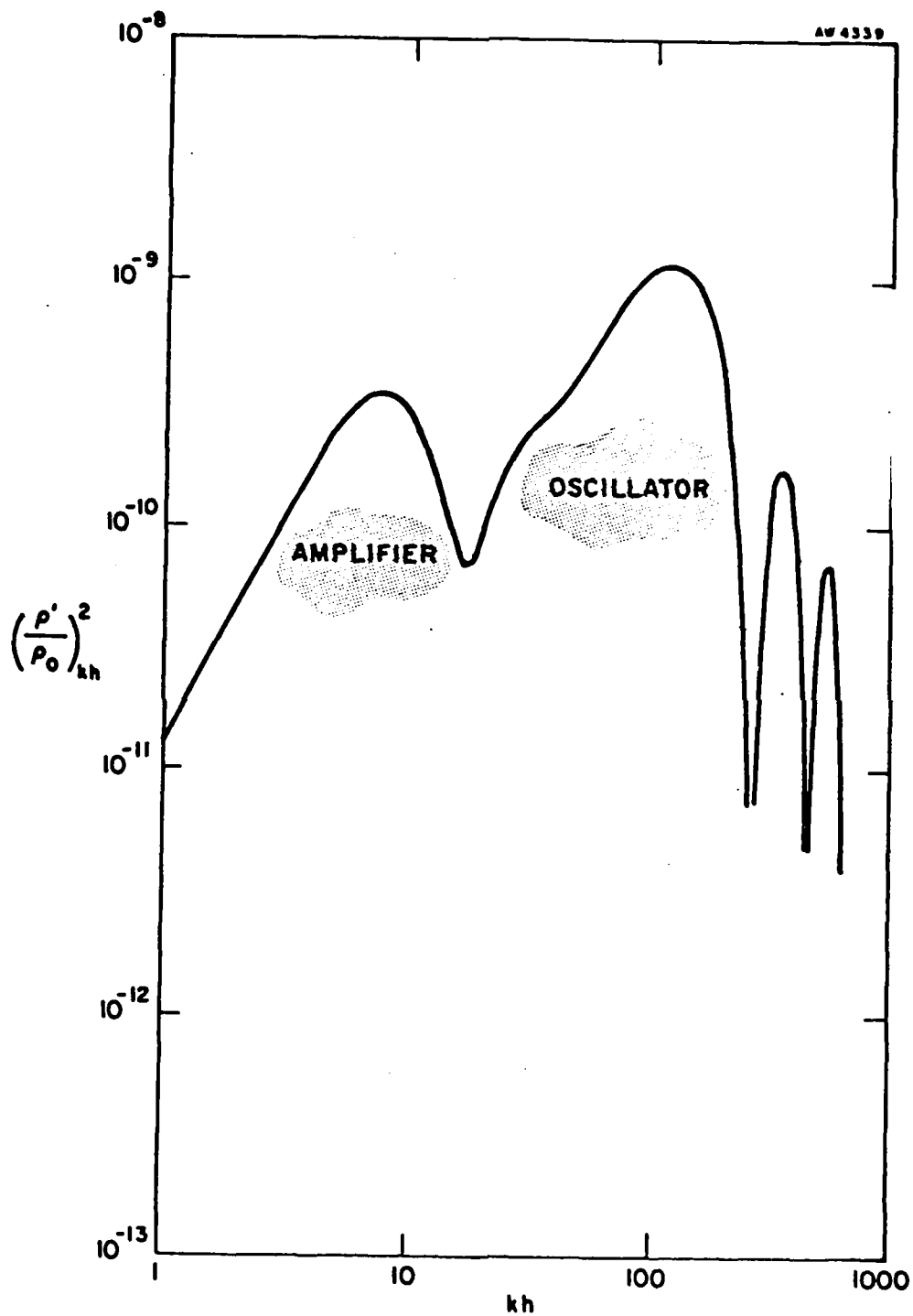


Figure 8. Power spectrum of initial acoustic disturbance of NRTC Raman cell design.

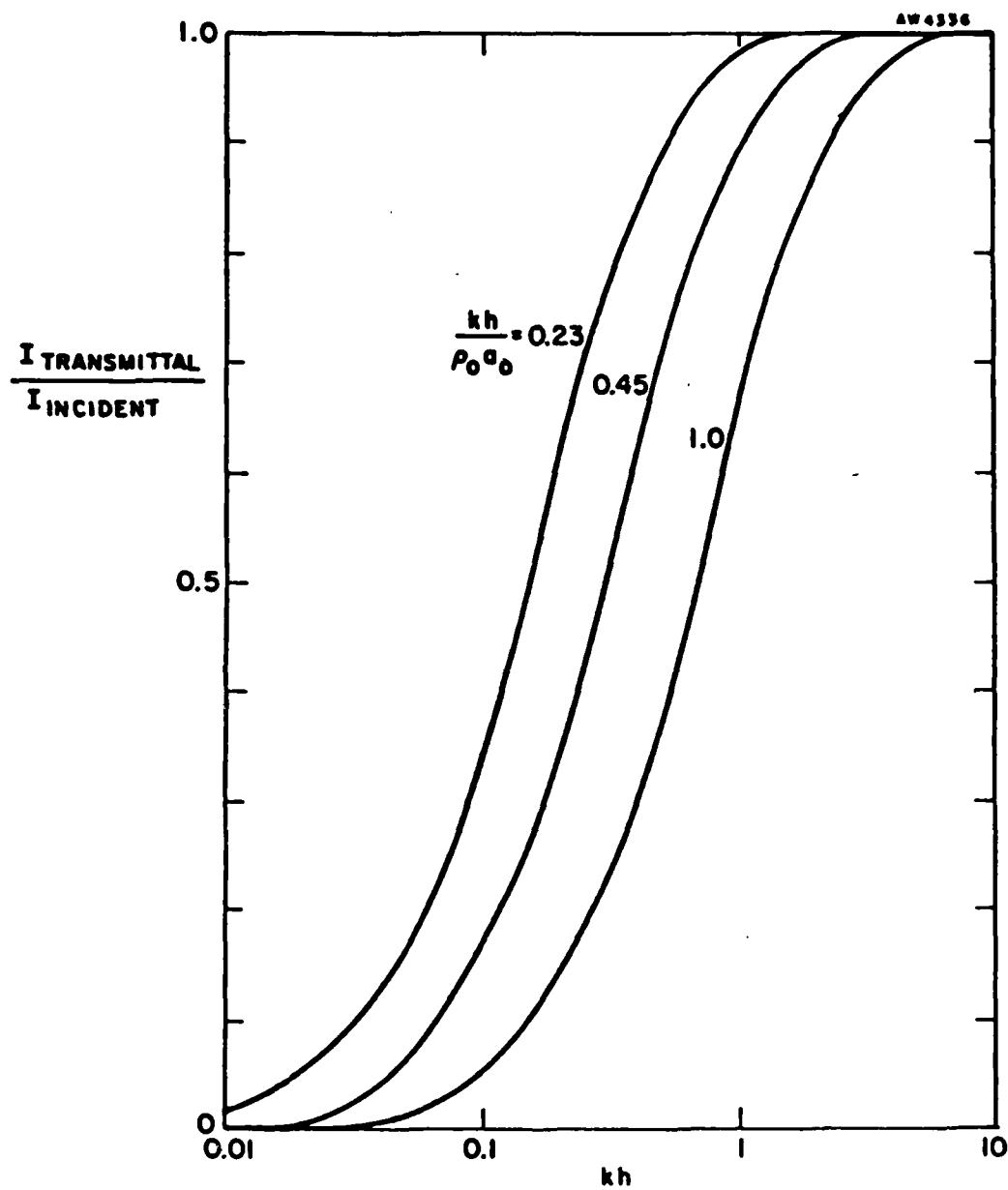


Figure 9. Transmitted acoustic intensity as a function of wave number.

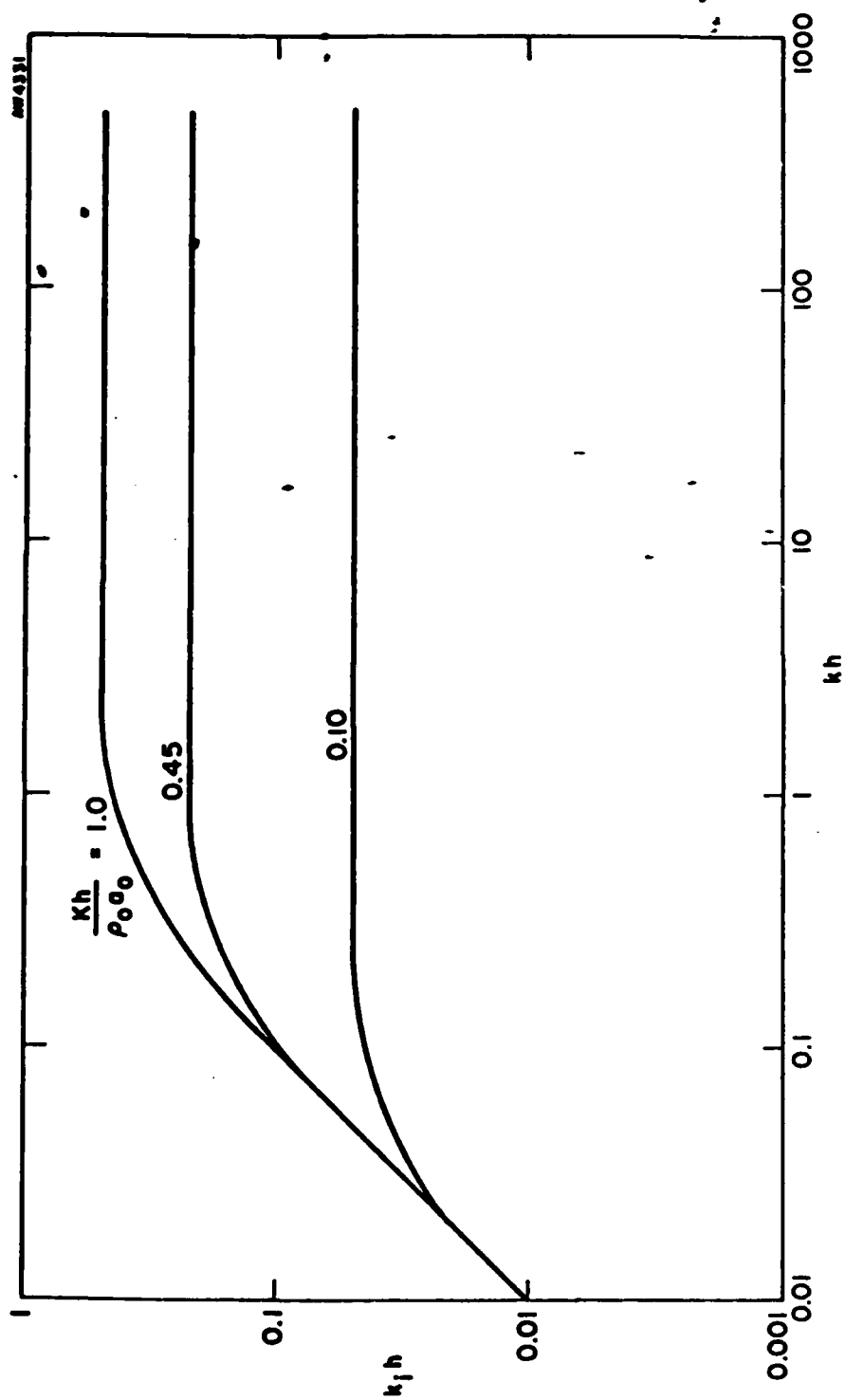


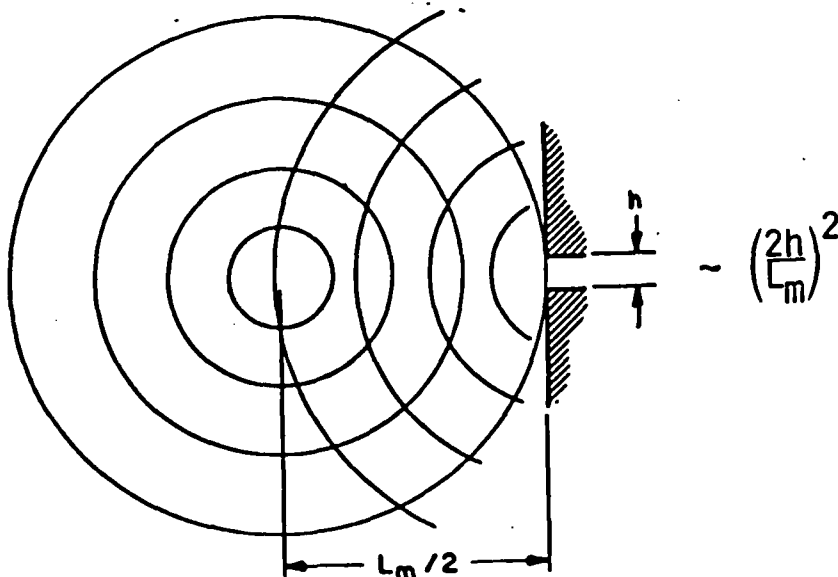
Figure 10. Dissipation of acoustic intensity as a function of wave number.

$kh/\rho_0 a_0 \sim 0.45$ the dissipation will cause the acoustic intensity to drop as e^{-1} every five channel heights. This is of course more than adequate for the many transits, but it is appropriate only so long as the wave is embedded within the acoustic material.

In the actual muffler design, the acoustic wave travels in an open channel as illustrated in figure 11. For long waves, $kh \leq 1$, the waves decay as though they were entirely embedded in the material. For short waves, however, as seen in figure 12, the muffler is totally ineffective. Fortunately, other effects, viscosity in particular, mitigate this limitation.

In figure 13 the effective attenuation caused by the finite aperture and the actual attenuation caused by viscosity at a rep rate of 25 Hz is seen to dramatically narrow the width of the spectrum, and interestingly the originally perceived dominance of the oscillator. In addition to the attenuation caused by the muffler, the design has two additional important attenuation features: geometric relief and upstream plenum leakage.

The geometric relief, as illustrated below, is a result of the



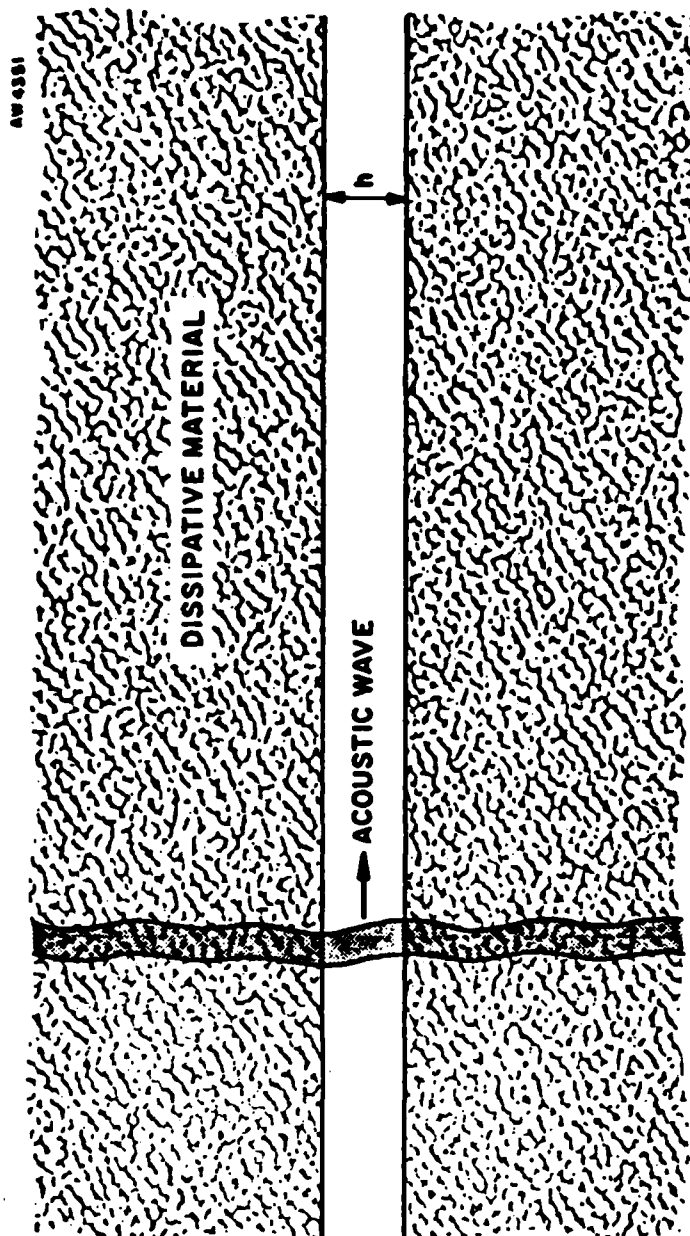


Figure 11. Illustration of open channel muffler.

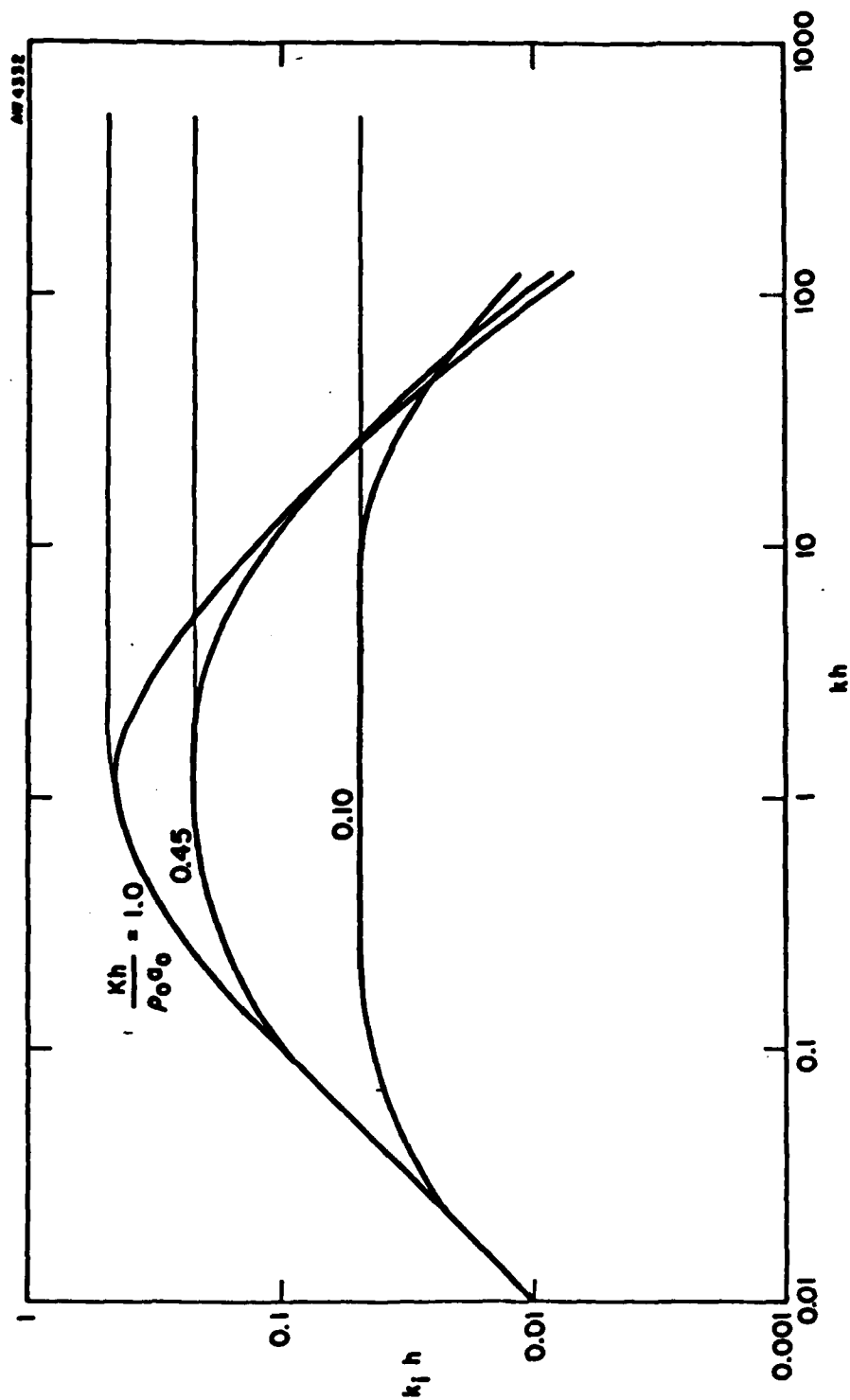


Figure 12. Effect of open channel on acoustic attenuation.

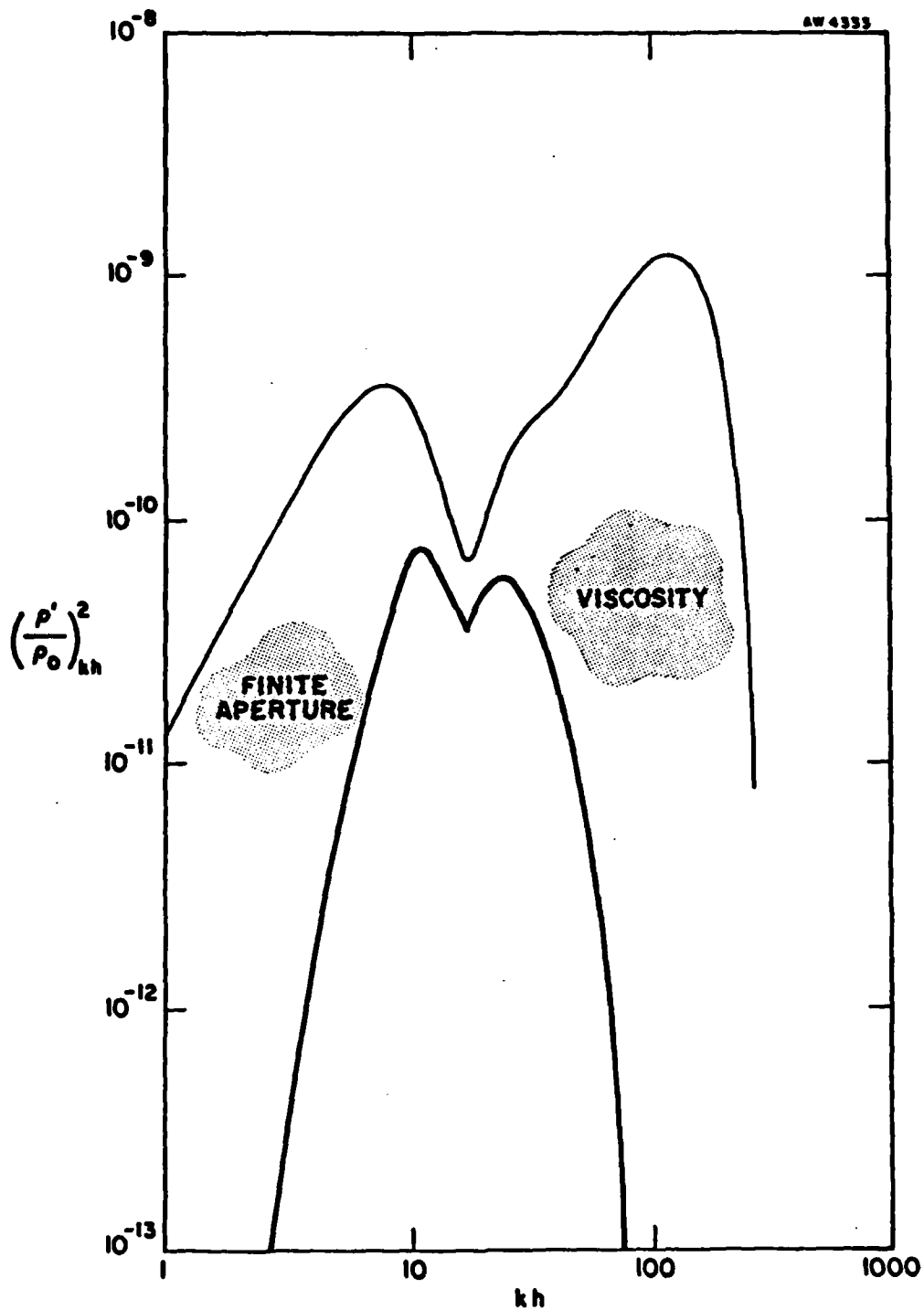


Figure 13. Effects of finite aperture and viscosity (25 Hz).

open character of the design and the transparency of the acoustic material. Only those waves traveling in the channel are at issue. The attenuation of all others passing through the dissipative material is overwhelming. The two-dimensional character of the field causes an effective reduction or attenuation of intensity equal to $(2h/L_m)^2$.

The upstream plenum is designed to be focused and hence reflect nearly all waves back downstream. However, a conservative estimate based on a nonfocused plenum has been made with

$$\frac{dI}{dt} = -I \cdot \frac{h}{L_m} \cdot \frac{a_o}{2L},$$

where I is the intensity of the acoustic field in the upstream plenum and L_m is a characteristic length of the plenum. Both of these effects and the open channel muffler are combined in figure 14, where the final disturbance is presented. The final value is $(\rho'/\rho_o)_{rms} \sim 5 \times 10^{-7}$, a value that is five times smaller than the required $(\rho'/\rho_o)_{rms} \sim 2.5 \times 10^{-6}$ necessary for a beam that is 1.2 times diffraction limited (Poseidon Research Memo No. 149).

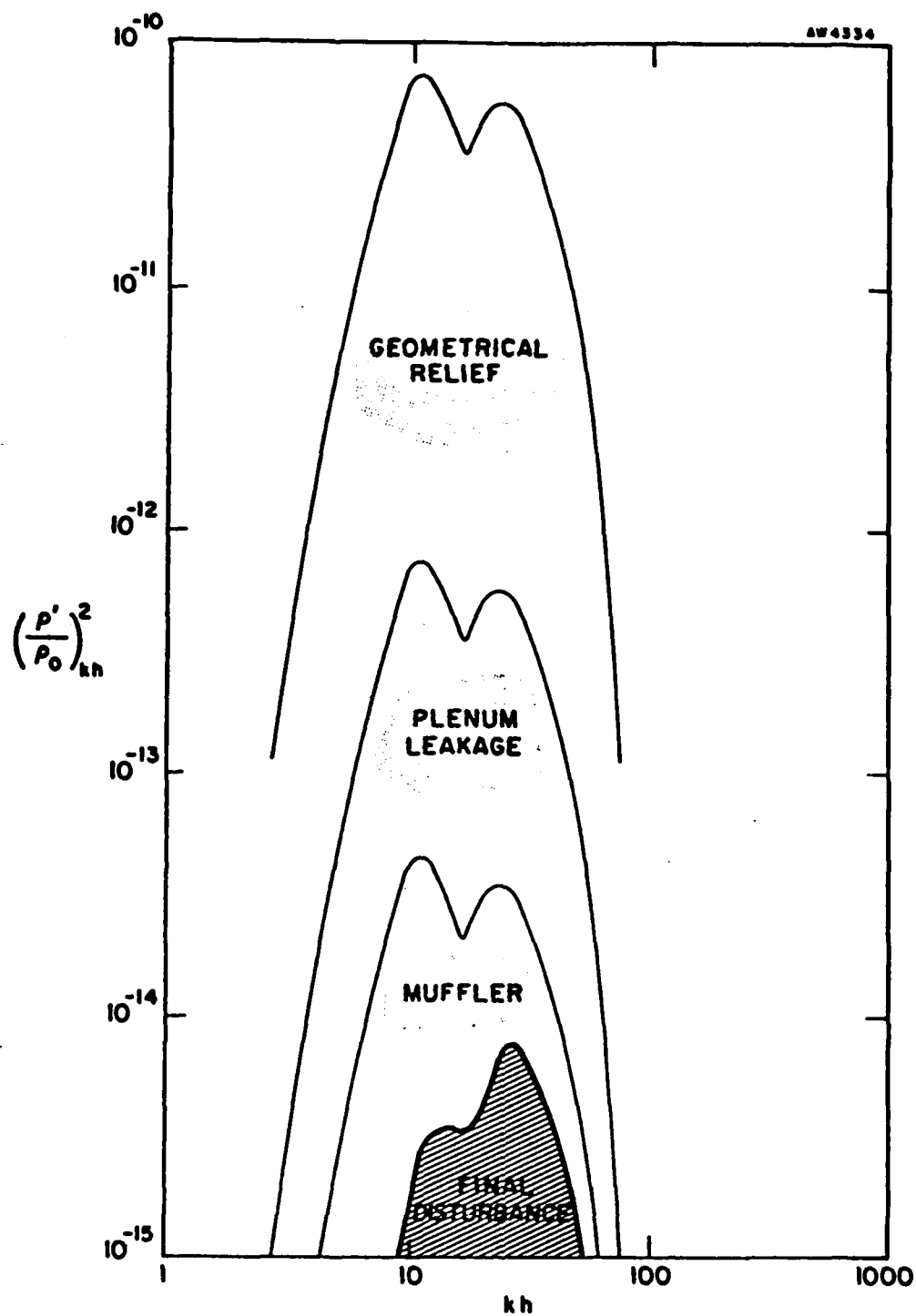


Figure 14. Power spectrum decay caused by various design elements.

3.3 Random Disturbances

There are two sources of random free-stream density fluctuations: 1) adiabatic density fluctuations produced by turbulent velocity fluctuations, and 2) isobaric density perturbations caused by temperature fluctuations.

For adiabatic disturbances,

$$\left(\frac{\rho'}{\rho_o}\right)_{\text{rms}} \sim 0.7 M_c^2 \left(\frac{u'}{U}\right)_{\text{rms}}^2,$$

where M_c is the cavity Mach number and u'/U is the fractional turbulent velocity fluctuations in the cavity. For the Northrop Raman cell, $M_c \sim 10^{-3}$, $u'/U \sim 10^{-1}$, and $(\rho'/\rho_o)_{\text{rms}} \sim 10^{-8}$. Clearly, adiabatic fluctuations are irrelevant to our design.

The final source of disturbance to be evaluated is density fluctuations caused by temperature fluctuations. Following Prandtl's hypothesis,

$$\frac{\rho'}{\rho_o} \sim \left(\frac{\Delta T}{T_o}\right) \frac{u'}{U_o}.$$

From Poseidon Research Memo No. 149, $(\rho'/\rho_o)_{\text{allowable}} = 4 \times 10^{-5}$, and the requirement on ΔT is 1200×10^{-4} or 0.12°C . This is clearly the most restrictive design constraint of the system and it must be treated with great care in any subsequent design.

In addition to wall temperature variations, which can be controlled by external insulation, the primary sources of temperature variations will be entropy waves and large-scale temperature variability caused by heat exchanger temperature nonuniformity.

Entropy "waves", which are no more than thermal disturbances, will be created when acoustic waves from the upstream plenum impinge on the heat exchanger. The magnitude of these disturbances can be estimated from the formula,

$$\frac{\Delta T}{T} = \frac{\gamma - 1}{\gamma} C_{D_L} M_L \left(\frac{\Delta p}{p_o} \right)_{\text{incident}},$$

where C_{D_L} is the local drag coefficient of the screen and can be taken as ~ 1 . M_L is the local Mach number, which for the Raman cell is $\sim 10^{-3}$, $(\Delta p/p_o)_{\text{incident}} = (\Delta p/p_o)_{\text{plenum}} \sim 10^{-4}$ and hence $\Delta T/T \sim 10^{-7}$, which independent of turbulent mixing poses no problems.

This leaves temperature variations emanating from the heat exchanger as our last design issue. For a volumetric flow rate of coolant water of 10 gpm through the heat exchanger, the maximum temperature rise is 0.03°C (see Section 3.4). Hence, even in the absence of turbulent mixing, the density variations

$$\frac{\rho'}{\rho_o} \sim \left(\frac{\Delta T}{T} \right) \left(\frac{u'}{U} \right) = 1 \times 10^{-5},$$

a factor of four below the allowable levels.

3.4 Heat Exchanger and Power Requirements

The first question that must be asked is whether a heat exchanger is needed at all. For a total thermal energy deposition of 3.33 J/pulse and at a frequency of 25 Hz, the temperature rise in the 8-m long 1-m diameter cylindrical pressure vessel is 0.16°C/min or 9.6°C/hr. Since continuous operation is a design requirement and since small wall temperature differences are acceptable, it is concluded that indeed a heat exchanger is necessary.

After suitable nondimensionalization, the Lytron tube-fin heat exchanger performance can be expressed as

$$\frac{Qd}{A_x k (T_w - T_\infty)} = 1.15 P_r^{1/3} R_d^{1/2},$$

$$\frac{\Delta p}{\frac{1}{2} \rho u_x^2} = 4.0,$$

and

$$\text{Power} = 4 \cdot \frac{1}{2} \rho u_x^2 \cdot u_c A_c,$$

where Q is the rate at which heat is removed, d is the diameter of the heat exchanger tubes, A_x is the total frontal area of the heat exchanger, k is the thermal conductivity of the gas, $T_w - T_\infty$ is the temperature difference between the heat exchanger wall and the gas, P_r is the Prandtl number, and R_d is the Reynolds number based on the tube diameter and the local gas velocity u_x . For a return duct diameter of 30 cm, the temperature difference $T_w - T_\infty = 0.9^\circ\text{C}$ and the power requirement is 0.2 hp. More importantly, we can maintain a

temperature rise in the coolant water (this is a major source of the large-scale temperature variation) of 0.03°C by using a volumetric flow rate of coolant water of 10 gpm. Rather than use tap water that is usually at a far different temperature than room temperature, the design calls for a coolant reservoir, as illustrated in figure 15.

The power requirement is comparable to that required to push the gas through the acoustic material and with the return losses the total power requirement will be approximately 0.5 hp.

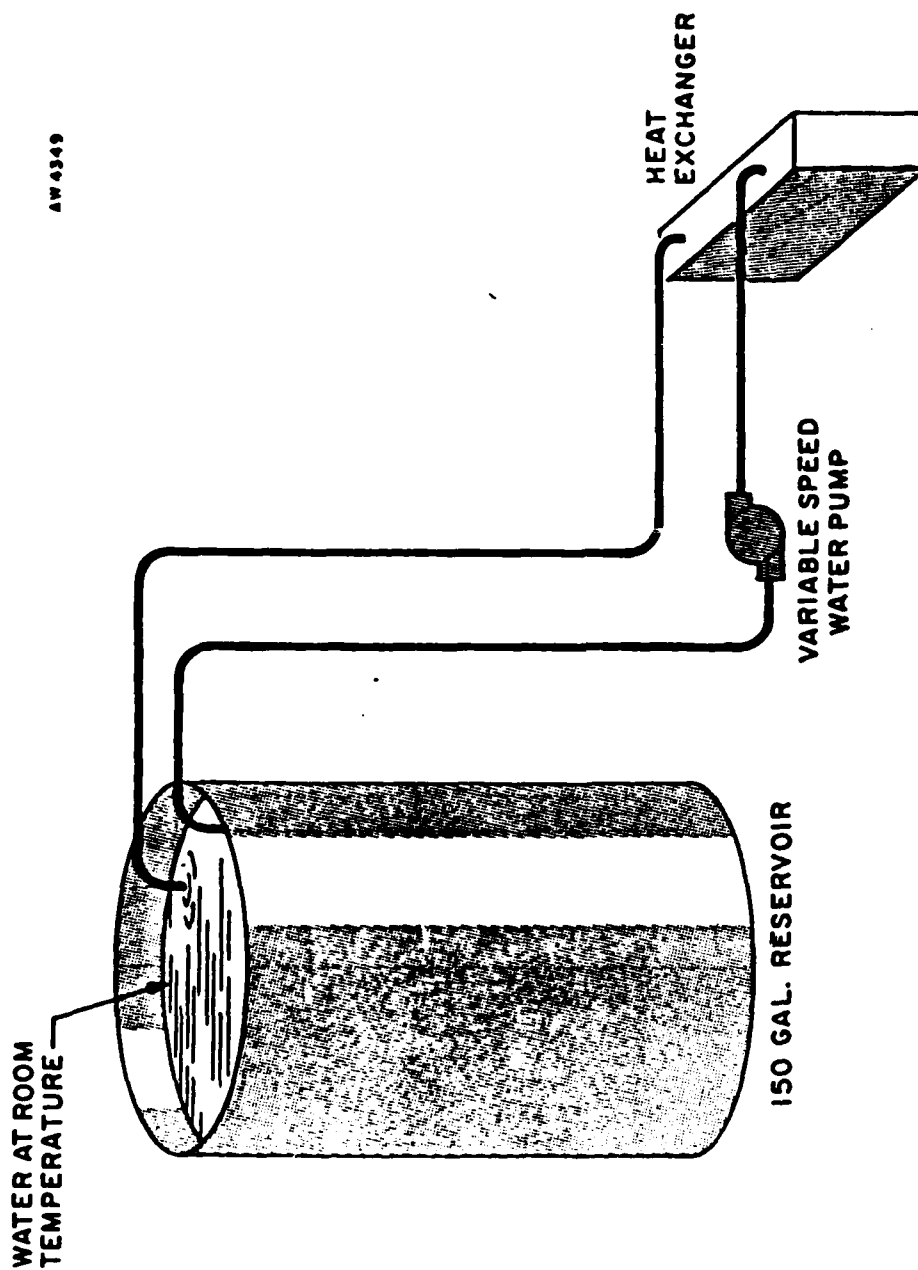


Figure 15. Coolant reservoir.

4. References

Lewis, J. E. 1982 Analytical design review of the DARPA/NRTC flowing Raman cell experiment. Poseidon Research Briefing No. 82-2.

Lewis, J. E. 1982 Preliminary design review of the DARPA/NRTC flowing Raman cell experiment. Poseidon Research Briefing No. 82-14.

Lewis, J. E. 1981 Flowing Raman cell experiment design -- A tradeoff study. Poseidon Research Memo No. 149.

Morris, J. H., Levin, J., Crow, S. C., and Hurdle, P. M. 1980 Further investigations of flow and acoustics in pulsed excimer lasers. Poseidon Research Report No. 32.

Wright, W. M. and Medendorp, N. W. 1968 Acoustic radiation from a finite line source with N-wave excitation. *J. Acous. Soc. Am.*, Vol. 43, No. 5.

END

FILMED

8-83

DTIC